

3. SITE 801¹

Shipboard Scientific Party²

BACKGROUND AND OBJECTIVES

Ocean Drilling Program (ODP) Site 801 was first drilled during Leg 129 in December 1989 as part of a series of drill sites aimed at recovering Jurassic sediment and oceanic crust in the Pacific Ocean (Lancelot, Larson, et al., 1990). The objectives of the leg were related to understanding the paleoenvironment of the Jurassic super ocean, which covered a large part of Earth at that time. Earlier attempts to recover Jurassic sediments and basement in the western Pacific had been hampered by the presence of overlying Cretaceous volcanoclastic turbidites, sills, flows, and chalk-chert horizons. Leg 129 was the first to succeed in recovering Jurassic oceanic basement in the Pacific Ocean, and the Hole 801C rocks are still the oldest (~170 Ma) sampled in the ocean basins (Pringle, 1992). The hole was reentered and logged during Leg 144, and a drill-string packer experiment was carried out to determine basement permeability (Haggerty, Silva, Rack, et al., 1995; Larson et al., 1993).

During Leg 129, ODP Hole 801C was cased to ~481 meters below seafloor (mbsf) and reached a total depth of 594 mbsf, ~130 m into the oceanic crust. Leg 185 drilling operations involved deepening the basement section of Hole 801C by an additional 341.4 m. The principal scientific objective involved definition of the primary and secondary mineralogy and geochemistry, as well as the physical properties of the Jurassic crust. The oceanic crust represented in Hole 801C is assumed to be representative of that subducted into the Mariana Trench. Although further from the trench than other potential reference sites, Site 801 offers the advantage that it is an established ODP basement hole in which deep penetration of the upper 450 m of normal Jurassic oceanic crust was considered possible in about three weeks of drilling and logging operations. Comparisons with other deep sites in oceanic basement indicated that a total penetration in excess of 400 m was considered adequate to traverse the upper oxidative zone of altered crust. This up-

¹Examples of how to reference the whole or part of this volume.

²Shipboard Scientific Party addresses.

per zone is enriched in elements such as K, U, and B and in CO₂ and H₂O, all of which are important in the geochemical budgets in the subduction factory.

The deep penetration into Jurassic oceanic crust also provided an opportunity to compare the igneous compositions, alteration styles, and physical properties of old, fast-spreading Pacific crust with other deeply drilled sections of oceanic crust of different ages and spreading rates. Site 801 was also unique in providing an opportunity to examine the magnetic nature of the basement in the Jurassic magnetic quiet zone.

Bacteria have been located in association with ridge axis hydrothermal systems and within the seafloor sediment column as deep as 800 m (Thorseth et al., 1992; Parks et al., 1994; Fisk et al., 1998; Furnes and Staudigel, 1999; Shipboard Scientific Party, 1999). The possibility that bacterial activity may occur in oceanic crust as old as that at Site 801 provided the motivation for sampling the basement for culturing and DNA extraction in the search for extremophile life. To control the extent of contamination from surface waters, drilling mud, and drilling tools, we undertook a series of contamination tests as part of the operations at Site 801.

Prior to reentering Hole 801C, a sediment core was taken with the rotary core barrel (RCB) in the top 20 mbsf, designated as Hole 801D. This core was taken as a control for microbiological tests and sampling techniques to be conducted at Site 1149. Hole 801D is described herein for sediment character, biostratigraphy, and selected physical properties.

Hole 801C is an ODP legacy hole and a geochemical reference site in the oldest in situ oceanic crust drilled on Earth.

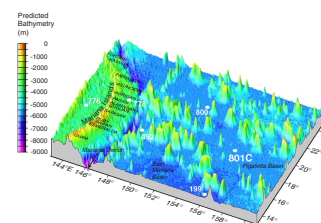
Previous Results from Basement Drilling at Site 801

Hole 801C is located at 18°38.538'N, 156°21.588'E, in 5674 m water depth in the Pigafetta Basin (Fig. F1). A seismic section showing the total penetration at the site on both Legs 129 and 185 is given in Figure F2. The sedimentary section is characterized by an upper (56 m) pelagic clay unit, which overlies a 63-m chert-porcelanite unit. These are underlain by thick (192 m) volcanoclastic turbidites of probable Albian age and represent redeposited material from the Magellan Seamount chain. A second unit, chert radiolarite (125 m), underlies the volcanoclastics and gives way to 20 m of Callovian red radiolarites and claystones. These overlie basement located at 461.6 mbsf in Hole 801B.

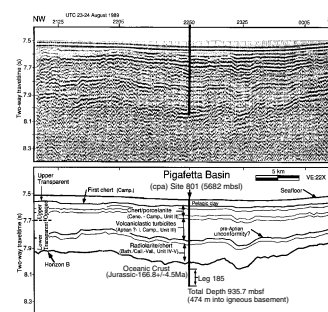
The basement cores from Leg 129 were brought on board the *JOIDES Resolution* during Leg 185 and were examined, scanned for digital photographs, scanned on the multisensor track (MST), and resampled. In this chapter, some of the data from Leg 129 basement cores has been incorporated with that for the newly cored intervals.

A simplified section of the basement recovered during Leg 129, radiometric ages, Zr concentrations, and the bulk porosity from downhole measurements are given in Figure F3. The uppermost igneous units are alkaline in character and are probably best interpreted as basaltic to doleritic sills (Floyd et al., 1992; Floyd and Castillo, 1992). Ar/Ar radiometric ages on laser-fused samples (Pringle, 1992) give a weighted mean age of 157 Ma for this alkaline unit. The igneous units are intercalated with chert-rich sediments, which are often baked at the contact with the basalt. This alkaline sequence is 60.2 m thick and overlies a Si and Fe oxyhydroxide-rich hydrothermal unit, for which logging results (Larson et al., 1993) indicate a thickness of ~20 m. Fluid temperatures of formation calculated for the deposit give temperatures of ~16°–60°C (Alt et

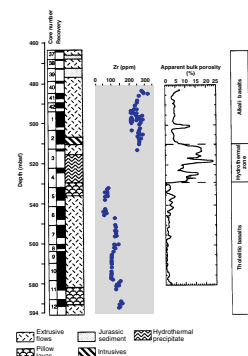
F1. Bathymetric map showing location of Hole 801C, p. 65.



F2. Seismic section and stratigraphy of Site 801, p. 66.



F3. Lithostratigraphic section of Hole 801C basement, with Ar/Ar ages and apparent porosity, p. 67.



al., 1992). These fluids controlled the alteration budget of the underlying pillow basalt, which contains celadonite, glauconite, carbonate, smectite, K-feldspar, and silica as secondary minerals.

Approximately 63 m of volcanic rock was drilled below the hydrothermal deposit. The alteration intensity is highly variable in these rocks, and their colors vary from gray black to green gray to light brown. Parts of this core were clearly altered under a high fluid flux regime. The lowermost flows, in Cores 129-801C-9R and 10R, are relatively unaltered and are highly resistive with high sonic velocities. These characteristics are further evaluated in “**Physical Properties**,” p. 35, and “**Downhole Measurements**,” p. 38. Ar/Ar fusion dates on two samples from the section below the hydrothermal deposit define the age of these lavas as <171 Ma and >162 Ma (Pringle, 1992).

Geochemical studies (Floyd and Castillo, 1992) indicate that these volcanics are normal mid-ocean-ridge basalt (MORB) tholeiites. They are olivine and plagioclase phyric and relatively primitive in composition with MgO as high as 10 wt% and Zr as low as 50 ppm. A trend to more evolved compositions, defined by higher Zr content, is observed toward the base of the hole.

Hole 801C was logged during Legs 129 and 144 and was relogged during Leg 185. The results are combined in this chapter for the entire logged section below the casing. Porosity measurements obtained during Leg 144 (Fig. F3) show the high porosities measured in the hydrothermal zone. The exceptionally high permeability of this zone was measured by Larson et al. (1993) in a drill-string packer test.

OPERATIONS

Leg 185 began at 0835 hr on 12 April 1999 with the port call in Hong Kong. At 1005 hr on 18 April the port call ended when *JOIDES Resolution* departed the Yiu Lian terminal. The planned transit of 2400 nmi to Site 801 was accomplished in near-perfect weather and calm seas. The vessel navigated to the Global Positioning System coordinates of Hole 801C and launched a positioning beacon at 1000 hr on 28 April. The transit had been accomplished in 235 hr (9.79 days) at an average speed of 10.5 kt.

Hole 801D

Immediately after the beacon launch, assembly of the bottom-hole assembly (BHA) began. Once the BHA and the vibration-isolated television (VIT) frame arrived at reentry depth, a quick search was made to locate the reentry cone of Hole 801C. When a strong sonar target had been determined to be the cone, the ship was positioned 100 m east of the cone in preparation for Hole 801D. A seafloor punch core had been requested for microbial studies; therefore, the top drive was picked up and water was pumped through the drill string at a high rate to clean it. A rotary core barrel (RCB) system inner core barrel then was pumped into place, and the drill string was lowered. Under TV observation, the core bit tagged the seafloor at a depth of 5685 m below driller's datum at 0710 hr on 29 April. To increase chances of recovering an adequate amount of the soft sediment, the bit was pushed as far as possible (19.3 m) into the seafloor. The bit then was pulled clear of the seafloor, and the inner core barrel was retrieved by wireline. About 9.4 m of soft mud was recovered when the core barrel was laid out, ending Hole 801D at

0830 hr. Because an interval greater than the length of a core barrel had been penetrated, the recovery was designated a “wash core” (1W) (Tables T1, T2).

Hole 801C

As soon as the top drive had been rigged down, the bit was repositioned for reentry. About 45 min of maneuvering were required to coax the drill string over the reentry cone. Hole 801C was reentered at 1015 hr on 29 April.

The bit then was lowered into the open hole to 468 mbsf. A water sample from the undisturbed borehole had been requested for microbial studies, and the top drive was again picked up in preparation for a sampling run with the water sampling temperature probe (WSTP). The bit was lowered without circulation to 490 mbsf, the WSTP was landed at the bit, and time was allowed for the preset timer to open the sampling valve. Upon recovery of the WSTP, however, no sample had been collected. A second WSTP attempt then was made with the bit lowered to 540 mbsf, just below a known interval of unstable hole. A good water sample was obtained, and the pipe trip continued with the top drive deployed and a RCB inner core barrel in place.

An obstruction, or “bridge,” that had stopped logging tools in this hole during Leg 144 was encountered by the drill string at 546 mbsf. The obstruction was cleared easily with rotation and circulation, but the effect of “pushing something down the hole” was noted. Rubbly fill was encountered ~3 m off the recorded total depth. The fill was washed to total depth at 594.3 mbsf, where torque and rough running indicated the presence of loose rocks on the bottom of the hole. After a few minutes, the rocks were broken up and the coring of Core 13R began (Tables T1, T2).

Continuous RCB coring then proceeded under ideal weather and motion conditions for 3 days. The first two cores were cut at a rate of penetration (ROP) of ~2.0 m/hr. The ROP increased slightly on each core because of increasingly fractured rocks with an accompanying downtrend in recovery from excellent to low (i.e., from 89% in Core 15R to 32% in Core 20R). Anomalous drilling parameters on Core 21R (i.e., an abrupt decrease in ROP accompanied by increased drill string torque and slightly low circulating pressure readings), and over 36 rotating hr on the bit were considered sufficient reason to trip the drill string for a bit change. Average recovery for the 79.3 m cored with Bit No. 1 was 52%. At 2230 hr on 2 May, the core bit arrived on deck and was found to be in excellent condition, with bearing seals still effective and only a few broken tungsten carbide inserts.

Reentry scanning began at noon on 3 May after pipe tripping with Bit No. 2. Maneuvering for reentry consumed a frustrating 5 hr, primarily because of the subdued response of the long drill string to changes in the ship’s position. Reentry was made at 1700 hr, and the bit was run into the hole without incident. Coring of Core 22R began at 2200 hr on 3 May. Core recovery and ROP were quite variable, but there was a trend toward more massive rock units with depth with resultant higher recovery and lower penetration rates. Weather and hole conditions remained good, and 83 m of new hole was made before the bit was tripped on the basis of its 47.7 rotating hr. Core recovery for the interval was 44%.

A third bit was installed, and the drill string was tripped back toward the seafloor. After 7 hr lost to repairs of the cable head of the VIT and

T1. Coring summary, p. 170.

T2. Expanded coring summary, p. 171.

subsequent problems with flooding of the short oil-filled cable that connects the coaxial cable head to the telemetry pod of the VIT, maneuvering for reentry began at 0200 hr on 8 May. Again, the inhibited response of the long drill string to ship movement slowed the operation. At 0538 hr, a successful reentry stab was made. The trip into the hole was uneventful except that 14 m of soft fill was found. It was removed without difficulty, and coring recommenced at 1030 hr, 8 May. Core recovery and ROP were quite variable, with both the highest (i.e., 3.3 m/hr) and lowest (i.e., 1–2 m/hr) penetration rates to date encountered within the interval. Coring continued without incident through Core 42R at 869.1 mbsf. At that depth the bit had accrued 50 rotating hr, and the trip began for the fourth RCB bit. Bit No. 3 cored 112.5 m at an average ROP of 2.2 m/hr and with average core recovery of 53.5%.

A fourth RCB bit was tripped to the seafloor, and the swinging of the pipe was less troublesome with reentry accomplished in only 24 min of maneuvering time. Coring resumed at 869.1 mbsf at 0100 hr on 13 May. The first four cores were in altered pillow basalt units and produced relatively low recovery at fairly high penetration rates. On the next two cores, penetration slowed in fractured flow units, but recovery did not improve correspondingly. The bit run cored 57.1 m with an average ROP of 2.1 m/hr and an average recovery rate of 34.9%. To divide the remaining site operating time between logging operations and coring with the diamond core barrel (DCB) system, coring was stopped with only 27.3 rotating hr on Bit No. 4.

Diamond Core Barrel System Test

Two additional days had been allocated to Leg 185 for testing the DCB system. A 7¼-in diamond core bit with “carbonado” stones was selected for coring basalts. The drill string and VIT were run to reentry depth, and another quick reentry of ~10 min was achieved. Because more than 90 m of hole fill had been encountered by the logging operation, considerable caution was used on the return to total depth. The hole then was cleaned out to firm resistance, which was felt at 928.3 mbsf, 2.1 m deeper than the bottom of the previous core. The discrepancy was interpreted to be because of a difference in pipe stretch caused by the 40,000 lb difference in BHA weight between the two strings.

Coring with the diamond core bit deepened the hole by 7.4 m in 20.5 hr, and core recovery averaged 42% in hard, fractured basalt (Tables T1, T2). Although the DCB cut very slowly through the basalt, the recovered core appeared to contain more delicate features, such as complete interpillow hyaloclastites and abundant veins, than is typical for RCB core.

After the test was concluded, the drill string and the original acoustic beacon were recovered without incident. The 6¾-in drill collars were returned to the drill collar racks, the rig was secured for sea, and *JOIDES Resolution* departed Site 801 at 1330 hr on 19 May.

SEDIMENTOLOGY AND BIOSTRATIGRAPHY

Lithostratigraphy

Coring at Site 801 started with a mudline core from Hole 801D that was cored with the RCB from the seafloor down to 19.3 mbsf. The relationship between the depth in core to the actual depth below sea level is

not clear. The zeolite-bearing brown clay from Core 185-801D-1W is attributed to lithologic Unit I as defined during Leg 129 (Shipboard Scientific Party, 1990).

Unit I, Brown Pelagic Clay

Intervals: 129-801A-1R to 7R-4, 29 cm, and 185-801D-1W
Depth: 8.0–63.8 mbsf (Hole 801A) and 0.0–19.3 mbsf (Hole 801D)
Thickness: 55.8 m (Hole 801A) and at least 19.3 m (Hole 801D)
Age: Cenozoic to Maastrichtian–Campanian? (Hole 801A) and Holocene to Oligocene (Hole 801D)

The homogeneous, dark reddish brown pelagic clays with zeolites in Core 185-801D-1W are identical to the lithofacies encountered in that depth interval at Site 801 of Leg 129. The sediment is carbonate free and mostly consists of colorless to reddish brown aggregates of clay to very fine silt size. These “red brown semi-opaque objects” are common in the pelagic brown clays at other Pacific sites (Yeats, Hart, et al., 1976). The clay becomes slightly darker downcore, but no corresponding compositional change was observed in smear slides. Zeolites are rare to common, but very conspicuous components, because there are hardly any other silt-sized or larger grains. Euhedral specimens display crystal habits, common brown inclusions, and etched crystal faces that are typical for phillipsite (Kastner, 1979). Many phillipsite crystals are twinned, some showing perfect cross twinning or complex-sector twinning. Accessory components include rare ichthyoliths, Mn micronodules, and trace amounts of volcanic glass, detrital quartz, and one suspect greenish tectite particle.

No bedding planes and only one potential burrow were observed in the core. The reason for the virtual lack of sedimentary structures is not entirely clear. The presence of tracer beads in the central parts of this core may suggest that the homogeneous aspect of the sediment is due to drilling disturbance (see “[Hole 801D](#),” p. 54), but their presence may also be related to the very high porosity of the sediment as suggested by the low bulk density (see “[GRAPE Density Measurements](#),” p. 36). Except for the uppermost 25 cm of the core, which is soupy, the clays resist gentle deformation. The relatively firm nature of the clays leads us to assume that severe drilling-induced disturbance was limited to the soupy interval at the core top and that the lack of structures is not drilling related. Original absence of compositional differences seems equally unlikely because it would imply that sedimentation did not change during the >10-m.y. interval represented by the core (assuming a sediment accumulation rate of <1 m/m.y.; Shipboard Scientific Party, 1990). As an alternative, we propose that the lack of discernible bedding planes and of discrete burrows is an effect of pervasive bioturbation. This is supported by the red sediment color, which suggests that oxygenation was sufficient to allow benthic activity to be vigorous enough to disrupt any original sedimentary structures. Moreover, the correct stratigraphic order of ichthyolith (fish remains) assemblages, which consistently testifies to a younging toward the top of the core (see “[Biostratigraphy](#),” p. 7), is incompatible with pervasive drilling disturbance of the sediments.

Unit VI, Interpillow Radiolarian Chert and Radiolarian Limestone

Intervals: 129-801B-37R-1, 7 cm, to 44R-3, 47 cm, and 185-801C-14R through 16R
Depth: 461.6–590.9 mbsf
Age: Callovian or older

During Leg 185, interpillow sediments were recovered from ~90 m below the lowermost interpillow sediments recovered during Leg 129. The corresponding lithologic unit during Leg 129 was labeled “interbedded basalt and silicified claystone (chert).” We describe here only those materials that contain at least some pelagic material. During Leg 185, bright-colored sedimentary interpillow material was found ~150 m below Bathonian–Callovian (middle Jurassic) dated chert in Core 129-801B-39R and ~90 m below the deepest occurrence of interpillow material in Core 129-801C-5R to a total depth of 156 m into basement. Various brown-colored and dusky red to dusky green chert and epitaxially recrystallized radiolarian limestone, as well as siliceous, yellowish brown alteration material, were found to contain spherical and cone-shaped objects that resemble radiolarians under the binocular microscope (see “Biostratigraphy,” below). Occasionally, bedding surfaces in the chert and sand-sized chert intraclasts record redeposition phenomena.

Biostratigraphy

Pelagic brown clays cored in Hole 801D are barren with respect to calcareous and siliceous microfossils but contain fairly well preserved ichthyolith assemblages. The >250- μm fraction contains only few ichthyoliths, whereas the >64- μm fraction contains common to abundant ichthyoliths. The core catcher and three additional samples were studied to obtain biostratigraphical constraints on these otherwise unfossiliferous clays. More than 40 species were recognized in the well-preserved assemblages. Many long-ranging species were recorded in the four studied samples, such as *Rectangular saw-toothed*, *Triangle with triangular projection*, *Triangle with high inline apex*, *Triangle with base angle*, and *Five peaks irregular base*. The occurrence of *Narrow triangle ragged base* in Sample 185-801D-1W-2, 32–40 cm, points to a late Miocene or younger age. In Sample 185-801D-1W-4, 80–88 cm, ichthyoliths are abundant; the last downhole occurrence of *Circular with line across* is recorded, indicating a middle Miocene age for this sample. The assemblage in Sample 185-801D-1W-6, 50–58 cm, records the last downhole occurrence of *Three narrow peaks* and the first downhole occurrence of *Plain ellipse*, suggesting an early Miocene age. Sample 185-801D-1W-CC contains *Skewed four or five peaks*, *Polygonal cavity*, *Polygonal cavity long rays*, *Flexed-triangle shallow inbase >120*, and *Five peaks flared base*. Co-occurrence of these species indicate a late Oligocene to early Miocene age for this sample, according to Doyle and Riedel (1985) and Firth and Hull (1993). Many undescribed morphotypes occur in the studied samples, together with several specimens that resemble undescribed morphotypes of possible Cretaceous samples. If this interpretation is confirmed by shore-based studies, the clays in Core 185-801D-1W could show reworking of Cretaceous sediments during the middle Miocene.

Interpillow sediment from Leg 129 was used for preliminary radiolarian biostratigraphic analysis. Precise dating of the basal sediments at

Site 801, where the oldest (middle Jurassic) in situ oceanic crust has been recovered, is extremely important (1) in calibrating the oldest M-sequence magnetic anomalies, (2) to developing a Jurassic time scale for estimating seafloor spreading rates for the Pacific, and (3) improving plate tectonic models for the Pacific and other areas. During the transit from Hong Kong to Site 801, radiolarites from Cores 129-801B-37R, 39R, and 40R were resampled. The main objectives were to (1) revise the data of Matsuoka (1991, 1992) in light of the new data on radiolarian occurrence, systematics, and biochronology and (2) obtain a more precise age of the basal sedimentary unit (Unit V) and of the chert interbedded with basalts (Unit VI).

Unit V consists of alternations of red radiolarite and claystones; Unit VI is composed of interbedded basalt and silicified claystone (chert) (Shipboard Scientific Party, 1990). Matsuoka (1991) studied in detail two samples from the lower part of Unit V (Samples 129-801B-37R-1, 16–20 cm, and 35R-3, 24–26 cm). The faunal assemblage characterizes the middle part of the *Tricolocapsa conexa* Zone (Matsuoka, 1983; Matsuoka and Yao, 1986). Most of the species found have also been reported from the central Atlantic (Baumgartner, 1984; Yamamoto et al., 1985) and western Tethys regions (Baumgartner, 1984, 1987). Based on the correlation with the zonation proposed by Baumgartner (1984, 1987) for the Tethyan radiolarites, Matsuoka (1991, 1992) assigned a Bathonian–Callovian age to the *Tricolocapsa conexa* Zone. According to the most recent radiolarian biozonation of the INTERRAD Jurassic–Cretaceous Working Group (1995) Sample 129-801B-35R-3, 24–26 cm, can be attributed to the UAZ 6 (mid-Bathonian) and Sample 129-801B-37R-1, 16–20 cm, to the UAZ 5–6 (latest Bajocian–mid-Bathonian) (Matsuoka, 1995).

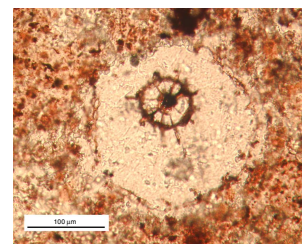
In this study, two new samples (Samples 129-801B-37R-1, 0–6 cm, from Unit V and 39R-1, 8–11 cm, from Unit VI) were examined in detail. Radiolarians are abundant, but preservation is generally poor. With careful hand picking it was possible to identify several specimens to the species level. Table T3 lists radiolarian species from the two samples. Thirty-five species are identified in Sample 129-801B-37R-1, 0–6 cm, and ten species in Sample 129-801B-39R-1, 8–11 cm. The difference in species diversity between the two samples may be because of the difference in preservation. In Sample 129-801B-37R-1, 0–6 cm, the co-occurrence of *Orbiculiforma* (?) sp. X, *Hexasaturnalis tetraspinus*, *Tricolocapsa* (?) sp. aff. *T. fusiformis*, and *Spongocapsula perampla* characterizes the UAZ 6 (mid-Bathonian). The faunal combination in Sample 129-801B-39R-1, 8–11 cm, of *Guexella nudata*, *Stichocapsa robusta*, *Ristola* (?) *turpicula*, *Orbiculiforma* (?) sp. X, and *Tricolocapsa* (?) sp. aff. *T. fusiformis* indicates the UAZ 5–6 (latest Bajocian–mid-Bathonian).

Based on the new work described here, and the new biochronology since Leg 129, we propose a revised age for the basal sediments at Hole 801C to latest Bajocian–mid-Bathonian. Shore-based studies may allow refinement of this age assignment.

Moreover, thin sections from Hole 801C interpillow material, which occurs ~170 m below these dated sediments, have revealed spherical and cone-shaped radiolarian morphotypes that belong to the spumellarian and nassellarian suborders (Fig. F4), as well as common fecal pellets.

T3. Radiolarian taxa, p. 176.

F4. Well-preserved internal structure of a radiolarian, p. 68.



Depositional History

Pelagic Brown Clays

The pelagic brown clays recovered at Hole 801D belong to a widespread depositional facies of the Cenozoic to Holocene Pacific. These clays are characterized by a deficiency in biogenic, volcanogenic, and terrigenous particles (e.g., Murray and Renard, 1891; Arrhenius, 1963). The lack of calcareous microfossils points to a deposition well below the Cenozoic open-ocean calcite compensation depth (CCD) (Berger, 1970). In addition, the absence of siliceous microfossils suggests that the clays were deposited below oligotrophic waters, similar to modern sediments from below the North Pacific Gyre (Davies and Gorsline, 1976). The rarity of volcanic and terrigenous detritus attests to distal position of the drill site. The very low accumulation rates on the order of <1 m/m.y., the relative abundance of ichthyoliths, and the presence of a suspect tectite fragment corroborate this interpretation.

Interpillow Radiolarian Chert and Limestone

Interpillow cherts and limestones recovered in Core 185-801C-13R and below contain replaced radiolarian tests as well as fecal pellets. These sediments were trapped between pillows and sheet flows, and the elevated temperatures associated with pillows and flows are likely to be responsible for the partial recrystallization of the sediment (see "[Base-ment Alteration](#)," p. 18). The presence of microfossils and metabolic products of organisms that thrive in the photic zone of the ocean suggests that normal pelagic sedimentation contributed, at least partly, to the interpillow material. Scarce nannofossils found during Leg 129 and the carbonate-bearing lithologies may either indicate deposition above the Middle Jurassic CCD or special conditions to enable the preservation of carbonate (Shipboard Scientific Party, 1990). The absence of carbonate in the sediments overlying the volcanic basement suggests that Site 801 had subsided to below the CCD by the end of volcanic eruptions.

Summary

The sedimentary section at Site 801 had already been drilled during Leg 129, and recovery of sediments during Leg 185 was limited to a wash core (Hole 801D) and to the interpillow sediment (Hole 801C) that is interbedded with basalts below 594 mbsf. Pelagic brown clays from the wash core contain very little terrigenous material and testify to the distal position of Site 801. The clays are barren with respect to calcareous and siliceous microfossils, but they contain rich ichthyolith assemblages that indicate a late Miocene to late Oligocene age for this core. Accumulation rates were on the order of <1 m/m.y., a value that is characteristic of the distal Pacific, away from volcanic arcs, riverine terrigenous input, the Asian dust plumes, or the oceanic zones of high biological productivity. The interpillow sediment consists of dusky red and dusky green cherts and recrystallized radiolarian limestone and is found more than 150 m below the sediment/basement contact; bedding surfaces and radiolarian ghosts are occasionally preserved.

BASEMENT STRATIGRAPHY

Introduction

A total of 339.30 m of basement was cored during Leg 185 (Cores 185-801C-13R through 52M), deepening Hole 801C to 935.70 mbsf. Recovery averaged 47.28%, with six cores having 80% recovery and six cores having 20% recovery (Figs. F5A, F5B, F6; Table T4). Cores 185-801C-14R through 17R at the top of the cored interval had good recovery (average = 71.85%), and Cores 18R through 26R had relatively poor recovery (average = 41.75%). Recovery improved again from Cores 27R through 31R (average = 66.44%) and then deteriorated toward the base of the hole. In general, the intervals of good recovery correlated with the presence of thicker massive flow units in the cores, whereas the intervals of poorer recovery coincided with zones of thinner and more fractured or altered units dominated by pillow basalts, interpillow material, and breccia (see Fig. F5A, F5B).

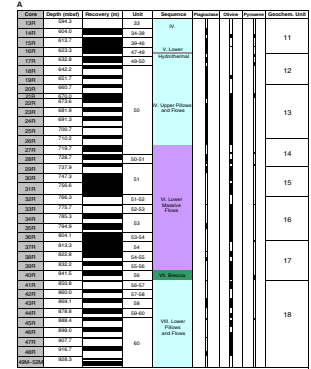
The rocks recovered from Hole 801C during Leg 185 are primarily aphyric basalts. Minor amounts of plagioclase and olivine were observed as phenocryst phases, but they were rarely abundant enough to permit the addition of a mineral modifier to the rock name. Rarely basalts contained 1%–2% phenocrysts, and these were classified as sparsely aphyric. The aphyric basalts include a mixture of thick massive flow units, thinner (<50 cm) pillow-dominated units, and some intermediate thickness (50 cm to 1 m) units that could represent either pillows or flows. In addition, a hydrothermal unit was encountered in Core 185-801C-16R, and several intervals of breccia, hyaloclastite, and interpillow or interflow recrystallized sediment were obtained throughout the cored section (Fig. F7).

The lithology in Hole 801C (see Fig. F5A, F5B) has been summarized, on the basis of basement stratigraphy and geochemical and logging data, into major eruptive sequences (numbered in roman numerals) comprising an upper section of alkali basalts (I) and tholeiitic massive flows (III) separated by a hydrothermal zone (II) at 510–530 mbsf. Beneath these massive flows, in the material drilled during Leg 185 (>590 mbsf), there is a section consisting of pillows and flows (IV) and a lower hydrothermal zone (V) at 625 mbsf. Between Cores 185-801C-26R and 27R, at 720 mbsf, there is a major change in the cooling unit thickness, which correlates with a break on the gamma and resistivity logs (Fig. F5B). This change marks the top of the lower sequence containing massive flows (VI). Beneath these flows (840 mbsf) there is a thick breccia sequence (VII), and toward the base of the hole (850–930 mbsf) the cooling unit thickness decreases again in the lower section, which consists of pillows and thin flows (VIII).

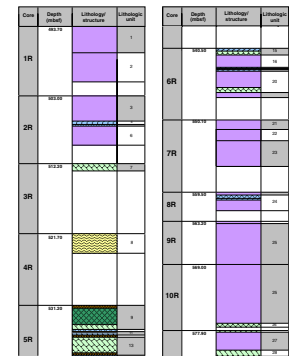
Lithologic Units

The last core retrieved from Hole 801C during previous drilling at this site, Core 129-801C-12R, is characterized by a 2.5-m-thick aphyric basalt flow. This flow was given the unit number 32. Lithologic units assigned during Leg 185 are numbered beginning with Unit 33 (i.e., numbering is continued from the end of Leg 129). In total, 28 units were identified, although most of these contain subunits of breccia or individual cooling units. Lithologic units were assigned on the basis of a major change in lithology or a change in basalt mineralogy. Some of these, for example Unit 50, are continuous over many cores (Cores 185-

F5. Summary of lithology, p. 69.

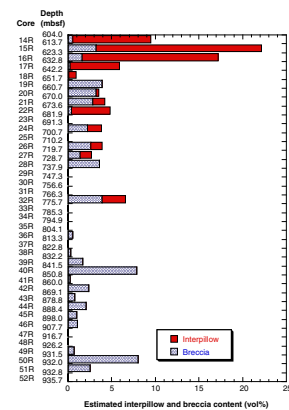


F6. Basement stratigraphy and unit boundaries, p. 71.



T4. Igneous core description log, p. 177.

F7. Volume percent of breccia and interpillow materials, p. 77.



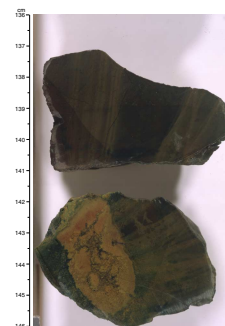
801C-17R through 28R); in this case subunits were identified on the basis of the presence of glassy contacts or fining of grain size toward the margins of flows. Thin intervals of sediment or interpillow material and breccia were noted as boundaries between subunits, whereas thicker intervals were distinguished as individual subunits when they were >5–10 cm.

The basement stratigraphic log (Table T4; also see 801_MIN.XLS in the “Supplementary Materials” contents list) includes all the igneous core description data for Leg 185 Hole 801C: unit or subunit number, depth, interval thickness, lithology, texture, structure, color, presence or absence of chilled margins, comments, and the location of shipboard samples. The log also includes the same information for Cores 129-801C-1R through 12R recovered during Leg 129. The igneous stratigraphy for all of Hole 801C (data from both Legs 129 and 185) is plotted as a stratigraphic column (Fig. F6; also see the Igneous Mineralogy Description Logs in the “Supplementary Materials” contents list). Primary igneous structure was described on the basis of the size of the units: units or subunits >1 m in thickness were denoted as flows, those between 50 cm and 1 m in thickness were noted as either pillows or flows, and those <50 cm in thickness were noted as pillows. Descriptions of the more important characteristics of Leg 185 Hole 801C lithologic units are presented in the following paragraphs.

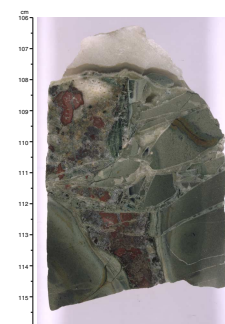
The first core recovered, Core 185-801C-13R, contained only one section consisting entirely of debris that was probably dislodged from the walls of the hole at the end of Leg 129 or when logging during Leg 144. The debris included several pieces of aphyric basalt, some interpillow material, and a piece from the distinctive hydrothermal unit in Core 129-801C-4R (Unit 8). These pieces were assigned to Unit 33. Unit 34, observed in Core 185-801C-14R, consists of a 2-m-thick aphyric basalt flow, similar in character to Unit 32, which was drilled during Leg 129. The upper contact of this flow was not observed, and the lower contact of the flow in Unit 32 was not observed in Core 129-801C-12R; therefore, it is possible that these two units are continuous. Beneath this flow, still in Core 185-801C-14R, a sequence of pillow lavas (Units 35 and 37) was encountered, separated by cherty pelagic sediments (Unit 36). Unit 38 is also characterized by a sequence of pillows and thin flows. The pillows and/or thin flows vary in thickness from 11 to 68 cm. Curved and chilled or glassy pillow rims were commonly observed, and recrystallized cherty sediments (Fig. F8), hyaloclastite, and breccia intervals (Fig. F9) were commonly encountered between pillows. This sequence of thin pillows and interpillow materials (Fig. F10) continues into Core 185-801C-15R, Units 39–43. Units 44 and 45 both represent single flows; Units 46, 47, and 49 are mixed units containing thin flows, pillows, interpillow sediments, and breccias. Unit 48 in Core 185-801C-16R is a distinctive marker horizon useful for correlating the recovered core section with the downhole logs. It consists of a highly silicified yellow-brown hydrothermal deposit (Fig. F11), very similar in character to the hydrothermal deposit Unit 8 in Core 129-801C-4R. Both above and below the lower hydrothermal deposit, there are intervals of highly altered and recrystallized interflow sediments.

Unit 50 contains a sequence of aphyric basalt pillows and flows that vary in thickness, although thinner flow units and pillows predominate. The recovery of this unit is relatively poor, with the recovery possibly biased toward thicker units. Thus, there may be even more pillows and interpillow material within the cored section than we recovered. Varying proportions of interpillow recrystallized sediment (e.g., see

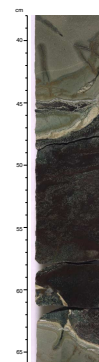
F8. Cherty interpillow sediments, p. 78.



F9. Basalt and interpillow breccia, p. 79.



F10. Pillow margins without glass, p. 80.



F11. Contact between Unit 48 and interpillow material, p. 81.



Figs. F12, F13), hyaloclastite (Fig. F14), and breccia are observed between some of the cooling units, and where these intervals are thicker than 5 cm they are identified on Figure F6 as individual subunits. Contacts were not always observed; therefore, cooling units were defined using chilled or glassy pillow or flow margins (Fig. F15), or obvious changes in grain size. The subunits in Unit 50 of which there are 76, range up to 2 m in thickness with one thicker, 4.5-m flow found in Core 185-801C-27R.

Unit 51 (Cores 185-801-29R through 31R) is distinctive in that it contains two massive flows, 7.0 and 9.3 m thick, respectively. Units 52 and 53 are again mixed units, consisting of thin flows, pillows, and breccias (e.g., see Figs. F16, F17), although flow thickness appears to increase progressively toward the base of Unit 53. Unit 54 in Cores 185-801C-36R through 38R contains the thickest flow, 12 m in thickness. It is also the coarsest flow, microcrystalline at its margins grading to medium grained in the center. This flow contains an unusual distribution of vesicles (see Figs. F18, F19), a number of thick veins, and intensely altered patches (see “Basement Alteration,” p. 18). Units 55, 58, and 60 are again mixed units, dominated by thinner flow and pillow units. Units 57 and 59 are single flows. Unit 56 is a 5.0-m-thick breccia interval, where the basalt clasts are angular to subangular, ranging in size from <1 to 40 cm. The larger clasts, however, are often fragmented and cut by veins. The cement is carbonate rich toward the top of the unit and saponite rich toward the base of the unit. Because of its thickness, we interpreted the breccia as tectonic and possibly fault related, as opposed to being a brecciated flow top or base. Slickenlines were observed on some vein surfaces within this unit, which lend support to the tectonic interpretation.

Contacts, Presence of Glass, Changes in Grain Size, and Presence of Vesicles

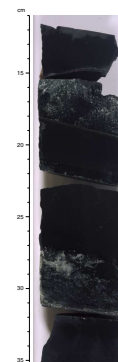
The contacts of many of the thicker and more massive flows were not recovered, and in these cases, cooling units were identified on the basis of the presence of chilled margins (e.g., Fig. F15), changes in grain size from fine grained to microcrystalline or hypocrySTALLINE at the flow margins, or changes in lithology. Contacts between pillows were rare, although for some adjacent pieces both had glassy rims, as would be expected at the margins of stacked pillows. Fresh glass is present in several places (see Table T5), in particular in Cores 185-801C-18R, 28R, and 42R, nearly always associated with pillow rims or hyaloclastite intervals.

Grain size is fairly uniform downhole. Most of the basalts are microcrystalline, occasionally with hypocrySTALLINE or glassy margins, whereas thicker units or more massive flows tend to grade toward fine grained in the center. Only the thickest flow, in Unit 54, reaches medium grain size (>1 mm). Small vesicles (up to 1 mm in diameter) are present in most of the samples, whereas larger vesicles (>5 mm in diameter) are more rare. Again, only Unit 54 contains a significant proportion of these larger vesicles, which are occasionally aligned along a specific horizon (e.g., see Fig. F18). The distribution of vesicles is often quite variable over short distances. For example, in Section 185-801C-37R-2, there is a change from an absence of vesicles to a significant proportion (5%–10%) of vesicles over a distance of only 20 cm (see Fig. F19).

F12. Basalt flow base and recrystallized sediment, p. 82.



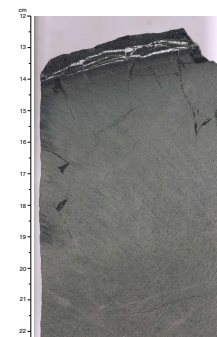
F13. Thin flow units with basalt clasts, p. 83.



F14. Altered hyaloclastite, p. 84.



F15. Glassy rim of an aphyric basalt pillow, p. 85.



Breccia and Hyaloclastite

Brecciated intervals are fairly common within the cored section. Both cement-supported and clast-supported varieties are present. Breccias were only recorded as units or subunits if the interval thickness was >10 cm. In most cases highly fractured and broken pillows with filled fractures were considered largely as in situ pillows; the term breccia is reserved for cement-supported breccias (see Fig. F17). Hyaloclastite intervals are encountered less commonly and over smaller intervals, particularly within pillow sequences (e.g., in Section 185-801C-19R-2). The hyaloclastites are often preserved on the outer edge of chilled or glassy pillow rinds, and they consist of glassy shards and fragments in a carbonate and saponite cement (Fig. F14). Some of the hyaloclastite breccia intervals (e.g., interval 185-801C-28R-3, 53–59 cm) contained fresh glass (Fig. F16).

Sediments and Undifferentiated Interpillow or Interflow Material

Interflow or interpillow sediments occur in the upper part of the cored interval. The last appearance of chert as interpillow material downhole is in Core 185-801C-17R, at 637.2 mbsf. The interflow or interpillow sediments (see Fig. F8) are described in *“Sedimentology and Biostratigraphy,”* p. 5, and are, therefore, not included here. Interpillow material is distinguished from breccia by the absence of angular clasts of basalt and/or glass. Interpillow material (including metasediment, metavolcaniclastics, and alteration phases) occurs in Cores 185-801C-14R through 18R (Figs. F10, F11, F12, F13), 20R to 22R, 25R to 27R, and 32R. Below Core 185-801C-32R, interpillow materials were not observed, but volcanic breccias and hyaloclastites are present down to the bottom of the hole. Interpillow material is documented in detail (see the *“Site 801 Vein Log,”* p. 230; also in *ASCII format*) and is also noted in the igneous core description log (Table T4) for intervals >5 cm. Interpillow material makes up 2.5% of material cored in Hole 801C during Leg 185. The volume percent of interpillow material per core is shown in Figure F7 and is plotted with the volume percent of breccia intervals. Overall, the volume percent of interpillow material decreases downhole, from 19% to 1% for Cores 185-801C-15R to 18R. Beyond Core 185-801C-18R, until it disappears after Core 32R. Interpillow material ranges from none observed to 5% per core. The nature and occurrence of interpillow material is discussed in further detail in *“Basement Alteration,”* p. 18.

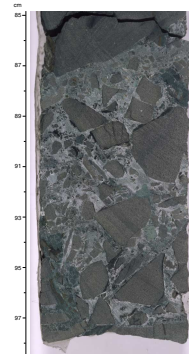
Hydrothermal Unit

A massive, yellow-stained, silicified, Fe-rich hydrothermal unit (Unit 48) occurs in Sample 185-801C-16R-3, 0–43 cm (see Fig. F11). This unit is very similar to Unit 8 in Core 129-801C-4R (Shipboard Scientific Party, 1990), which was interpreted to be a hydrothermal deposit formed by precipitation of iron and silica from low-temperature hydrothermal fluids. However, sedimentary laminations were also observed (Shipboard Scientific Party, 1990), suggesting a sedimentary contribution. Sublinear, contorted laminations observed in Unit 48 also suggest a sedimentary contribution to this material, which was later cemented by silica.

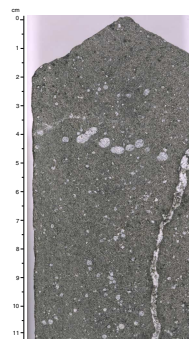
F16. Hyaloclastite breccia, p. 86.



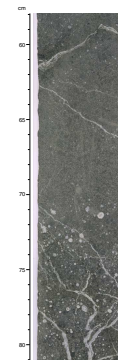
F17. Aphyric basalt breccia, p. 87.



F18. Aphyric basalt with carbonate-filled vesicles, p. 88.



F19. Variable distribution of vesicles, p. 89.



T5. Location of volcanic glass, p. 194.

Summary

The major part of the cored basement consists of aphyric basalts having either flow or pillow structure. Numbered from the base upward, the summarized volcanic sequences (Fig. F5A, F5B) in Hole 801C basement are pillow basalts and minor flows (VIII; >850 mbsf); a breccia sequence (VII; 840–850 mbsf); thick lava flows (VI), some of which approach 15 m in thickness with well-defined rubbly bases (720–850 mbsf); a pillow-dominated zone (IV) with well-developed interpillow horizons (595–720 mbsf); and an ocherous, Fe-Si-rich, low-temperature hydrothermal unit (V) occurring within Sequence IV (630 mbsf). The upper pillows and flows above the lower hydrothermal unit have abundant interpillow sediments, some of which contain radiolarians. The presence of pelagic sediments in the igneous units above signals quiescence in igneous activity, or possibly off-axis eruptions. Three sequences were defined for the section drilled during Leg 129. These are upper massive flows (III), upper hydrothermal sequence (II), and alkali basalts (I). The ocherous hydrothermal units are unique to Hole 801C. Although similar types of deposits exist near the modern East Pacific Rise and elsewhere on the seafloor, they have never been drilled elsewhere in oceanic basement. Fresh glass was recovered in more than 20 cores and is the oldest fresh glass recovered from the oceans.

IGNEOUS PETROLOGY AND GEOCHEMISTRY

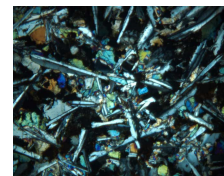
Petrology

The mineralogy of the igneous rocks recovered during Leg 185 from Hole 801C was estimated for several pieces per section by hand lens and binocular microscope identification. The results are noted in 801_MIN.XLS (see the “[Supplementary Materials](#)” contents list) and are summarized in the visual core description logs (see the “[Core Descriptions](#)” contents list). In addition, a total of 83 thin sections from Hole 801C were investigated during Leg 185, including seven from the Leg 129 basement cores. The thin sections from Leg 185 were chosen within representative lithologies, generally coinciding with X-ray fluorescence (XRF) samples, as well as within specific features, such as contacts, veins, phenocryst-rich intervals, and highly altered intervals. The approximate proportions and sizes of minerals (groundmass and phenocrysts) in thin section were estimated for both primary and secondary minerals. The thin-section descriptions are included in “[Site 801 Thin Sections](#),” p. 133. The primary mineralogy is summarized in Table T6.

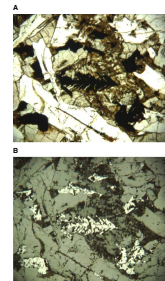
Generally, the igneous rocks recovered in Hole 801C during Leg 185 are aphyric to slightly phyric plagioclase- and/or olivine-bearing basalts. Euhedral plagioclase laths of an average size of 0.1–1.4 mm are present in each thin section as a major part (35%–60%) of the groundmass (Fig. F20). Subhedral pyroxenes ranging from 0.02 to 0.6 mm form the second major constituent (12%–45%) (also in Fig. F20). Small (<0.01–0.1 mm) dispersed oxides (mainly magnetite) are always present, typically with an euhedral or skeletal morphology (Fig. F21A, F21B). Olivine is rare (<10%) in the groundmass and when present is always altered (Fig. F22A, F22B). It is found in euhedral to subhedral forms ranging from 0.04 to 0.4 mm in size. The last major constituent of the groundmass is interstitial cryptocrystalline, brownish devitrified

T6. Summary of primary mineralogy, p. 196.

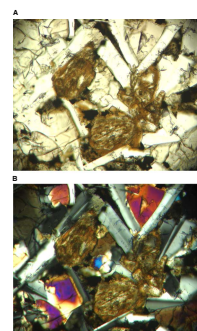
F20. Typical groundmass of the basalts, p. 90.



F21. Skeletal magnetites, p. 91.



F22. Saponite-altered olivines, p. 92.



glass (Fig. F23). Basalts that consist of >40% interstitial material (or glass) are typically found in or near chilled pillow or flow margins and are, therefore, denoted as chilled basalts. Many of these chilled basalts contain fresh glass, but a complete spectrum from fresh (Fig. F24) to devitrified (Fig. F23) was observed; some basalts contain up to 30% devitrified glass (Fig. F25). Vesicles are ubiquitous in all thin sections but generally make up 1%, except in Sample 185-801C-37R-3 (Piece 1A, 37–40 cm) (thin section [TS] 62) where vesicle content approaches 10%.

The crystallinity of the basalts investigated ranges from holohyaline in chilled margins (e.g., TS 24; Sample 185-801C-16R-5, 107–110 cm) (Fig. F26) to holocrystalline in pillow and flow interiors (e.g., TS 63; Sample 185-801C-37R-5, 37–40 cm) (Fig. F27). Correspondingly, the grain size ranges up to medium grained. Most basalts show seriate textures of heterogranular plagioclase. In glassy pillow rims, plagioclase (Fig. F26), olivine, and sometimes pyroxene (Fig. F28A, F28B) are present as phenocrysts. Quenched textures also occur (Figs. F29, F30) but were not systematically distinguished. The proportion of the different groundmass minerals does not vary with depth (Fig. F31), although the size of the crystals in the groundmass reaches a maximum in Core 185-801C-37R at 815–820 mbsf (Fig. F31), which corresponds to the medium-grained interior of a massive flow (see “Lithologic Units,” p. 10).

Phenocrysts are rare within the basalts drilled in Hole 801C during Leg 185. Generally, plagioclase is the most common and largest phenocryst observed (Figs. F32, F33, F34; Table T6). Olivine and pyroxene phenocrysts are even rarer and are present only in the upper and lower parts of the Leg 185 section of Hole 801C (Fig. F32; Table T6). In crystalline samples, olivine phenocrysts are essentially always altered (Fig. F35) (see “Basement Alteration,” p. 18), although an unaltered euhedral olivine of ~0.1 mm was found in one sample of fresh glass (TS 67; Sample 185-801C-42R-2 [Piece 1B, 126–128 cm]). This olivine contains a large fluid inclusion (Fig. F36).

Phenocryst abundances observed in thin section are somewhat different from those observed in hand specimen. For example, olivine phenocrysts were more commonly described in hand specimen than in thin section. One reason for this is that thin sections represent only a small part of the rock and may not necessarily represent the sample as a whole. On the other hand, the abundance in hand specimen may be overestimated because alteration leads to lustrous, black crystals, which are very obvious in hand specimen.

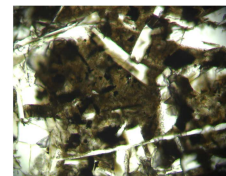
Compared to the Leg 129 basalts in the upper parts of Hole 801C (Shipboard Scientific Party, 1990), which contain as much as 10% plagioclase phenocrysts, the Leg 185 basalts are phenocryst poor.

Geochemistry

Introduction

Characterizing the basaltic geochemistry at Site 801 was a key step toward quantifying and refining the igneous lithologic units defined by hand-specimen and thin-section observations. Geochemical data were used to define units that were not evident in hand specimen descriptions. Shipboard geochemical analyses also provided high-precision data, which aided in determining magmatic crystallization sequences and parent magma characteristics. As a means of identifying the geochemical features of the basement rocks, selected samples from Hole

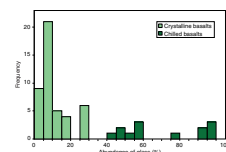
F23. Cryptocrystalline materials with plagioclase laths and oxides, p. 93.



F24. Contact between pillow and interpillow material, p. 94.



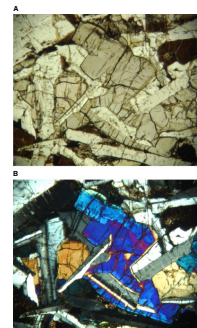
F25. Frequency of glass in basalts, p. 95.



F26. Euhedral plagioclase phenocrysts, p. 96.



F27. Medium-grained basalt, p. 97.



801C were analyzed for major and trace elements by shipboard XRF (Table T7). In most cases, samples were chosen to identify downhole trends in the least-altered basalt, although a few samples were taken to characterize specific styles of alteration (e.g., pale green alteration; Sample 185-801C-15R-7, 72–74 cm) or different varieties of interpillow material (e.g., recrystallized interpillow sediment; Sample 185-801C-16R-3, 60–62 cm).

These new data expand the existing geochemical data set for rocks recovered from Holes 801B and 801C during Leg 129 (Castillo et al., 1992), which includes fresh and altered basalt samples from 466 to 591 mbsf (0–125 m into basement). Floyd and Castillo (1992) divided the basalts from Leg 129 Holes 801B and 801C into two distinct geochemical categories, an upper alkali basalt sequence (~60 m thick) and a lower tholeiitic sequence (through Core 129-801C-12R), separated by ~20 m of ocherous hydrothermal deposit. The new Leg 185 data consist of 51 XRF major element analyses and 50 trace element analyses, 3 of which are of interpillow material and the remaining 48 of fresh and altered basalts, spanning a depth range of 605–920 mbsf. The data acquired from Core 185-801C-14R correlate well with the existing Site 801 data set, continuing the chemical trends observed in the tholeiites of Core 129-801C-12R.

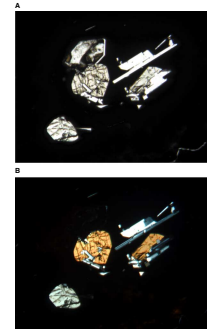
Results

Alteration plays a substantial role in the observed geochemistry of the lavas drilled at Site 801. Commonly, the degree of alteration is most readily gauged by a few sensitive geochemical parameters such as the loss on ignition (LOI), which is roughly equivalent to the total H₂O and CO₂ of the rock, or the K₂O content of the basalt. For the purpose of determining the primary igneous character of the basalts, samples with >2 wt% LOI or >1 wt% K₂O were therefore excluded from consideration. No observable relationship between LOI and elements such as Mg, Zr, or Cr exists, suggesting that alteration has not significantly affected these elements in most rocks and that these abundances are primary in the basalts.

On a broad scale, a simple geochemical trend dominates most of the sequence drilled during Leg 185. MgO decreases upward (Fig. F37A) through Core 185-801C-16R, illustrating that the lavas at this site are more primitive at the base and become more evolved (less MgO rich) with time. Trace elements also show a consistent trend. The incompatible element Zr is enriched in magmatic liquids with increasing degrees of crystal fractionation. Consistent with the trend in MgO, Zr shows a systematic increase uphole (Fig. F37B), indicating more primitive magma at depth in the hole. In contrast, the lower hydrothermal deposit in Core 185-801C-16R marks an abrupt change in the course of magmatic evolution. The upper tholeiites recovered in Cores 185-801C-14R through 16R, and in Cores 129-801C-5R through 12R, show a reversal of the geochemical trends from those deeper in the section. MgO values in the shallower section steadily increase, whereas Zr values decrease toward the top of the tholeiitic sequence.

Within these larger geochemical trends, however, excursions from the general pattern take place over smaller depth ranges and define more extreme chemical compositions. Small-scale breaks and trends within the data identify more subtle and localized changes in basalt chemistry, which can be used to segregate the entire sequence of basalt from Site 801 into 18 distinct geochemical units. These units are most

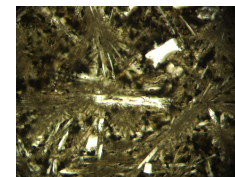
F28. Assemblage of phenocrysts, p. 98.



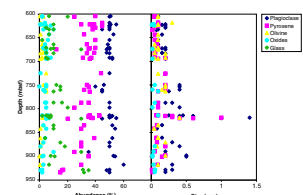
F29. Dendritic overgrowths on plagioclase phenocryst, p. 99.



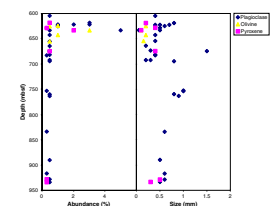
F30. Divergent, branching fibers of plagioclase, p. 100.



F31. Mineral abundance and size of groundmass with depth, p. 101.



F32. Phenocryst abundance and size with depth, p. 102.



distinctive on a plot of Zr vs. depth and are reinforced by consistent changes in MgO and Cr (Fig. F37B), and by changes in the character of the downhole logs.

The subset of least-altered basalts recovered during Leg 185 forms a trend consistent with crystallization of olivine + plagioclase + clinopyroxene. The trend in MgO vs. Al₂O₃ (Fig. F38), for example, follows a calculated liquid line of descent (Weaver and Langmuir, 1990), which predicts the changing composition of a magma as crystals are fractionated from a parent liquid. Sample 185-801C-46R-2, 75–77 cm, was chosen as the parent liquid, and the resultant calculation predicted co-crystallization of olivine and plagioclase over the temperature range of 1195°–1150°C, with a third phase (clinopyroxene) saturating at 1150°C. Samples deviating significantly from the trend of the line may have accumulated as much as 1% olivine or 5% plagioclase phenocrysts. One percent of olivine accumulation is consistent with proportions observed deeper in the section. Basalt with as much as 5% plagioclase phenocrysts, however, was not encountered in any of the basement drilled during Leg 185. The high-Al samples are interspersed throughout the sequence and, thus, cannot be explained by either a separate liquid line of descent or by the simple addition of plagioclase phenocrysts to the basalt. When examined in thin section, however, plagioclase phenocrysts in some of these samples show slight evidence of resorption, which could explain an increase of Al₂O₃ in the liquid.

Two basalts (Samples 185-801C-48R-1, 42–44 cm, and 48R-3, 14–16 cm) deviate significantly from the trend predicted by the liquid line of descent. These two samples represent the basalt deepest in the drill hole for which shipboard XRF data are presently available. For these samples to conform to the predicted trend, >2% olivine must be included with the basalt. In hand specimen, however, they do not display a significant increase in phenocryst abundance. It is possible that these samples are related to a different parent magma and fall along a separate liquid line of descent, but the available data are inconclusive and the question of their origin remains open.

Relating these rocks by crystal fractionation is important for determining the magmatic history of the basalts at Site 801, but identifying mantle characteristics and understanding the origin of the parent magma are equally critical tasks. The Zr/Y of a magma is not affected by crystal fractionation, but rather the ratio reflects the nature of the mantle source (enriched vs. depleted) and the degree of partial melting. The downhole trend in Zr/Y for the tholeiites of Site 801 is remarkably consistent (Fig. F37D), varying only slightly from a value of 3, suggesting that the mantle and melting processes at this site changed very little over time.

Discussion

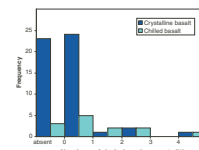
Shipboard XRF analyses provide a continuous geochemical record of basalt recovered during Legs 129 and 185. Downhole trends in MgO and Zr indicate a primitive magma at the bottom of Hole 801C, which evolved toward more fractionated lavas in Core 185-801C-16R then generally back toward more primitive compositions in Core 129-801C-5R.

Smaller trends within the data, however, show short periods of fractionation and intervals of injection of more primitive magma. The break between geochemical Units 14 and 15 (Fig. F37) is a prime example of a significantly fractionated magma that experienced a simulta-

F33. Plagioclase phenocryst, p. 103.



F34. Abundance of plagioclase phenocrysts in basalts, p. 104.



F35. Altered olivine phenocryst, p. 105.

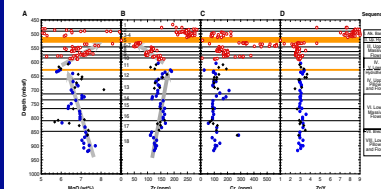


F36. Fresh olivine phenocryst, p. 106.



T7. Shipboard XRF analyses, p. 198.

F37. MgO, Cr, Zr, and Zr/Y plotted vs. depth, p. 107.



neous increase in MgO and decrease in Zr at 735 mbsf. This abrupt change in chemistry is consistent with the addition of more primitive, high MgO–low Zr material into the magma chamber.

The least-altered basalt samples fall largely along a single liquid line of descent, indicating that the entire sequence of basalt recovered during Leg 185 could have originated from the same parent magma. Data from the superfast spreading segment of the southern East Pacific Rise (EPR at 15.00°–18.72°S) (Sinton, 1991) fall along a similar trend (Fig. F38) and provide a meaningful comparison, because this segment of the EPR represents a possible modern-day analog for the ridge that produced the eruptive sequence at Site 801.

The Zr/Y value changes only slightly downhole, showing little change in either the mantle source or the degree of melting. The data from Hole 801C are comparable to, although more fractionated than, MORB from the modern Mid-Atlantic Ridge (MAR) (Fig. F39), with Zr/Y falling close to a value of 3. When compared to the modern EPR (8°–15°N), however, Hole 801C Zr/Y ratios are significantly lower, indicating that the modern EPR is either tapping a more enriched mantle or experiencing a lower degree of partial melting.

Summary

The basement drilled during Leg 185 consists mainly of aphyric basalts. Plagioclase, pyroxene, and olivine phenocrysts are rare but are present throughout Hole 801C. The groundmass phases are plagioclase, pyroxene, magnetite, interstitial devitrified glass, and rarely olivine.

Shipboard geochemical analyses reveal simple evolutionary trends within Hole 801C, corresponding to events of primitive magma injection and subsequent fractionation. An overall trend is observed toward more evolved lavas in Core 185-801C-16R and back to more primitive compositions in Core 129-801C-5R. These geochemical trends have been used to divide the core into 18 geochemical units. Basalts analyzed during Leg 185 are all related to the same parent magma and vary only slightly from a dominant mantle signature, which is similar to, although more depleted than, modern EPR MORB.

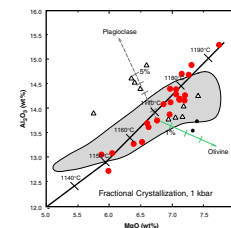
BASEMENT ALTERATION

Results from Leg 129

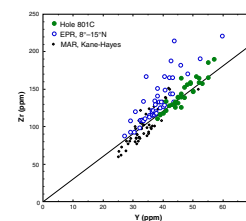
Previous coring at Site 801 during Leg 129 (Holes 801B and 801C) penetrated 60.2 m of alkali basalts and 63.1 m into the underlying tholeiitic basalts, which are separated from the alkali basalts by an ~9.5-m-thick silicified hydrothermal iron oxide deposit (Lancelot, Larson, et al., 1990). Thus, total basement penetration was 132.7 m. Alteration of the basalts recovered from Site 801 during Leg 129 was studied by Alt et al. (1992) and has since been re-examined by J.C. Alt and D.A.H. Teagle (unpubl. data). These authors divided alteration into several different types. Most of the alteration observed in the Leg 129 section at Site 801 is typical of that observed elsewhere in the upper oceanic crust and results from interaction of basalts with seawater fluids at temperatures of 0°–50°C (Alt et al., 1992; summary in Alt, 1999).

Dark gray rocks are the most abundant and are present throughout the Leg 129 tholeiitic section. These rocks are the least altered, generally containing 2%–20% by volume secondary minerals, and are character-

F38. MgO vs. Al₂O₃ for least-altered basalts, p. 108.



F39. Zr vs. Y for least-altered basalts, p. 109.



ized by saponite and calcite replacing olivine and filling pore space and by common disseminated pyrite. Chemical changes caused by alteration are slight. Dark gray type alteration also affects the alkali basalts, but these are more intensely altered than the tholeiites (30%–80% vs. 2%–20% altered). Celadonite and Fe oxyhydroxides are locally present in the dark gray tholeiites in millimeter- to centimeter-wide alteration halos along veins.

Brown rocks are similar to the dark gray alteration type but contain abundant disseminated iron oxyhydroxides, in some cases with celadonite present as well. These rocks reflect greater fluxes of oxygenated seawater than the dark gray pyrite-bearing rocks.

The hydrothermal deposit at 521.7–531.2 mbsf consists of silicified ochreous material and was formed on the seafloor at temperatures of 15°–60°C (Alt et al., 1992). Green alteration in the Leg 129 section is found only in the primitive tholeiites of Unit 5 at 531–535 mbsf, just beneath the hydrothermal deposit, and is probably related to upwelling hydrothermal fluids that formed the deposit. The green rocks are intensely veined and recrystallized (80%–100%) to celadonite, glauconite, montmorillonite, K-feldspar, calcite, and titanite. Buff-colored rocks are closely associated with the green rocks from 531 to 535 mbsf. The buff rocks are highly altered (60%–80%) to smectite, calcite, and titanite.

Major questions to be addressed by further coring in Hole 801C during Leg 185 were the deeper distribution of alteration types and the chemical effects of alteration on the crust. On the basis of other drilled sections, it was expected that the effects of seawater alteration would decrease with depth (Staudigel et al., 1995; Alt et al., 1996). This section documents the presence of veins, breccias, interpillow sediments, altered basalts, and chemical changes resulting from alteration of the rocks that were cored in Hole 801C during Leg 185.

Results from Leg 185

Secondary phyllosilicates in rocks from Leg 185 Hole 801C were identified by color and hardness in hand specimen, by optical properties in thin section, and by analogy with well-studied minerals identified in the shallower section of Hole 801C cored during Leg 129 and in other sections of oceanic crust. The identification of phyllosilicates in the Leg 185 rocks remains tentative, however, pending further shore-based study.

Throughout the following sections we refer to volume percentages of alteration types, breccias, and veins. We assume that the surface areas of these features on the cut faces of the core, when converted to area percent, are equivalent to volume percent of the core, similar to modal analyses of a thin section.

Veins and Breccias

Veins, halos, breccias, and interpillow sediments observed in the archive half of the cores were recorded in the vein log (see the “[Site 801 Vein Log](#),” p. 230; also in [ASCII format](#)). The logs include the record of abundance, volume, width, and mineralogy of the veins calculated per core.

Based on the texture, shape, and filling, we defined three major types of fractures. Veins are interpreted to result from brittle failure and subsequent filling by a variety of minerals. Interpillow materials are mainly sediments filling the spaces between basalt pillows. Breccias are com-

posed of angular to subangular clasts of altered or fresh basalt with a cement. Abundances and distributions of veins, breccias, and interpillow material are illustrated in Figures F40, F41, and F42.

Vein Types, Mineralogy, and Abundance

Approximately 3500 veins were logged during core description, and veins make up 1%–4% by volume of the core (Fig. F40). The volume percent of veins for each core was estimated by calculating the volume of veins relative to the volume of the core recovered.

The vein materials are mostly calcite, saponite, celadonite, iron oxides or sulfides, and silica (quartz and chalcedony). The veins are commonly composed of a combination of these minerals, but several end-member types were defined based on the main mineralogy. A summary of the different types of veins is reported in Table T8. Carbonate (mostly calcite) and saponite veins are by far the most common and are present as multiple generations. Veins range in thickness from ~0.1 to ~50 mm. The orientations of the veins are subhorizontal to oblique in the cut face of the core, but vertical veins several decimeters long, are not uncommon.

Calcite

Carbonate, principally as calcite, is the most abundant vein mineral. Pure carbonate veins (e.g., >90%) correspond to one-third of all veins. Carbonate in veins comprises 1% by volume of all material recovered from the volcanic section of Leg 185 Hole 801C. In general, decreases in the proportion of carbonate in veins per core correspond with a reduction of the average vein thickness for that core. Identification of coarse-grained calcite and fibrous aragonite in some veins must be confirmed by X-ray diffraction (XRD) analyses. Some unusual subvertical carbonate veins in Section 185-801C-37R-2 are associated with highly vesicular lava and may reflect a local increase in fluid pressure and related hydraulic fractures.

Saponite

Saponite is the major mineral filling thin veins (~0.1 mm thick). These veins clearly represent filled fractures that allowed fluid access to the fresh rocks. Dark alteration halos and disseminated pyrite rims are ubiquitously associated with saponite veinlets but represent a very low proportion of the core.

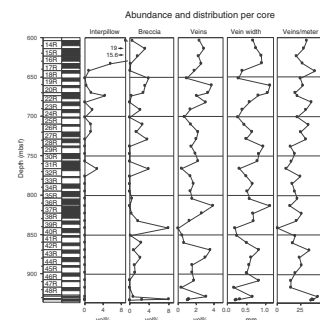
Calcite + Saponite

Veins are commonly filled with both carbonate and smectite identified as saponite. The proportion of carbonate to saponite in this “end-member” type ranges from 40% to 60%. The carbonate generally occupies the central portion of the larger veins and, thus, is a later mineral. The properties of these veins, such as the average width, are intermediate between those of the saponite and the calcite-type veins.

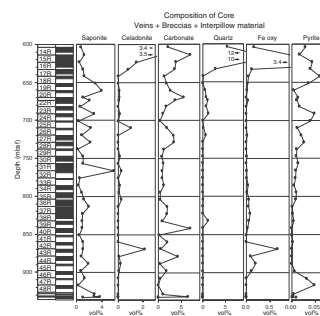
Celadonite

Celadonitic phyllosilicates are locally abundant, but pure celadonite veins are scarce. Celadonitic patches are associated with large veins of carbonate and/or saponite and brecciated zones. Celadonite veins are

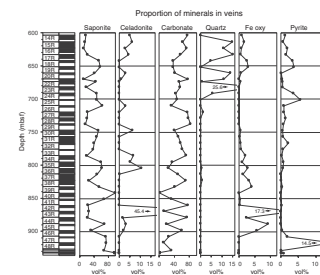
F40. Abundance and distribution of veins, breccias, and interpillow material, p. 110.



F41. Volume percent of minerals and rock materials, p. 111.



F42. Proportions of minerals in veins, p. 112.



T8. Vein types, p. 201.

commonly characterized by wide, dark alteration halos as wide as 2 cm (intervals 185-801C-43R-2, 125–130 cm, and 37R-5, 60–65 cm) and are locally oxidized or stained with Fe oxyhydroxide (43R-3, 48–58 cm).

Pyrite

Pyrite veins are generally present as minute veinlets (0.1 mm thick) and are randomly oriented. Pyrite may also be present locally in fractures filled with smectite and/or carbonate. Some alteration halos associated with veins (see “[Mixed Veins](#),” p. 21) contain disseminated fine-grained pyrite.

Iron Oxyhydroxide

Iron oxyhydroxides are found mostly in thin veins but may be present as disseminated minerals and as staining saponite within larger veins and in alteration halos. In some cases, iron oxides clearly replace pyrite in small saponite + pyrite veins. Enrichment in iron oxyhydroxide is recorded in the more oxidized sections of Hole 801C (i.e., between 905 and 970 mbsf) and in the upper 50 m of the section drilled during Leg 185.

Chalcedony/Quartz

Silica veins (i.e., >70% SiO₂) represent <0.5% of the veins recorded in Hole 801C. However, silica is locally enriched in the veins in the upper section of the hole, between 600 and 700 mbsf. Silica-bearing veins are significantly larger than the other veins and tend to be associated with the breccias and interpillow material. In many cases, silica, like carbonate, appears to be a late phase (e.g., Samples 185-801C-27R-1, 50–55 cm, and 16R-1, 70–71 cm). The largest veins may be related to the siliceous hydrothermal deposits (e.g., Sample 185-801C-15R-1, 129 cm).

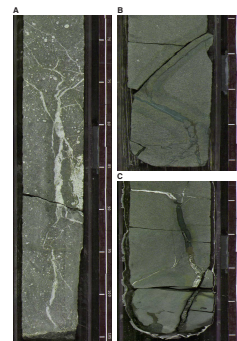
Mixed Veins

Mixed veins are generally irregular to sinuous in shape and are associated with wide, mixed brown and dark alteration halos. In some sections, the veins exhibit branching and anastomosing forms. Green clay (saponite or celadonite) and calcite probably filled the veins during several reopening events. Some thick, long vertical veins with these features are recorded in different parts of Hole 801C (e.g., intervals 185-801C-44R-2, 73–147 cm (4 mm thick); 37R-5, 57–126 cm (10 mm thick); 31R-6, 30–77 cm (0.7 mm thick); 31R-6, 91–136 cm (1.8 mm thick); 38R-1, 45–86 cm (5 mm thick); and 37R-3, 1–40 cm (4 mm thick). For the vertical veins at interval 185-801C-37R-5, 57–126 cm, carbonate is present in extensional fractures, with or without cutting the saponite vein. The associated mixed brown and dark alteration halo is 15 mm wide. The heterogeneous nature of these vein fillings is in some cases emphasized by changes in mineralogy along the length of the vein (Fig. [F43C](#)).

Breccias and Hyaloclastites

The breccias in Hole 801C were divided into two types:

F43. Veins with alteration halos, p. 113.



1. Breccias are highly irregular zones filled with angular to subangular basalt clasts cemented mainly by late carbonate, but also lesser saponite, quartz, and celadonite. The thickness of these breccia zones ranges from 10 mm to 1 m. Included in this type are the “jigsaw-puzzle” breccias, where clasts of basalt can be fitted to each other. Some breccias are composed of basalt clasts showing evidence for alteration, oxidation, and vein development prior to cementation. For example, a typical breccia is observed in Figure F44C. Some thick veins include clasts of basalt and could correspond to an initial stage of development of breccia (Fig. F43A).
2. Hyaloclastites are defined where basaltic glass shards, derived from chilled pillow margins, are cemented by secondary minerals, typically calcite and saponite. (Fig. F44).

The average proportion of cement in breccias is 20%, but it varies from 1% to 99%. The breccia cements are dominantly carbonate (44%) and saponite (39%), with lesser amount of celadonite (11%) and minor quartz (5%). Breccia in Core 185-801C-40R extends over 77 cm (from 0 to 77 cm) and is composed of large, angular, slightly displaced blocks linked by a network of saponite and carbonate veins.

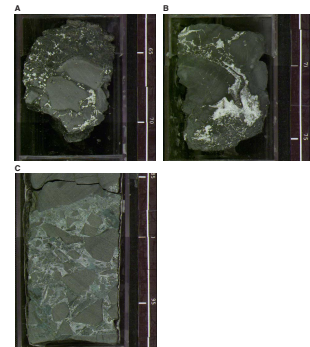
Variation of Vein Density and Breccias with Depth

The density of veins in the basement is highly variable (Fig. F40). At 700 mbsf (Core 185-801C-25R), 850 mbsf (Core 41R), and 916 mbsf (Core 48R), the proportions of veins and fractures per core are below 1 vol%, and intervals of slightly altered, dark gray rocks are common. These zones of restricted fracturing and fluid flow exhibit only limited chemical change (see “Alteration Geochemistry,” p. 27) and slight recrystallization. Clay-cemented breccias are common throughout Hole 801C but are very heterogeneously distributed. The proportion of breccias is the highest in Core 185-801C-40R (i.e., ~8 vol%). Hyaloclastites make up 1–3 vol% of Cores 185-801C-19R, 24R, 28R, 32R, and 42R.

The frequency of veins per meter does not correlate with the volume percent of veins per core; rather, the latter depends on the average thickness of veins in each core. The density of veins for each core correlates neither with percentage recovery nor with the proportion of breccias; however, for cores consisting completely of massive basalt, vein frequency is generally lower than for those comprising pillows and breccias (e.g., Core 185-801C-31R). The minimum vein abundance of Core 185-801C-41R corresponds to a large brecciated unit and is not representative of the abundance of secondary minerals in that core (Fig. F40). The average density of veins in Hole 801C is 24 veins/m, which increases locally to 40 veins/m in Core 185-801C-18R (Fig. F40). This mean value is slightly lower than in other sections of upper oceanic crust, which contain 27 veins/m (Hole 896A) and 31 veins/m (Hole 504B) (Alt et al., 1996).

The maximum vein abundance in Hole 801C is in the cores drilled with the diamond bit: for Cores 185-801C-49M through 52M, the average density of veins is 39 veins/m corresponding to 2.08 m of rocks recovered. The increase of vein abundance in this section reflects the greater proportion of highly fractured pillow lavas and hyaloclastites. However, the difference in abundance of veins and breccias in different sections of Hole 801C, and particularly between Cores 185-801C-48R and 49M, may not be significant and could be an artefact of measure-

F44. Types of hyaloclastite and breccia, p. 114.



ment caused by variable core recovery between RCB and DCB bits. The data presented in Figure F40 indicate that there is no simple relationship between core recovery, vein abundances, and lithologic units. However, it is possible that variations in recovery are related to the presence or absence of veins and fractures along which the core breaks into small pieces and is ground up during drilling.

Fe oxyhydroxide-bearing and pyrite-bearing veins tend to not be present together, and their distributions correlate with the proportion of celadonite and saponite, respectively. There is no clear overall depth trend in vein mineralogy or alteration along this profile of the upper oceanic crust because the lower section between 850 and 950 mbsf is characterized by the presence of alternations of oxidative and reducing alteration effects (Figs. F41, F42).

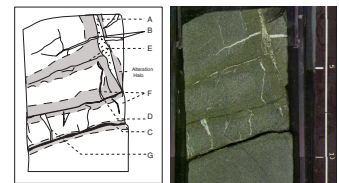
Based on the composition, abundance, and distribution of breccias, interpillow sediments, and veins (Figs. F40, F41, F42), however, two major units are distinguished:

1. The upper section of Leg 185 Hole 801C includes cores between 600 and 700 mbsf (Cores 185-801C-13R to 24R). This section is characterized by the presence of silicified interpillow sediments (e.g., as much as 19 vol% in Core 185-801C-19R). The vein density of 27 veins/m is high, and the vein minerals include (in order of abundance) carbonate, saponite, silica, celadonite, pyrite, and iron oxyhydroxides. This unit is transitional from the hydrothermal deposit and the highly altered basalt recovered during Leg 129 (Cores 129-801C-4R and 5R) to the lower, less altered section of Hole 801C.
2. The lower section of Hole 801C (~700–900 mbsf) consists mainly of pillows, massive units, and thin flows. Although there is significant scatter, the major feature of this unit is the common occurrence of brecciated zones, including hyaloclastites, and the local enrichment of constituents such as saponite (e.g., Core 185-801C-32R), celadonite (Core 43R), carbonate (Core 40R), iron oxyhydroxides (Core 43R) or pyrite (Core 48R). The vein abundance of 20 veins/m in this section, excluding Cores 185-801C-49M through 52M, is lower than in the upper section.

Crosscutting Relationships among Veins

Many veins are braided and branching, and crosscutting is common. In general, most of the oblique and vertical veins have very irregular shapes suggesting that they were generated during several stages. Carbonate veins tend to be late, with carbonate minerals (calcite and rare aragonite) filling reopened saponite veins and cutting saponite veins. On the other hand, thin-section observations indicate that saponite can occur locally as intergrowths with carbonate minerals. Clear crosscutting relationships between veins were observed in only a few cases. In one sample, at least three generations of carbonate and saponite veins are present (Fig. F45). Alteration halos are associated with both subhorizontal and vertical veins. The thin saponite veins are commonly accompanied by dark alteration halos, but pure carbonate veins do not have these features. Reopening of saponite veins and their filling with carbonate are apparently accompanied by formation of late alteration halos. This reactivation could be a result of late tectonic movement, as suggested by offset carbonate veins.

F45. Diabase cut by several generations of veins, p. 115.



Interpillow Sediments

Interpillow sediment represents material that was originally deposited on the ocean floor and has subsequently been recrystallized and possibly altered by basement fluids. Interpillow sediment contains calcite, chalcedony, quartz, smectite/celadonite, and iron oxyhydroxide in varying proportions (Fig. F46) and is distinguished from breccia and hyaloclastite by the scarcity of fresh or altered clasts of basalt and/or glass. Interpillow sediment makes up 2.5% of core recovered from Leg 185 Hole 801C (Fig. F40). Interpillow sediments were observed in Cores 185-801C-14R through 18R, 20R through 22R, 25R through 27R, and 32R. Below Core 185-801C-32R interpillow sediment was not observed. Overall, the volume percent of interpillow material decreases downhole (Fig. F40).

Some of the mineralogical and microscopic morphological details of interpillow sediments are displayed as photomicrographs in Figure F47. The occurrences of radiolarian tests provide evidence for the original deposition of interpillow sediment as pelagic sediment.

Two types of contacts were observed between lavas and interpillow sediment: (1) pillow rim/sediment contacts and (2) flat basalt/sediment contacts (Fig. F48). Pillow rim/sediment contacts are characterized by a chilled pillow margin at the sediment/lava interface. In many cases flat basalt/sediment contacts appear to be lava flows that were injected into interpillow sediment. Some of these contain clear examples of centimeter-scale patches of sediment included within fine-grained basalt. Because of incomplete core recovery the actual thickness of individual units is uncertain, but observed thickness of interpillow sediment units range from 1–2 cm (Fig. F47H) to 39 cm for the cherty hydrothermal interpillow unit of interval 185-801C-16R-3, 0–39 cm. Overall, the thickness of individual interpillow sediment horizons decreases with depth.

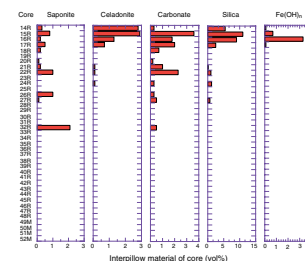
The distribution of interpillow material is reflected in downhole variations in the proportions of SiO₂ and celadonite, which decrease from ~18% and 3%, respectively, in Core 185-801C-14R to values of <1% below Core 17R (Figs. F42, F45). Silica in the interpillow sediments is typically fine chalcedony and/or quartz. However, as seen in Figure F47E, there are some fibroradial occurrences of chalcedony, and the conversion of chalcedony to finely crystalline quartz is also observed (Fig. F47F). In thin section celadonite is present as massive groundmass (Fig. F47B), as discrete crystals (Fig. F47C), and as pore-filling material (Fig. F47E).

Within interpillow material, the abundance of carbonate ranges from 4 to 90 vol% and saponite ranges from 2 to 80 vol%. Saponite is shown as a pore-filling material (Fig. F47A, F47E) and intergrown with calcite (Fig. F47C).

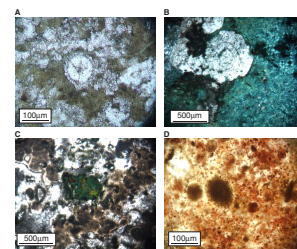
The occurrence of calcite (Fig. F47A, F47B, F47C, F47E, F47F, F47G, F47H) suggests wholesale recrystallization. The radiolarian depicted in Figure F47A sits in a matrix of calcite and has itself been replaced by calcite. Calcite in Figure F47B shows concentric growth zones, indicating its introduction as a secondary phase. Calcite in Figure F47E is subhedral and appears to have crystallized around small opaque crystals. Figure F47H shows a calcisphere (~0.75-mm diameter) near the calcite/basalt interface that is probably of biologic origin.

The presence of Fe oxyhydroxides in interpillow material was recognized in hand specimen by red or yellow staining and in thin section by spherulitic and disseminated iron oxides (Fig. F47D, F47G). Interpillow

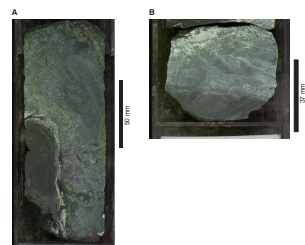
F46. Interpillow material of core, p. 116.



F47. Altered interpillow sediment, p. 117.



F48. Interpillow sediment/lava interface, p. 119.



units containing significant amounts of Fe oxyhydroxides are found in Cores 185-801C-14R through 17R, 22R, and 27R. In Core 185-801C-16R, Fe oxyhydroxide represents 21 vol% of the interpillow material. This is related to the presence of a second silica- and iron-rich hydrothermal unit (lithologic Unit 48; interval 185-801C-16R3, 0–43 cm), which consists of 5- to 100-mm spherules and filaments of iron oxyhydroxide in a matrix of granular quartz (<1–50 mm grain size).

Siliceous interpillow material, which was probably originally pelagic radiolarian ooze that has been recrystallized and possibly hydrothermally altered, represents periods of sedimentation and/or channelled sediment flows during hiatuses between periods of volcanic activity. Carbonate material may represent original calcareous sedimentation or a later authigenic precipitate. The presence of Fe oxyhydroxides may result from precipitation from hydrothermal fluids within interpillow spaces beneath the seafloor, or as hydrothermal sediment at the seafloor. Variation in the abundance of interpillow sediment with depth may reflect the rate of production of lava flows; the paucity of interpillow sediments below Core 185-801C-32R may be a result of rapid lava production and accumulation rates at a fast-spreading ridge, whereas slower, off-axis lava accumulation at the top of the section would possibly have allowed greater accumulation of interpillow sediments.

Alteration of Basalts

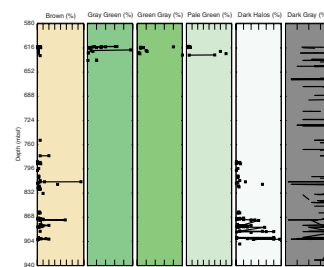
Various types of alteration were encountered in Hole 801C basement rocks drilled during Leg 185. The alteration halos adjacent to veins or exposed surfaces are described in the following section.

Dark Gray Alteration

Pervasive but slight background alteration affects most of the basalt cores starting with the first core (i.e., Section 185-801C-13R-1, at the depth of 594.3 mbsf) down to the bottom of the hole at 935.7 mbsf (Fig. F49). As a result of this alteration, the basalts display a dark gray color when wet that becomes a lighter gray or brownish gray when dry. This alteration is pervasive and not specifically focused along veins or exposed surfaces. Rocks affected by this dark gray background alteration typically contain 2%–15% secondary phases by volume.

This background alteration results from the complete replacement of rare olivine phenocrysts by smectite and, much more rarely, the partial replacement of plagioclase and augite phenocrysts by smectite. On the other hand, plagioclase microlites and intergranular plumose or dendritic augite are generally unaltered. Titanomagnetite is unaltered to slightly altered to titanomaghemite, exhibiting minor shrinkage cracks. In the groundmass, the rare interstitial glass is totally replaced by smectite. Smectite and minor calcite fill vesicles and miarolitic voids, which are generally not abundant. In thin sections, smectite varies in color from dark brown to pale greenish to yellowish brown, but it is typically black in hand specimen. Based on previous work at Site 801 and elsewhere, this widespread smectite is most likely saponite (Alt et al., 1992; Alt, 1999). Recrystallized igneous sulfide globules are locally common, as are disseminated secondary pyrite and minor marcasite.

F49. Distribution of alteration types, p. 120.



Pale Green Alteration

Pale green color is restricted to intense pervasive alteration (up to 80% by volume) of basalts locally in Sections 185-801C-15R-1 to 16R-3 of Units 39 to 49 (i.e., from 613 to 626 mbsf) (Fig. F50). This type of alteration is due to the total replacement of the rare olivine phenocrysts by a tan to green smectite and intense replacement of plagioclase phenocrysts and microlites by abundant calcite and tan smectite. Plagioclase phenocrysts are less altered than the microlites. Both secondary minerals also fill vesicles and miarolitic voids and pervasively replace the groundmass. Preliminary XRD results indicate that the smectite is dioctahedral, probably a montmorillonite. Apatite was also identified by XRD. Celadonite and green nontronite are occasionally observed filling voids in halos along veins. Fine-grained pyrite is disseminated through the groundmass and particularly in bands outside alteration halos along veins. Pale green alteration progressively grades through a gray-green alteration zone (see below) into dark gray adjacent rocks within the same core section (e.g., Section 185-801C-15R-7) (see Fig. F50).

Gray-Green Alteration

Gray-green alteration is present in Sections 185-801C-15R-1, 15R-2, and 15R-5, in which it can be the dominant alteration type (up to 95% of the section), and also in Sections 16R-1 and 17R-2, where it is much less important (2 and 20 vol%, respectively). Gray-green altered rocks represent the intermediate alteration type between intensely altered pale green rocks and the typical pervasive dark gray background alteration.

Calcite is the most abundant secondary phase in gray-green altered rocks. It locally replaces plagioclase and olivine phenocrysts and fills vesicles and miarolitic voids, where it is sometimes associated with chalcedony. It is also the main vein mineral. Clinopyroxene appears to be unaltered. The groundmass is partly (20%) replaced by calcite and smectite. Titanomagnetite is intensely altered to titanite, and abundant disseminated pyrite is present in the groundmass.

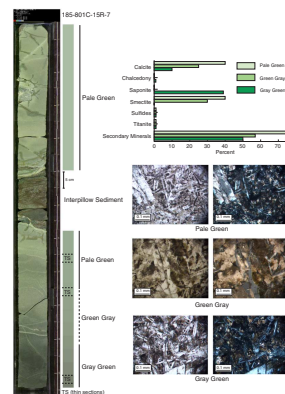
Hyaloclastite and Glass Alteration

Even though fresh basaltic glass is found nearly down to the bottom of the hole, glass from glassy pillow rims or hyaloclastites is generally strongly altered to smectite. Hyaloclastite glass shards are altered to smectite, whereas the cement is commonly calcite or smectite. It is remarkable that no zeolite has been observed in any of the hyaloclastite or glassy pillow rims of Hole 801C. Phillipsite is typically a very common result of “palagonitization” (i.e., the low-temperature alteration of basaltic glass by seawater).

Alteration Halos along Veins

Alteration halos along veins are common in Hole 801C core, and their occurrences are recorded in the vein logs (see the “[Site 801 Vein Log](#),” p. 230; also in [ASCII format](#)). Widths of alteration halos range from ~1 to 18 mm. Several types of halos were recognized in hand specimen, and their mineralogy was determined in thin section:

F50. Alteration types and gradational nature of boundaries, p. 121.



1. Dark alteration halos are present throughout most of the core but are particularly abundant in Cores 185-801C-14R through 15R, 22R through 24R, 43R, and 44R (Figs. F43, F51). In these halos, pore space is filled and olivine is replaced by celadonite-nontronite and Fe oxyhydroxides. Narrow (0.1–1.0 mm) bands of disseminated pyrite are present just outside the dark halos in many cases. Most dark halos occur within host rocks displaying typical dark gray smectitic background alteration, but in Core 185-801C-15R dark halos also occur in the intensely altered pale green rocks.
2. Brown alteration halos are common locally in the core, particularly in Cores 185-801C-15R and 43R through 46R, with minor amounts locally in Cores 28R through 39R. Brown halos are characterized by the presence of abundant Fe oxyhydroxides disseminated in the groundmass and staining smectite-filled pores and replacing olivine. Celadonite-nontronite may also be present.
3. Rare pale green halos in Cores 185-801C-14R through 17R are associated with meter-scale intense pale green alteration and probably represent similar alteration, which has been restricted to local fluid-flow pathways. These pale green halos were not studied in thin section, however, so this interpretation remains tentative.
4. Mixed brown plus dark alteration halos are present in Cores 185-801C-34R through 38R and 43R through 46R (Fig. F43). These grade from brown Fe oxyhydroxide-rich zones adjacent to the vein, to very dark gray or green oxide-poor zones extending farther away into the typical dark gray host rock. The mixed halos contain celadonite-nontronite and abundant Fe oxyhydroxide replacing olivine and interstitial material and filling pores and vesicles.

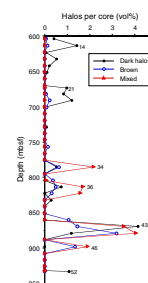
Dark alteration halos were commonly difficult to detect in hand specimens. We discovered that thorough washing of the surface and partial drying enabled better detection of such halos. Narrow pyrite bands were in some cases logged in the vein log. Many of these pyrite bands may border dark alteration halos that were unrecognized because of the lack of a significant color difference in hand specimen. It is likely, therefore, that the abundance of dark halos described above is underestimated in the vein and alteration logs (see the “Site 801 Vein Log,” p. 230, and “Site 801 Alteration Log,” p. 216; both also in ASCII format).

Alteration halos have a sporadic distribution in the cores but are most abundant in coarser grained massive units in Cores 185-801C-34R, 36R, 37R, and 43R through 46R (Fig. F51). The abundance of halos in these units must reflect local permeability and fluid flow, but formation of halos may be enhanced by coarser grain size and intergranular porosity and permeability of the rocks.

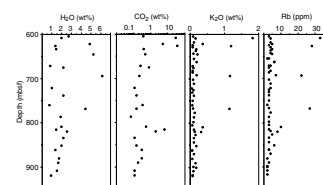
Alteration Geochemistry

The typical basalts from Leg 185 that are slightly altered to the pervasive dark gray background alteration exhibit little or no chemical changes, although there is scatter to slightly elevated K_2O , Rb, H_2O , and CO_2 contents, and increased LOI as the result of alteration and formation of secondary smectite, celadonite, and calcite (Fig. F52; Table T9). Several samples were selected specifically to study alteration effects, in-

F51. Alteration halos per core, p. 122.



F52. XRF analyses, p. 123.



T9. Volatile and alkali data vs. depth, p. 202.

cluding one altered interpillow hyaloclastite, a pale green intensely altered rock, and two alteration halos along veins. Altered rock compositions were compared to the mean least-altered rock composition from the same igneous chemical unit, with samples having clearly elevated LOI, K₂O, Rb, and/or CaO contents excluded from the calculations of least-altered rocks. It is assumed that Al, Ti, and Zr are immobile during alteration and that any change in the concentrations of these elements reflect density changes or dilution effects during alteration. Altered rock compositions are thus normalized to constant Ti, Al, and/or Zr, and the ratio of normalized altered rock to mean fresh rock has been plotted in Figures F53, F54, F55, and F56.

The intensely altered pale green rock from geochemical Unit 11 (Core 185-801C-15R) has undergone a 22% decrease in density. Losses of Mg, Fe, Mn, and Ni (Fig. F53) are related to the breakdown of olivine, pyroxene, and titanomagnetite. Loss of Zn reflects the complete replacement of titanomagnetite by titanite, and Cu depletion results from breakdown and loss of igneous sulfide minerals. Contents of K₂O, Ce, and Ba are significantly elevated, but Rb is apparently not enriched.

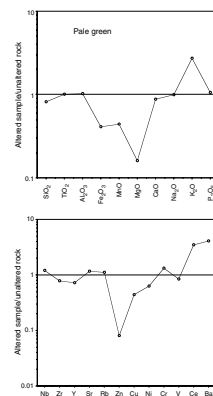
An interpillow hyaloclastite from geochemical Unit 13 (Core 185-801C-24R) exhibiting typical dark gray background alteration was analyzed (Fig. F54). This sample comprises 30% slightly altered basalt, 50% glass totally altered to smectite, and 20% matrix (95% saponite and 5% calcite). The sample exhibits gains of MgO, K₂O, and Rb, elevated LOI, and losses of MnO, CaO, Ni, Cu, and Ba. The significant gains of K and Rb suggest that celadonite or other K-rich phase(s) may be present but not detected in hand specimen.

Two alteration halos along veins in geochemical Unit 16 were analyzed (Figs. F55, F56). Both comprise mixed brown plus dark halos along saponite + calcite veins. Minor amounts of dark gray host rock and vein material may be included in these samples. A thin section taken adjacent to Sample 185-801C-37R-6, 33–35 cm, contains saponite, abundant disseminated Fe oxyhydroxides, and two small (0.4 mm) calcite veinlets. Compared to fresh rock, this halo is enriched in K₂O, Rb, CaO, and total Fe and has a high LOI (Fig. F56). Ni and Zn exhibit slight depletions related to breakdown of olivine and titanomagnetite.

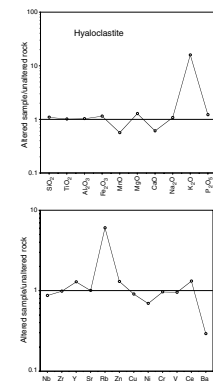
The chemical composition of the alteration halo of Sample 185-801C-36R-4, 112–114 cm (Fig. F55), is generally similar to that analyzed from Core 37R, but the former exhibits only gains of alkalis and a slight loss of Cu. Apparent changes in other elements are not significant.

As a very rough estimate, the total section cored during Leg 185 has experienced an increase of ~17% in K₂O and Rb contents as the result of seawater alteration (see Table T10) (assuming that (1) all breccias are altered as the analyzed hyaloclastite, (2) all halos are represented by those analyzed, (3) celadonite veins contain 8 wt% K₂O, and (4) unaltered rocks contain 0.08 wt% K₂O). In this crude estimate, ~13% of the total alkali budget is contained in breccias, ~4% in alteration halos along veins, ~4% in celadonite veins, and the remainder (~83%) in essentially unaltered basalt. If 2.3 vol% interpillow sediment containing 1.5 wt% K₂O is added to this estimate, then the K₂O content of the Leg 185 section is 60% greater than in fresh basalt alone, with 27% of the total alkali budget residing in interpillow sediment.

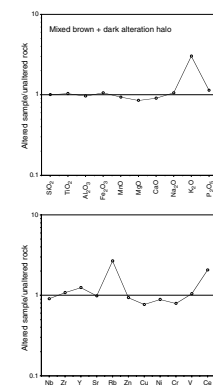
F53. Chemical composition of altered pale green sample, p. 124.



F54. Chemical composition of altered hyaloclastite, p. 125.



F55. Chemical composition of an alteration halo along a vein, Sample 185-801C-36R-4, p. 126.



Summary

In the basalt cored during Leg 185 in Hole 801C we logged ~3500 veins, which comprise 1.8 vol% of the recovered core. The main vein types are calcite, saponite, and calcite plus saponite, with lesser amounts of celadonite, iron oxyhydroxide, pyrite, and silica (quartz and chalcedony).

The recovered cores include an estimated 1.5 vol% breccias and hyaloclastite and 2.5 vol% interpillow sediments. Breccias contain an average of 20% cement, comprising mainly saponite (39%) and calcite (44%), but also minor celadonite and silica. Some hyaloclastites include fresh glass, but most are highly altered to smectite and calcite and have undergone an order of magnitude enrichment in K₂O and Rb, and exhibit slight loss of Ca in exchange for Mg from seawater. Interpillow sediments comprise mainly chert and limestone but also contain iron oxides, smectite, and celadonite-nontronite and may include a low-temperature hydrothermal component. Alkali contents are high (1.5 wt% K₂O and 30 ppm Rb).

Most (~95%) of the basalts are slightly altered and contain <15 vol% secondary minerals (saponite, calcite, and pyrite) replacing olivine and interstitial material, and filling pore space. Chemical changes are small, including slightly elevated K₂O and Rb contents, losses on ignition, and sporadic CaO enrichments.

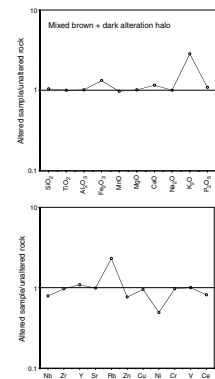
Intensely altered pale green basalts occur at 613–626 mbsf (Cores 185-801C-15R to 16R) and are probably related to upflow of low-temperature hydrothermal fluids feeding the hydrothermal iron-silica deposits at 520–531 and 625 mbsf. The pale green rocks are intensely altered (80%) to calcite, smectite, and celadonite (plus minor titanite, pyrite, and iron oxyhydroxide). Chemical changes are significant, including losses of Mg, Fe, Mn, Ni, Zn, and Cu, and gains of K₂O, Ce, and Ba.

Alteration halos, 1–18 mm wide, are common along veins in the slightly altered basalts. These halos include dark, brown, and mixed brown and dark types, and are characterized by the presence of celadonite-nontronite filling pores and replacing olivine and interstitial material, by abundant disseminated iron oxyhydroxides, and commonly by disseminated pyrite in the host rock just outside the halo. Alteration halos comprise 1.7 vol% of recovered core and are present locally throughout the section, but are most common in massive units below 780 mbsf (Cores 185-801C-34R, 36R, 37R, and 43R through 46R)

The Leg 185 section can be divided into two general zones. The upper portion, from 600 to 700 mbsf (Cores 185-801C-13R to 24R) has a higher abundance of veins (mean = 27 veins/m), contains almost all of the interpillow sediment intervals, includes common breccias throughout, and contains common silica-bearing veins. This interval also includes the small interval of hydrothermal iron-silica material at 625 mbsf and the associated intensely altered pale green rocks, as well as the zone of variable hole diameter from the caliper log (~625–715 mbsf) (see “[Borehole Characteristics](#),” p. 41).

The lower portion of the hole, from ~700 to ~900 mbsf, has a lower abundance of veins (mean = 20 veins/m), a general absence of interpillow sediment and silica-bearing veins, and limited occurrences of breccias. These all coincide with a zone of constant hole diameter from the caliper log (see “[Borehole Characteristics](#),” p. 41). This portion of the core also contains the most abundant oxidized alteration halos (780–

F56. Chemical composition of an alteration halo along a vein, Sample 185-801C-37R-6, 33–35 cm, p. 127.



T10. Alkali budget estimate, p. 203.

900 mbsf), as well as peaks in abundances of veins of celadonite and iron oxyhydroxide.

The lowermost few meters of core (Cores 185-801C-48R through 52M) are characterized by an increase in pyrite veins and a peak in vein abundance of 39 veins/m, which occurs in the 2.08 m of basalt in Cores 185-801C-49M through 52M. The latter may be related to diamond coring in this interval, but a similar maximum in vein abundance (40 veins/m) also is found in Core 185-801C-18R, which was cored by standard RCB.

The major secondary minerals present in the Site 801 section drilled during Leg 185 (saponite, calcite, celadonite, and pyrite) are generally similar to those of the Leg 129 section and other upper crustal sections and result from interaction of basalts with seawater fluids at temperatures of $\sim 0^{\circ}$ – 50° C (Honnorez, 1981; Alt et al., 1992; summary in Alt, 1999). Relatively low seawater fluid fluxes result in the dominant pyrite-bearing dark gray alteration, whereas locally greater fluxes of oxygenated seawater cause the oxidation observed in the brown rocks and alteration halos. Celadonitic alteration along fractures may be related to diffuse flow of distal, cooled hydrothermal fluids at the spreading axis (see paragraph immediately below) or precipitation from cold seawater-derived basement fluids (Alt, 1999).

Alteration of the Site 801 section can be interpreted based on previous work on the Leg 129 section and by analogy with other studied oceanic basement sections (Staudigel et al., 1995; Alt et al., 1996; Alt, 1999). The tholeiitic section of Legs 185 and 129 was formed at a fast-spreading mid-ocean ridge at ~ 165 Ma (Pringle, 1992). The hydrothermal iron-silica deposit formed on the seafloor at the spreading axis, at temperatures probably $< 50^{\circ}$ C (Alt et al., 1992). Hydrothermal fluids were most likely derived from high-temperature reactions at depth, which produced acid fluids enriched in alkalis, metals, silica, and sulfide (Edmond et al., 1979). It was cooled, distal hydrothermal fluids, however, that resulted in the formation of the hydrothermal iron deposit at the seafloor. The intensely altered green rocks immediately beneath the deposit represent the feeder zone for the hydrothermal deposit, with the buff-colored rocks transitional to less altered dark gray host rocks. The much less intense alteration and formation of celadonitic minerals and chalcedony in veins and alteration halos along fractures at greater depths may be related to circulation of similar distal hydrothermal fluids at the ridge axis (Alt et al., 1992; summary in Alt, 1999). The intense pale green alteration observed in Cores 185-801C-15R and 16R is also probably related to the feeder zones for the hydrothermal deposit in Core 129-801C-4R and the smaller hydrothermal sediment interval in Core 185-801C-16R. The pervasive dark gray background alteration and local brown oxidizing alteration resulted from subsequent circulation of seawater fluids at low temperatures, beginning at the spreading center but continuing on ridge flanks and farther off axis. Carbonate veins form relatively late in the sequence, and the multiple generations of carbonate veins in the uppermost Leg 129 section are suggested to result from continued formation of carbonates as the crust ages (Alt and Teagle, 1999). Rb/Sr dating of celadonites from Site 801 gives an isochron age of 132 Ma, suggesting that celadonite remained open to exchange for ~ 30 m.y. or that the isotopic system was reset somehow at 132 Ma (Bourasseau, 1996).

The alkali basalt section at Site 801 formed ~ 7 m.y. after the tholeiites (Pringle, 1992), and re-examination of the rocks and overlying sediments during Leg 185 suggests that the alkali basalts were intruded as

sills between the hydrothermal deposit and the overlying sediments. The reason for the more intense alteration of the alkali basalts compared to the tholeiites is uncertain but may be related to greater primary volatile concentration or simply to differences in permeability (because of a larger grain size) and greater fluid fluxes through the alkali basalts. It is not clear whether magmatic or tectonic activity related to the formation of the alkali basalts influenced fracturing, fluid flow, and alteration in the underlying tholeiitic section cored during Leg 185.

Perhaps a surprising feature of the Leg 185 section is that alteration, at least as shown by the presence of dark, brown, and mixed alteration halos along veins, is greater in the lower portion of the section than at the top. Evidence from other well-documented deep basement sites suggests that the effects of cold seawater alteration, although clearly heterogeneous, generally decrease with depth (Staudigel et al., 1995; Alt et al., 1996). Oxidation effects (brown altered rocks) are abundant in the alkali basalts at Site 801 and make up a significant proportion of alteration in the Leg 129 tholeiitic section (~10%) (J.C. Alt and D.A.H. Teagle, unpubl. data), but the dark gray, pyrite-bearing background alteration is by far the dominant alteration type below 550 mbsf. Alteration of the uppermost crust at Site 801 was controlled by local hydrological conditions, with circulation of larger volumes of oxygenated seawater focused at the very top of the tholeiite section and at depth through massive units in the lower part of the section (below 780 mbsf).

A preliminary estimate indicates that the total section cored during Leg 185 has experienced an ~17% increase in K₂O and Rb contents as the result of alteration with seawater. Adding interpillow sediment to this estimate increases the bulk K₂O content of the Leg 185 section to 60% greater than in fresh basalt alone, with 27% of the total alkali budget residing in interpillow sediment.

PALEOMAGNETISM

Magnetic Susceptibility

In addition to remanent magnetization, magnetic susceptibility was measured on all cores as a result of established shipboard procedures. Those procedures include whole-core sections measured with the MST and archive-half sections measured by the archive multisensor track (AMST) (see **“Instrumentation Used,”** p. 27, in the **“Explanatory Notes”** chapter). The redundancy is the consequence of the fact that routine AMST data gathering was done for the first time during this leg. AMST software now ensures that the susceptibility of unrecovered intervals in the core is not measured; therefore, sample volume is well known (as opposed to the merely relative values of the past), and reasonably accurate susceptibility values are now obtained. The greater accuracy of AMST relative to MST susceptibility measurements was demonstrated by an experimental test that included discrete sample, AMST, and MST susceptibility measurements; the results are reported in **“Measurements and Procedures,”** p. 29, in the **“Explanatory Notes”** chapter. In the test, the AMST gave approximately the same values as obtained from discrete samples. The far greater accuracy of the values of susceptibility per volume measured on the AMST makes these data preferable to those of the MST. Discrete samples may not need to be measured in the future.

The data for the Hole 801C basaltic basement obtained from both instruments are plotted in interpolated form in Figure F57. No volume correction was applied to the MST data because the appropriate amount of correction is difficult to establish and because the greater accuracy of the AMST determinations makes correction of MST data redundant. The short intervals of significantly higher susceptibility values in Figure F57 correspond to the presence of thick flow units (e.g., Cores 185-801C-30R through 31R at ~745–765 mbsf, or Cores 37R through 38R between 810 and 830 mbsf), which possess coarse-grained magnetite. A large difference occurs between the two curves at depths of 710–900 mbsf. This depth range encompasses all of the thick flow units, which possess inherently greater susceptibility because of the presence of coarser grained magnetite. Both the presence of the higher susceptibility material and the lack of valid volume information for the MST instrument probably account for the discrepancy between the two instruments in this region.

Remanent Magnetization

Methods

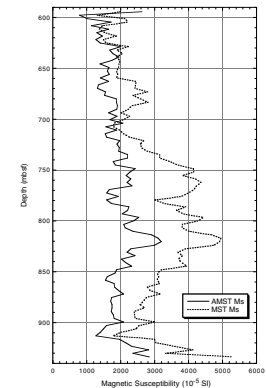
All sections of the archive halves of the whole cores were measured and demagnetized with the shipboard automated long-core cryogenic magnetometer. Measurements on the recovered basement cores were made at 5-cm intervals through each core section. Prior to demagnetization, fragmented core pieces were carefully reconstructed to their original unfragmented form using Styrofoam spacers in the trays, and unoriented core pieces were removed. Thus, the continuous measurements obtained present as complete a representation of the remanent magnetization of the core as possible.

The nominal width of the sensor region of the magnetometer is >20 cm; thus, each measurement represents a weighted average of the remanent magnetization of at least 20 cm of basalt or of basalt plus empty spaces between core pieces. For this reason, discrete samples also were taken, so that more precise values of the remanent inclination and intensity could be obtained and so that vectors removed by demagnetization and various rock-magnetic properties could be examined in greater detail.

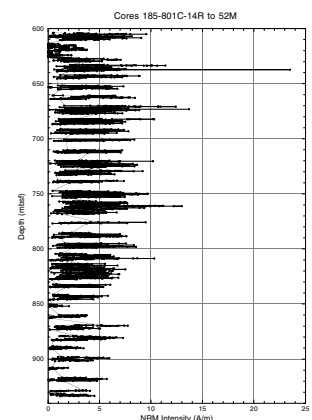
Results

The natural remanent magnetization (NRM) measured by the shipboard magnetometer prior to any demagnetization generally possessed intensities of 2–4 A/m (Fig. F58). NRM intensities average ~4 A/m down to ~830 mbsf; below, values are a little lower, between 2 and 3 A/m. The higher intensities coincide with the presence of thick basalt flows. The last of the thick flows occurs in Core 185-801C-38R. This is also the level at which NRM intensities change from a dominance of values between 3 and 5 A/m to ones between 0.5 and 4 A/m (Fig. F58). The thick flows likely have coarser grained titanomagnetites than the pillow basalts; hence, the correlation of intensity and flow thickness suggests that a significant portion of the NRM intensity observed is an induced, rather than remanent, magnetization. The induced magnetization may result either from imposition of a drilling remanence, such as is nearly always observed in ODP cores or may be a remanence induced by the present geomagnetic field.

F57. Shipboard magnetic susceptibility measurements, p. 128.



F58. Intensities of NRM, p. 129.



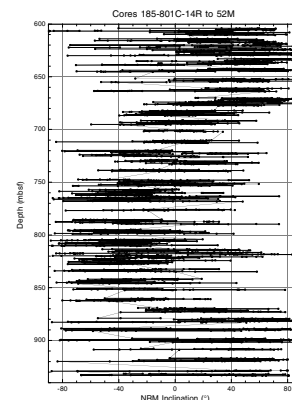
The NRM inclinations of the archive halves of all cores obtained from Hole 801C during Leg 185 are shown in Figure F59. These results are startling in that they display several polarity intervals, and the entire sequence forms a sinusoidal pattern of polarity changes. Particularly surprising are the numerous flows displaying intermediate directions between flows of opposite polarity directions. NRM inclinations were measured from two-thirds of the discrete samples collected, and their inclinations display the same sinusoidal pattern (Fig. F60) as the long-core sections. In addition, numerous flows possess intermediate magnetic directions.

Archive halves were routinely demagnetized at alternating fields (AFs) of 2, 5, 10, 15, 20, 25, 30, and 35 mT. Samples of normal, reversed, and transitional inclination flows show the same responses to AF demagnetization (see Fig. F61A, F61B, F61C, respectively). The sinusoidal signature remains through demagnetization; the results after demagnetization at 10 mT are shown in Figure F62. Above 10 mT, progressive acquisition of anhysteretic remanence (ARM) occurs with increasing field strength, which, as discussed more fully in “Instrumentation Used,” p. 27, in the “Explanatory Notes” chapter, gradually obscures the remanent signature. The ARM acquisition is first apparent in the thick flows at ~15 mT but eventually (~25 mT) affects the pillow basalts as well. Thus, above 10 mT, the remanent signature becomes progressively more obscured by ARM acquisition. The sample in Figure F61B shows the beginning of a the typical trend away from the characteristic remanent magnetization direction of this reversed polarity sample and toward the direction of the field existing at the AF coils (the direction of that field is ~190° declination and 80° inclination). Figure F61C shows a sample of normal polarity magnetization with incipient acquisition of the ARM.

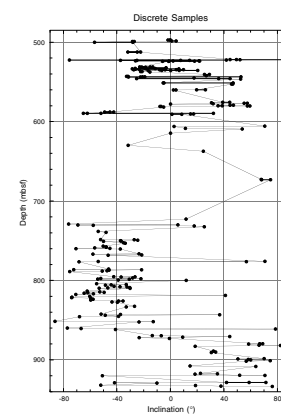
The data of Figure F62 indicate three changes of geomagnetic field polarity. Moreover, the upper portion of the tholeiite sequence obtained during Leg 129 (Wallick and Steiner, 1992) indicated two additional polarity intervals. The Leg 129 sequence ended in normal polarity, whereas that cored during Leg 185 begins with reversed polarity; ~10 m between the two sequences was not recovered. The Leg 185 sequence begins with Southern Hemisphere reversed polarity between 600 and 680 mbsf. The designations of normal and reversed polarity were determined from the results obtained during Legs 129 and 144. During Leg 129, the Southern Hemisphere location of the plate during the mid-Cretaceous was clearly established by the normal polarity signature in the sedimentary section of Site 801 during the 25-m.y.-long normal polarity of the geomagnetic field, the Cretaceous Normal Polarity Superchron (Steiner and Wallick, 1992). By extrapolation, the first tholeiites encountered were determined to have a Southern Hemisphere reversed polarity remanence (Wallick and Steiner, 1992). Downhole logging of Hole 801C with a three-axis magnetometer during Leg 144 confirmed that the tholeiite section has a Southern Hemisphere reversed polarity direction, that changed downhole to normal polarity (Ito et al., 1995).

The average inclination in the entirely reversed or normal polarity intervals is ~45°. Because several polarity intervals are encompassed by this section of basaltic crust, secular variations of the geomagnetic field definitely have been averaged; therefore, the 45° value is the true site inclination, corresponding to a site paleolatitude of 27° at the time of oceanic crust formation.

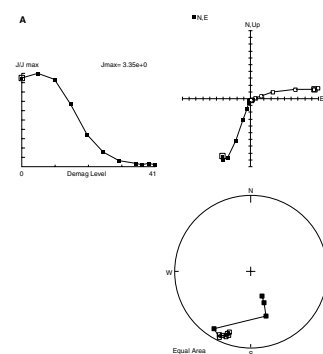
F59. Inclination vector of NRM, p. 130.



F60. Inclination vector of the untreated remanent magnetization, p. 131.



F61. Demagnetization diagrams, p. 132.



The section between 600 and 630 mbsf contains reversed polarity in the least-altered basalts. Much of Cores 185-801C-15R and 16R contain basalts and interflow sediments that have been extensively altered to green or tan colors, and the middle of Core 16R contains a zone of hydrothermal deposits. The magnetic signature associated with both the hydrothermal zone and the altered zones is one of very low inclinations. Both green or tan basalts and the altered interpillow and interflow sediments have exclusively very low (nearly zero) inclinations. The alteration overprinted the basalts because little-altered basalts in Cores 185-801C-14R and 17R on either side of this altered interval have notably steeper positive inclinations. Similar characteristics are associated with most zones of greenish alteration higher in the hole, cored during Leg 129. The similar magnetic directions suggest that the alteration and the emplacement of the hydrothermal deposit are related events. Presumably, these events occurred when the plate was near the equator and, perhaps, are related to the Oxfordian unconformity recorded in the overlying sedimentary sequence at a time when the site lay on the equator (Steiner and Wallick, 1992).

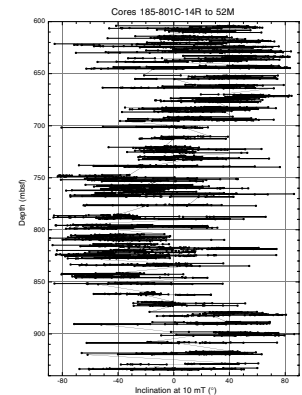
Below Core 185-801C-16R (~633 mbsf), basalts with visible large-scale alteration features, such as saponite replacement and carbonate vesicle and vein fillings, display the same remanences as those without such changes. Basalts with excessive celadonite or gray and brown halos also do not appear to have their remanence altered relative to nearby unaltered basalt. Thus, generally speaking, two remanent magnetic signatures were observed in Hole 801C tholeiites, one presumed to be associated with crystallization and the other with the hydrothermal alteration event. The remanent signature associated with the hydrothermal event is visible only as deep as Core 185-801C-16R.

Summary

Site 801 is a unique basement site in that the drilling penetrated nearly 400 m into oceanic crust that has very low amplitude, or an absence of magnetic anomalies. This is a characteristic of Middle Jurassic basement in all oceans and termed the "Jurassic Quiet Zone" (JQZ). Many hypotheses have been advanced in order to explain the absence of lineated anomalies: the mid-Jurassic JQZ occurred in a time (1) without geomagnetic field reversals, (2) of anomalously low geomagnetic field intensity, or (3) of very rapid reversals. The continuous measurements of remanent magnetization obtained from the Hole 801C cores with the shipboard magnetometer show gradual changes in the magnetic field direction from one polarity interval to the other, with flows between those of opposite polarities displaying intermediate inclination values. In combination with the previous results from Leg 129, the basement of Hole 801C shows as many as six polarity intervals over 400 m. The drilling results indicate that the igneous basement at Site 801 erupted in a period of rapid polarity alternations of the geomagnetic field. Hence, these data indicate that the explanation for the origin of a "quiet" magnetic signature in the JQZ lies in the existence of numerous superposed flows of opposite polarities of magnetization.

The presence of numerous flows with directions intermediate to those of the normal and reversed polarity flows suggests excessively rapid extrusion rates. The present-day East Pacific Rise is the fastest among oceanic spreading ridges, spreading at 10–15 cm/yr (whole rate). The geomagnetic field during relatively recent Earth history requires 2000–5000 yr to fully reverse its direction. The reversal highest in the

F62. Inclinations plotted against depth below seafloor, p. 135.



section that is displayed in Figure F62 occupies ~100 m between the fully reversed to the fully normal direction. At the fastest EPR spreading rates and the minimum known reversal rate duration, one would expect a full reversal of the geomagnetic field direction to occupy ~160 m of extrusive basalt, assuming continuous extrusion. This example shows that the Site 801 magnetic observations of the highest reversal of Figure F62 certainly are generally consistent with known reversal and spreading rates. Since extrusion is probably not continuous, the observed 100 m for the full reversal appears reasonable. However, the lower reversal in Figure F62 (845–900 mbsf) appears less reasonable in terms of present knowledge. That reversal is found over 55 m of the basaltic column, but fewer transitional flows appear to exist. In particular, at 875–880 mbsf, the directional change between two consecutively cored intervals (Cores 185-801C-43R to 44R) is much larger than elsewhere, perhaps suggesting a less continuous extrusion rate during this reversal. However, a breccia unit that could be interpreted as a fault was present, thus 55 m may not represent the full thickness of the transition.

In summary, this remarkable record of geomagnetic field behavior in the basaltic column of Hole 801C requires one or a combination of two mechanisms, both of which are somewhat poorly known at present. The number of flows with intermediate directions suggests that the ridge was spreading extremely fast, equal to or at a greater rate than the fastest rates observed today. Alternatively, or in addition, the geomagnetic field may have had a somewhat different component composition than that at present and in the recent past. At present the dipole field component dominates the quadripole component, but in the Middle Jurassic, perhaps the dipole was subordinate and the quadripole dominant. This arrangement provides one possible mechanism for the prominence of nondipolar directions observed between the polarity intervals in Hole 801C.

PHYSICAL PROPERTIES

Introduction

The physical properties of primary crystalline rocks removed from depth and measured at atmospheric pressures are strongly related to both the original porosity and secondary porosity associated with stress unloading and the coring process. Alteration products, infilling of fractures and voids with secondary phases, and contributions from sediment, also influence the physical state of the recovered oceanic crust. Thus, physical properties measurements are indicators of lithologic type, texture, and degree of alteration and are used to assess the physical state of the oceanic crust with depth and to establish the correlation between downhole measurements and cored material.

MST measurements on whole-core sections from Hole 801C were obtained during Leg 185 and half-core sections within igneous basement were obtained during Leg 129. The MST includes instruments that measure magnetic susceptibility, gamma-ray attenuation evaluator (GRAPE) bulk density, and natural gamma radiation (NGR). We determined *P*-wave velocities from split cores in liners in the transverse *x* direction. Velocity measurements in the transverse (*x* and *y*) and longitudinal (*z*) directions on cut cubes allowed us to investigate possible velocity anisotropy. Index properties on cut samples including wet bulk density,

grain density, porosity, and water content were calculated from measurements of wet mass, dry mass, and dry volume. We also measured thermal conductivity on split cores. MST measurements were the only physical properties data collected from Hole 801D (the single seafloor punch core) (see “Physical Properties,” p. 36, in the “Explanatory Notes” chapter.

Index Properties

Index properties were measured on 156 samples obtained adjacent to cut cubes that were used for velocity determinations. Additional samples were obtained in material that was too fragile to be cut into a cube. A salt correction assuming 3.5% interstitial fluid salinity was applied. The precision of these measurements (density, porosity, and velocity) is ~2% of the measurement for each property. Results are presented in Table T11 and displayed in Figure F63 and include comparable results obtained during Leg 129 for the igneous section (i.e., tables 6 and 7 in the “Site 801” chapter of Lancelot, Larson, et al., 1990). The average wet bulk density of all basement samples (including those from Leg 129) is $2.76 \pm 0.17 \text{ g/cm}^3$ and varies between 2.13 and 2.99 g/cm^3 , and porosity varies from 0.6% to 33.3% with a mean of $7.6\% \pm 5.6\%$ and a median value of 6.1%. Density and porosity show the expected negative correlation (Fig. F64). These plots also indicate that samples classified as flows generally have higher density, higher velocity, and lower porosity than samples classified as pillows. The greatest variation in porosity and density is in Cores 185-801C-14R through 17R (~604–630 mbsf) and is associated with samples identified as interpillow material, hydrothermal deposits, and variably altered basalt. Neither density nor porosity appear to vary systematically with depth. The seven samples with porosity >20% are in the heavily altered flow units at 541 and 545 mbsf and in altered (pale green and dark green) pillow units at 621, 626, 627, 819, and 932 mbsf. These samples are also characterized by the six lowest average velocities (3237–4150 m/s), and the seven lowest densities (2.13–2.47 g/cm^3). The lowest porosity measured (0.6%) is in silicified red-brown interpillow material from Core 185-801C-15R, but generally the lowest porosities are associated with the least-altered basalt. All samples classified as breccia have porosity above the median value.

GRAPE Density Measurements

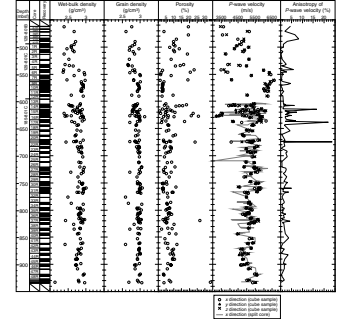
Bulk density was measured by the GRAPE every 4 cm for 4 s on unsplit sections of core from Hole 801C drilled during Leg 185. The continuous GRAPE density measurements are compared to discrete samples of wet bulk density from Hole 801C in Figure F65. The large scatter in GRAPE density values results from the discontinuous core (empty space and/or rubble zones). The generally lower values (relative to discrete samples), where core is relatively continuous, are due to smaller core diameters than calibration cores. MST measurements, including GRAPE density values from Hole 801D, are shown in Figure F66. All reference to density in this report will be to the individual gravimetric samples.

Natural Gamma Radiation

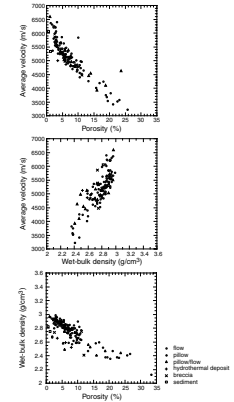
We measured NGR every 10 cm for 20 s on unsplit sections of core from Hole 801C drilled during Leg 185 and on working-half cores from the basement section drilled during Leg 129. Peak values (15–20 cps) oc-

T11. Physical properties of discrete samples, p. 204.

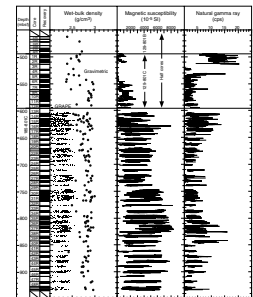
F63. Index properties and compressional wave velocities, p. 136.



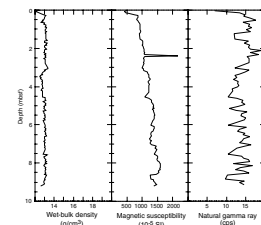
F64. Crossplots of data from igneous section, p. 137.



F65. MST measurements vs. depth, p. 138.



F66. MST data for Hole 801D, p. 139.



curred only within the upper alkalic section above 510 mbsf. The majority of the tholeiitic section is characterized by low gamma-ray counts (<6 cps) punctuated by relatively high values (7–15 cps) in narrow zones, such as the highly altered basalt (celadonite and glauconite) at ~530 mbsf and within broader zones, also associated with obvious zones of alteration, between ~600 and 640 mbsf (Cores 185-801C-14R to 17R), and 805–850 mbsf (Cores 185-801C-36R to 40R) (see Fig. F65 and “Correspondence between MST-NGR Data and Features in the Core,” p. 56). At the individual core scale, NGR often appears inversely correlated to magnetic susceptibility and appears to be qualitatively related to the amount of potassium-rich alteration products such as celadonite (i.e., high alteration associated with high NGR and low magnetic susceptibility). It is also possible that remobilization and fixation of uranium in zones of alteration contributes significantly to the total gamma-ray count in certain intervals. The NGR profile exhibits fluctuations and general trends that are similar to those of the downhole spectral gamma-ray logging data and will be particularly useful for core-log integration (see “Downhole Measurements,” p. 38).

Magnetic Susceptibility

We measured magnetic susceptibility every 4 cm for 4 s on unsplit sections of core from Hole 801C drilled during Leg 185 and on working-half cores from the basement section drilled during Leg 129 (Fig. F65). At the individual core scale, magnetic susceptibility varies inversely with gamma-ray counts and is low within intervals of relatively high alteration, hydrothermal deposits and interpillow material and uniformly high within thick massive flow units. Comparison of three independent susceptibility measurements, the MST, AMST, and discrete samples are discussed in “Paleomagnetism,” p. 27, in the “Explanatory Notes” chapter.

Compressional Wave Velocity Measurements

We determined compressional wave velocities in three mutually perpendicular directions (x, y, and z) on discrete samples (cubes) and in the x direction on split-core sections in a liner (Tables T11, T12; Fig. F63). Velocities from the split core correspond well with those from individual cubes. The average velocity value from each sample cube (i.e., $[V_x + V_y + V_z]/3$) ranges from 3237 to 6591 m/s with an average 5153 ± 640 m/s through the entire igneous section drilled during Legs 129 and 185. The greatest variation in velocity occurs in Cores 185-801C-14R to 17R (~604–630 mbsf) and is associated with samples identified as interpillow material, hydrothermal deposits, and variably altered basalt. Velocity values on discrete samples correlate well with those of in situ downhole velocity measurements (see “Downhole Measurements,” p. 38). Velocity anisotropy is negligible (<5%) for the majority of samples; however, four values of over 15% anisotropy correspond to interpillow sediment and a pillow with a vertical carbonate vein. There is no clear relationship between depth and velocity, although, velocity, density, and porosity are well correlated throughout the section (Fig. F64). A set of samples exhibiting velocities >6000 m/s fall outside the linear trend between velocity vs. density and velocity vs. porosity (Fig. F64). These samples are all within massive tholeiites in Cores 129-801C-5R to 12R (~542–581 mbsf) and correspond to the greatest resistivity values observed at Site 801 (see “Downhole Measurements,” p. 38). Similar

T12. Compressional wave velocity on split cores, p. 208.

zones of relatively high velocities (and resistivities) occur within thick flow units in Cores 185-801C-27R to 28R, 30R to 31R, and 37R to 38R. An extended zone of relatively low velocities (<5100 m/s) is found within Cores 185-801C-43R through 46R.

Thermal Conductivity

Thermal conductivity measurements were taken once per core on split-core sections on samples that were at least 20 cm long, massive, and relatively unaltered (i.e., no interpillow, hydrothermal, or breccia was sampled). Thermal conductivity is listed in Table T13 and plotted with depth in Figure F67. Thermal conductivity of igneous basement cored during Legs 129 and 185 ranges from 1.49 to 4.98 W/(m·K) and averages 1.85 ± 0.53 W/(m·K). Although thermal conductivity varies little downhole, there is a clear offset at ~585 mbsf, from values above 2 W/(m·K) to values below 1.8 W/(m·K).

Summary

Physical properties of oceanic basement at the hand-sample scale are strongly influenced by the extent of alteration as well as lithologic type and texture. We developed preliminary relationships between physical properties and the visible indications of basalt alteration and with various important components of oceanic crust (interpillow material, sediment, and hydrothermal deposits). These relationships were used to establish the correlation between cored material and physical/chemical measurements obtained with downhole tools and are, therefore, an important component in the fundamental objective of reconstructing a complete crustal stratigraphy through core-log integration. For example, the observation that hydrothermal deposits are of lower porosity and of higher density and velocity relative to highly altered basalt (and are thus relatively high resistivity units), allowed the correlation of continuous, high-resolution resistivity images using the Formation Micro-Scanner tool (FMS) within the hydrothermal interval in Core 185-801C-16R (see “Downhole Measurements” below). The clear relationship between the NGR signature and patent alteration features also formed the basis for a K budget for the core (see “Using Natural Gamma Ray to Calculate Potassium Budgets,” p. 55).

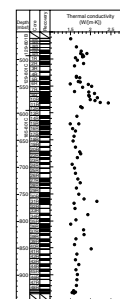
DOWNHOLE MEASUREMENTS

Logging Overview

Downhole measurements were made in Hole 801C during Leg 185 after completion of drilling with the RCB and before testing of the DCB. Three logging runs were performed consisting of one pass with the triple combo tool string and two passes with the FMS/sonic tool string. In all runs, the tool strings were lowered to within 70–90 m of the total hole depth cored by the RCB (926 mbsf) and were logged up to the bottom of the casing (483 mbsf) installed during Leg 129. Access to the lower reaches of Hole 801C by the tool strings was likely limited by soft fill that had washed back into the hole or by a bridge created by a breccia unit cored between 840 and 850 mbsf.

T13. Thermal conductivity values, p. 210.

F67. Thermal conductivity vs. depth, p. 140.



Run 1

The triple combo tool string was deployed first and measured porosity, density, resistivity, and natural gamma-ray emissions to within 70 m of the total hole depth. The tool string included the hostile environment natural gamma sonde (HNGS), hostile environment lithodensity sonde, accelerator porosity sonde, dual laterolog (DLL), and temperature acceleration pressure sensor (TAP). The dual induction tool (DIT) was replaced by the DLL because of the potential for resistivity values of the massive basalt flows to exceed the dynamic range of the DIT (0.2–2000 Ω m). The logging run went very smoothly, and continuous, high-quality data were obtained even though the heave compensator on the take-up winch was not functioning during this run. The problem was remedied in subsequent lowering of the FMS/sonic tool string.

Run 2

The FMS/sonic tool string was used to measure microresistivity (FMS), seismic velocity, magnetic field, and natural gamma-ray emissions to within 90 m of the total hole depth. The tool string included the natural-gamma spectrometry tool (NGT), dipole sonic imager (DSI), FMS, and general purpose inclinometer tool. Problems with the DSI prevented the measurement of seismic velocities during this lowering; however, the other tools provided continuous and high-quality data.

Run 3

For the second FMS/sonic run, the DSI tool was replaced with the long spacing sonic sonde (LSS) to obtain seismic velocity measurements. The tool string was then lowered to within 90 m of the total hole depth. During this logging run, the tool string encountered two sections of the borehole that impeded progress on the uphaul. The first “sticky” section was at ~820 mbsf and appeared to be the result of debris and cuttings from above falling down on top of the tool string. The second sticky section occurred at ~480 mbsf and appeared to coincide with a rugose section of the borehole within the hydrothermal zone identified during drilling operations of Leg 129 and logging operations of Leg 144. Even though this logging run was not as smooth as the previous two, the resulting data were still of high quality and provided continuous coverage up the borehole.

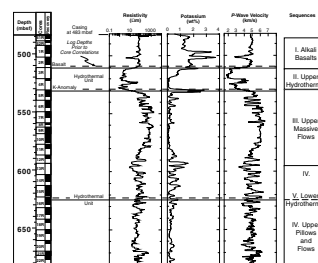
All logging runs were registered relative to the cores and the bottom of the Leg 129 casing as described in the next section. For each of the logging runs, the location of the casing was easily identified by the sudden change in data recorded by various instruments (e.g., resistivity and caliper width).

Correlation between Logs, Cores, and Cored Intervals

The logs were correlated with both the cores and the cored intervals by matching various distinctive features in the logs to the same or related features in the cores. The specific cores used for these correlations are Cores 129-801C-3R and 5R and 185-801C-16R, all of which have distinctive features associated with bounding recovered hydrothermal units.

Core 129-801C-3R (Fig. F68) is a 0.95-m massive alkali basalt, which lies at or just above the top of the upper hydrothermal unit that is espe-

F68. Cores and cored intervals correlated to logs, p. 141.



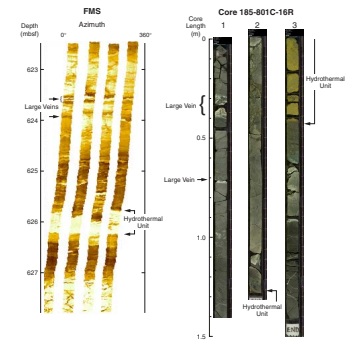
cially well defined by a pronounced change in logged values of resistivity and velocity. Core 129-801C-5R contains very altered tholeiitic basalt with a large increase in potassium content, especially in Sections 1 and 2. This potassium anomaly correlates with the pronounced potassium peak observed in the gamma-ray logs. Finally, Core 185-801C-16R is made up of several units that include the lower hydrothermal unit starting at the bottom of Section 2 and mainly recovered in Section 3 (Fig. F69). This hydrothermal unit correlates with a distinctive microresistivity signature in the FMS logs. The FMS signature of this hydrothermal unit (Fig. F69) is a distinctive 40-cm-thick unit of high resistivity. The upper and lower boundaries are both abrupt, suggesting a marked change in lithology at both levels. The upper boundary undulates, whereas the lower boundary is nearly horizontal. These dimensions and characteristics are very similar to those of the hydrothermal unit in the recovered core between intervals 185-801C-16R-2, 126–128 cm, and 16R-3, 0–42 cm (Fig. F69).

A solution that brings the above three units in the cores and logs into coincidence is to place the bottom of the casing pipe at 483 mbsf (6168 meters below rig floor [mbrf]), as observed on the resistivity log (Fig. F68). This solution leaves unaffected the core depths recorded during Leg 129 and subsequently in the same sequence during Leg 185 (Figs. F68, F69). This is a relative downward shift of 2 m for the logs because it was thought during Leg 129 that the bottom of casing was at 481 mbsf (6166 mbrf). Also recorded during Leg 129 was the bottom of the “rathole” drilled to accept the casing string at 491 mbsf (6176 mbrf). However, the dual-caliper log on the FMS logs clearly shows only 9 m of open rathole below the bottom of casing, not the 10 m implied by the above estimates. Moreover, the open 9-m rathole is extremely smooth, suggesting that the 3-m expansion joint built into the casing string during Leg 129 is fully open, and thus the bottom of casing is actually at 482 mbsf (6167 mbrf). The additional 1 m of relative offset probably resulted from a bookkeeping error that placed the top of Core 129-801C-1R at least 1 m deeper than its actual depth. To correlate the logs to the cores, we prefer to lower the depths of the logs by 2 m and leave the cored intervals as they were recorded and published for Leg 129. This solution has the disadvantages of placing the bottom of casing 1 m lower than its probable actual depth and producing a 2-m mismatch with the logs taken during Leg 144 (Shipboard Scientific Party, 1993; Larson et al., 1993) because these logs were calibrated to the bottom of casing at 481 mbsf (6166 mbrf). We believe that these disadvantages are outweighed by the benefits from retaining the cored intervals from Legs 129 and 185 at their originally published and recorded levels, respectively.

Inspection of Figure F68 suggests that 2 m is the minimum shift between the originally recorded depths of the logs and cores that is necessary to bring the three features in question into coincidence. Another 1–2 m of offset in the same sense would not violate the previously described data in any of the three cores or logged intervals. However, we believe that the offset can be fixed at 2 m and, furthermore, that the cored intervals can be tied to that offset with the following observations and logic.

Cored intervals are more difficult to relate to logs than features within cores because the former requires complete core recovery of the interval in question, whereas the latter only requires identification of a common unit in both the cores and logs. If correct, the 2-m shift proposed here between the cores and logs implies that Core 185-801C-16R

F69. FMS microresistivity correlated to core images, p. 142.



recovered the complete section from its top, down to the hydrothermal unit, because the proposed shift places the hydrothermal unit in the logs at exactly the same level as it is in the core. A larger relative shift would require that the excess difference was missed in the cored interval somewhere between the top of Core 185-801C-16R and the hydrothermal unit. Close inspection of the FMS logs reveals two low-resistivity units at 1.8–1.9 and 2.1–2.3 m above the top of the hydrothermal unit (Fig. F69). These appear to correlate with two large veins of calcareous precipitate in the core at intervals 185-801C-16R-1, 70–72 cm, and 27–37 cm. In the core, these veins are present at ~2.0 and 2.3–2.4 m above the top of the hydrothermal unit, respectively. Other basaltic units between the veins and hydrothermal units also can be generally identified in the FMS logs.

Thus, it appears that the complete section was recovered between the upper large vein at interval 185-801C-16R-1, 27–37 cm, and the hydrothermal unit (Fig. F69). If we make the fairly reasonable assumption that the full section also was recovered in the top 27 cm of this core, then complete recovery occurred between the top of the cored interval and the hydrothermal unit. This allows us to place the top of this cored interval of Core 185-801C-16R at 2.7 m above the top of the hydrothermal unit relative to the FMS logs after the 2-m relative shift proposed above (Fig. F69). This cored interval was recorded at 623.3 mbsf (6308.3 mbrf). We consider this correlation to be precise within ~10–20 cm.

Downhole First-Order Observations

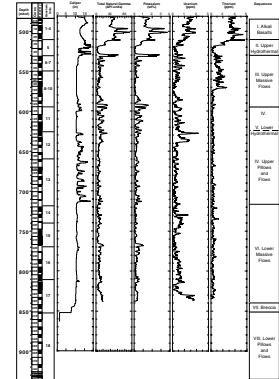
Overall, the postprocessing of the data produced continuous and very high quality records of downhole formation properties. These data are in very good agreement between the various tools, separate logging runs, core observations, and previously recorded logging data. The following is a summary of the initial observations from the logging data.

Borehole Characteristics

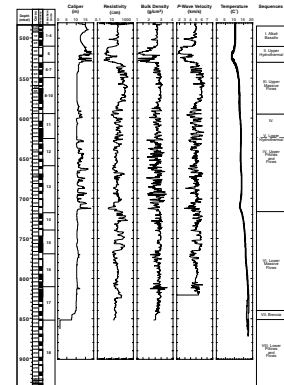
The size and shape of the borehole and its deviation with respect to north are recorded by the calipers of the FMS/sonic tool string and by the slim-hole lithodensity logging tool (HLDT) section of the triple combo tool string. These data are important for postprocessing other logging data (e.g., HNGS, seismic velocity, and magnetic field data). In addition, the uniformity and smoothness of a borehole can often be an indicator of the quality of data collected, as well as the integrity and rock type comprising the borehole walls.

For the majority of the borehole, the walls are relatively smooth and uniform with a typical diameter of ~11 in (~28 cm) (Figs. F70, F71, F72). These uniform portions correspond to the upper (III) and lower (VI) massive flow sequences, respectively. More rugose sections of the borehole are located within the upper hydrothermal zone (510–530 mbsf), at the interface between Sequence III flows and Sequence IV pillows and flows (580–600 mbsf), and within the Sequence IV pillows and flows below the lower hydrothermal unit (625–715 mbsf). There are several locations within the upper hydrothermal zone where the diameter of the borehole exceeds the limits of both the FMS and HLDT calipers (>16 in [>40 cm]), and in these locations data quality is expected to be very low. Within the remainder of the borehole, the data are continuous and appear to be of very high quality.

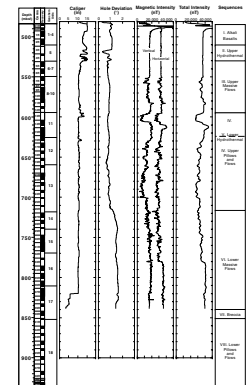
F70. Radioactive element logging measurements in Jurassic basement in Hole 801C, p. 143.



F71. Geophysical logging measurements in Jurassic basement in Hole 801C, p. 144.



F72. Magnetic measurements in Jurassic basement and deviation from true vertical in Hole 801C, p. 146.



Natural Radioactivity

On each logging run, natural radioactivity was measured continuously with either the HNGS or NGT. Both tools utilize scintillation detectors to determine the gamma radiation emitted by the decay of radioactive elements within the formation. Spectral processing of the measured gamma radiation identifies characteristic radiation peaks that are used to determine the concentrations of potassium (K, in weight percent), thorium (Th, in parts per million) and uranium (U, in parts per million). These values are combined to provide a measure of the total gamma-ray counts and uranium-free or computed gamma-ray counts. Corrections to the HNGS are made to account for variability in borehole size and borehole-fluid potassium concentrations.

The overall character of the total gamma-ray exhibits a general, but not monotonic, decrease in radioactivity with depth (Fig. F70), and these data are similar to the data collected during Leg 144 in the region of data overlap (483–560 mbsf). The highest gamma-ray counts are associated with Sequence I alkali basalts (480–510 mbsf) and the highly altered green tholeiitic basalts at the top of the Sequence III flows (~530 mbsf) cored during Leg 129 (Shipboard Scientific Party, 1990). Another region of elevated gamma-ray counts is near the top of the upper pillows and flows section (580–640 mbsf) and appears to be associated with a high frequency of pillow basalts, breccias, or interbedded siliceous sediments.

The potassium concentration closely mimics the total gamma-ray pattern, but the uranium and thorium concentrations are significantly different. Both the uranium and thorium data exhibit elevated concentrations within the alkali basalt section (480–510 mbsf); however, the uranium concentration is elevated at two distinctive peaks (~630 and 640 mbsf). These uranium peaks may be associated with the lower hydrothermal unit or sediments bounding the hydrothermal unit. Other increases in uranium occur at the top (725–750 mbsf) and at the base (830–845 mbsf) of Sequence VI flows.

The thorium data exhibit relatively high concentrations within the minimally altered tholeiitic basalts of Sequence III flows (535–580 mbsf). The source of these high thorium values is not well understood because geochemical analyses of discrete samples from this region (Castillo et al., 1992) exhibit extremely low values typical of MORB (<0.2 ppm Th). A similar pattern of thorium concentration is also observed in the Leg 144 logging data (Shipboard Scientific Party, 1993). This inconsistency probably reflects an artifact from the spectral processing of the HNGS and NGT tools.

Resistivity

The electrical resistivity of the formation was measured with the DLL tool and provides a rough estimate of the porosity of the formation. The DLL provides two resistivity measurements labeled “deep” and “shallow” on the basis of respective horizontal depths of penetration of the current into the formation. Both measurements are virtually identical throughout the logged interval (Fig. F71), suggesting the absence of a preferred fracture direction within the formation (Pezard and Anderson, 1989).

Inspection of the electrical resistivity data (Fig. F71) suggests that the measured interval may be separated into four main sections based on the variability and magnitude of the measured resistivity: top (483–590

mbsf), shallow (590–715 mbsf), intermediate (715–765 mbsf), and deep (765–850 mbsf). The top zone is characterized by long-wavelength, large-amplitude resistivity variations and coincides with the alkali basalt and hydrothermal and tholeiitic basalt sections cored during Leg 129. The highest and lowest resistivity values for the entire borehole are measured within this zone and correspond to Sequence III flows and Sequence II hydrothermal unit, respectively. The shallow zone has intermediate resistivity values that oscillate at a very high frequency. This portion of the borehole coincides with Sequence IV characterized by alternating layers of pillow basalts, thin flows, breccias, and interbedded silicic sediments. The intermediate zone has relatively high resistivity values with a longer wavelength variability. This section corresponds to the top of Sequence VI characterized by relatively thick (>2 m) flow units that are separated by less frequent pillow basalts and breccias. The deep section has fairly constant intermediate resistivity values, except in the region of a massive basalt flow between 810 and 825 mbsf where resistivity reaches a local maximum.

Density

The HLDT uses the detection of scattered gamma rays from a radioactive cesium source to determine the bulk density of rock units. These measurements are very sensitive to the integrity and smoothness of the borehole walls; therefore, the bulk density values along the more rugose sections of the borehole may be of lower quality than the data obtained along the more uniform sections.

The bulk density for the majority of the borehole is fairly constant with an average value of $\sim 2.7 \text{ g/cm}^3$ (Fig. F71). The most notable exception is in the region of the upper hydrothermal unit (i.e., 510 to ~ 530 mbsf) where the bulk density approaches 1 g/cm^3 . This anomalous section as well as the increased amplitude of the variability in the more rugose section of the upper pillows and flows section may be an artifact resulting from poor contact of the sensors with the rugose borehole walls. Overall, the variability of the bulk density closely mimics the general character of the resistivity measurements. In addition, the bulk density values are very similar to the density measurements made on discrete samples presented in “[Index Properties](#),” p. 36.

Seismic Velocity

The LSS uses two acoustic transmitters and two receivers to record the full waveform of sound waves that travel along the borehole wall. Compressional wave velocity (V_p) is determined through the depth-derived compensation principle, whereas acoustic travel times recorded at one depth are combined with a second set of readings at another given depth.

The compressional wave velocities above and below ~ 580 mbsf exhibit a very different character (Fig. F71). Above 580 mbsf, extreme velocity values are observed and correspond to the upper hydrothermal unit ($V_p = \sim 2 \text{ km/s}$) and the upper massive flow section ($V_p = >6 \text{ km/s}$). This high-velocity unit corresponds very well with velocity measurements obtained from discrete samples described in “[Compressional Wave Velocity Measurements](#),” p. 37. The alkali basalt section has more intermediate velocity values of 5 km/s . Below 580 mbsf, the compressional wave velocities increase slightly with depth and exhibit a high frequency variability. A notable increase in velocity at 740–765

mbsf is coincident with massive basalts cored within the Sequence VI flows.

Magnetic Field

Downhole magnetic field measurements were made with a three-axis fluxgate magnetometer that enabled the calculation of the horizontal and vertical magnetic intensity, inclination, and declination. Generally, the magnetic field directions are used to orient the FMS traces with respect to magnetic north and to calculate the deviation of the hole from true vertical if the NRM of the formation is negligible. However, within a borehole with rocks having a strong NRM different from the present-day magnetic field, such as oceanic basalt, this magnetic orientation is distorted. In this case, we acquire valuable information on the NRM directions and intensities in those rocks.

Comparisons with data recorded during Leg 144 (Ito et al., 1995) show that higher intensities were recorded in the vertical-field component during Leg 185, although the horizontal-field component is essentially identical for both legs. Initial qualitative comparisons with the Leg 144 vertical-field data suggest a constant offset of ~2900 nT. More quantitative comparisons will be made postcruise to verify the nature of this offset. The source of the additional vertical-field component could be the sonic tools run with the FMS string during Leg 185. During Leg 144 the FMS was run separately. A similar vertical-magnetization enhancement (although an order of magnitude less) was attributed to the permanent magnetization of the logging cable during Leg 148 in Hole 504B using a German magnetometer (Worm et al., 1996).

At least four distinct regions can be identified in the total magnetic intensity data (Fig. F72). The shallowest portion of the hole (483–550 mbsf) has magnetic intensity values that are remarkably uniform and monotonous and correspond to low magnetization values measured on Cores 129-801C-1R to 6R. Below this region, short-wavelength, small-amplitude variations in the intensity are present until ~595 mbsf. At this point, a large-amplitude, long-wavelength variation occurs in the uppermost portion of Sequence IV (595–620 mbsf). The source of this large-amplitude variation is difficult to determine because the core recovery in this portion of the borehole is very low. This large-amplitude variation also marks the upper limit of a long-wavelength variation in total magnetic intensity that continues until ~780 mbsf. Below 780 mbsf, the total magnetic intensity is relatively large and fairly uniform.

For the majority of the borehole, the horizontal and vertical components of magnetic intensity are generally in phase and exhibit similar patterns of variability, with the vertical component having a magnitude that is about half of the horizontal component. In three regions, however, the vertical and horizontal components appear to be out of phase (640–670, 710–745, and 760–780 mbsf). The in-phase relations suggest original magnetization in the Southern Hemisphere during the Middle Jurassic, whereas the out-of-phase relations suggest subsequent remagnetization in the Northern Hemisphere during the Cretaceous, as described by Ito et al. (1995). Additional detailed analysis and measurements are required to verify and quantify these initial, tentative observations.

The FMS/sonic tool string also contained three orthogonally oriented accelerometers that were used to estimate the angular deviation from true vertical of the borehole. This estimate is distorted by the shape of the borehole within the upper hydrothermal unit but appears very con-

sistent elsewhere. Hole deviation averages $\sim 1^\circ$ off true vertical from the bottom of the casing pipe down to about the base of the upper pillows and flows at ~ 720 mbsf. Below that level, hole deviation averages $\sim 1.5^\circ$ to the bottom of the logged interval at 840 mbsf.

Temperature

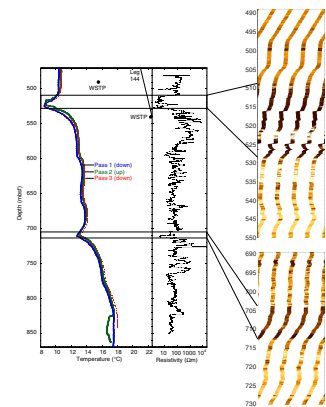
The TAP memory temperature tool was mounted on the bottom of the triple combo tool string to provide a continuous record of the borehole temperature. Because of the large amount of drilling mud circulated during drilling, the temperature in the borehole immediately after completion of coring is almost uniform and close to the seafloor temperature (Bullard, 1947; Lachenbruch and Brewer, 1959). The few hours elapsed between the end of mud circulation and logging do not allow the borehole to equilibrate to the undisturbed surrounding basement temperature, and the recorded data are typically lower than the basement temperature. Because the logging string was lowered twice to the bottom of the hole, temperatures were recorded three times along the way—twice on the way down and once on the way up—between the two logging runs (Fig. F73). The difference between the various passes measured only hours apart shows generally a progressive return to thermal equilibrium, but the comparison with temperature measured during Leg 144 (seven years after Leg 129 drilling) and with discrete temperature measurements made with the WSTP before drilling during Leg 185 at 490 and 540 mbsf (see Fig. F73 and “Temperature,” p. 52) indicate the actual extent of the necessary recovery. If the data do not provide the temperature of adjacent lithologic units, they can, however, indicate intervals with distinct thermal and hydraulic properties in the borehole.

In Figure F73, two 10- to 20-m-thick intervals centered approximately at 520 and 710 mbsf display negative temperature anomalies that suggest a slower return to equilibrium. In the same figure, the resistivity log and the FMS images show that these intervals have very low resistivity. The shallower of the intervals corresponds to a fossilized hydrothermal zone where a packer experiment during Leg 144 had suggested a high permeability (Larson et al., 1993) but failed to measure the actual value. The deeper of the intervals corresponds to a dramatic change in the lithologic character of the formation (as indicated in the caliper log) and to the approximate location of the igneous Sequences IV–VI boundary. The present temperature anomalies indicate that the two intervals could be high-permeability sections that have been invaded by the cold drilling fluids, have been drawn to lower temperatures by the invasion, and are consequently recovering more slowly from the drilling process. The fact that the anomalies are limited to the vicinity of these intervals shows, however, that they do not correspond to active hydrothermal conduits where significant pressure gradients would generate borehole-scale temperature disturbances.

Formation MicroScanner Data

The FMS produces high-resolution borehole images that mimic visual geologic features in or just behind the borehole wall. Initial processing of the raw FMS data into electrical images was performed aboard ship using proprietary Schlumberger software. The FMS imagery is provided in two formats—static and dynamic displays. The static display (e.g., Fig. F69) shows resistivity variations over long sections of data and

F73. Downhole temperature and FMS data, p. 147.



allows the identification of major lithologic units. The dynamic display adjusts the resistivity variations over much shorter sections of data and can be used to study individual features within major lithologic units. Initial analysis of these data indicates that high-quality data were obtained for the vast majority of the borehole. A sample of these data is shown in Figure F69 where the FMS data are compared to Core 185-801C-16R. Another qualitative comparison of the FMS imagery data with high-recovery core sections (e.g., Core 185-801C-37R) shows a very good correspondence with fractures, veins, and regions of low microresistivity.

Summary

Continuous, high-quality downhole measurements in Hole 801C were made during Leg 185 after completion of drilling with the RCB and before testing of the DCB. Three logging runs were performed, consisting of one pass with the triple combo tool string and two passes of the FMS/sonic tool string. In all three logging runs, the tool strings were lowered to within 70–90 m of the total hole depth cored by the RCB (926 mbsf) and were logged up to the bottom of the casing pipe (483 mbsf) installed during Leg 129.

Comparison of the logging data (e.g., FMS and resistivity) with the recovered cores identified a 2-m discrepancy between the depths of the cores and the logs within Hole 801C. Although the recorded depths of both the cores and the logs are in error, we have chosen to lower the depths of the logs by 2 m and leave the depths of the cored intervals as they were recorded and published for Leg 129 and in this volume.

The general character of the various logging data correlate very well with the lithologies recovered from drilling. High natural gamma radiation values associated with K, U, and Th are present within the alkali basalt section (483–510 mbsf), the highly altered tholeiitic basalt (525–530 mbsf) below the upper hydrothermal unit, and the upper half of Sequence IV pillows and flows (590–640 mbsf). Other notable, but enigmatic increases in gamma radiation are associated with uranium (730–750 and 820–840 mbsf) and thorium (530–570 mbsf).

Downhole measurements obtained with the triple combo tool string exhibit very good internal agreement with formation lithologies. In particular, relatively high resistivity, bulk density, and seismic velocity are associated with the more massive flow units (530–595 and 715–760 mbsf). Anomalously low values for all three measurements are observed within the upper hydrothermal unit (510–530 mbsf). The relative smoothness and rugosity of the borehole wall, measured with the calipers during each of the logging runs, correlates very well with the cored lithologies. The more uniform and massive flow units have much smoother walls than the sections of the borehole characterized by interlayers of pillows, flows, sediments, and breccias.

Initial analysis of the FMS microresistivity data indicates that high-quality data were obtained for the vast majority of the borehole. A qualitative comparison of the FMS imagery data with high-recovery core sections (e.g., Core 185-801C-37R) shows a very good correspondence with fractures, veins, and regions of low microresistivity. The FMS images were of sufficient quality to provide evidence for depth adjustments of the core depths with a precision of 10–20 cm.

The magnetic data are difficult to interpret without additional analyses, but the downhole magnetic intensity measurements exhibit an interesting large-amplitude variation at the top of Sequence III (595–630

mbsf). This larger amplitude variation also marks the top of a long wavelength change in intensity that continues until ~780 mbsf.

INTERSTITIAL WATER CHEMISTRY AND HEADSPACE GAS

For interstitial waters, the mudline wash core taken as Hole 801D was sampled at a frequency of one 5-cm whole-round sample per section of the core for a total of six samples. The chemical analyses of these samples indicate that the composition of the interstitial water in the core is very similar to that of inferred bottom water (Table T14). Considering that the core was an RCB push core compressing as much as several tens of meters of sediment into the core liner, advection and mixing of the interstitial fluids is likely responsible for the essentially constant composition with depth. Headspace gas was not measured in this core.

MICROBIOLOGY

Igneous samples from Hole 801C selected for microbiological studies represent a range of environments within the volcanic basement, including massive basalt, fractured basalt, and different types of alteration and vein filling. Core liners were split and core samples were chosen for microbiological analyses as well as for fluorescent microsphere and perfluorocarbon tracer (PFT) analyses. Table T15 gives a core-by-core list of samples collected for each type of analysis. Thin sections of volcanic glass were examined for “microbial” and chemical alteration patterns. Drilling fluid, surface seawater, and borehole water were collected to enumerate and characterize background levels of microbes potentially introduced during the drilling process. Sediment samples collected from Core 185-801D-1W were used to test sampling protocols and tracer techniques in preparation for sediment sampling at Site 1149.

Site 801

Microbiological Analyses

Details of Hole 801C samples used for microbiological analyses are shown in Tables T16 and T17 and complete petrographic descriptions of the six samples used for the full suite of microbiological analyses are given in “Sample Descriptions of Rocks Used in Microbial Cultures,” p. 48. The analyses included cultivation at 1 atm; enumeration of cells by epifluorescence microscopy; observation of cells with scanning electron microscopy (SEM); DNA extraction and community characterization; in situ hybridization; and maintenance at in situ pressure. An additional 11 samples were maintained at in situ pressure with no additional culturing medium. Additional culturing experiences were started on the ship using anaerobic media (see “Microbiology,” p. 31, in the “Explanatory Notes” chapter). Cultures started from Sample 185-801C-23R-1 (Piece 10, 119–125 cm) were incubated in 25° or 30°C incubators, within 3°C of in situ temperature (Table T16) and at in situ pressure of 620 atm. The pressure cultures were incubated at 25°C for one month, then transferred to 1 atm before the end of the leg. Cultures will be analyzed onshore for products of metabolism and for the presence of cells by microscopy. Shore-based analyses of preserved rock samples will in-

T14. Chemical composition of interstitial waters, p. 211.

T15. Microbiology and tracer tests, p. 212.

T16. Cores sampled for in situ microbiological cultures, p. 213.

T17. Thin sections examined for microbial alteration, p. 214.

clude enumeration of cells, SEM, DNA extraction, in situ hybridization, and cultivation at in situ pressure.

Tracer tests were carried out as a part of Leg 185 microbiology studies to determine whether it is possible to collect microbiological samples without contamination introduced during drilling or sample handling. Eight fluorescent microsphere and two PFT tests were conducted on cores from Hole 801C. Methods used for these tests and results can be found in “[Methods for Quantifying Potential Microbial Contamination during Deep Ocean Coring](#)” (Smith et al., 2000) and in Smith et al. (in press). Fluorescent microspheres were not observed in the crushed interior rock used for the microbiological analyses, even though they were detected on the outside of the cores (see Table T18). PFT was detected in the cores, indicating that 0.01–0.03 μL drill water/g of rock had penetrated the rock. (see Table T19 and Figs. F74, F75). Based on the abundance of cells in surface seawater at Site 801 (see below), this volume of drill water would translate into 3–13 cells/g of rock.

Sample Descriptions of Rocks Used in Microbial Cultures

Sample 185-801C-14R-3 (Piece 9, 106–110 cm); 607.6 mbsf

This sample was taken from lithologic Unit 37 (Sequence IV), which consists of pillow basalts and interpillow material (Fig. F76). The basalt is fine grained to glassy and is aphyric. In Figure F76 the right side of Piece 8 and the left side of Piece 9 are basalt, and the lower left (greenish) of Piece 8 and the right side of Piece 9 are the interpillow material. The vertical white zone in the center of Piece 8 that separates the basalt from the interpillow material is mostly calcite. A thin section was made from a pillow margin and interpillow material from 10 cm lower in the core (Sample 185-801C-14R-3, 120–122 cm), which is the same material as found in Piece 9. The thin section contained altered volcanic glass, calcite, celadonite, and chalcedony that have filled open spaces. The glass contained some olivine that has been altered to iron oxides and altered laths of plagioclase (Fig. F77). The sample that was crushed and was used to inoculate cultures was mostly interpillow material similar to the right half of Piece 9 in Figure F76.

Sample 185-801C-16R-5 (Piece 10, 84–87 cm); 629.7 mbsf

This section of the core contains pillow basalts with interpillow material composed of fractured basalt, glass, and secondary minerals. Some pillow basalts enclose breccia made of basalt clasts cemented with calcite (Fig. F78). The clasts are typically 0.5–1 cm across and some have been oxidized, giving them their red color. This sample also has secondary sulfides. The presence of both secondary sulfides and oxidized basalt clasts indicates that conditions have evolved from oxidizing to reducing. The rock also has irregular rounded voids that are filled with calcite (Fig. F78). A photomicrograph of a thin section from Sample 185-801C-16R-5, 107–110 cm (Fig. F79), shows a contact between glass and clay and calcite infilling of a void space that is ~20 cm deeper in the hole than the biological sample. The glass is no longer fresh and has dark halos around crystals and voids and along the contact between the clay and the glass.

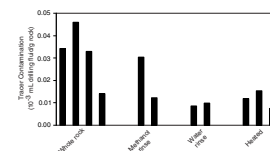
Sample 185-801C-23R-1 (Piece 10, 119–125 cm); 683.1 mbsf

This basalt flow or pillow lava is lithologic Subunit 44 of Unit 50 (Sequence IV). The core is part of geochemical Unit 13. Along with Pieces 8

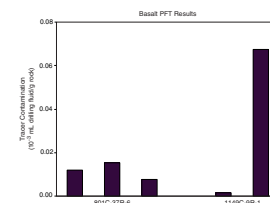
T18. Thin sections in fluorescent microsphere tests, p. 215.

T19. Cores analyzed for PFT microbiological contamination studies, p. 216.

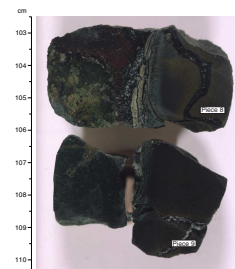
F74. Perfluoro(methylcyclohexane) in igneous rock samples, p. 148.



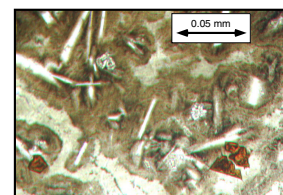
F75. Comparison of perfluoro(methylcyclohexane) in rock samples, p. 149.



F76. Core containing pillow basalts with interpillow material, p. 150.



F77. Glassy pillow rim, p. 151.



and 9, it makes up a complete lava flow, with grain size increasing toward the middle of this subunit. Piece 10 has two veins that are filled with more than 90% carbonate and 1% or 2% sulfide, and the remainder is clay (Fig. F80). A thin section of this sample shows that ~10% of the original rock has been replaced with secondary clay and calcite, and some minerals also contain secondary sulfide. This rock appears to be the least altered of the rocks used for microbiological studies. A thin section from Sample 185-801C-23R-1, 27–28 cm, is from ~1 m shallower in the hole and is from lithologic Unit 50, but it appears to be from rock very similar to that used for the biological samples. The groundmass is composed of plagioclase, pyroxene, and opaque cubes of titanomagnetite. Approximately 1% of the vesicles are filled with clay. Figure F81 shows that the plagioclase and pyroxene appear fresh and that there is some secondary clay between grains of groundmass and in vesicles.

Sample 185-801C-27R-3 (Piece 5, 19–34 cm); 722.7 mbsf

This sample contains volcanic glass, interpillow material, and pillow rims (Fig. F82). The top of Piece 5 (as shown in Fig. F80) is missing in the archive photo because it was removed as soon as the core arrived on deck in order to minimize biological contamination. The basalt of Piece 5 is relatively fresh. A thin section from Piece 2 (Fig. F83) shows that the interpillow material is made of calcite, clay, chert, recrystallized radiolarians, and iron oxyhydroxide. Some fresh glass is also present.

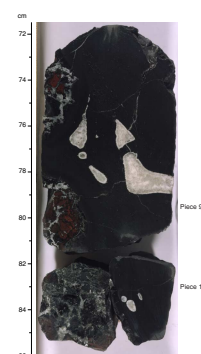
Sample 185-801C-37R-1 (Piece 1, 27–33 cm); 813.6 mbsf

Core 37R contains most of the thickest lava flow from Hole 801C, and this piece is from near the top of the flow. The basalt is similar to others at this site in terms of chemical composition, and it contains olivine phenocrysts (<1% of the rock) that have been completely altered to clay. Many of the veins in this unit are filled with clay and some are filled with calcite. The vein shown in Figure F84, which was crushed for microbiological studies, was composed primarily of calcite. Other veins in this piece contain abundant saponite clay and minor iron oxides. Of the three thin sections taken from Section 37R-1, one was from the interval 27–29 cm and corresponds to the location of this sample. The thin section shows that the vein is filled carbonate with <5% iron oxides. Outward from the vein in the groundmass of the basalt are three parallel zones of different secondary mineralogy. The first is a 2-mm-wide zone where the groundmass has been stained red with iron oxides, magnetite is more abundant than in the groundmass or the other zones, and sulfides are absent. The next zone is ~1.5 mm wide, is free of red staining, and has low magnetite abundance and no sulfides. The third zone is ~0.5 mm wide and has ~10% secondary sulfides and no red iron oxides (Fig. F85).

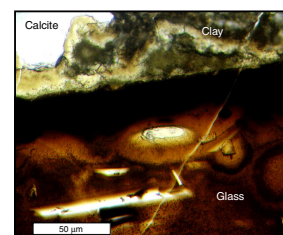
Sample 185-801C-52M-1 (Piece 3, 50–52 cm); 933.3 mbsf

The final sample used for inoculating cultures was Piece 3 from the last unit (Unit 60) and the last core (Core 52M) collected at this site (see the “Core Descriptions” contents list). The veins in this section are primarily filled with smectite clay, and the vein used for this study was ~1 mm thick and appeared to be completely filled with clay and sulfide. Based on thin section 52M-1, 43–45 cm, the rock is relatively fresh and contains ~5% saponite replacing interstitial material in the groundmass. The fresh groundmass is plagioclase, augite, and opaque oxides. There is a small amount of secondary pyrite. A thin section from Unit

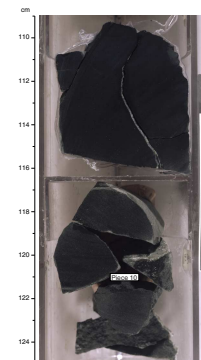
F78. Pillow basalts and intrapillow breccia, p. 152.



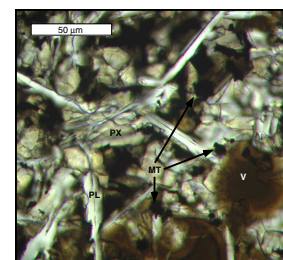
F79. Glass, clay, and calcite shown in photomicrograph, p. 153.



F80. Basalt flow with fractures and veins, p. 154.



F81. Plagioclase, pyroxene, and magnetite grains, p. 155.



60, but from Core 50M, has similar mineralogy and also contains a vein filled with pyrite and chalcedony (Fig. F86). This suggests that fluids in these fractures were reducing compared to fluids at higher levels that oxidized the surrounding groundmass (see Fig. F77).

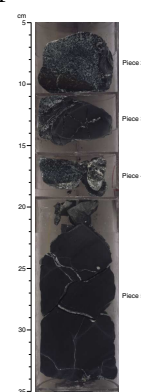
Microbial Alteration of Volcanic Glass

The extent of the subsurface biosphere in the oceanic crust is of major importance to understanding chemical fluxes on Earth. Evidence of microbial activity in basalt glass from the ocean basins has been reported previously (Thorseth et al., 1992; Furnes et al., 1996; Giovannoni et al., 1996; Fisk et al., 1998; Torsvik et al., 1998; Furnes and Staudigel, 1999). The evidence includes concentrations of carbon, DNA, phosphorus, and microbe-sized particles in areas where the glass is being altered to clay. Associated with chemical and visual clues of microbes are a variety of alteration fronts in glass (i.e., densely pitted or intermittently distributed tunnels) that do not appear to be caused solely by abiological chemical activity. Microbes are also known to weather a number of igneous minerals, but evidence for this in deep-sea basalts has not yet been reported. A survey of the occurrence of alteration textures in volcanic glasses from surface and subsurface basalts indicates that the microbial alteration phenomenon is widespread in the oceanic crust (Fisk et al., 1998). Basalt glass with ages of 3–145 Ma appear to be affected by microbial alteration. These basalts were collected from the ocean floor and from depths >1500 mbsf. Only glasses from high-temperature (>140°C) environments appear not to have microbial alteration textures. Other factors that might prevent microbes from living in the oceanic crust are the absence of metabolic substrates, low fluid flux, or excessive pressure.

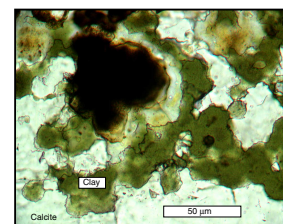
Hole 801C is important for determining if old, stable crust can support microbial life and for potentially extending the known depth of the deep biosphere in the oceans; therefore, volcanic glass from Hole 801C was studied for evidence of microbial activity. The location of fresh glass from flow margins, pillow margins, and hyaloclastites are reported in Table T5. Thin sections were made from nine of these samples and examined microscopically. Six of the thin sections come from a 50-m interval in Core 129-801C-12R and Cores 185-801C-13R to 17R between 588 and 637 mbsf (Table T17). One thin section is from Core 185-801C-32R at 767 mbsf, and the last two thin sections are from Cores 42R and 48R in a 40-m interval (881–920 mbsf). In two cases, where little glass remained in the core, the thin sections failed to intersect the glass margin. Of the seven thin sections that had glass, four contained the style of alteration similar to the microbial alteration seen in younger and shallower oceanic crust. These styles of alteration are documented in Figure F87. Additional glasses will be examined in shore-based studies.

The four samples shown in Figure F87 all have the characteristic alteration patterns associated with microbial activity. It is possible that these are fossil textures and that nothing was living in the rocks at the time they were drilled. If the textures in Figure F87 are the result of microbial activity, however, we hypothesize that life was present and that fluid was circulating through the crust when the basalts were collected. This is because as the chemical front progresses, it recrystallizes the glass to clay and destroys the microbial alteration textures. Thus, for microbial alteration to be observed in the basalts, it must continually occur ahead of the chemical alteration front.

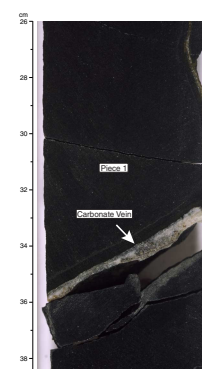
F82. Interpillow glass, carbonate, and clay, p. 156.



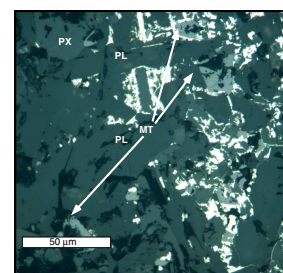
F83. Calcite matrix enclosing clay and iron oxides, p. 157.



F84. Calcite vein in lava flow, p. 158.



F85. Plagioclase, pyroxene, and titanomagnetite with secondary sulfides, p. 159.



Additional evidence of the presence of microbes in these samples may come from chemical mapping of thin sections for DNA, carbon, and phosphorus. Confirmation that the patterns of tunnels and alteration observed in Hole 801C are the consequence of microbial activity will require culturing microbes, microbial experiments using glass substrates, and molecular analysis of microbial DNA.

In addition to the irregular alteration that could be caused by the localized activity of microbes, there is alteration in Hole 801C that does not have the attributes of microbial alteration. Chemical alteration acting along the edge of a fracture would be expected to produce smooth alteration fronts in an isotropic substrate such as glass. This is observed in three samples from Hole 801C (Fig. F88).

The absence of microbial alteration in three of the seven thin sections that contain glass from Hole 801C is unusual in our experience of examining glass in seafloor basalts. Temperatures in the hole are between $\sim 21^\circ$ and 33°C , based on the extrapolation of the temperature gradient measured by Larson et al. (1993) for the upper 90 m of basement; thus, temperature should not prevent microbial growth. High pressure may prevent some microbes from living at great depth, but presently this effect has not been thoroughly investigated. Fluid flow, however, may be restricted by the filling of fractures and veins with secondary minerals. This could limit the supply of metabolic substrates required for microbial growth. Fluid flow might be directly related to the porosity of the formation. Porosity (measured at atmospheric pressure) of rocks near the glassy samples in Table T17 ranges from 2.2% to 15.6% (see “Index Properties,” p. 36), but there does not appear to be any correlation of porosity with the occurrence of microbial alteration. Other proxies for fluid flow might be the width of veins, the volume of veins, or the number of veins per meter of core (see Fig. F40), but these also do not appear to correlate with the presence of microbial textures in the glass. Shore-based studies of alteration mineralogy may help us understand the causes of the absence and presence of microbial textures.

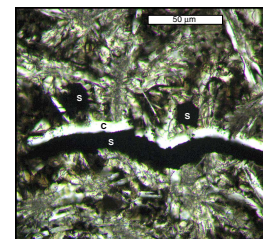
Microbial alteration occurs in the basalts near the top and the bottom of Hole 801C, but presently we are not sure what controls the distribution of organisms. The absence of organisms at intermediate levels of Hole 801C suggests that this environment is less habitable than other deep-sea, subsurface environments.

Water Sampling

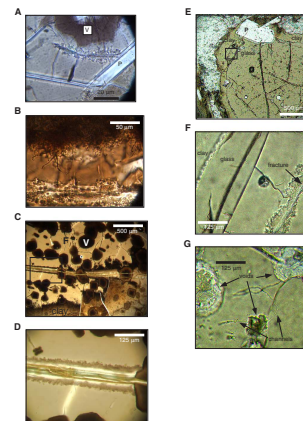
Surface- and drill-water samples were analyzed to evaluate the background cell levels and microbial population composition introduced into the formation during drilling. Drill water is surface seawater, but it was interesting to study both samples since additions to the drill water, such as mud and grease, could affect the microbial population.

A sample of water from the drill pipe was collected when it was opened to retrieve the core barrel for Core 185-801C-32R. This sample contained 2.5×10^5 cells/mL ($\pm 6 \times 10^4$ cells/mL). The surface seawater sample from the launch (see “Water,” p. 31, in the “Explanatory Notes” chapter) contained 4.2×10^5 cells/mL ($\pm 2.1 \times 10^5$ cells/mL). These numbers are typical for surface waters and are not statistically different. Separate aliquots of the surface seawater sample were incubated at downhole pressure (620 atm) and temperature (30°C) and inoculated into anaerobic growth media. Cultures will be started under pressure on shore and will be compared to those started on board. Both water sam-

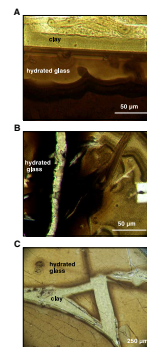
F86. Microcrystalline groundmass with filled fracture, p. 160.



F87. Photomicrographs of glass samples, p. 161.



F88. Examples of glass alteration fronts, p. 163.



ples were preserved for shore-based DNA extraction and community analysis.

Borehole Sampling

The conditions in the borehole were investigated with two lowerings of the WSTP tool (Barnes, 1988). The undisturbed water in Hole 801C could be an excellent in situ microbial culture, and we wished to sample it before it was disturbed by drilling. Our first attempt to sample formation water (WSTP1) at 490 m was not successful, but the temperature was determined (Fig. F89; Table T20). The second attempt (WSTP2) at 540 m was successful both in collecting a sample and in determining the water temperature. Approximately 100 mL of gas and 310 mL of water was withdrawn from the relief valve in the overflow reservoir with syringes to avoid contamination with air or other potential contaminants. The sample coil was taken to the microbiology lab, and 23 mL of water was withdrawn in the anaerobic chamber for culturing of cells and DNA analysis. Sample coil fluids and overflow gas and water were split for shipboard and shore-based chemical analyses (Table T21). Samples of 17 mL were stored in a pressure vessel for later culturing experiments.

Temperature

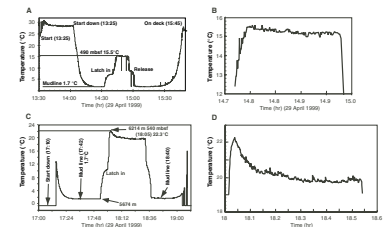
Temperatures at the ocean floor (mudline) were 1.7°C on both deployments of the WSTP (Fig. F89), which is consistent with bottom-water temperature in this part of the Pacific (Dietrich, 1963). Because the mudline temperatures were taken inside the drill string, the string appears to have cooled to the bottom temperature. Inside the hole, the drill string also appears to have started to approach ambient temperatures. As the WSTP was lowered on the cable from the mudline to the drill bit, it recorded an increase in temperature inside the drill string. In the case of WSTP1 the increase was from 1.7° to 7°C at a depth of 460 mbsf and for WSTP2 the temperature increased from 1.7° to ~10°C at 510 mbsf. The tool was then latched into the drill bit, the temperature probe extended ~50 cm below the drill bit, and the temperature was recorded in the undisturbed open hole. Next, the whole drill string was lowered ~30 m to depths of 490 and 540 mbsf for deployments WSTP1 and WSTP2, respectively. While the string was being lowered, the temperature increased ~8°C in WSTP1 and ~12°C in WSTP2. This suggests that there was a relatively large temperature gradient in this part of the hole. The final temperature we recorded at 490 mbsf was 15.5°C, and that measured at 540 mbsf was 22.3°C (Table T20; Fig. F90). The highest recorded temperatures at these depths were chosen as the ambient temperatures (Fig. F90). These highest temperatures occurred shortly after the probe reached its maximum depth. The probe was left in place for 10 min and during this time the temperature decreased slightly, which we attribute to the pumping action of the drill string in the hole. Even though sea conditions were calm, the probe was only 50 cm below the end of the drill string, and small motions of the drill string could have mixed cool water down the hole.

During Leg 144, temperatures within Hole 801C were measured (Larson et al., 1993) from the bottom of the casing (480 mbsf) to 570 mbsf, and within this interval the temperature gradient was linear and can be calculated using the equation

$$T^{\circ}\text{C} = 8.17 + 0.0268 \text{ depth (mbsf)}.$$



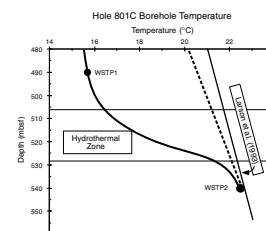
F89. Time and temperature record of water sampling runs, p. 164.



T20. WSTP data, p. 217.

T21. WSTP aliquot distribution, p. 218.

F90. Water temperatures in Hole 801C, p. 165.



The temperature measured in the undisturbed hole at 540 mbsf during Leg 144 (22.6°C) is nearly identical to the temperature we measured at this depth during Leg 185 (22.3°C). However, the temperature measured during Leg 144 at 490 mbsf is 6°C more than our measurement (15.5°C). The difference in the two measured temperatures at 490 m may be caused by the introduction of cooler water from shallower in the hole by the lowering of the drill string. Alternatively, the lower temperature may be due to surface seawater being drawn into the formation between 490 and 540 mbsf.

The major hydrothermal zone in this hole extends from 512 to 528 mbsf. During Leg 144 permeability was estimated using a packer (Larson et al., 1993), and it was hypothesized that the most permeable region of the hole was located within the hydrothermal zone. Negative temperature anomalies and low resistivity between 515 and 530 mbsf from the downhole logs measured after drilling during Leg 185 (see “[Temperature](#),” p. 45) indicates that this zone is highly permeable. If the 6°C temperature anomaly of WSTP1 is due to the gradual drawdown of surface water into the hydrothermal region, then this is a relatively recent phenomenon, as there was no evidence of drawdown in the temperature survey of Larson et al. (1993). This leads to two possibilities. The anomalously cool water at 490 mbsf in Hole 801C is caused by the mixing of water within the cased hole during the deployment of WSTP1 or to renewed drawdown of water in the hole, possibly stimulated by the packer tests.

Water Chemistry

Water was analyzed chemically to determine the origin of the water collected with WSTP2. Results indicate that the collected water was normal bottom water mixed with some distilled water that came from the coil (Table [T20](#)). High levels of Li are attributed to the grease used in the WSTP.

Microbial Abundance

Sterilization of sampling equipment is critical in obtaining uncompromised microbiological samples. Prior to deployment, the WSTP samplers were flushed with 1 ppm chlorine dioxide followed by 0.2- μ m-filtered Nanopure water. This water was not sterile because it was pumped into the WSTP from nonsterile carboys with an inline pump that also was not sterile. The total abundance of microbial cells in the Nanopure water before and after it passed through the WSTP was determined by epifluorescence microscopy. Results are shown in Table [T22](#). The first time the WSTP tools were flushed, there were slightly higher levels of microbes in the outgoing wash water as compared to the ingoing water, indicating that cells were flushed out of the WSTP. The final wash before sampling showed no significant difference between ingoing and outgoing water. Residual levels of cells in the WSTP tools were 10³ cells/mL (Table [T22](#)). After flushing, the sample coil was filled with 0.2- μ m-filtered Nanopure water, and the sample reservoir was emptied and filled with nitrogen. The tool was stored at room temperature for at least 12 hr before use. Although WSTP1 failed to collect a water sample, the Nanopure water remaining in the coil was collected and cells were enumerated in this water (Table [T22](#)). Results showed that the cells in the coil had undergone four generations of cell growth, with an approximate generation time of 3 hr. The second WSTP tool was successful in collecting water from 540 mbsf. Total cell numbers in the WSTP reservoir were 9600 (\pm 6000) cells/mL (Table [T22](#)). Assuming cell growth oc-

[T22](#). Cell counts of WSTP water, p. 219.

curred at the same rate as in WSTP 1 after the sampler was sealed, 30%–60% of these cells are likely to be contaminants. This is an approximate estimate, but it shows that there was considerable contamination in the WSTP. Major modifications would be required if the WSTP is to be used for microbiological sampling in the future. Ideally, a 0.2- μm filter that withstands the 1500-psi pump pressure would be placed in line after the pump for flushing and pressure testing the sampler. Alternative types of water samplers that are easier to sterilize should be investigated if water sampling for microbial investigations is to be a part of future legs.

Hole 801D

A single push core was taken in Hole 801D. The rationale for taking this core was to test sampling protocols and tracer techniques in preparation for eventual sediment sampling at Site 1149. Samples to determine the total abundance of microorganisms and for community characterization were taken from whole rounds from each of the six sections of Core 185-801D-1W. Samples for abundance (0.5 cm³) were preserved in formalin (2% final concentration), and samples for microbial community analysis were frozen in liquid nitrogen and stored at -70°C . In addition to the microbiological samples, a contamination test using fluorescent microspheres was conducted in Hole 801D. Smear slides were prepared from whole rounds to examine the presence of microspheres (see “[Methods for Quantifying Potential Microbial Contamination during Deep Ocean Coring](#)” [Smith et al., 2000] and Smith et al., in press). Microspheres were observed in both the interior and exterior of every section, suggesting that the core was disturbed during the drilling process (see “[Lithostratigraphy](#),” p. 5). This is corroborated by pore-water chemistry data (see “[Interstitial Water Chemistry and Headspace Gas](#),” p. 47). Disturbance of the core was expected given that this wash core was taken from the mudline to 19.3 mbsf; thus, there was a large amount of solid and aqueous advection during coring. The disturbance and contamination were also enhanced by the high porosities of the sediments. The methods for sampling the spheres were modified for Site 1149 to provide quantitative data for estimating the amount of contamination in sediment samples.

Summary

Igneous rock samples were collected from Hole 801C for microbiological analyses. The core interiors were isolated in anaerobic conditions, used to inoculate microbial cultures, and examined microscopically. Samples were preserved for shore-based analyses, which will include enumeration of cells, SEM, DNA extraction, in situ hybridization, and cultivation at in situ pressure.

The primary microbiological objective for Leg 185 was to determine the types and abundance of microbes in unconsolidated sediments, sedimentary rocks, and igneous rocks of the oceanic crust. This goal could only be achieved if uncontaminated samples were obtained. Contamination tests were carried out to determine the extent of contamination introduced into the samples by the drilling and sampling processes. Results suggest that microbial contamination of samples used for microbiology is unlikely, although some drilling fluid did penetrate the rock (see Figs. [F74](#), [F75](#), and Table [T19](#)).

Observation of thin sections from Hole 801C showed signs of both microbial and chemical alteration in basaltic glass. Four of the seven thin sections that contained glass showed microbial alteration patterns.

Surface, drilling, and borehole water samples were collected to determine background microbial populations that could be introduced into the formation during drilling. These samples will be evaluated in parallel with rock samples. A water sample was collected of the water in Hole 801C before drilling. The water was determined to be bottom water. A good microbiological sample was not obtained because it was not possible to sterilize the sampler. Water temperatures were measured at two depths in Hole 801C.

A sediment push core was collected in Hole 801D. Samples from this core were used to test microbiology and tracer methods in advance of sediment coring at Site 1149.

USING NATURAL GAMMA RAY TO CALCULATE POTASSIUM BUDGETS

Introduction

A primary objective of drilling Hole 801C during Leg 185 was to quantify the chemical alteration of Jurassic basement in the west Pacific in order to calculate geochemical fluxes into the Mariana subduction zone. Although important to geochemical mass balances, estimating the bulk compositions of altered basement is difficult because of the extremely heterogeneous nature of alteration domains in basalt. Consequently, most studies of basement alteration focus on styles and mechanisms of water-rock reaction and not absolute budgets. If basement alteration involved long homogeneous sections of rock, then chemical analyses of discrete samples may adequately represent the compositional variations in the core and can be easily summed. However, when the chemical composition of the basement varies on the scale of millimeter- to centimeter-sized veins, halos, or interpillow domains, then the analytical problem becomes extremely complicated.

The continuous collection of data on whole-round cores using the MST provides a potentially powerful complement to discrete sampling and analysis for estimating the bulk composition of long sections of core. In particular, the NGR emission data reflect the chemical composition of the cores and relate simply to the concentrations of K, Th, and U, the dominant, naturally occurring radioactive elements in rocks. Although this provides only a limited view of the total chemical variation in the core, K and U are two elements that are enriched and intimately associated with alteration zones in the upper oceanic crust. If the MST-NGR data can resolve variations in basement alteration, then this information will not only help to guide discrete sampling efforts for more comprehensive chemical analyses but also provide a clear tie to the downhole logs. In fact, the MST-NGR data are the only continuous core data collected in Hole 801C that can be compared directly to the logs. If the MST-NGR data can be calibrated to K, Th, or U concentrations, it would provide an excellent control on the bulk composition of the recovered core.

There are some difficulties, however, in using the MST-NGR data for quantitative analysis. The first is that there is currently no calibration for the NGR data; the output is in counts per second (cps) and not elemental concentrations. The second is that although multichannel spec-

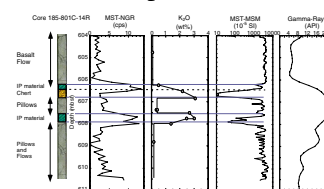
tral data are collected, the results are not integrated into K, Th, and U peaks separately but as the sum of the gamma-ray counts. Finally, although alteration domains may be enriched in K and U (>2 wt% K₂O and >0.5 ppm U), the K, U, and Th abundances in MORB are extremely low (generally <0.2 wt% K₂O and <0.3 ppm Th and U) and thus may be below the detection limit of the technique. To assess these problems, we conducted studies during Leg 185 to ascertain the effectiveness of the MST-NGR data in measuring the chemical composition of the basement cores. These were neither extensive nor systematic studies; for a more in-depth discussion of limitations, improvements, and applications of the ODP MST-NGR data, see Blum et al. (1997) and Hoppie et al. (1994).

Correspondence between MST-NGR Data and Features in the Core

The first consideration is whether the MST-NGR data relate to observable alteration domains in the core. Figure F91 shows a schematic lithologic section of Core 185-801C-14R, along with the MST-NGR and MST-magnetic susceptibility (MS) data. The MST data were measured every 10 cm for 20 s (NGR) and every 4 cm for 4 s (MS) (see “Physical Properties,” p. 35). Also shown for comparison are the downhole gamma-ray logs and K₂O measurements of discrete core samples by atomic absorption (see “Analysis of Potassium in Basalts by Atomic Absorption Spectrometry,” p. 24, in the “Explanatory Notes” chapter for methods) (Table T23). We chose this core for examination because NGR measurements show a simple pattern of low count rate regions with two large peaks midway through the core, and the variations span almost the full dynamic range of the tholeiite section in Hole 801C. These variations in NGR correspond closely to features in the core. The low count rates in the upper 2.3 m are in a minimally altered massive basalt flow, which we expect to have low MORB-like K, U, and Th values throughout. The low expected K abundances are confirmed by the low K₂O atomic absorption (AA) values (0.074 wt%), and although U and Th data are not available at this time (but will be collected onshore), we expect them to be as low as <0.3 ppm Th and U, which are typical of the less altered basalt cored during Leg 129 (Castillo et al., 1992). Both NGR peaks correspond to celadonite-bearing interpillow siliceous sediment. Celadonite is the main K-rich alteration mineral, and in general, its presence correlates with high NGR counts, high K concentration and a blue-green color in the cores. The rest of the core consists of less altered basaltic pillows and flows, all with low NGR counts. MS is generally out of phase with NGR because alteration reduces MS, and siliceous interpillow material has low intrinsic MS. A similar trend to the MST-NGR is shown by the K₂O core data, if we assume that the discrete K₂O measurements are typical of the sampled lithologic units. Finally, the downhole gamma-ray log (from the triple-combo string) shows the same over-all pattern, albeit greatly smoothed, such that the two peaks merge into one large one. Thus, the MST-NGR data show a great deal of coherence with the measured K₂O abundances, the gamma-ray logs, and the patent alteration and sedimentary features in the core.

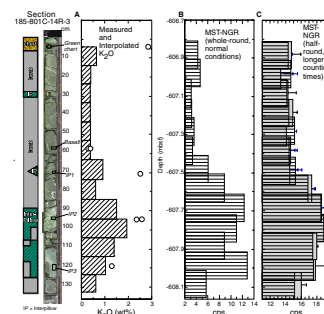
Whereas the MST-NGR data appear to faithfully reflect the broad features of the core at the scale of meters, they also record features on the scale of tens of centimeters. Figure F92 shows the NGR data within a single section of core (Section 185-801C-14R-3), alongside a digital photo of the core. Again, the variations in the MST-NGR values closely

F91. Comparison between MST and K₂O data, p. 166.



T23. K₂O analyses, p. 220.

F92. MST-NGR and core K₂O data for Section 185-801C-14R-3, p. 167.



follow the lithologic changes in the core, from low count rates in the basalt at the top of the section to high count rates in the green interpillow material at the bottom of the section. This section was also subsampled for AA K_2O analyses, and the five analyses generally confirm the NGR variations. The AA analyses are on small samples (a few 100 mg or $<1\text{ cm}^3$), and, thus, do not sample the core at the same length scale as the MST. The MST measurements are taken every 10 cm with a footprint of at least $\pm 10\text{ cm}$ and possibly as great as $\pm 14\text{ cm}$ from the point of measurement (Hoppie et al., 1994). To calibrate MST-NGR data at a similar sampling rate, the AA analyses were used to generate a synthetic data set at 10-cm intervals. This was accomplished by considering the length scale over which the AA sample was representative. For example, we assume the sample at 60 cm is typical of the unaltered basalt from 10 to 90 cm and that the interpillow sample at 70 cm only constitutes $\sim 25\%$ of the interval sampled by the MST from 60 to 80 cm, with the remainder being unaltered basalt. Table T24 gives the mixing proportions for each interval and resulting K_2O estimates for the entire section. Although there are differences in detail, in general, the MST-NGR trend closely corresponds to the estimated K_2O . The NGR shows a broader peak in the lower interpillow material and does not resolve small features such as the interpillow section at 70 cm. There are also decreases in the NGR counts, for example, at $\sim 110\text{ cm}$, which could result from decreases in core volume caused by rubbly intervals and spacers. Ideally, one should correct for volume changes, although Hoppie et al. (1994) found no significant decrease in count rate for as much as a 20% volume reduction in the core. Despite these effects, the first-order correspondence between the MST-NGR and K_2O measurements is sufficient to provide a calibration.

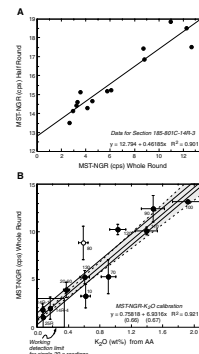
Calibration of Multisensor Track–Natural Gamma Radiation Data

To provide better NGR data for calibration, we passed Section 185-801C-14R-3 through the MST several times to improve the counting statistics. Because this test was run after the core was split, the count rates were no longer directly comparable with original whole-round core data. Fortunately, there is an excellent relationship between the half-round and whole-round cores (Fig. F93A), with the slope being roughly 50%, in accord with the relationship between volume percent of core and count rate found by Hoppie et al. (1994). We passed the section three times under normal parameters (10-cm interval with 20-s counts at each interval) and twice with longer counting times (10-cm interval with 60-s counts). The percent standard deviation on the three 20-s measurements averages 5%, which is better than the precision on the AA analyses ($\sim 10\%$). Figure F92 shows the average of the 20-s and 60-s runs, which agree well with each other and the K_2O data. These data form the basis of the calibration.

Ideally, the calibration should include homogeneous intervals of known K, U, and Th composition with the same matrix as Leg 185 Hole 801C cores (tholeiitic basalt), which could be measured with good precision on both the MST and by AA. Furthermore, it would be advantageous to be able to resolve the K, Th, and U contributions to the total gamma-ray data. Since neither of these conditions is met, such a calibration is necessarily imperfect. Homogeneous sections in the tholeiites exist only for the unaltered domains, and although there is good sam-

T24. MST and AA data for NGR, p. 221

F93. Calibration of MST-NGR measurements, p. 168.



ple control at the low NGR range, count rates are low and precision is worse. On the other hand, high NGR regions in the tholeiites are generally small and heterogeneous and, therefore, difficult to characterize analytically. The alkali basalts at the top of Hole 801C could provide homogeneous, high NGR samples for calibration, but because they contain abundant K, U, and Th, they are not a good match for the tholeiites. In general, alteration of the tholeiites involves predominantly K enrichment, with sporadic and sometimes unrelated U enrichment and little net change in Th (Staudigel et al., 1995; Castillo et al., 1992). This relationship is also reflected in the downhole gamma-ray logs, which resolve K, U, and Th contributions (Fig. F70). In the Leg 185 section, most of the NGR signal is attributed to K variations, with U increasing in a few intervals, and Th low in all the sections analyzed. Shore-based U and Th analyses on the cores will test this interpretation. Thus, although not ideal, our calibration assumes that the MST-NGR variations are largely because of K variations and that the variations observed in AA data in the tholeiites in Section 185-801C-14R-3 can be used to form the basis for a calibration. We augmented the data from Section 185-801C-14R-3 with a few other key intervals (long, minimally altered regions of Cores 14R and 25R, which is the core with the lowest NGR signals in the hole).

Figure F93B shows the calibration obtained, using the data shown in Figure F92 and in Table T24, with all MST-NGR data corrected to whole-round counts. The R^2 value on the calibration is very good (0.92), after removing a point at Sample 185-801C-14R-3, 80 cm, for which we do not have good control on the K_2O concentration (there is no measurement nearby, and its proximity to the large interpillow zone may lead to significant alteration and concomitant increase in K). Uncertainties on the slope and intercept are shown by the gray region (see Fig. F93B). In theory, the intercept should be zero if blank subtraction was performed correctly. However, there was no true blank for most of the points in the calibration, which were calculated from the half-round-whole-round relationship in Figure F93A. The blank on the MST-NGR is measured by analyzing at the beginning of the leg a long, whole-round liner filled with distilled water, which had no K, Th, or U, and shielded random background gamma rays approximately the same way as the rock whole rounds. These blank measurements are not strictly valid for the half-round data; thus, the calibration was not forced through the origin. For the low count rates (<5 cps) that are typical for most of the hole, the intercept contributes the greatest uncertainty in the calibration, exceeding NGR counting statistics and AA analytical errors. Uncertainty in the intercept leads to an error of $\sim\pm 0.1$ wt% K_2O .

Statistical detection limits are usually calculated from uncertainty in the background, but because we have no appropriate background measurements, we assessed working detection limits. It is clear from Figure F93B that even where many repeat measurements are available (as for Sections 185-801C-14R-4 and 14R-1 and Core 25R), it is impossible to resolve 0.1 wt% from the uncertainty in the intercept; thus, the detection limit is >0.1 wt% K_2O . We can also assume Core 185-801C-25R represents near background NGR, at 0.08 wt% K_2O (as in the core analysis). NGR values for Core 185-801C-25R vary from -0.45 to 3.2 , averaging 1 ± 1 cps standard deviation. Thus, count rates up to 3 cps are probably indistinguishable from background, and the corresponding K_2O (~ 0.35 wt%) may be considered a working detection limit for individual 20-s measurements. Increasing counting times on the MST and taking more

whole-round background measurements would improve the NGR detection limits.

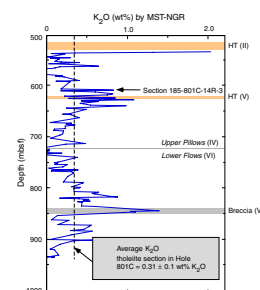
Results

The MST-NGR calibration can be used to obtain some useful estimates of the K_2O content of individual sections (such as Section 185-801C-14R-3), individual cores (such as 14R) and the entire Hole 801C tholeiitic section (the calibration is probably not robust for the alkalic section, where significant U and Th also contribute to the gamma-ray counts). The average MST-NGR counts for Section 185-801C-14R-3 (Fig. F92; Table T24) give an average K_2O of 0.87 wt%, with 7% relative standard deviation for the three standard (20 s) passes through the MST. This means that in a typical MST run, the precision on the NGR average could be ~7%. The absolute value of the MST-NGR K_2O concentration is higher than the average calculated from the actual core samples analyzed by AA (0.8 wt%). The difference between the two should be minimal because this section was used to calibrate the MST. The difference probably results from the high NGR counts around 80 cm in the section, which were excluded from the calibration. For this section either the K_2O is higher than estimated from the sparse AA data, in which case the AA average should be >0.8 wt%, or the interval contains significant U, which would lead to false high K_2O in the NGR counts. Nonetheless, the agreement is still within the 0.1 wt% K_2O error on the calibration, and the section is extremely enriched in K_2O (0.8–0.87 wt%) with respect to the unaltered rock (<0.1 wt%). In fact, Section 185-801C-14R-3 is one of the more gamma-ray enriched sections in the hole (Fig. F94). The NGT logging data for K_2O in the depth interval corresponding to Section 185-801C-14R-3 has higher K_2O than either the MST or AA averages and may reflect a lack of recovery of potentially K-rich inter-pillow zones.

Comparison between the calibrated MST-NGR data and the AA/XRF core data for the entire Core 185-801C-14R shows even better agreement, both at 0.45 wt%. Again, the NGT log data has higher K_2O values (0.53 wt%), which could reflect a recovery bias or a calibration shift in the logging data. In fact, at each scale, from section to core to entire hole, the logging data consistently give higher K_2O values than the MST data. Assessing the calibration of the logging data will be an important postcruise activity, and the MST data will form a critical tie point between the log and core data.

Applying the MST calibration to all sections downcore reveals three zones of high K_2O : one below the upper hydrothermal unit (II), one centered around the lower hydrothermal unit (V), and one coinciding with the large breccia unit (VII) in Core 185-801C-37R. The most K_2O -enriched zone is the upper one, where values extend as high as 2 wt% in the deep green celadonite-rich rocks in Core 185-801C-5R. The lower two zones peak at ~1 wt% K_2O . A minimum in K_2O occurs at ~720 mbsf, where there is a major lithologic boundary between flow-dominated and pillow-dominated cooling units and abundant fresh glass. These periodic high and low K_2O abundances downhole correspond to altered and less altered intervals, which contrast with a typical decrease downhole in K_2O that has been observed at Sites 504, 417, and 765 (Alt et al., 1986; Staudigel et al., 1995; Gillis et al., 1992). Perhaps the pattern of alteration at Hole 801C, with focused hydrothermal alteration zones, is a feature more typical of fast-spreading oceanic crust.

F94. K_2O vs. depth, p. 169.



The bulk K_2O calculated from the MST-NGR data for the entire tholeiitic section is 0.31 ± 0.1 wt% (Table T25; Fig. F94). At face value, it would seem that the average for the entire site is below the working detection limit and, thus, unresolvable from zero. The working detection limit applies only to single measurements, however. Because the tholeiite average includes many significant measurements at high cps, which will exert the most influence on an average, its value has significance. One way to test this is to assume that all MST measurements below 3 cps are indistinguishable from the fresh rock value of 0.08 wt% K_2O , whereas those above 3 cps are a significant measure of K_2O . The average calculated this way is 0.33 wt% K_2O , which is within error of the 0.31 wt% value determined from the simple average of the MST data.

Our estimate of the bulk K_2O in the tholeiitic section from the MST data (0.31 wt%) as well as the bulk K_2O from the logged interval (0.36 wt%) both exceed that calculated from the percentage of discrete alteration veins, halos, breccias, and interpillow material logged by the alteration team and a limited number of XRF analyses of these domains (0.13 wt% K_2O ; see "Alteration Geochemistry," p. 27, and Table T10). The difference may lie in part in the assumption that everything that was not a discrete alteration feature was fresh rock and that 97% of the tholeiite section has 0.08 wt% K_2O . This does not take into account any pervasive alteration of the rock; thus, this estimate is a minimum. Our MST estimate would require that the 97% of the core that did not contain patent alteration features has 0.27 wt% K_2O . An average K_2O of 0.31 wt% is lower than that calculated for Deep Sea Drilling Project (DSDP) Site 417 (0.56 wt%) (Staudigel et al., 1995). The technique laid out in this report could be used to calculate bulk K_2O at the few other sites drilled deeply into basement (Holes 504B, 765C, 332), to start to form a better understanding of the controls on seafloor alteration fluxes.

T25. Hole averages for MST-NGR and K_2O data, p. 222.

REFERENCES

- Abrams, L.J., Larson, R.L., Shipley, T.H., and Lancelot, Y., 1993. Cretaceous volcanic sequences and Jurassic oceanic crust in the East Mariana and Pigafetta basins of the Western Pacific. *In* Pringle, M.S., Sager, W.W., Sliter, W.V., and Stein, S. (Eds.), *The Mesozoic Pacific: Geology, Tectonics, and Volcanism*. Geophys. Monogr., Am. Geophys. Union, 77:77–101.
- Alt, J.C., 1999. Very low grade hydrothermal metamorphism of basaltic rocks. *In* Frey, M., and Robinson, D. (Eds.), *Low Grade Metamorphism*: London (Blackwell Scientific), 169–201.
- Alt, J.C., France-Lanord, C., Floyd, P.A., Castillo, P., and Galy, A., 1992. Low-temperature hydrothermal alteration of Jurassic ocean crust, Site 801. *In* Larson, R.L., Lancelot, Y., et al., *Proc. ODP, Sci. Results*, 129: College Station, TX (Ocean Drilling Program), 415–427.
- Alt, J.C., Honnorez, J., Laverne, C., and Emmermann, R., 1986. Hydrothermal alteration of a 1 km section through the upper oceanic crust, Deep Sea Drilling Project Hole 504B: mineralogy, chemistry, and evolution of seawater-basalt interactions. *J. Geophys. Res.*, 91:10309–10335.
- Alt, J.C., and Teagle, D.A.H., 1999. The uptake of carbon during alteration of ocean crust. *Geochim. Cosmochim. Acta*, 63:1527–1535.
- Alt, J.C., Teagle, D.A.H., Laverne, C., Vanko, D.A., Bach, W., Honnorez, J., Becker, K., Ayadi, M., and Pezard, P.A., 1996. Ridge-flank alteration of upper ocean crust in the Eastern Pacific: synthesis of results for volcanic rocks of Holes 504B and 896A. *In* Alt, J.C., Kinoshita, H., Stokking, L.B., and Michael, P.J. (Eds.), *Proc. ODP, Sci. Results*, 148: College Station, TX (Ocean Drilling Program), 435–450.
- Arrhenius, G., 1963. Pelagic sediments. *In* Hill, M.N. (Ed.), *The Sea* (Vol. 3): *The Earth Beneath the Sea: History*: New York (Wiley-Interscience), 655–727.
- Barnes, R.O., 1988. ODP in-situ fluid sampling and measurement: a new wireline tool. *In* Mascle, A., Moore, J.C., et al., *Proc. ODP, Init. Repts.*, 110: College Station, TX (Ocean Drilling Program), 55–63.
- Baumgartner, P.O., 1984. A Middle Jurassic-Early Cretaceous low-latitude radiolarion zonation based on unitary associations and age of Tethyan radiolarites. *Eclogae Geol. Helv.*, 77:729–837.
- , 1987. Age and genesis of Tethyan Jurassic Radiolarites. *Eclogae Geol. Helv.*, 80:831–879.
- Berger, W.H., 1970. Planktonic foraminifera: selective solution and the lysocline. *Mar. Geol.*, 8:111–138.
- Blum, P., Rabaute, A., Gaudon, P., and Allan, J.F., 1997. Analysis of natural gamma-ray spectra obtained from sediment cores with the shipboard scintillation detector of the Ocean Drilling Program: example from Leg 156. *In* Shipley, T.H., Ogawa, Y., Blum, P., and Bahr, J.M. (Eds.), *Proc. ODP, Sci. Results*, 156: College Station, TX (Ocean Drilling Program), 183–195.
- Bourasseau, I., 1996. L'altération de la croûte océanique jurassique et al genèse des sédiments métallifères associés (Bassin de Pigafette, Océan Pacifique NW) [Thèse de doctorat]. Univ. Louis Pasteur, Strasbourg I.
- Bullard, E.C., 1947. The time necessary for a borehole to attain temperature equilibrium. *Mon. Not. R. Astron. Soc., Geophys. Suppl.*, 5:127–130.
- Castillo, P.R., Floyd, P.A., France-Lanord, C., and Alt, J.C., 1992. Data report: Summary of geochemical data for Leg 129 igneous rocks. *In* Larson, R.L., Lancelot, Y., et al., *Proc. ODP, Sci. Results*, 129: College Station, TX (Ocean Drilling Program), 653–670.
- Davies, T.A., and Gorsline, D.S., 1976. Oceanic sediments and sedimentary processes. *In* Riley, J.P., and Chester, R. (Eds.), *Chemical Oceanography*: London (Academic Press), 1–80.
- Dietrich, G., 1963. *General Oceanography*: New York (Interscience).

- Doyle, P.S., and Riedel, W.R., 1985. Cenozoic and Late Cretaceous ichthyoliths. *In* Bolli, H.M., Saunders, J.B., and Perch-Nielsen, K. (Eds.), *Plankton Stratigraphy*: Cambridge (Cambridge Univ. Press), 965–995.
- Edmond, J.M., Measures, C., McDuff, R.E., Chan, L.H., Collier, R., and Grant, B., 1979. Ridge crest hydrothermal activity and the balances of the major and minor elements in the ocean: the Galapagos data. *Earth Planet. Sci. Lett.*, 46:1–18.
- Firth, J.V., and Hull, D.M., 1993. Ichthyolith biostratigraphy of deep-sea clays from the southwestern Hawaiian Arch. *In* Wilkens, R.H., Firth, J., Bender, J., et al., *Proc. ODP, Sci. Results*, 136: College Station, TX (Ocean Drilling Program), 27–43.
- Fisk, M.R., Giovannoni, S.J., and Thorseth, I.H., 1998. Alteration of oceanic volcanic glass: textural evidence of microbial activity. *Science*, 281:978–980.
- Floyd, P.A., and Castillo, P.R., 1992. Geochemistry and petrogenesis of Jurassic ocean crust basalts, Site 801. *In* Larson, R.L., Lancelot, Y., et al., *Proc. ODP, Sci. Results*, 129: College Station, TX (Ocean Drilling Program), 361–388.
- Floyd, P.A., Winchester, J.A., and Castillo, P.R., 1992. Geochemistry and petrography of Cretaceous sills and lava flows, Sites 800 and 802. *In* Larson, R.L., Lancelot, Y., et al., *Proc. ODP, Sci. Results*, 129: College Station, TX (Ocean Drilling Program), 345–359.
- Furnes, H., and Staudigel, H., 1999. Biological mediation in ocean crust alteration: how deep is the deep biosphere? *Earth Planet. Sci. Lett.*, 166:97–103.
- Furnes, H., Thorseth, I.H., Tumyr, O., Torsvik, T., and Fisk, M.R., 1996. Microbial activity in the alteration of glass from pillow lavas from Hole 896A. *In* Alt, J.C., Kinoshita, H., Stokking, L.B., and Michael, P.J. (Eds.), *Proc. ODP, Sci. Results*, 148: College Station, TX (Ocean Drilling Program), 191–206.
- Gillis, K.M., Ludden, J.N., Plank, T., and Hoy, L.D., 1992. Low-temperature alteration and subsequent reheating of shallow oceanic crust at Hole 765D, Argo Abyssal Plain. *In* Gradstein, F.M., Ludden, J.N., et al., *Proc. ODP, Sci. Results*, 123: College Station, TX (Ocean Drilling Program), 191–199.
- Giovannoni, S.J., Fisk, M.R., Mullins, T.D., and Furnes, H., 1996. Genetic evidence for endolithic microbial life colonizing basaltic glass/seawater interfaces. *In* Alt, J.C., Kinoshita, H., Stokking, L.B., and Michael, P.J. (Eds.), *Proc. ODP, Sci. Results*, 148: College Station, TX (Ocean Drilling Program), 207–214.
- Haggerty, J.A., Premoli Silva, I., Rack, F., and McNutt, M.K. (Eds.), 1995. *Proc. ODP, Sci. Results*, 144: College Station, TX (Ocean Drilling Program).
- Honnorez, J., 1981. The aging of the oceanic crust at low temperature. *In* Emiliani, C. (Ed.), *The Sea* (Vol. 7): *The Oceanic Lithosphere*: New York (Wiley), 525–587.
- Hoppie, B.W., Blum, P., and the Shipboard Scientific Party, 1994. Natural gamma-ray measurements on ODP cores: introduction to procedures with examples from Leg 150. *In* Mountain, G.S., Miller, K.G., Blum, P., et al., *Proc. ODP, Init. Repts.*, 150: College Station, TX (Ocean Drilling Program), 51–59.
- INTERRAD Jurassic–Cretaceous Working Group, 1995. Middle Jurassic to Lower Cretaceous radiolaria of tethys: occurrence, systematics, biochronology. *Mem. Geol. Lausanne*, 23:1172.
- Ito, H., Nogi, Y., and Larson, R.L., 1995. Magnetic reversal stratigraphy of Jurassic oceanic crust from Hole 801C. *In* Haggerty, J.A., Premoli Silva, I., Rack, F., and McNutt, M.K. (Eds.), *Proc. ODP, Sci. Results*, 144: College Station, TX (Ocean Drilling Program), 641–647.
- Kastner, M., 1979. Zeolites. *In* Burns, R.G. (Ed.), *Marine Minerals*. Mineral. Soc. Am., Rev. Mineral., 6:111–123.
- Lachenbruch, A.H., and Brewer, M.C., 1959. Dissipation of the temperature effect of drilling a well in Arctic Alaska. *U.S. Geol. Surv. Bull.*, 1083-C:73–106.
- Lancelot, Y., Larson, R.L., et al., 1990. *Proc. ODP, Init. Repts.*, 129: College Station, TX (Ocean Drilling Program).
- Langmuir, C., 1987. Testing the relationship between MORB chemistry and axial depth: new data from the Mid-Atlantic Ridge between the Kane and Hayes Fracture Zones. *Eos*, 68:1540.

- Langmuir, C.H., Bender, J.F., and Batiza, R., 1986. Petrological and tectonic segmentation of the East Pacific Rise, 5°30'N–14°30'N. *Nature*, 322:422–429.
- Larson, R.L., Fisher, A.T., Jarrard, R.D., Becker, K., and Ocean Drilling Program Leg 144 Shipboard Scientific Party, 1993. Highly permeable and layered Jurassic oceanic crust in the western Pacific. *Earth Planet. Sci. Lett.*, 119:71–83.
- Matsuoka, A., 1983. Middle and Late Jurassic radiolarian biostratigraphy in the Sakawa and adjacent areas, Shikoku, Southwest Japan. *J. Geosci., Osaka City Univ.*, 26:1–48.
- , 1991. Middle Jurassic Radiolarians from the Western Pacific. *Saito Ho-on Kai Spec. Publ.*, 3:697–707.
- , 1992. Jurassic and Early Cretaceous radiolarians from Leg 129, Sites 800 and 801, western Pacific Ocean. In Larson, R.L., Lancelot, Y., et al., *Proc. ODP, Sci. Results*, 129: College Station, TX (Ocean Drilling Program), 203–220.
- , 1995. Middle Jurassic to Early cretaceous radiolarian occurrence in Japan and the Western Pacific (ODP Sites 800–801). In Baumgartner et al. (Eds.), *Middle Jurassic to Lower Cretaceous Radiolaria of Tethys: Occurrence, Systematics, Biochronology*. Mem. Geol. Lausanne, 23:937–966.
- Matsuoka, A., and Yao, A., 1986. A newly proposed radiolarian zonation for the Jurassic of Japan. *Mar. Micropaleontol.*, 11:91–105.
- Murray, J., and Renard, A.F., 1891. Report on deep-sea deposits based on specimens collected during the voyage of H.M.S. Challenger in the years 1873–1876. In *Report on the Scientific Results of the Voyage of HMS Challenger 1873-76*: London (Her Majesty's Stationery Office).
- Parkes, R.J., Cragg, B.A., Bale, S.J., Getliff, J.M., Goodman, K., Rochelle, P.A., Fry, J.C., Weightman, A.J., and Harvey, S.M., 1994. A deep bacterial biosphere in Pacific Ocean sediments. *Nature*, 371:410–413.
- Pezard, P.A., and Anderson, R.N., 1989. Morphology and alteration of the upper oceanic crust from in-situ electrical experiments in DSDP/ODP Hole 504B. In Becker, K., Sakai, H., et al., *Proc. ODP, Sci. Results*, 111: College Station, TX (Ocean Drilling Program), 133–146.
- Pringle, M.S., 1992. Radiometric ages of basaltic basement recovered at Sites 800, 801, and 802, Leg 129, western Pacific Ocean. In Larson, R.L., Lancelot, Y., et al., *Proc. ODP, Sci. Results*, 129: College Station, TX (Ocean Drilling Program), 389–404.
- Shipboard Scientific Party, 1990. Site 801. In Lancelot, Y., Larson, R.L., et al., *Proc. ODP, Init. Repts.*, 129: College Station, TX (Ocean Drilling Program), 91–170.
- , 1993. Site 801. In Premoli Silva, I., Haggerty, J., Rack, F., et al., *Proc. ODP, Init. Repts.*, 144: College Station, TX (Ocean Drilling Program), 313–329.
- , 1999. Leg 180 summary. In Taylor, B., Huchon, P., Klaus, A., et al., *Proc. ODP, Init. Repts.*, 180: College Station, TX (Ocean Drilling Program), 1–77.
- Sinton, J.M., Smaglik, S.M., Mahoney, J.J., and Macdonald, K.C., 1991. Magmatic processes at superfast spreading mid-ocean ridges: glass compositional variations along the East Pacific Rise 13°–23°S. *J. Geophys. Res.*, 96:6133–6155.
- Smith, D.C., Spivack, A.J., Fisk, M.R., Haveman, S.A., Staudigel, H., and the Leg 185 Shipboard Scientific Party, 2000. Methods for quantifying potential microbial contamination during deep ocean coring. *ODP Tech. Note*, 28 [Online]. Available from World Wide Web: <<http://www-odp.tamu.edu/publications/tnotes/tn28/INDEX.HTM>>. [Cited 2000-05-23]
- , in press. Tracer-based estimates of drilling-induced microbial contamination of deep sea crust. *Geomicrobiol. J.*
- Staudigel, H., Davies, G.R., Hart, S.R., Marchant, K.M., and Smith, B.M., 1995. Large scale Sr, Nd, and O isotopic anatomy of altered oceanic crust: DSDP sites 417/418. *Earth Planet. Sci. Lett.*, 130:169–185.
- Steiner, M.B., and Wallick, B.P., 1992. Jurassic to Paleocene paleolatitudes of the Pacific Plate derived from the paleomagnetism of the sedimentary sequences at Sites 800, 801, and 802. In Larson, R.L., Lancelot, Y., et al., *Proc. ODP, Sci. Results*, 129: College Station, TX (Ocean Drilling Program), 431–446.

- Thorseth, I.H., Furnes, H., and Heldal, M., 1992. The importance of microbiological activity in the alteration of natural basaltic glass. *Geochim. Cosmochim. Acta*, 56:845–850.
- Torsvik, T., Furnes, H., Muehlenbachs, K., Thorseth, I.H., and Tumyr, O., 1998. Evidence for microbial activity at the glass-alteration interface in oceanic basalts. *Earth Planet. Sci. Lett.*, 162:165–176.
- Wallick, B.P., and Steiner, M.B., 1992. Paleomagnetic and rock magnetic properties of Jurassic Quiet Zone basalts, Hole 801C. In Larson, R.L., Lancelot, Y., et al., *Proc. ODP, Sci. Results*, 129: College Station, TX (Ocean Drilling Program), 455–470.
- Weaver, J.S., and Langmuir, C.H., 1990. Calculation of phase equilibrium in mineral-melt systems. *Comput. Geosci.*, 16:1–19.
- Worm, H.-U., Böhm, V., and Bosum, W., 1996. Implications for the sources of marine magnetic anomalies derived from magnetic logging in Holes 504B and 896A. In Alt, J.C., Kinoshita, H., Stokking, L.B., and Michael, P.J. (Eds.), *Proc. ODP, Sci. Results*, 148: College Station, TX (Ocean Drilling Program), 331–338.
- Yamamoto, H., Mizutani, S., and Kagami, H., 1985. Middle Jurassic radiolarians from Blake Bahama Basin, West Atlantic Ocean. *Bull. Nagoya Univ., Furukawa Mus.*, 1:25–49.
- Yeats, R.S., Hart, S.R., et al., 1976. *Init. Repts DSDP*, 34: Washington (U.S. Govt. Printing Office).

Figure F1. Bathymetric map of area around Hole 801C in Pigafetta Basin showing the location of the Mariana Trench, Mariana Islands, and surrounding seamounts. ODP Sites 776, 778, 800, and DSDP Sites 199 and 452 are also indicated.

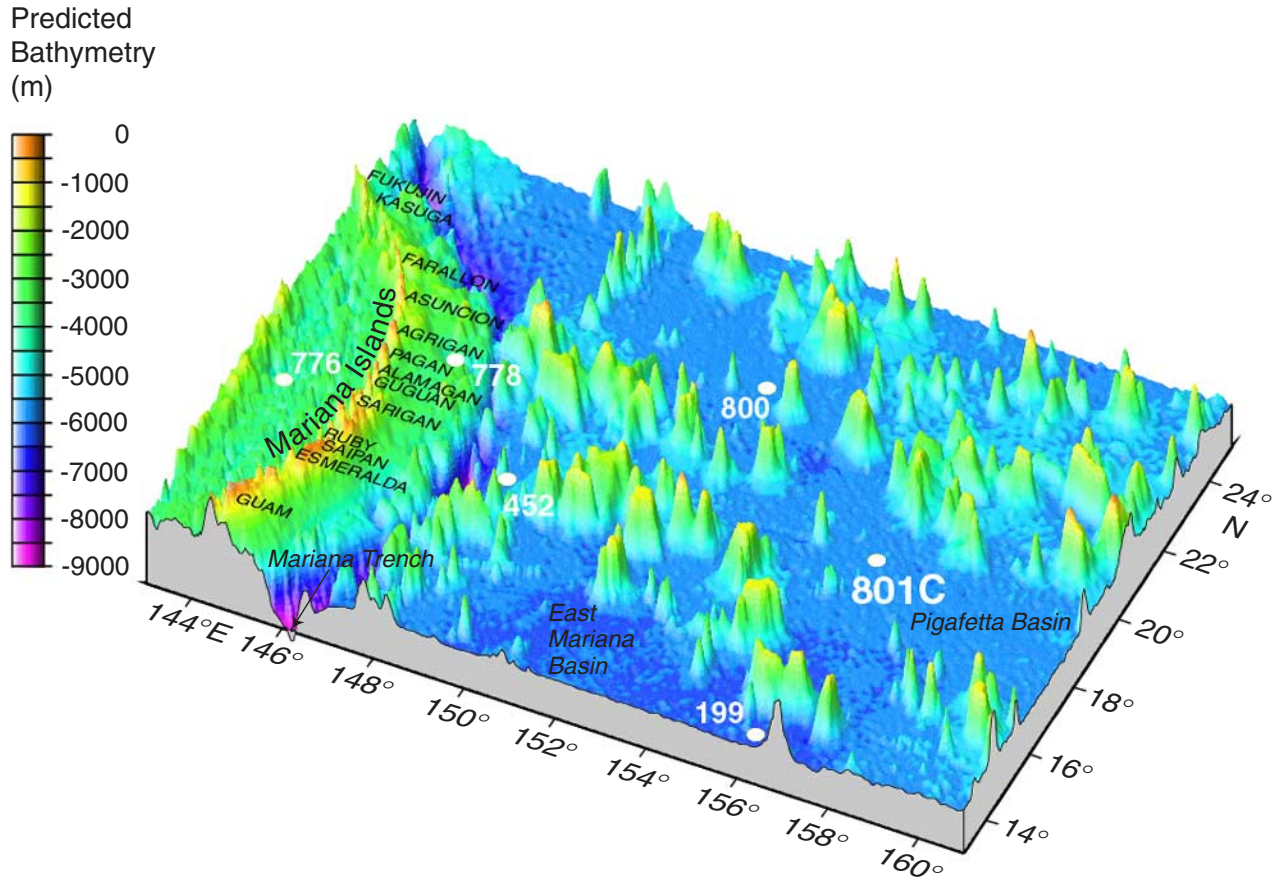


Figure F2. Seismic section showing the stratigraphy of Site 801. The total depth of penetration into the basement achieved during Leg 185 drilling is indicated (adapted from Abrams et al., 1993).

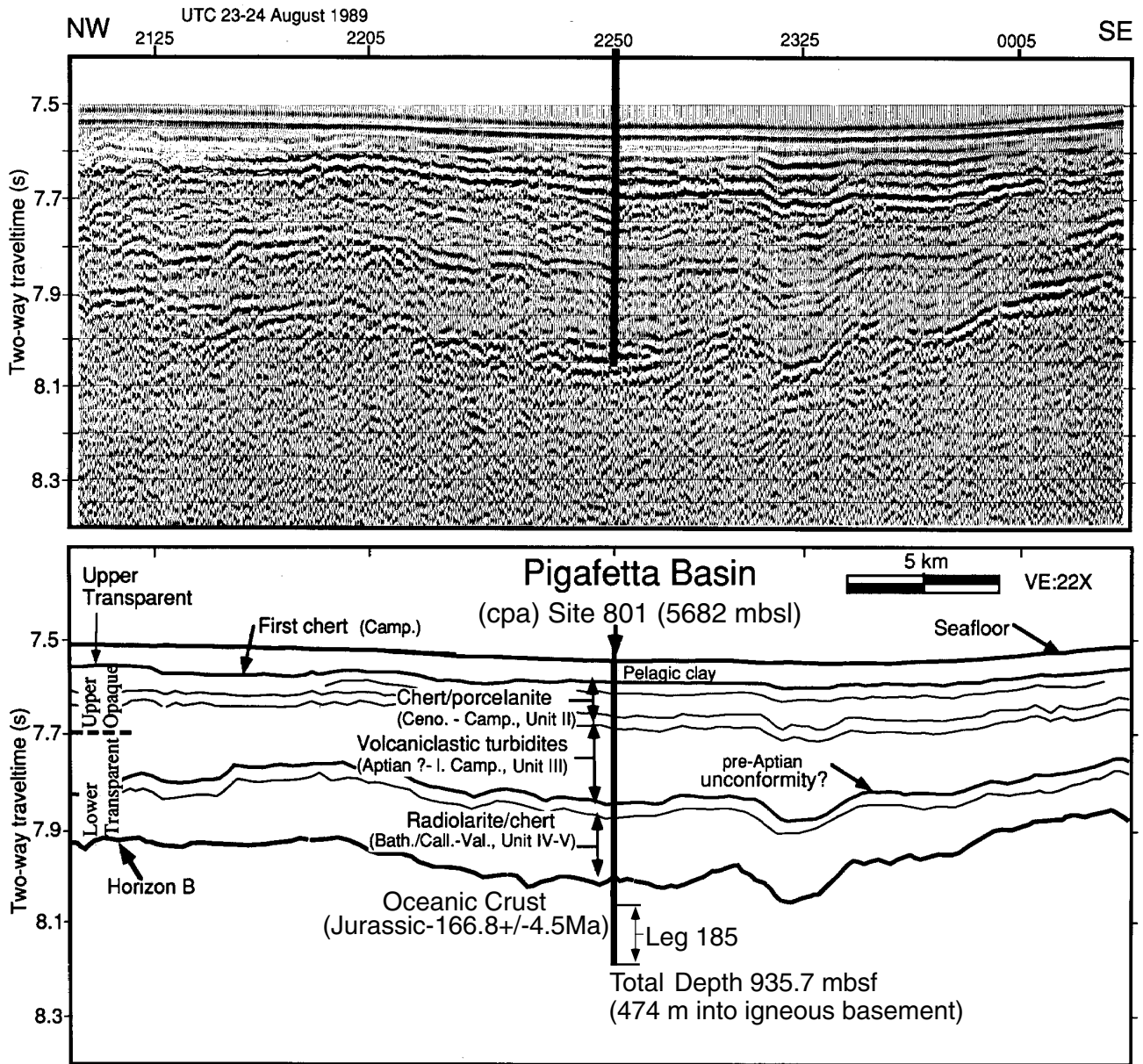


Figure F3. Lithostratigraphic section of Hole 801C basement, with Ar/Ar ages shown relative to (1) Zr compositions as a measure of magma types (note the high Zr of the alkaline magmas and the gradual increase in Zr downhole in the tholeiitic section) and (2) apparent porosity log showing the hydrothermal zone, which formed on the Jurassic ocean floor and is overlain by younger sediments and off-axis alkaline intrusions (modified from Larson et al., 1993).

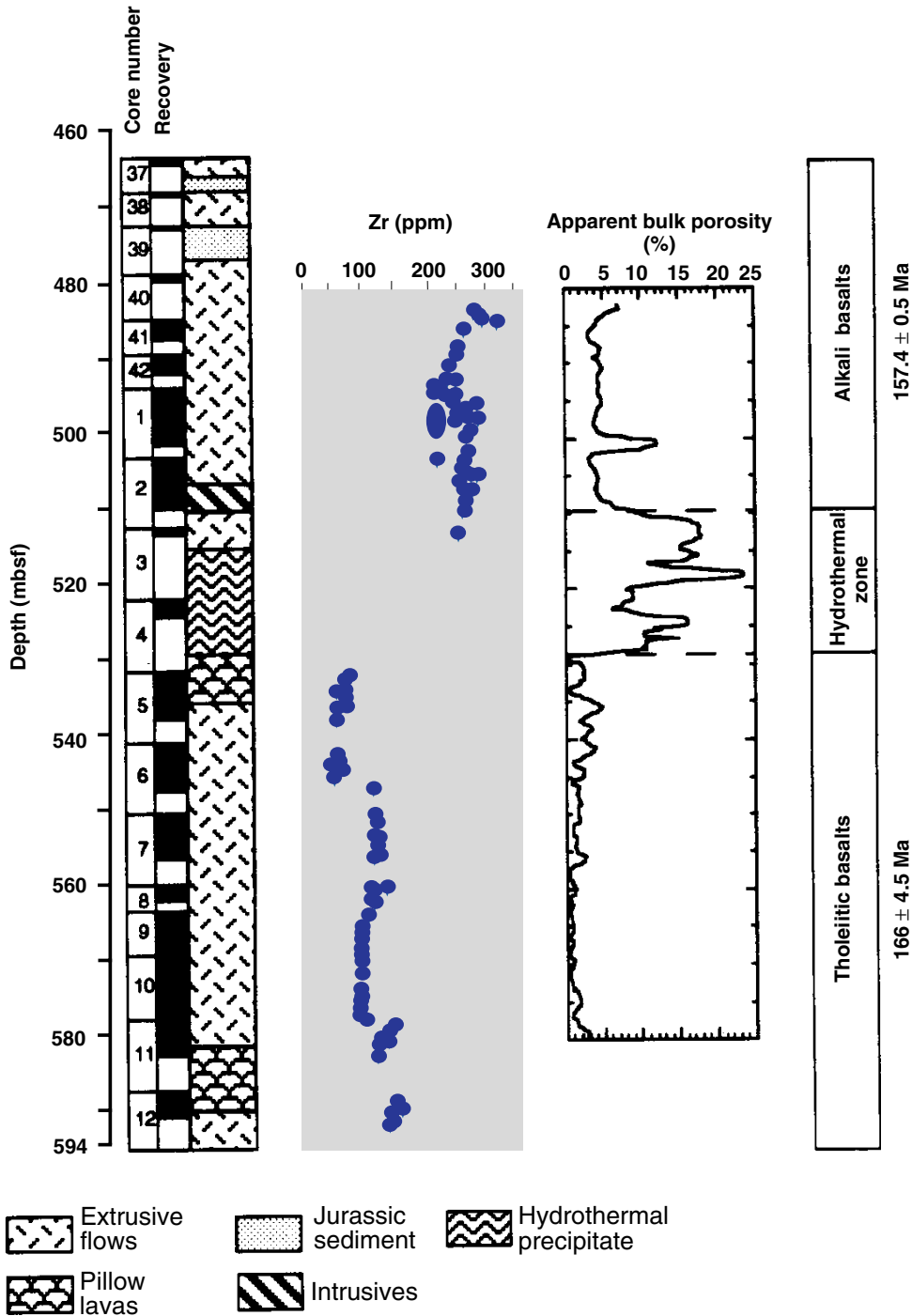


Figure F4. Photomicrograph of a radiolarian (suborder *Spumellaria*) with well-preserved internal structure from Sample 185-801C-15R-3, 123–127 cm (617.67 mbsf). The outer test wall is 200 μm across.

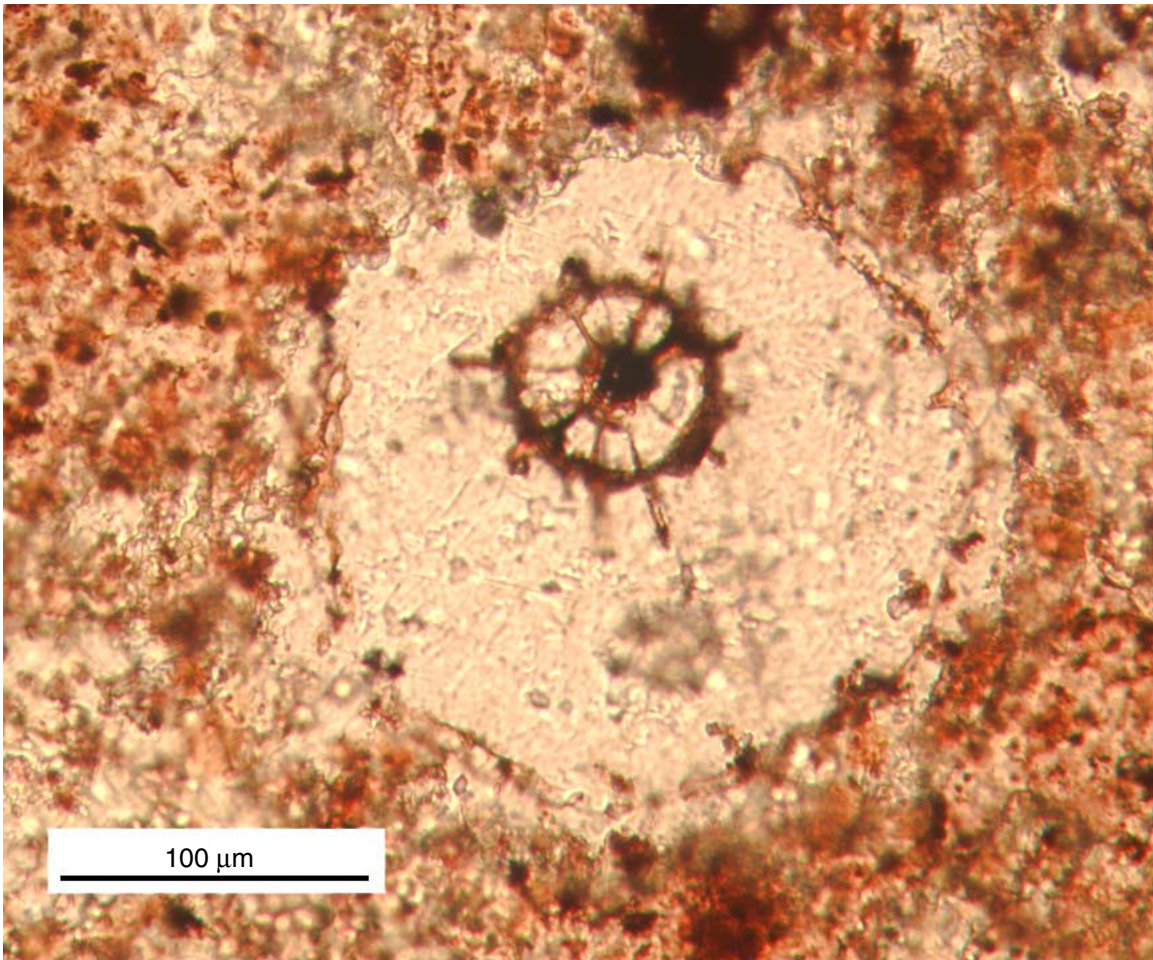


Figure F5. A. Hole 801C lithologic summary illustrating core recovery (black = recovered material; white = unrecovered material), lithologic units, major sequences, and geochemical units. Broad changes in the lithology, or primary igneous structure, are illustrated in the sequence column. The distribution of phenocryst mineralogy (estimated in hand specimen and shown by a black bar) and the geochemical units (based on shipboard X-ray fluorescence analyses) are also included. (Continued on next page.)

A

Core	Depth (mbsf)	Recovery (m)	Unit	Sequence	Plagioclase	Olivine	Pyroxene	Geochem. Unit
13R	594.3		33	IV.				11
14R	604.0		34-38					
15R	613.7		39-46					
16R	623.3		47-49	V. Lower Hydrothermal				12
17R	632.8		49-50					
18R	642.2		50	IV. Upper Pillows and Flows				13
19R	651.7							
20R	660.7							
21R	670.0							
22R	673.6							
23R	681.9							
24R	691.3							
25R	700.7							
26R	710.2							
27R	719.7							
28R	728.7		50-51	VI. Lower Massive Flows				14
29R	737.9							
30R	747.3		51					
31R	756.6							
32R	766.3		51-52					
33R	775.7		52-53					
34R	785.3		53					
35R	794.9							
36R	804.1		53-54					
37R	813.3		54					
38R	822.8		54-55					
39R	832.2		55-56					
40R	841.5		56	VII. Breccia				17
41R	850.8		56-57	VIII. Lower Pillows and Flows				
42R	860.0		57-58					
43R	869.1		58					
44R	878.8		59-60					
45R	888.4		60					
46R	898.0							
47R	907.7							
48R	916.7							
49M-52M	928.3							18

Figure F5 (continued). B. Cooling unit thickness with depth downhole, plotted alongside the resistivity and total natural gamma logs.

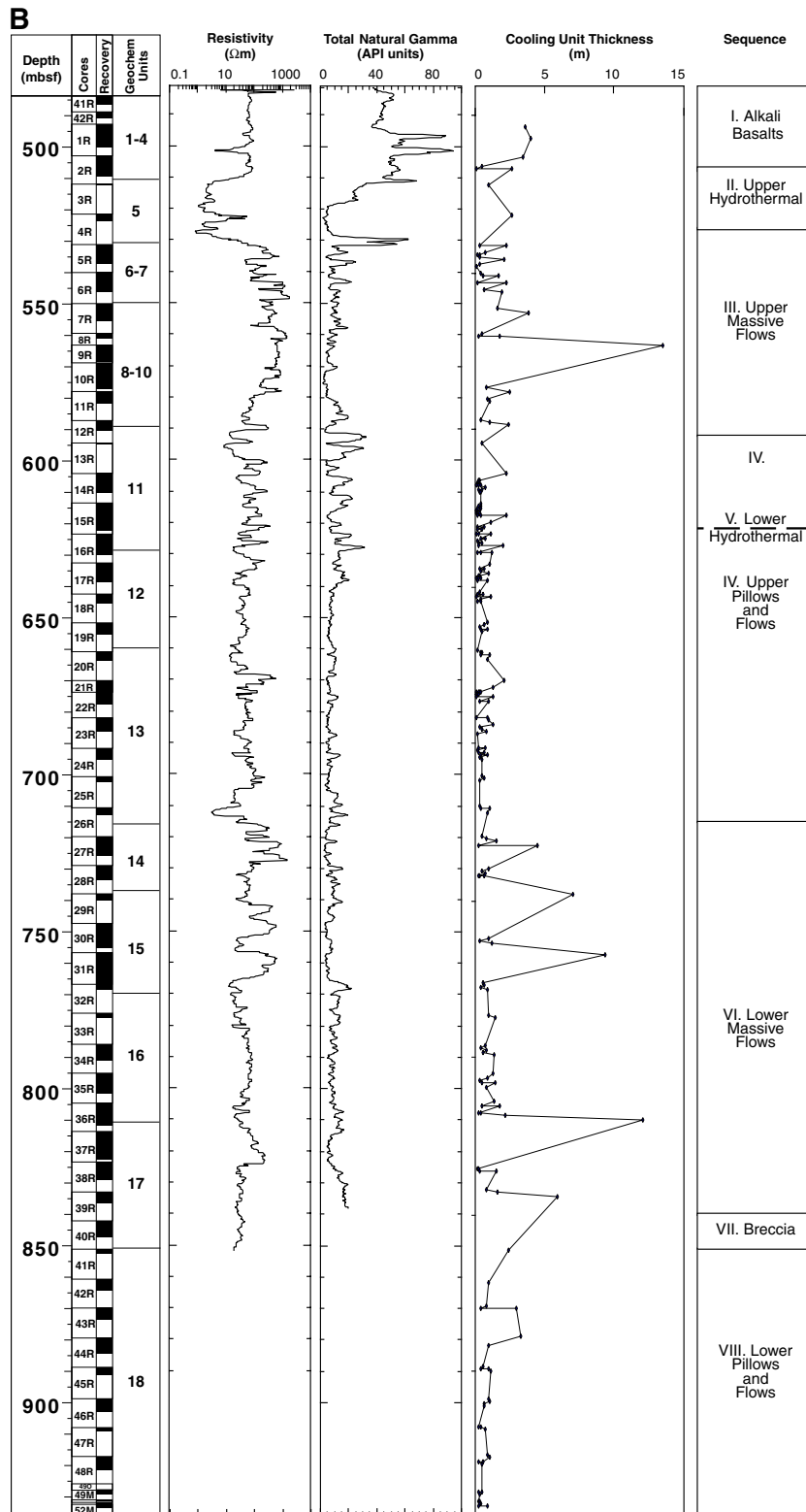
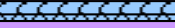


Figure F6. Basement stratigraphy and unit boundaries for Hole 801C. Depths are in meters below seafloor to the top of each core. Purple = flows >1 m thick; pale green = pillows or flows between 50 cm and 1 m thick; blue = pillows <50 cm thick; dark green = breccia-dominated intervals; brown = sediments and re-crystallized interpillow material; yellow = hydrothermal units; and peach = debris from the hole, Core 185-801C-13R only. Where subunits or cooling units occur, they are represented by a line and/or a change in lithology in the lithology/structure column. Data for Cores 1R–12R were collected during Leg 129, with some subunits added (in Units 9, 11, 13, 15, 20, and 24) after further observations were made during Leg 185. Data for Cores 13R through 52M were collected during Leg 185. All the data used to compile this figure are included in Table T4, p. 177. (Continued on next five pages.)

Core	Depth (mbsf)	Lithology/structure	Lithologic unit
1R	493.70		1
			2
2R	503.00		3
			4
			6
3R	512.20		7
4R	521.70		8
5R	531.20		9
			11
			13

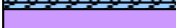
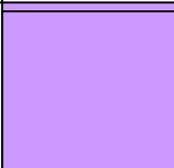
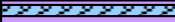
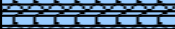
Core	Depth (mbsf)	Lithology/structure	Lithologic unit
6R	540.50		15
			16
			20
			
7R	550.10		21
			22
			23
8R	559.50		24
9R	563.20		25
10R	569.00		25
			26
	577.90		27
			28

Figure F6 (continued).

Core	Depth (mbsf)	Lithology/structure	Lithologic unit
11R			29
12R	587.30		31
			32
13R	594.30		33
14R	604.00		34
			37
			38
15R	613.70		39
			41
			43
			44
			45
			46
	623.30		47

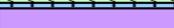
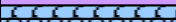
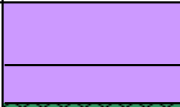
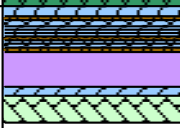
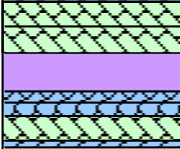
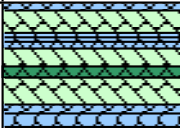
Core	Depth (mbsf)	Lithology/structure	Lithologic unit
16R			
			
			49
17R	632.80		
			49
			
			50
18R	642.20		
			50
			
19R	651.70		50
			
	660.70		50

Figure F6 (continued).

Core	Depth (mbsf)	Lithology/ structure	Lithologic unit
20R			
21R	670.00		50
22R	673.60		50
23R	681.90		50
24R	691.30		50
	700.70		50

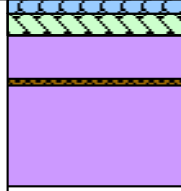
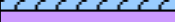
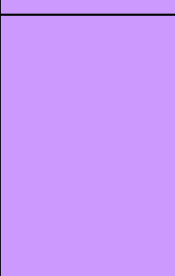
Core	Depth (mbsf)	Lithology/ structure	Lithologic unit
25R			
26R	710.20		50
27R	719.70		50
28R	728.70		50
			51
	737.90		51

Figure F6 (continued).

Core	Depth (mbsf)	Lithology/structure	Lithologic unit
29R			
30R	747.30	  	51
31R	756.60		51
32R	766.30	 	52
33R	775.70		52
			53

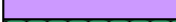
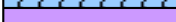
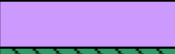
Core	Depth (mbsf)	Lithology/structure	Lithologic unit
34R	785.30	  	53
			
35R	794.90	    	53
36R	804.10	     	53
37R	813.30		54
38R	822.80	  	54
		 	55

Figure F6 (continued).

Core	Depth (mbsf)	Lithology/structure	Lithologic unit
39R	832.20		55
			
40R	841.50		56
			
41R	850.80		56
			
42R	860.00		57
			58
			
43R	869.10		58
			

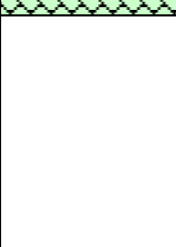
Core	Depth (mbsf)	Lithology/structure	Lithologic unit
44R	878.80		59
			60
45R	888.40		60
			
46R	898.00		60
			
			
47R	907.70		60
			
	916.70		60
			
			

Figure F6 (continued).

Core	Depth (mbsf)	Lithology/structure	Lithologic unit
48R			
49O	CORED WITH DIAMOND DRILL BIT		
49M	928.3		60
50M	931.50		60
51M	932.00		60
52M	932.80		60

Lithology/Structure

	Flows greater than 1 m thick		Sediments and recrystallized-interpillow material
	Pillows or flows between 50 cm and 1 m thick		Hydrothermal units
	Pillows less than 50 cm thick		Debris
	Breccia-dominated intervals		Interval not recovered

Figure F7. Estimated volume percent contribution of brecciated intervals and interpillow material to each core in Hole 801C. Interpillow material is more abundant toward the top of the section and not observed below Core 185-801C-32R, whereas breccia is present in variable amounts throughout most of the section.

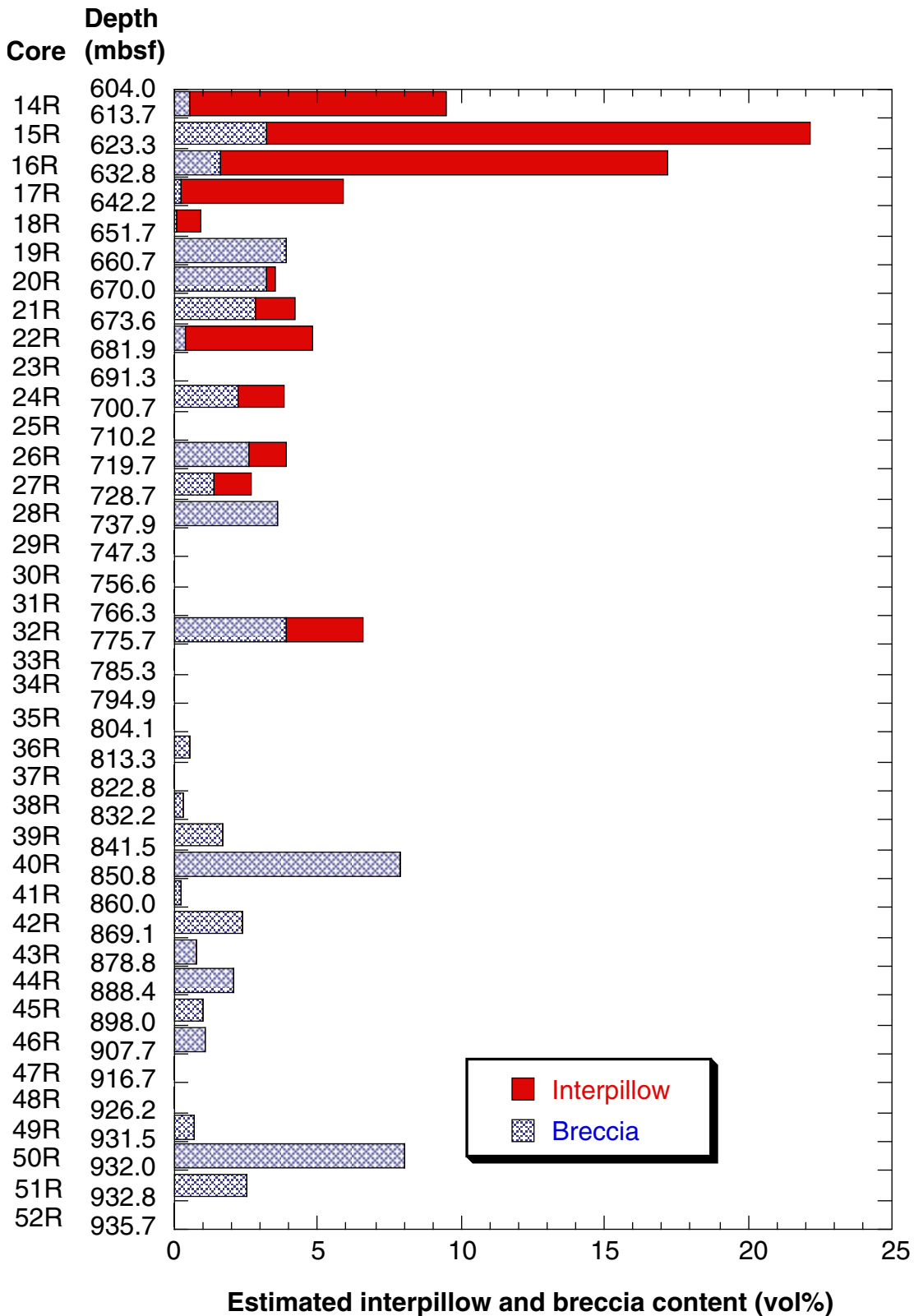


Figure F8. Dark brown and yellowish green cherty interpillow sediment from interval 185-801C-14R-2, 136–146 cm. Bedding or grain-size variation is observed perpendicular to the color banding. See “[Sedimentology and Biostratigraphy](#),” p. 5, for further description.

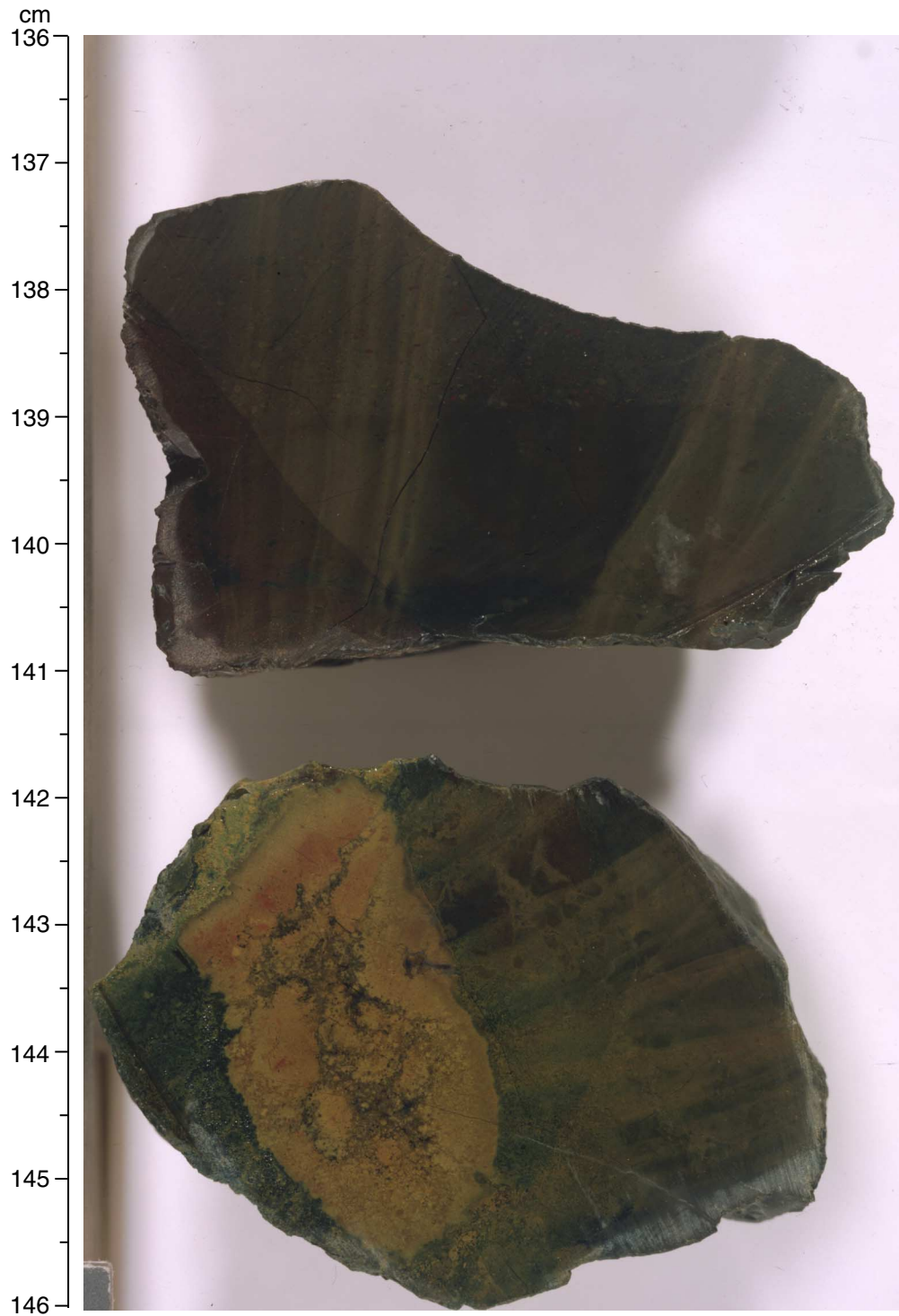


Figure F9. Altered pale green basalt and interpillow breccia with vein filling material from interval 185-801C-15R-1, 106–116 cm. The pillow margins are fractured and brecciated, and the cement is reddish brown with white interpillow material, which is probably recrystallized sediment.

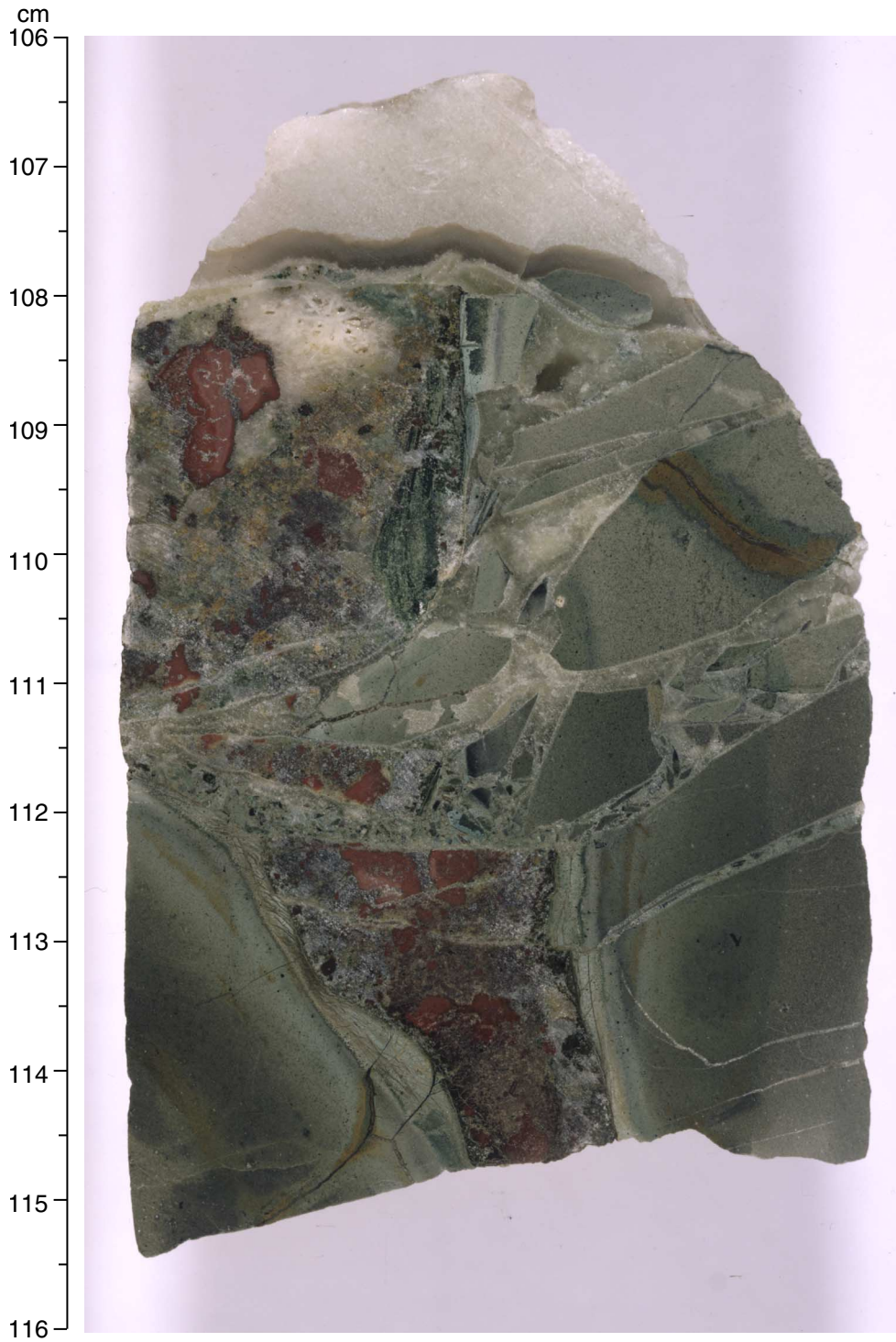


Figure F10. Altered pale green pillow margins with altered glass present in the pillow rims. Between the two pillow rims a 15-cm-thick interval of green and red-brown recrystallized interpillow material can be observed (interval 185-801C-15R-7, 38-66 cm).

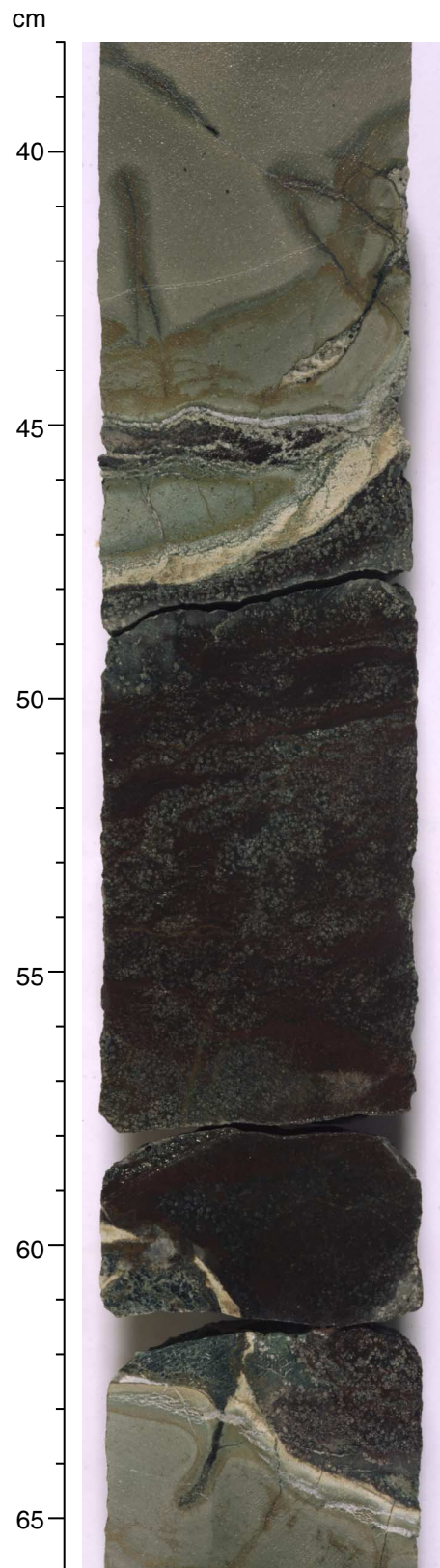


Figure F11. Boundary or contact between Unit 48, the silicified Fe-rich hydrothermal zone and the underlying altered and recrystallized sediment or interpillow material (interval 185-801C-16R-3, 34–64 cm).



Figure F12. Aphyric basalt flow base and incorporated intrapillow recrystallized sediment, which contain clasts of red-brown cherty sediments in a siliceous cement (interval 185-801C-16R-5, 54–66 cm).

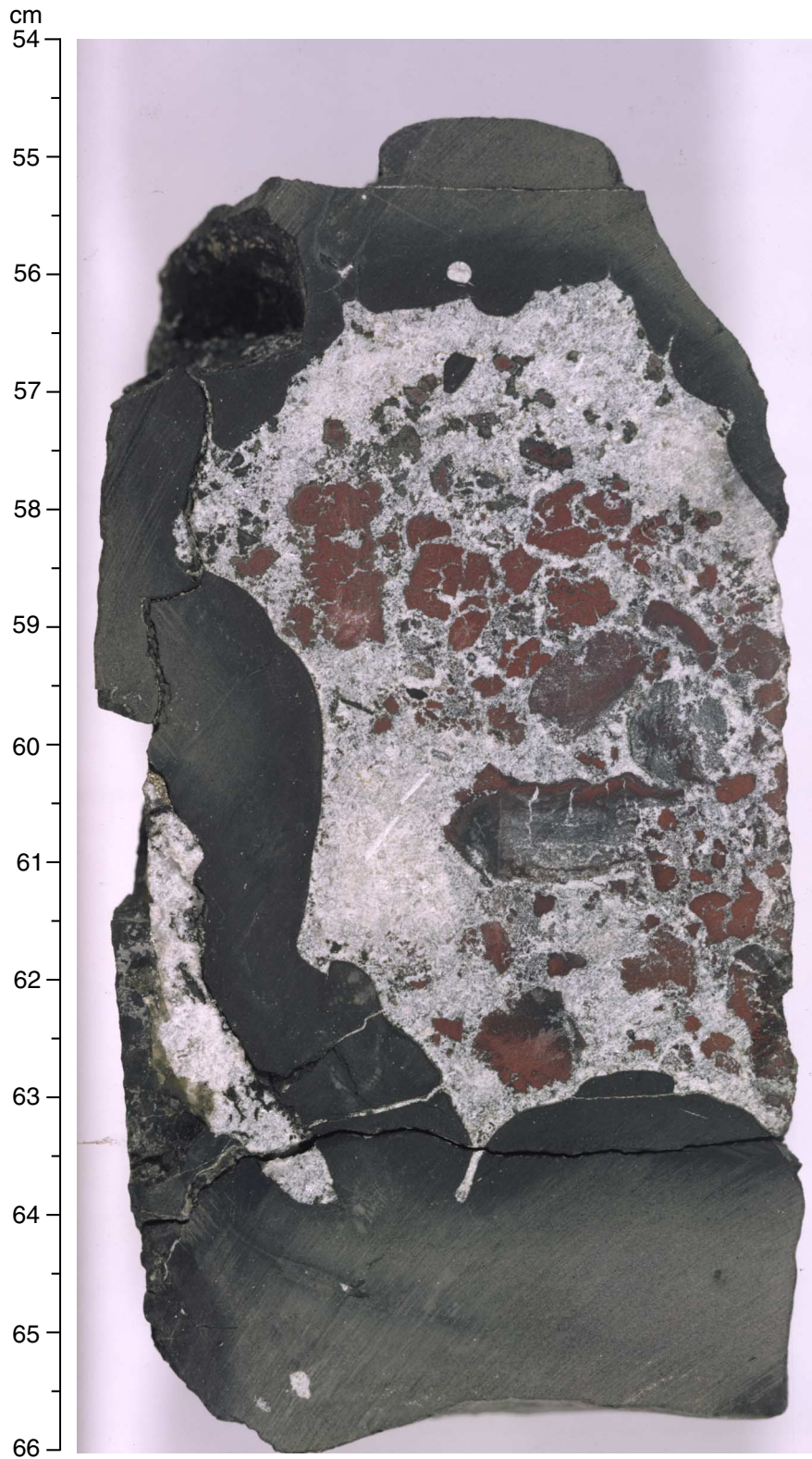


Figure F13. Thin flow units with interpillow or interflow recrystallized sediment as breccia cement containing angular-oriented microcrystalline aphyric basalt clasts (interval 185-801C-17R-4, 11-35 cm).

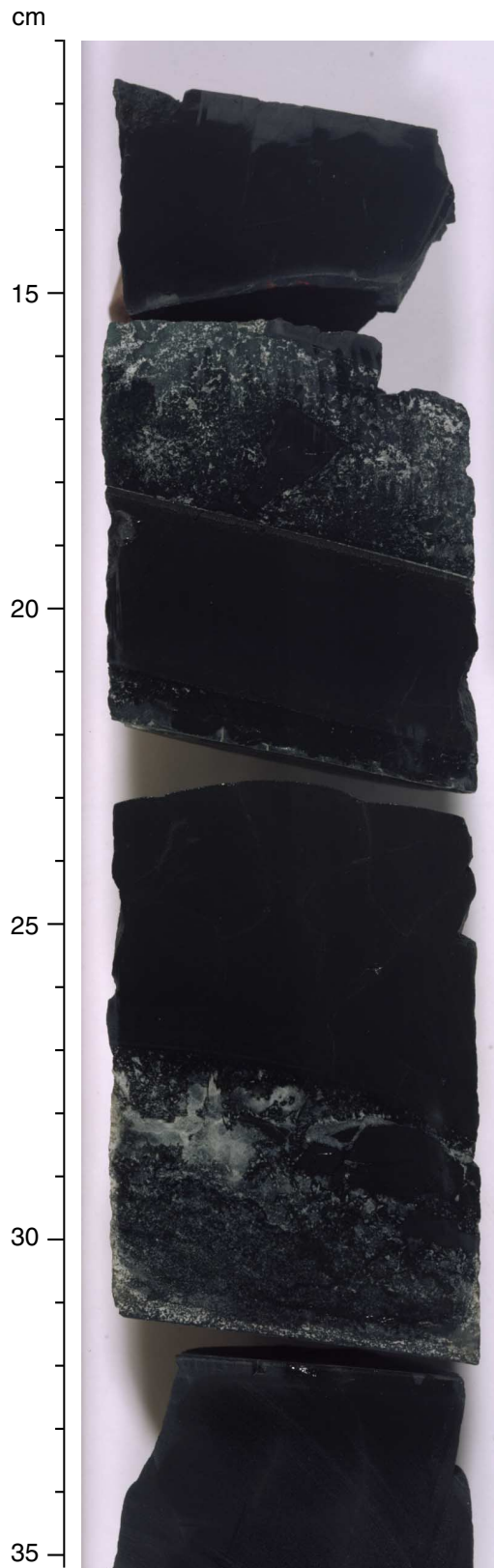


Figure F14. Altered hyaloclastite, containing altered glass shards and chilled basalt fragments from a pillow rim; shards are greenish black in color and exist within a carbonate and saponite cement (interval 185-801C-19R-2, 22–30 cm).



Figure F15. Glassy chilled rim of an aphyric basalt pillow (interval 185-801C-23R-1, 12–22 cm).

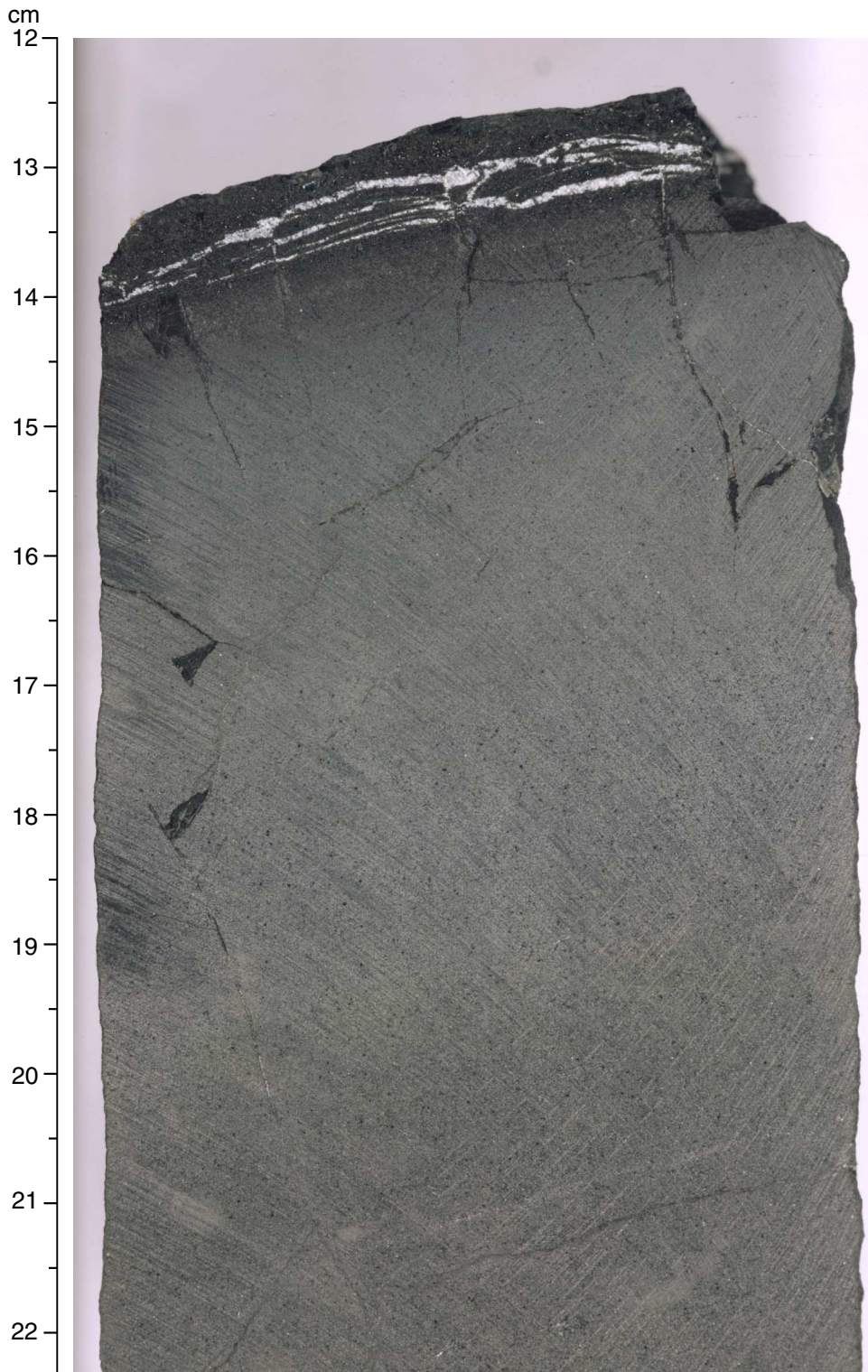


Figure F16. Hyaloclastite breccia with carbonate and saponite matrix and with fresh glass, and small aphyric basalt fragments. The fragments range in size from ~2 mm to ~4.5 cm, averaging between 0.5 and 1 cm (interval 185-801C-28R-3, 53-59 cm).



Figure F17. Aphyric basalt breccia with blue-green celadonite and carbonate cement. Angular to subangular microcrystalline basalt clasts are generally matrix supported, and they vary in size from <0.5 to ~5 cm (interval 185-801C-36R-3, 85–98 cm).

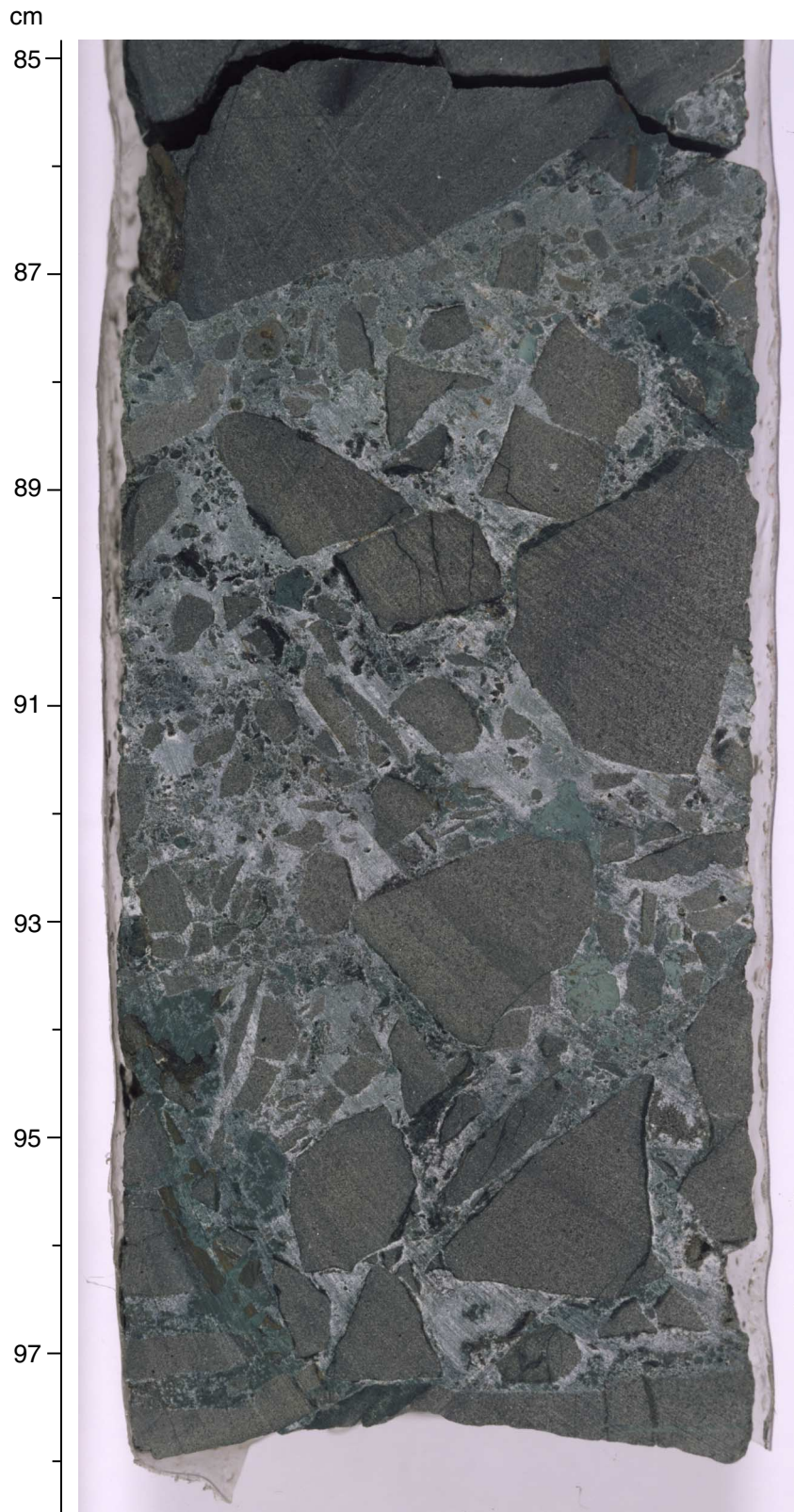


Figure F18. Alignment of large (>0.5 cm) carbonate-filled vesicles within the fine- to medium-grained aphyric basalt from Unit 54, the 12-m-thick massive flow (interval 185-801C-37R-2, 0–11 cm).

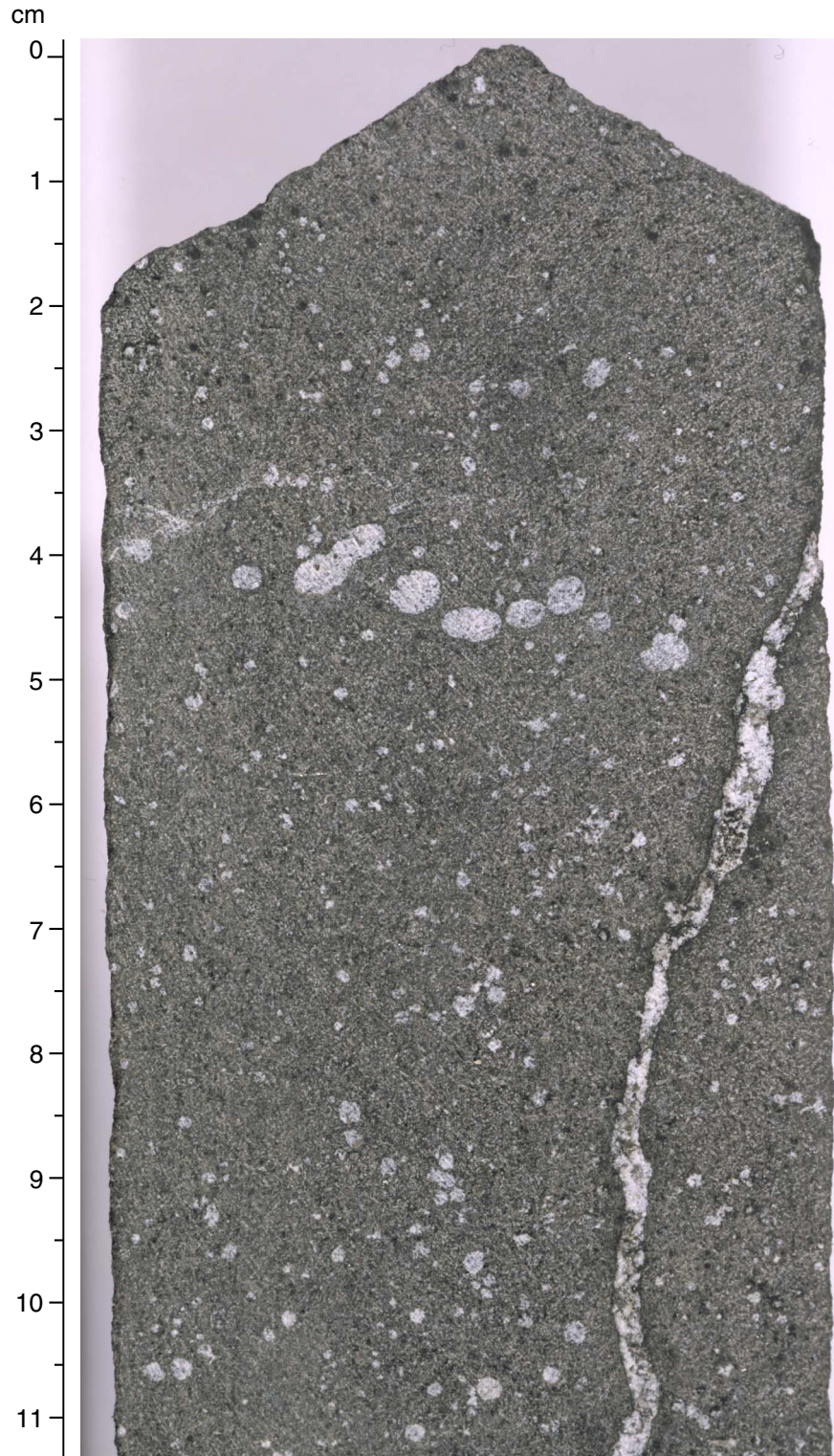


Figure F19. Variable distribution of vesicles (interval 185-801C-37R-2, 58–81 cm). A change is observed from a complete absence of vesicles to a significant proportion of vesicles over a distance of only 20 cm.

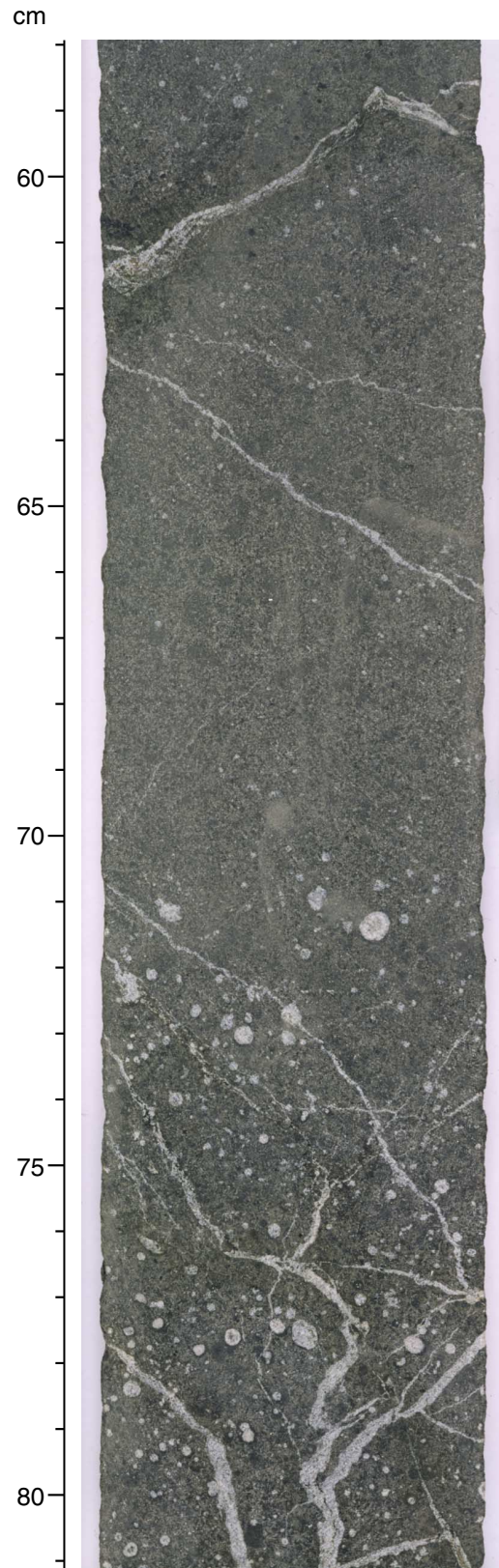


Figure F20. Typical groundmass of basalt. Plagioclase laths make up the major part of the groundmass, with subhedral pyroxenes. Sample 129-801B-32R-1, 67–69 cm; crossed polars; magnification = 50×; field of view = 5 mm.

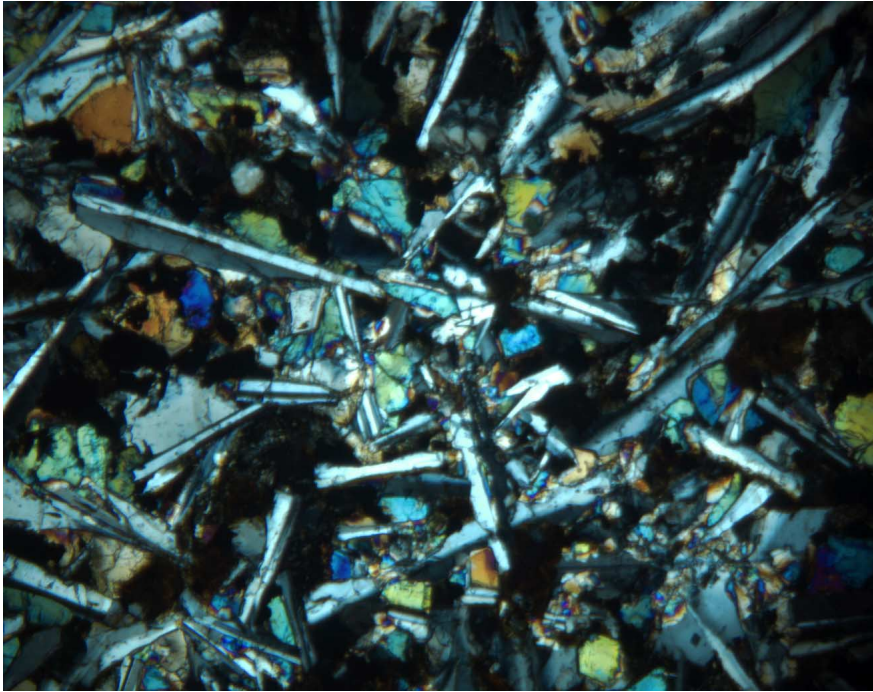
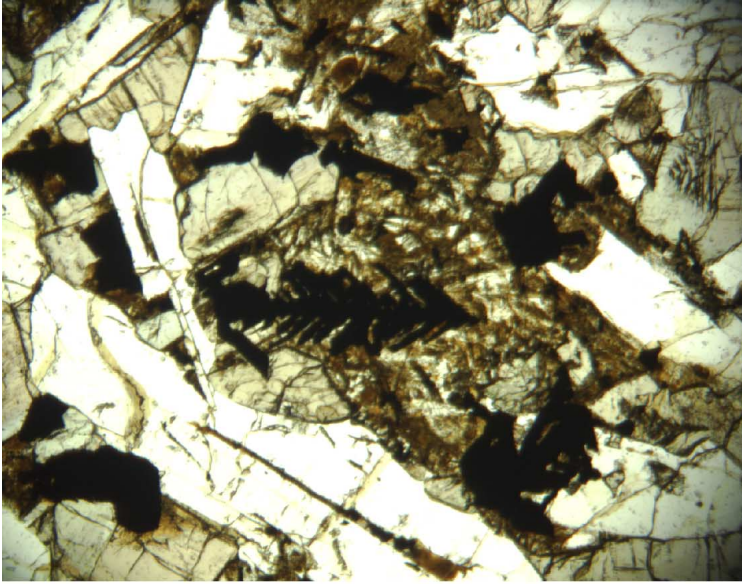


Figure F21. Skeletal magnetites in (A) plane-polarized light and (B) reflected light of the groundmass of Sample 129-801C-37R-5 (Piece 1A, 37–40 cm); magnification = 50×; field of view = 5 mm.

A



B

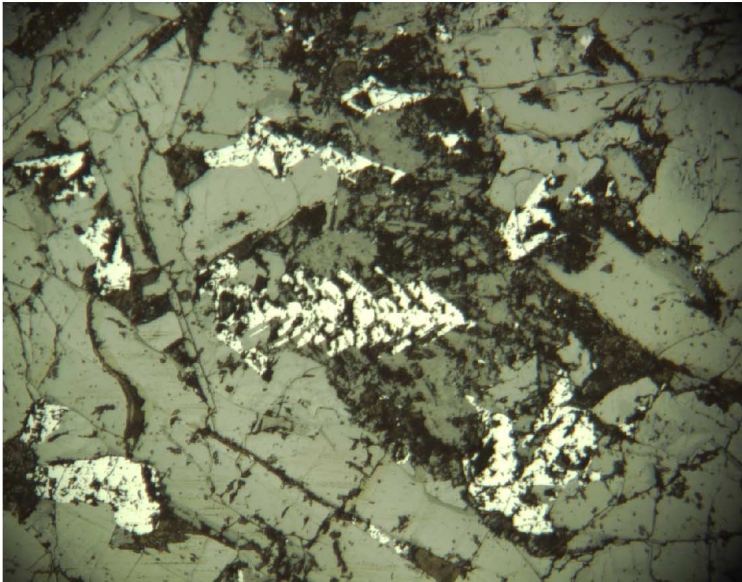


Figure F22. Olivine altered to saponite in Sample 129-801C-31R-3 (Piece 2B, 48–51 cm) in (A) plane-polarized light and (B) crossed polars. Magnification = 200 \times ; field of view = 0.5 mm.

A



B

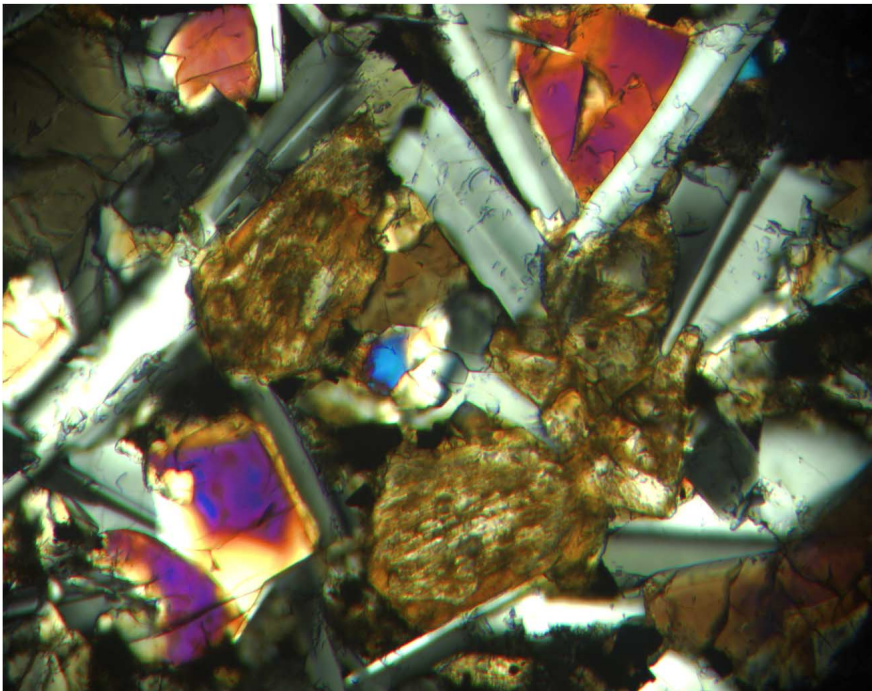


Figure F23. The intersertal dark matrix of this thin section consists of cryptocrystalline interstitial materials (devitrified glass), and plagioclase laths form the framework. Sample 129-801C-16R-1 (Piece 4F, 107–110 cm); plane-polarized light; magnification = 200×; field of view = 0.5 mm.

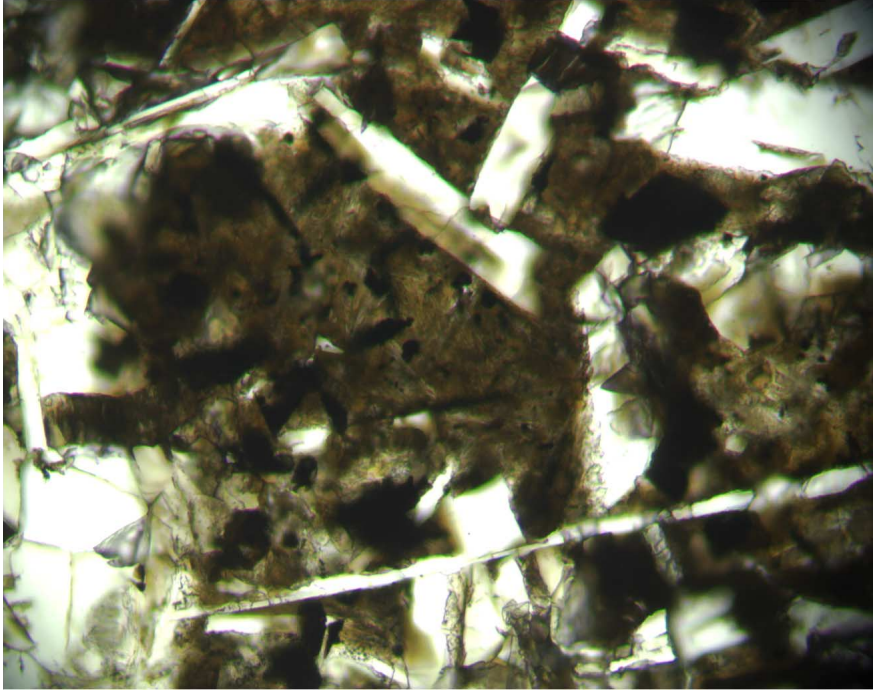


Figure F24. Chilled contact between pillow and interpillow material. The chilled pillow rim contains eu-hedral olivine (left of the center), some small plagioclase phenocrysts, and vesicles. Sample 185-801C-16R-5 (Piece 13, 107–110 cm); plane-polarized light; magnification = 50×; field of view = 5 mm.

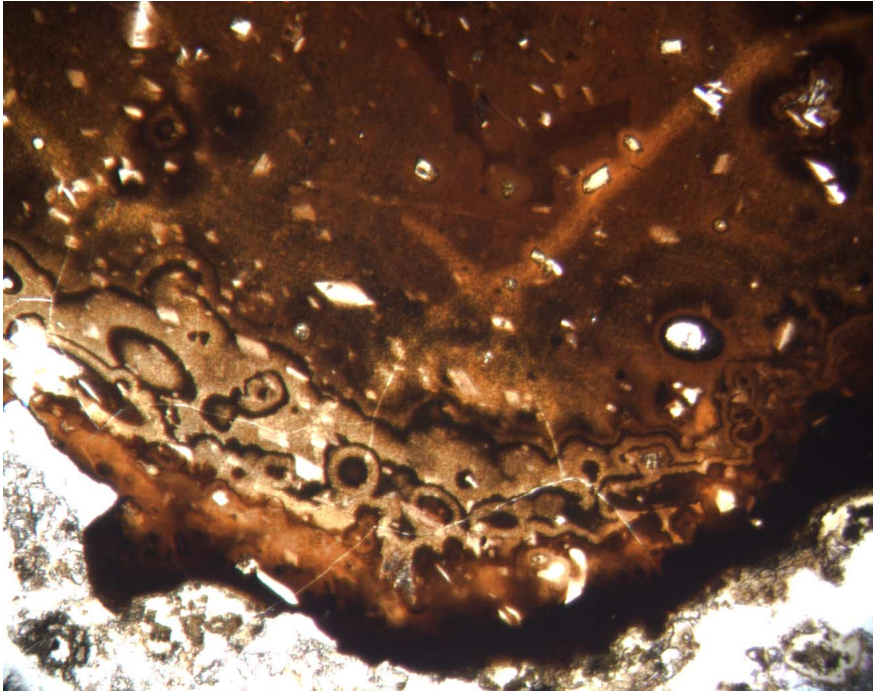


Figure F25. Frequency diagram showing the amount of (devitrified) glass in chilled and crystalline basalts. Samples containing >40% glass are termed "chilled"; samples containing <40% glass are termed crystalline.

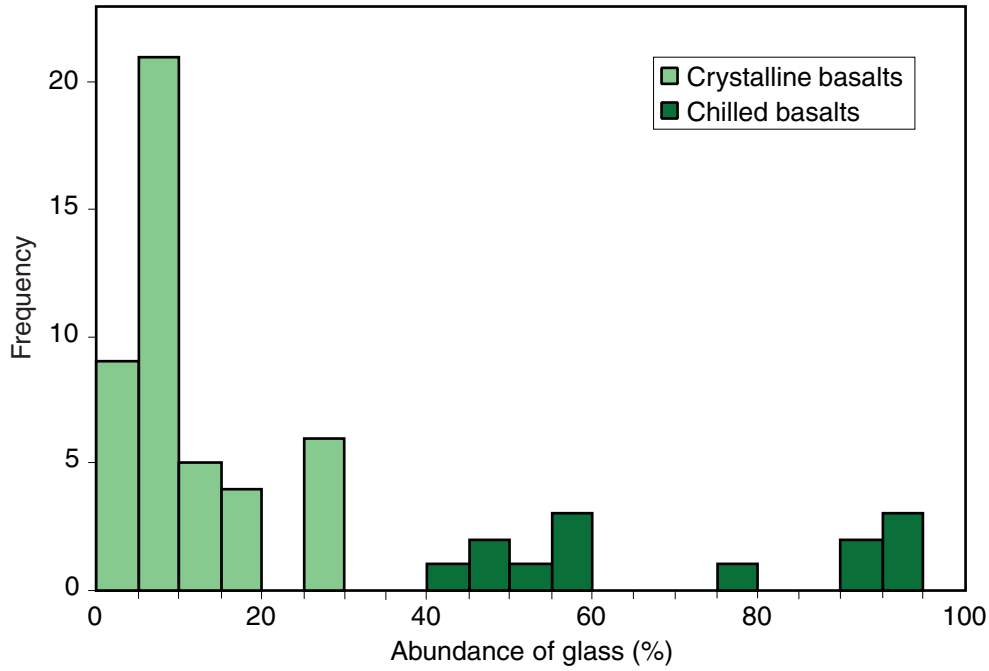


Figure F26. Plagioclase glomerocryst in a glassy pillow rim. Sample 185-801C-42R-2 (Piece 11, 126–128 cm); plane-polarized light; magnification = 50×; field of view = 5 mm.

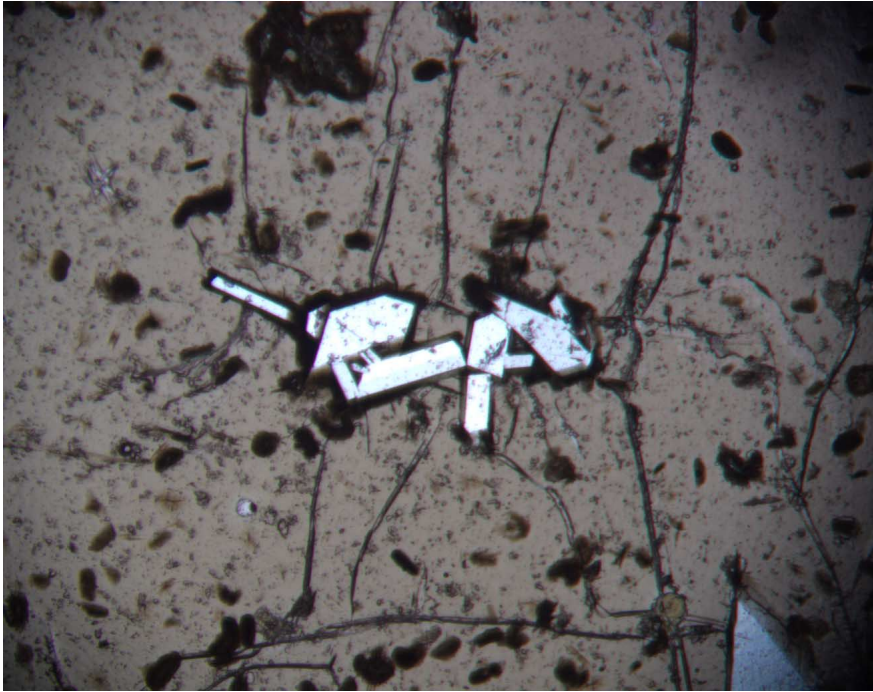
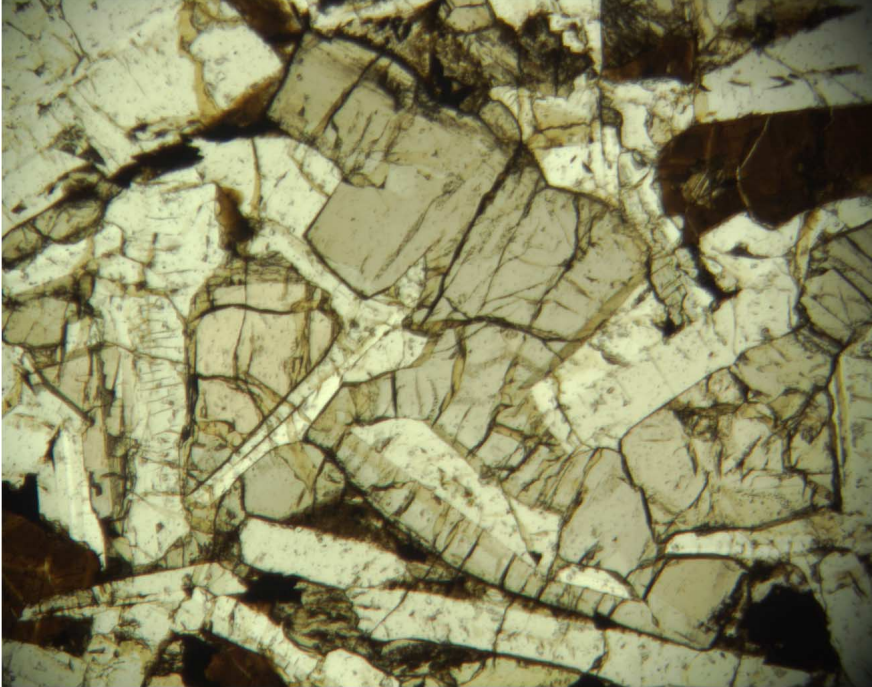


Figure F27. Medium-grained basalt of Sample 185-801C-37R-5 (Piece 1A, 37–40 cm) in (A) plane-polarized light and (B) crossed polars. Pyroxenes and plagioclases are intergrown, which denotes common growth during relatively slow cooling within flow interior. Note the small amount of dark interstitial material on the top and bottom of the photograph. Magnification = 50 \times ; field of view = 5 mm.

A



B

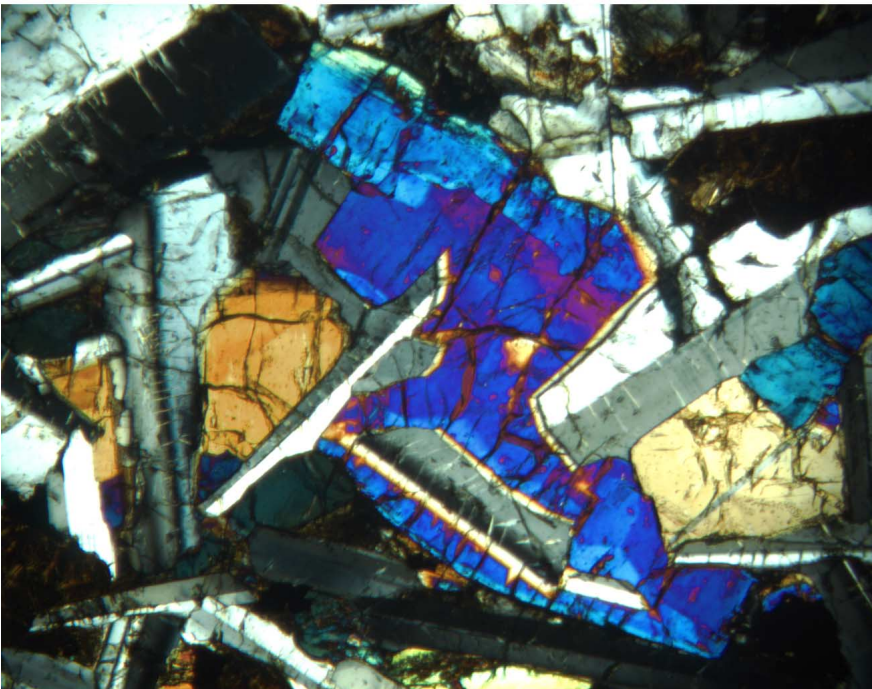
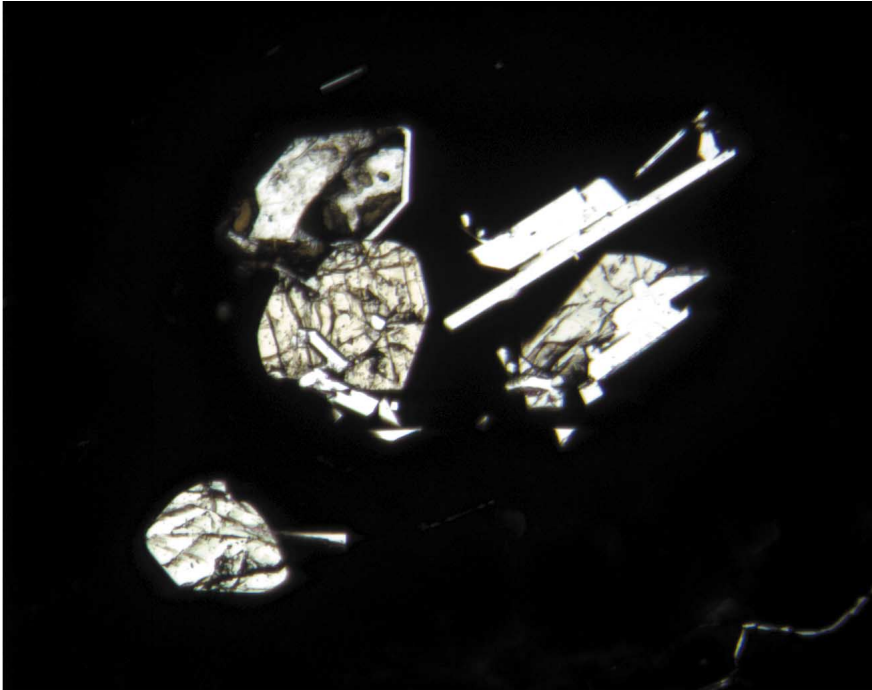


Figure F28. Assemblage of phenocrysts: euhedral plagioclase laths, subhedral pyroxenes, and olivine. A. Altered olivine (top of photograph, plane-polarized light). B. Pyroxene is orange to gray (crossed polars). Sample 185-801C-68R-2 (Piece 12, 121–131 cm); magnification = 50×; field of view = 5 mm.

A



B

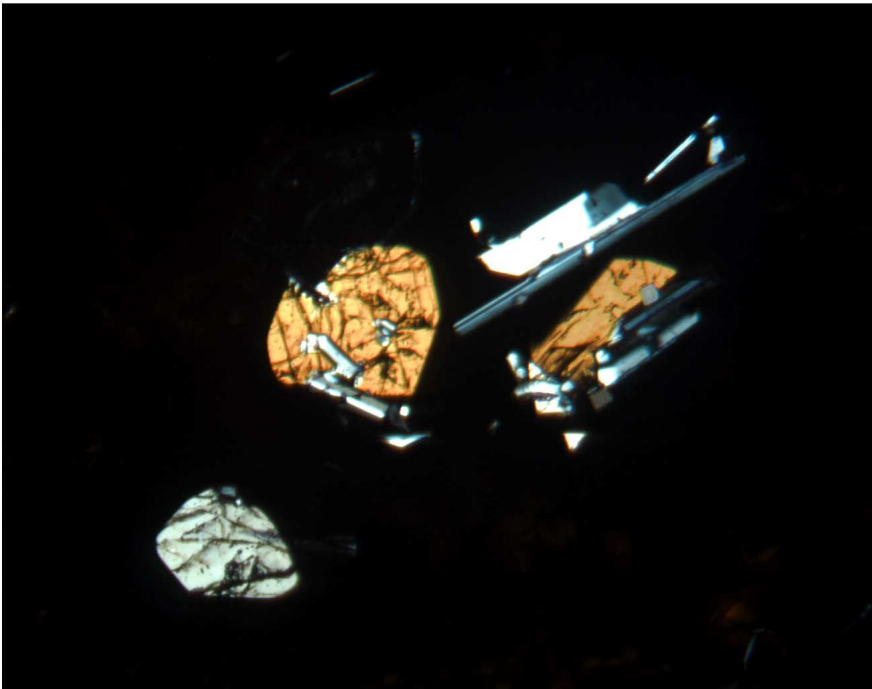


Figure F29. Dendritic overgrowths on plagioclase microlite in a chilled margin. Sample 185-801C-42R-2 (Piece 11, 126–128 cm); plane-polarized light; magnification = 200×; field of view = 0.5 mm.



Figure F30. Quenched (almost subvariolitic) texture of divergent, branching fibers of plagioclase close to a chilled margin. Sample 185-801C-33R-1 (Piece 12, 123–124 cm); plane-polarized light; magnification = 200×; field of view = 0.5 mm.

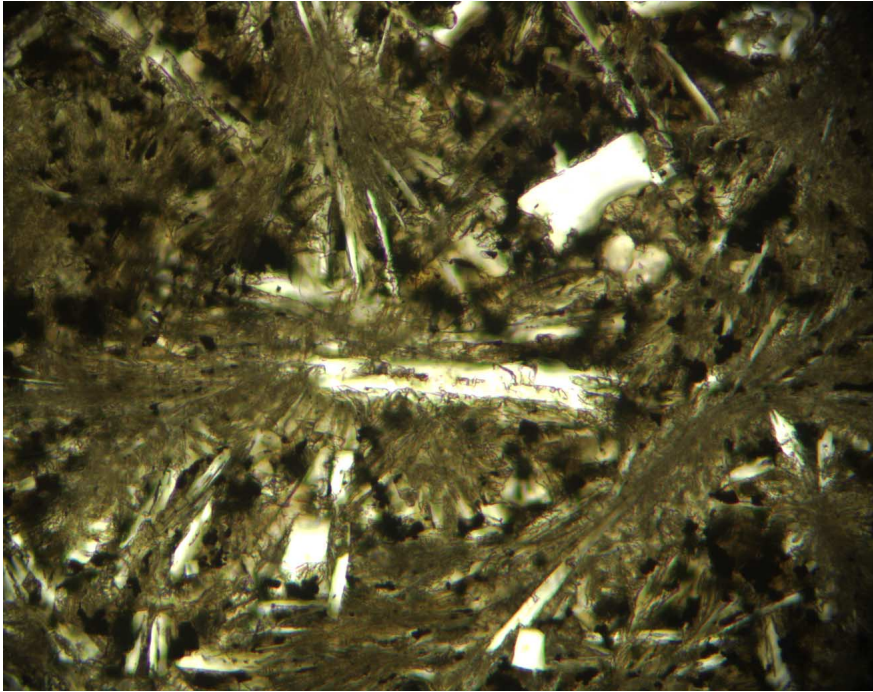


Figure F31. Abundance and size of groundmass phases with depth (from thin-section data in Table T6, p. 196).

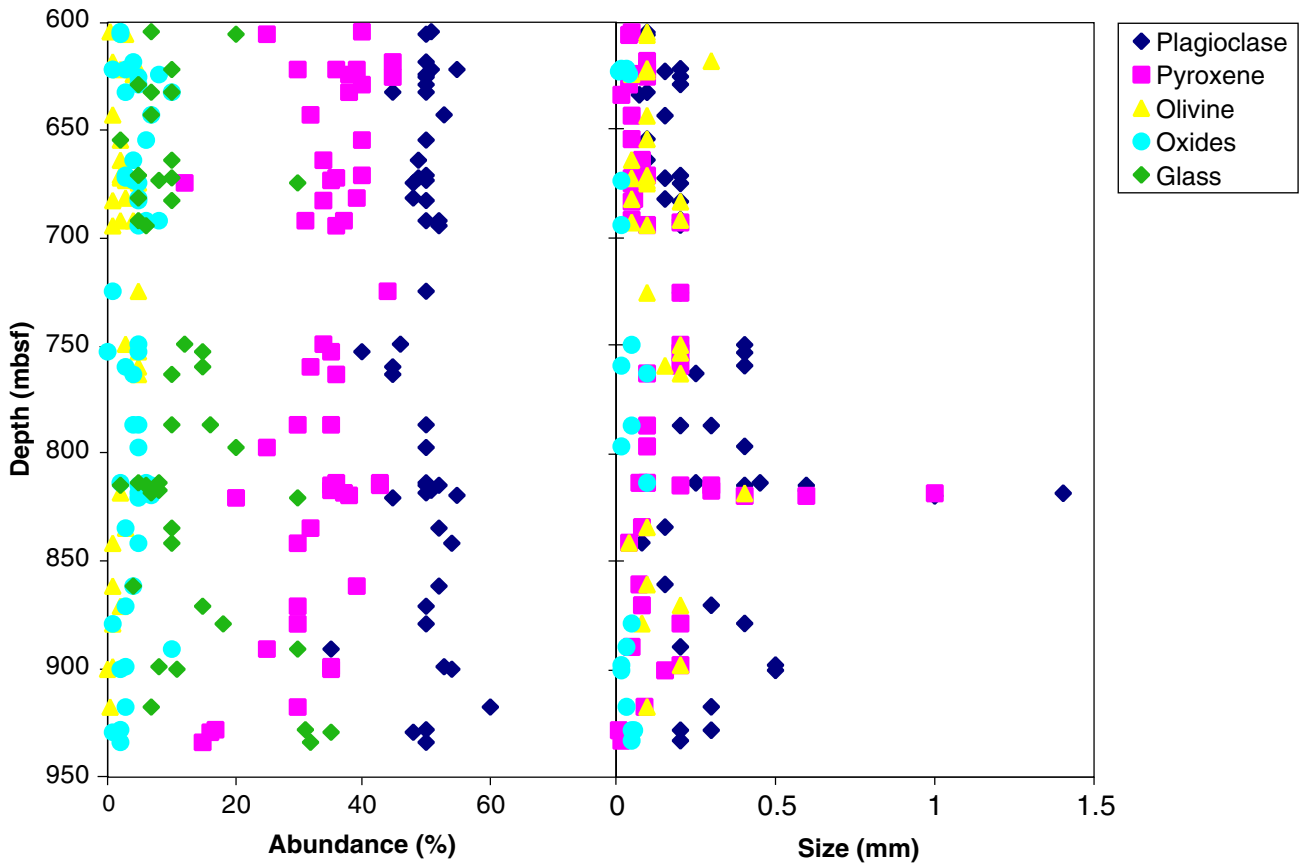


Figure F32. Phenocryst abundance and size with depth (from thin-section data in Table T6, p. 196).

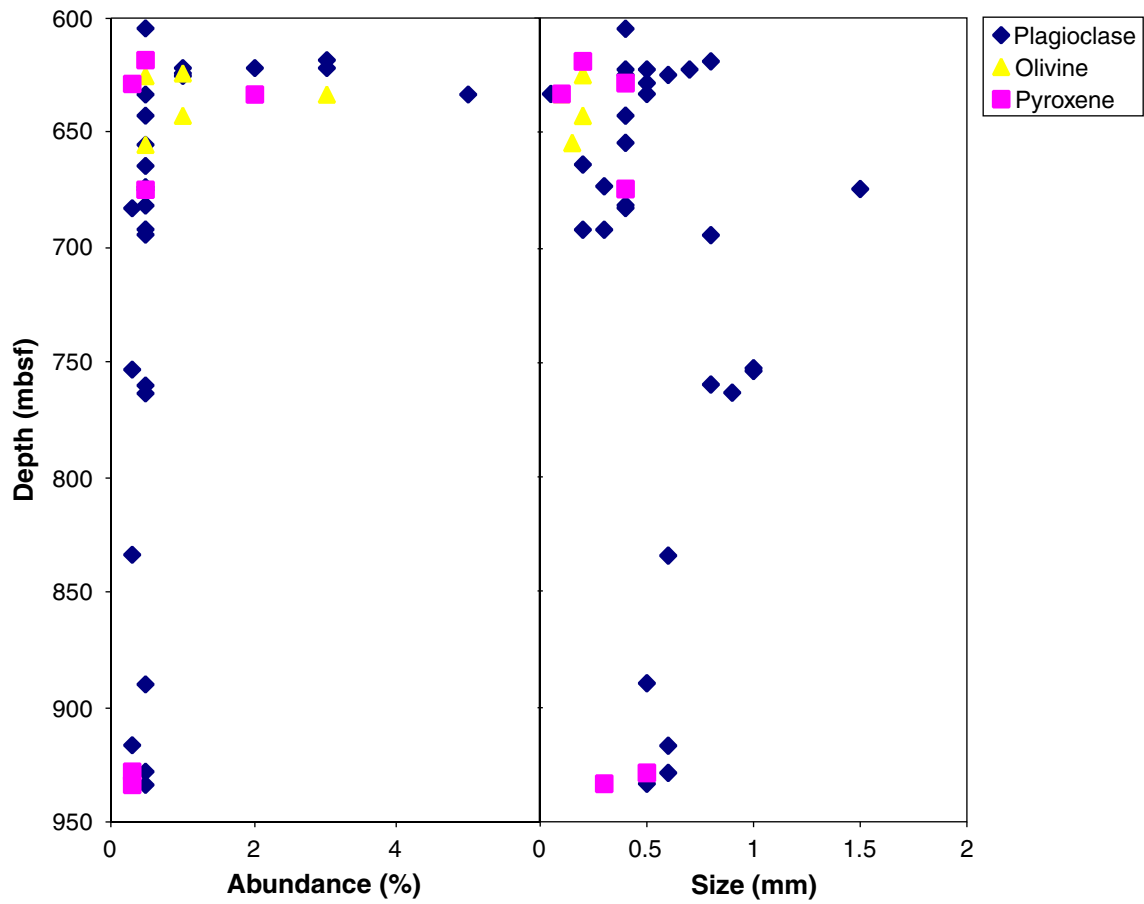


Figure F33. Twinned euhedral plagioclase phenocryst in crystalline basalt of Sample 185-801C-17R-1 (Piece 7A, 66–67 cm); crossed polars; magnification = 200×; field of view = 0.5 mm.

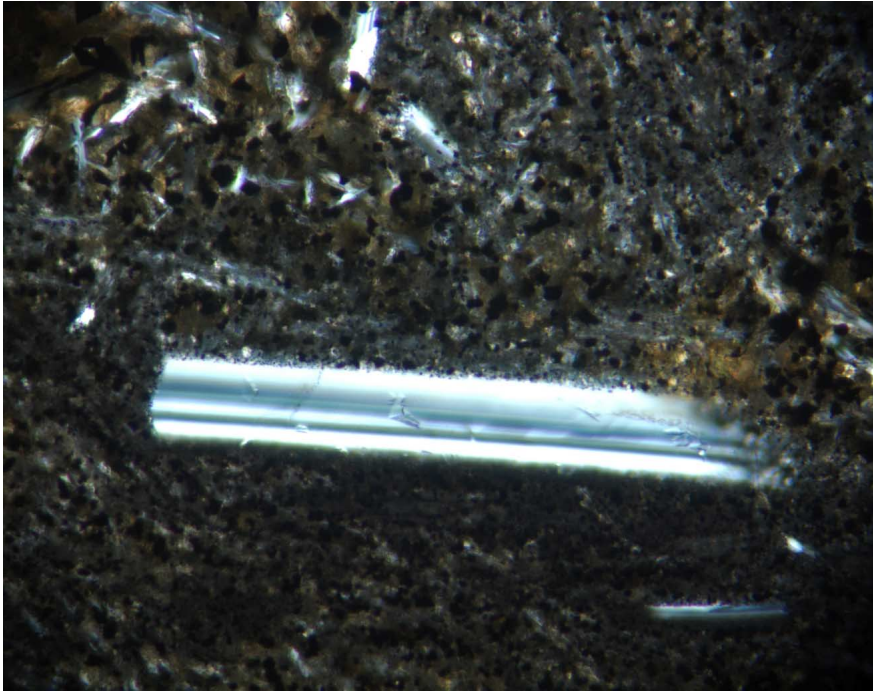


Figure F34. Histogram showing the abundance of plagioclase phenocrysts in crystalline and chilled basalts. Phenocrysts are absent in most thin sections.

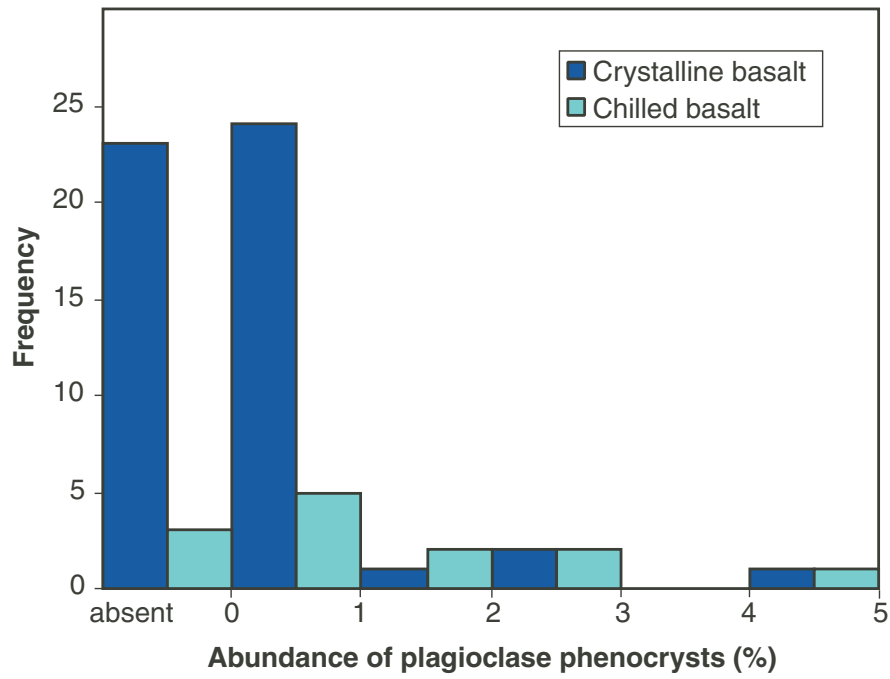


Figure F35. Altered euhedral olivine phenocryst. The olivine contains an unidentified inclusion. Sample 185-801C-15R-7 (Piece 1F, 106–108 cm); crossed polars; magnification = 200×; field of view = 0.5 mm.

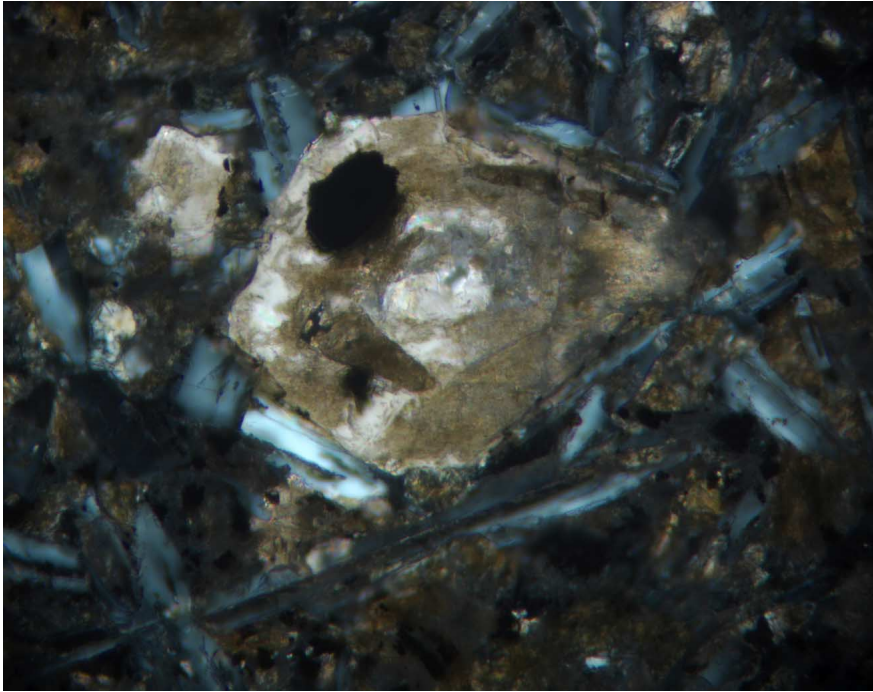


Figure F36. Fresh euhedral olivine phenocryst. The inner, darker part of the olivine is occupied by a fluid inclusion; the bubble is visible on the right of the center of the olivine. Sample 185-801C-42R-2 (Piece 11, 126–128 cm); plane-polarized light; magnification = 500×; field of view = 0.2 mm.

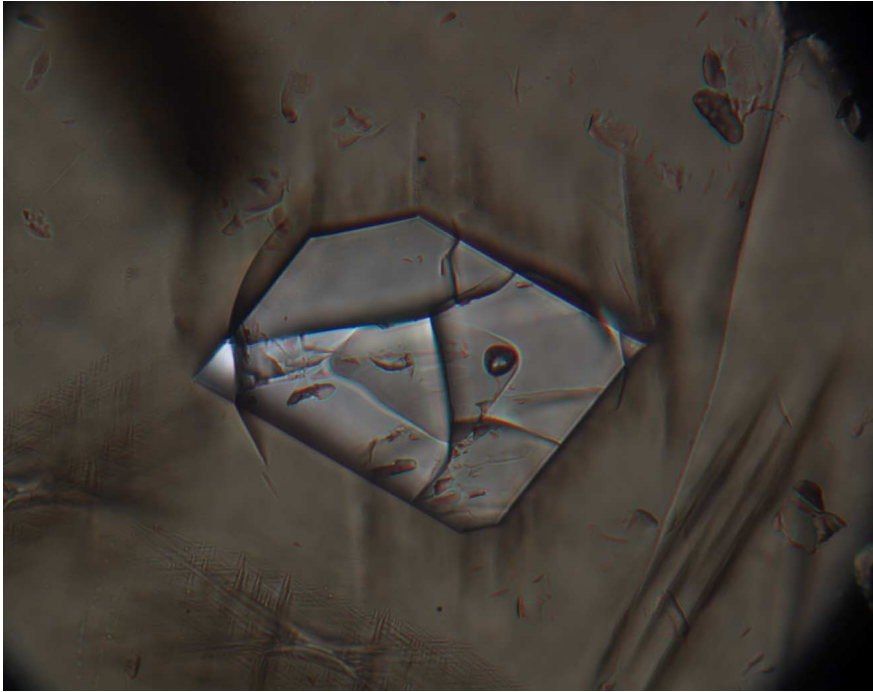


Figure F37. MgO, Cr, Zr, and Zr/Y plotted vs. depth at Site 801. Red (open) circles = data from Castillo et al. (1992); blue (solid) circles = the least-altered subset of shipboard XRF analyses from Leg 185; open diamonds = samples with >1 wt% K₂O and/or >2% LOI. Horizontal orange bands (shaded) represent the locations of upper and lower hydrothermal deposits. Horizontal lines and numbers on Zr plot illustrate geochemical units. Shaded arrows emphasize general geochemical trends in basement.

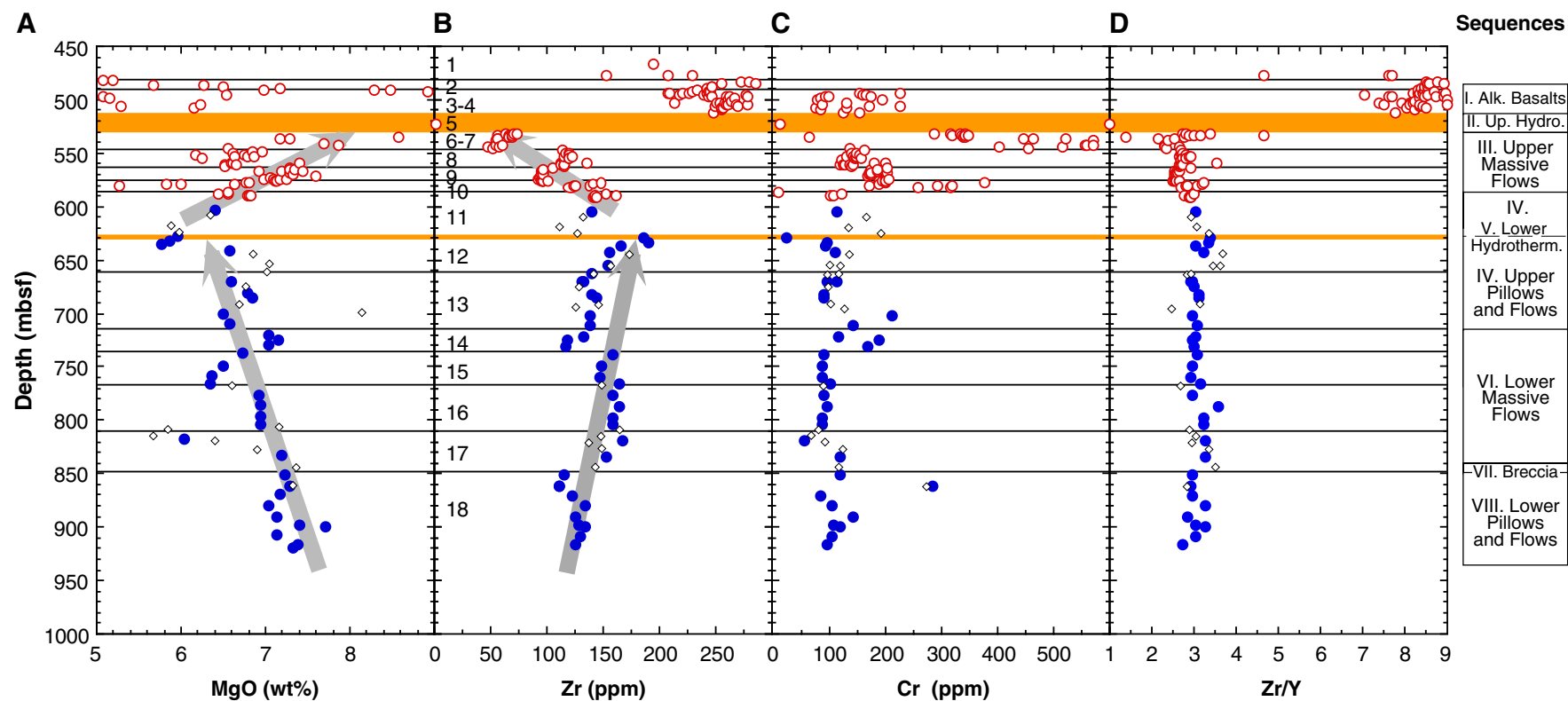


Figure F38. MgO vs. Al₂O₃ for Leg 185 least-altered basalts (solid [blue] circles, Fig. F37, p. 107). A calculated liquid line of descent (Weaver and Langmuir, 1990) from 1175° to 1130°C appears in black (thick line). Mixing lines toward An₇₅ plagioclase and Fo₇₅ olivine are shown in gray dashed and green thin solid lines, respectively. Large solid (red) circles are shipboard XRF analyses from Leg 185, open triangles are Leg 185 samples that require a mixture of >1% phenocrysts with the liquid; small solid (black) circles are samples from Core 185-801C-48R. The gray field represents the data range of glasses from the superfast spreading segment of the modern EPR (15°–18.72°S) (Sinton, 1991).

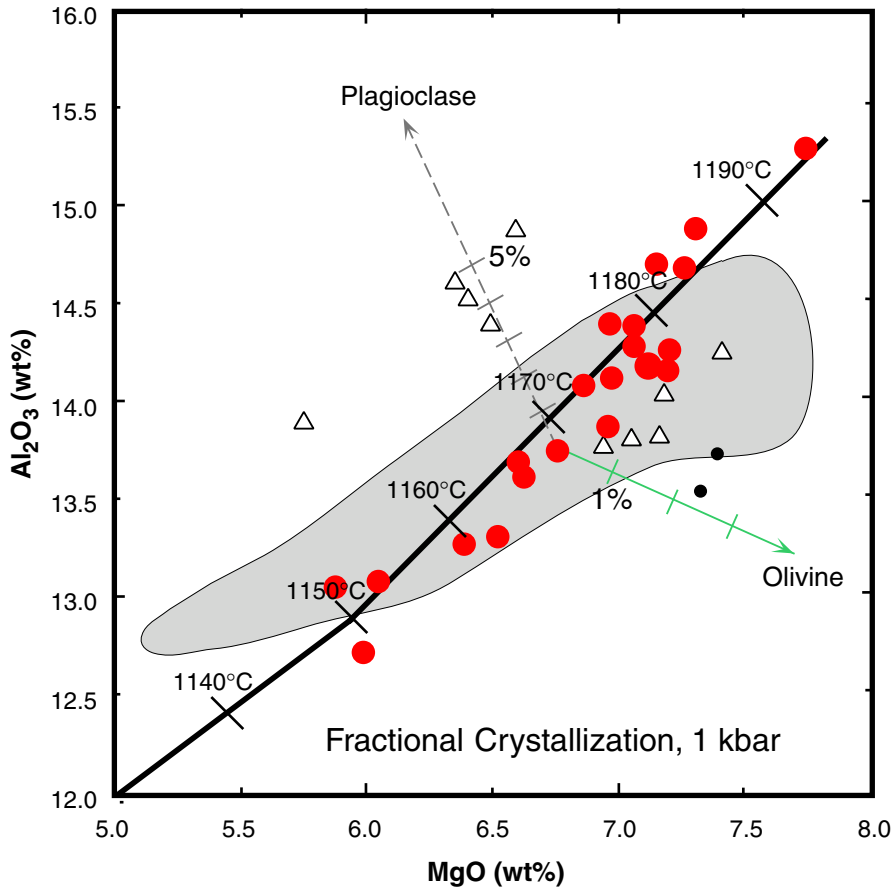


Figure F39. Zr vs. Y for Leg 185 least-altered basalts (solid [blue] circles, Figs. F37, p. 107, F38, p. 108). Solid (green) circles are shipboard XRF analyses from Leg 185, open (blue) circles are data from the modern East Pacific Rise (EPR) (8°–15°N) (Langmuir, 1987), open diamonds are data from the modern Mid-Atlantic Ridge (MAR) (between the Kane and Hayes fracture zones) (Langmuir et al., 1986). Black line corresponds to $Zr/Y = 3$.

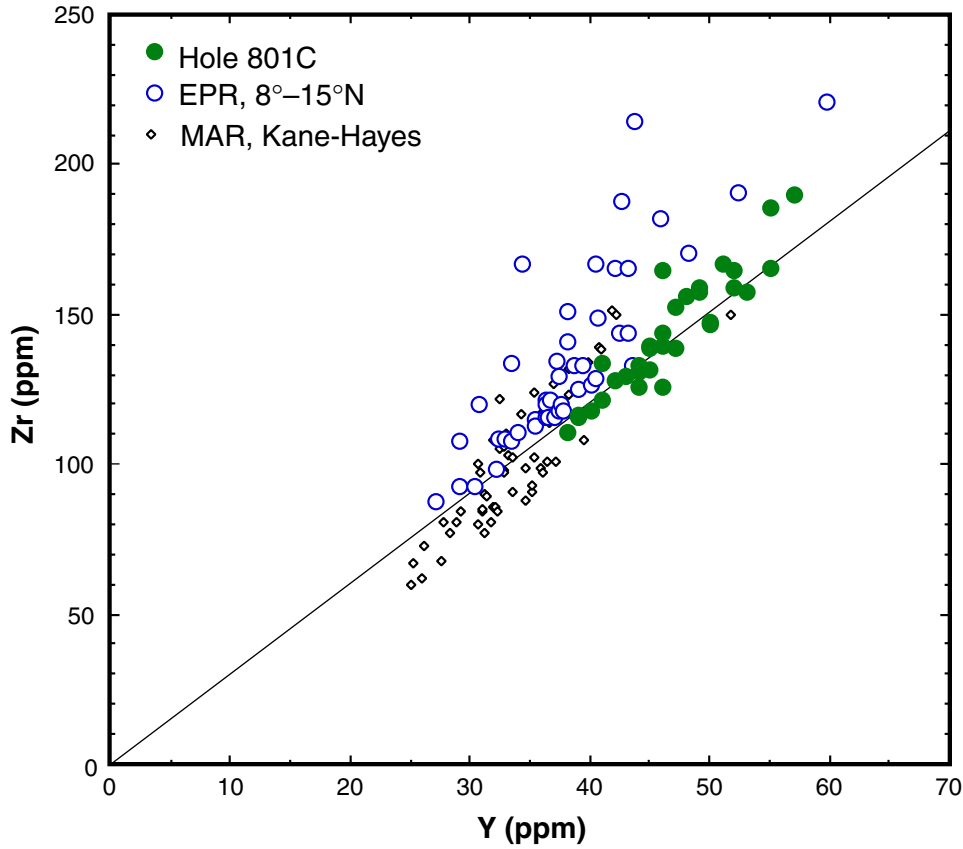


Figure F40. Abundance and distribution of veins, breccias, and interpillow material, Leg 185 Hole 801C. Numbers with arrows = off-scale values.

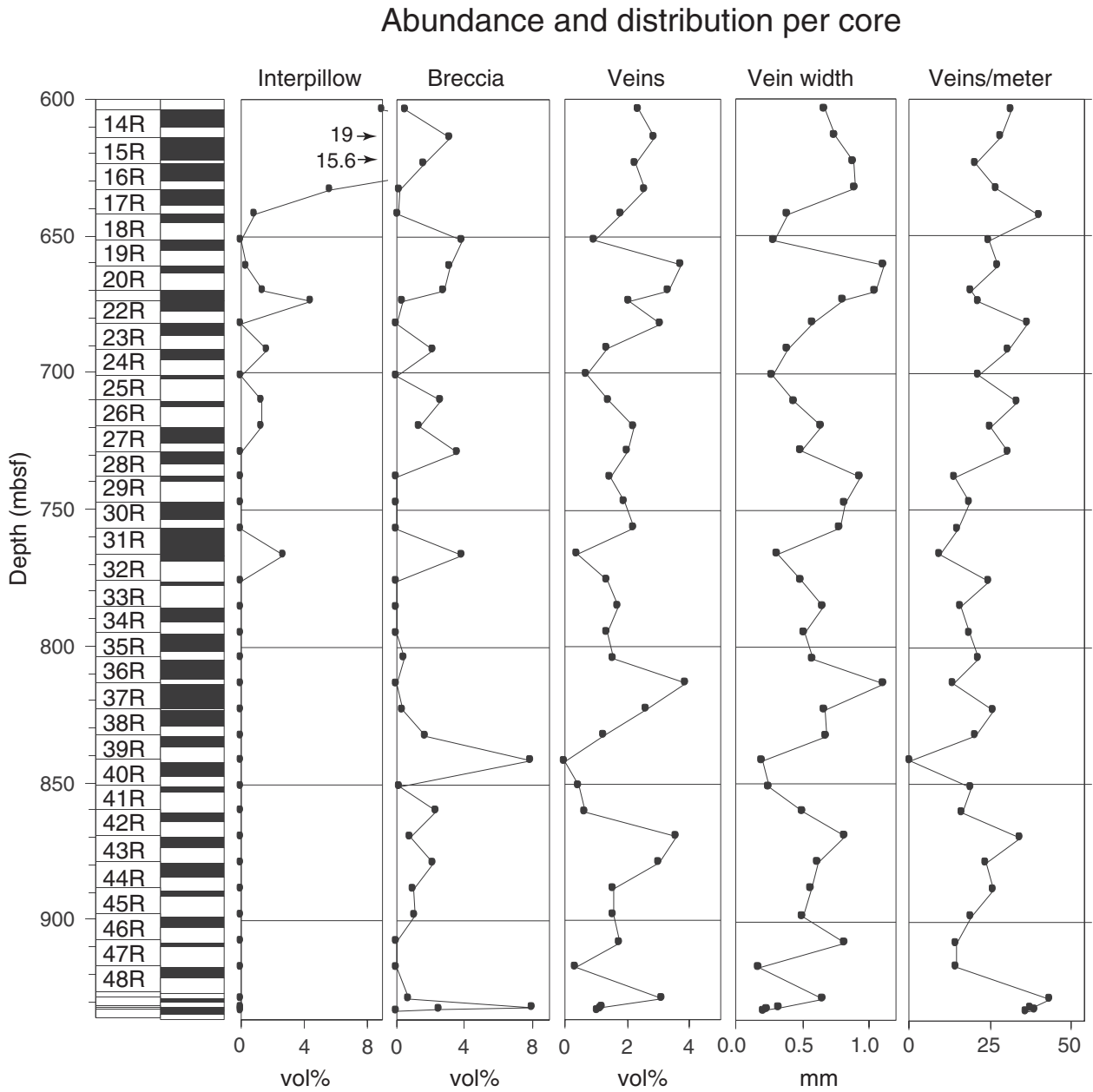


Figure F41. Volume percent of saponite, celadonite, carbonate, SiO₂, Fe oxyhydroxide, and pyrite in veins, breccias, and interpillow materials for each core. Breccias and interpillow components are calculated on the basis of estimated composition for each cored interval, Leg 185 Hole 801C. Numbers followed by arrows = off-scale values.

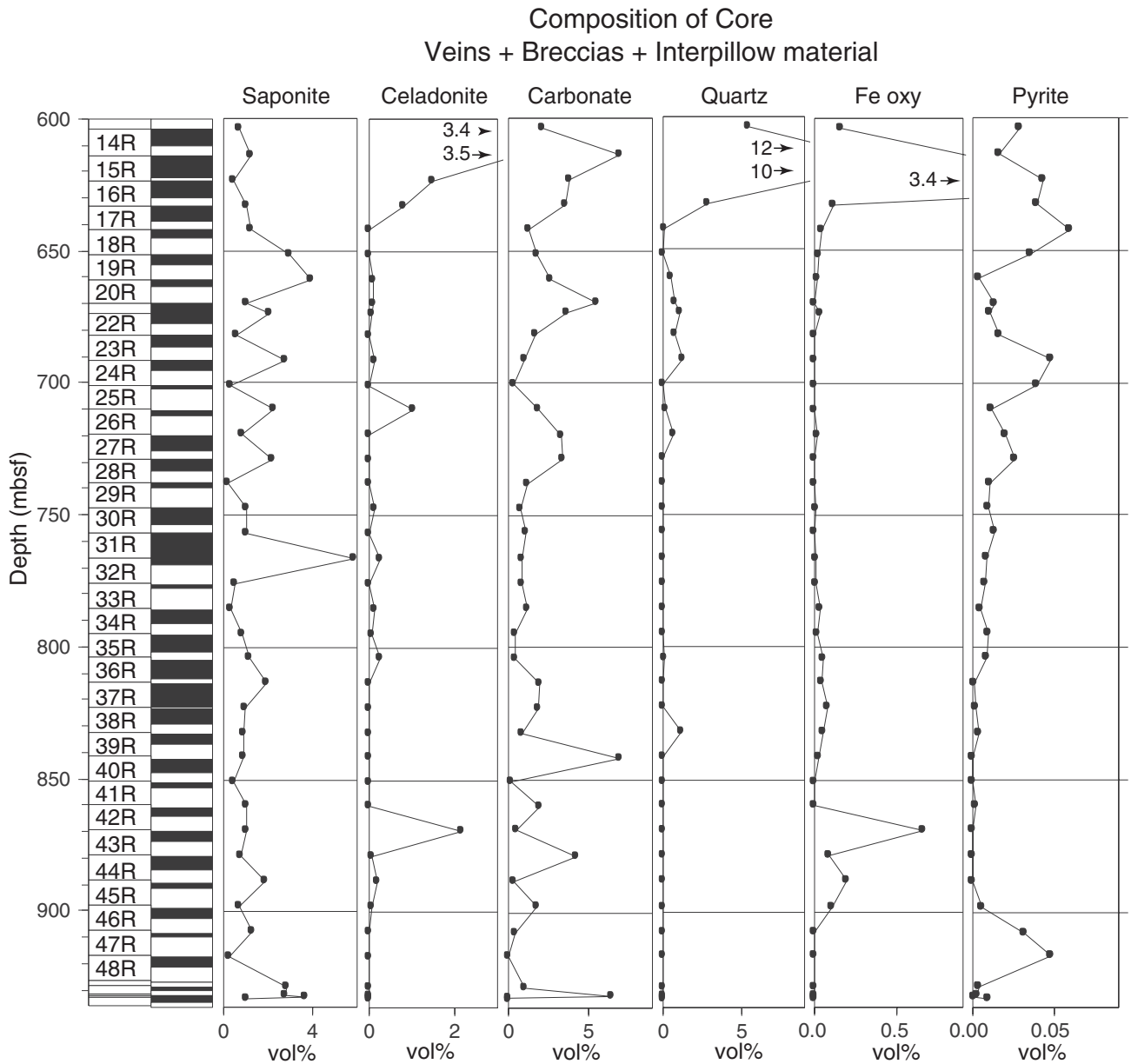


Figure F42. Proportions of saponite, celadonite, carbonate, SiO₂, Fe oxyhydroxide, and pyrite in veins for each core, Leg 185 Hole 801C, with proportions of different vein types totaling 100% for each core. Percentages are calculated from modal composition, length, and width of each vein. Numbers followed by arrows = off-scale values.

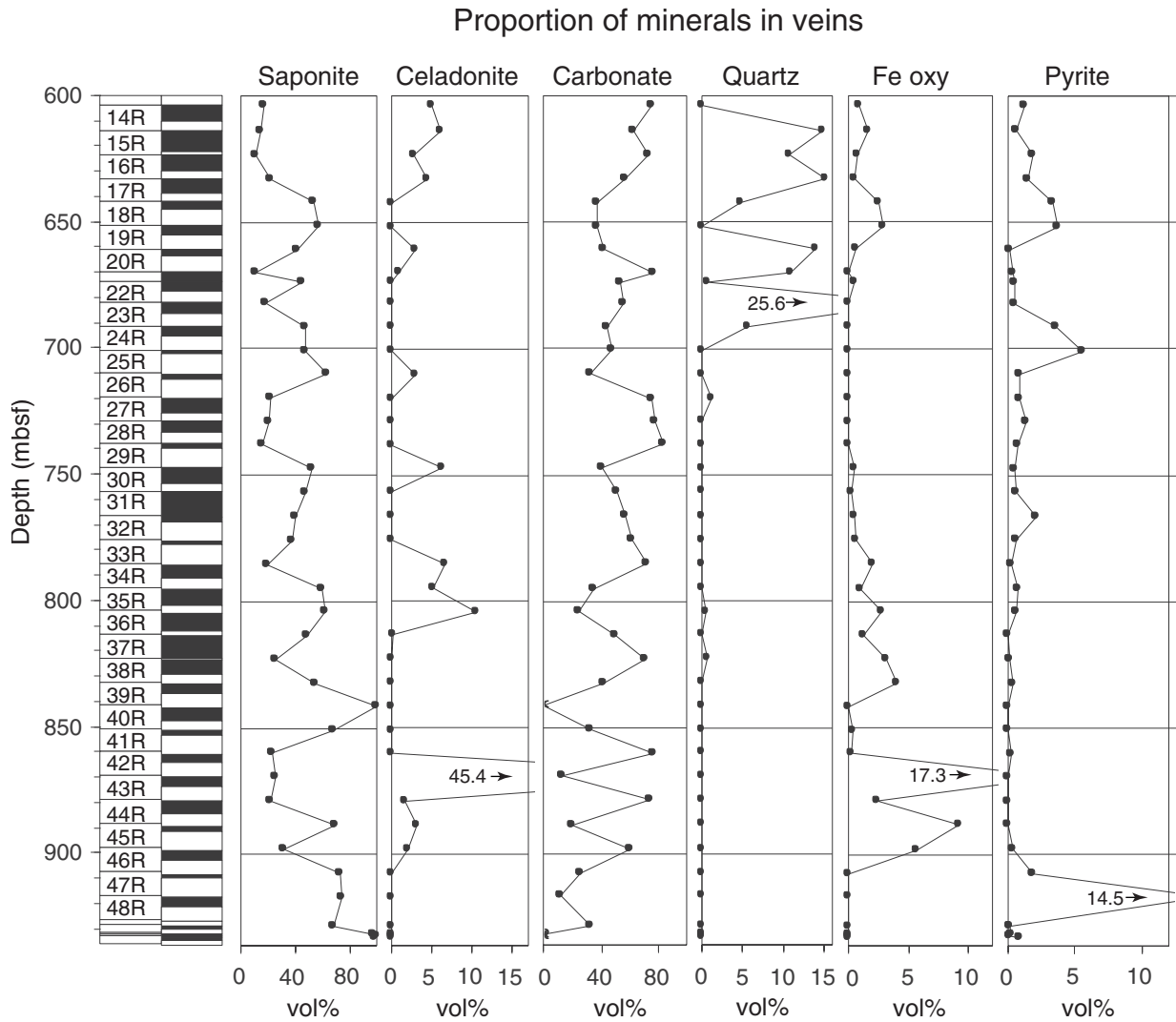


Figure F43. Illustrations of veins with alteration halos. **A.** Anastomosing subvertical carbonate veins in vesicular basalt. Centimeter-sized dark alteration halos occur along much of the large vein at center. Vesicles are filled with dark clay in the alteration halo and by calcite in the host rock (interval 185-801C-37R-2, 68–105 cm). **B.** Dark alteration halos along smectite and celadonite veins (interval 185-801C-43R-2, 115–135 cm). A 4-mm-wide celadonite vein (gray) cuts the sample diagonally from 127 to 130 cm. **C.** Subvertical mixed vein filled with calcite (white) at top left, celadonite (black) at center (75–83 cm), and a mixture of calcite and iron oxyhydroxide at bottom right (83–95 cm) (interval 185-801C-34R-3, 73–95 cm). The quality of the image reflects the AMST source.

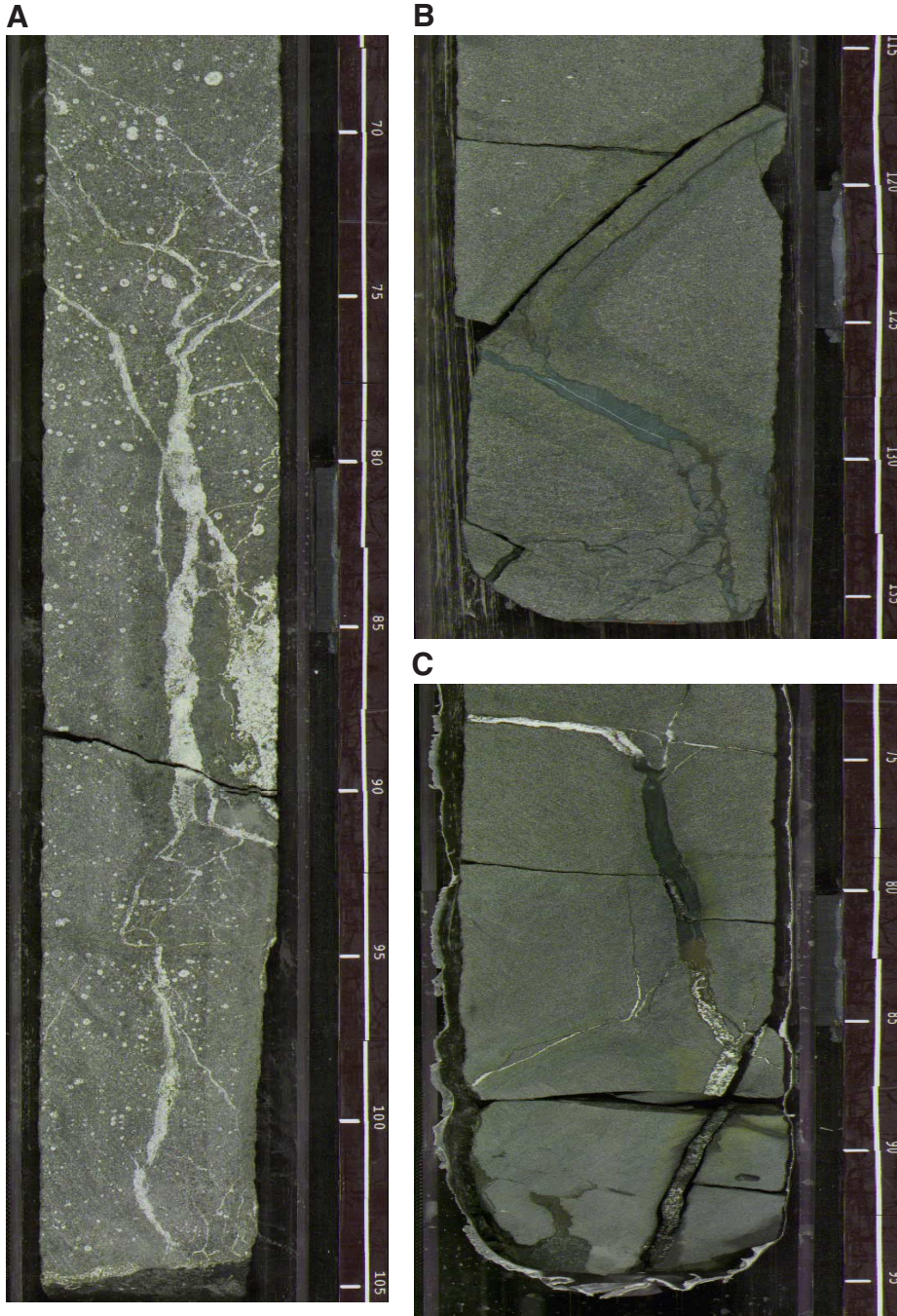
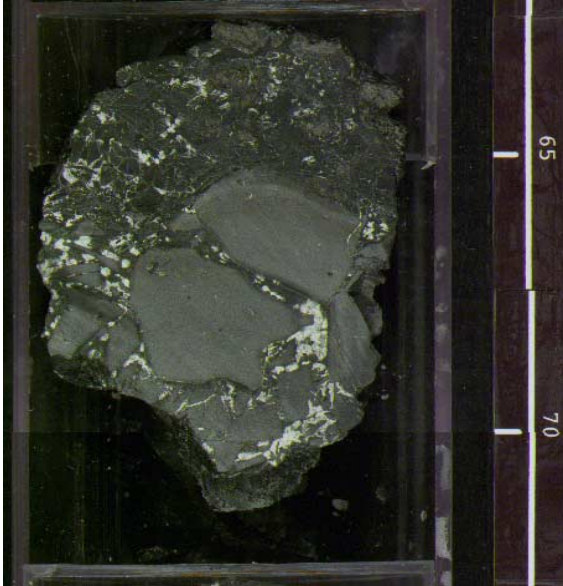
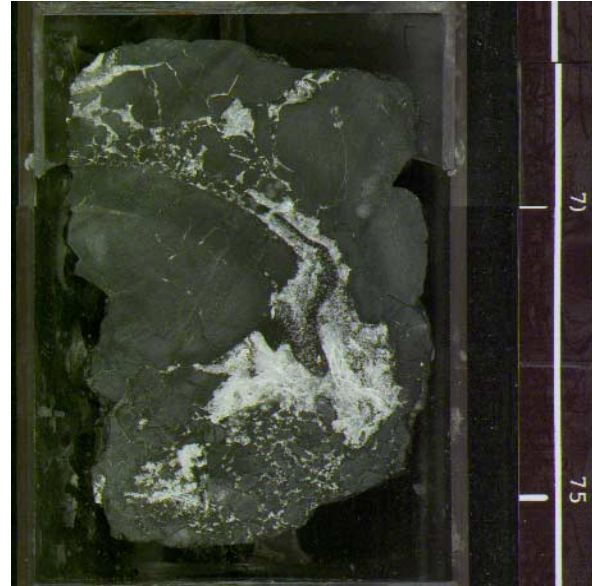


Figure F44. Photographs illustrating types of hyaloclastite and breccia from Hole 801C. A. Brecciated chilled pillow margin with hyaloclastite containing fresh glass and cemented by saponite (black) and calcite (white) (interval 185-801C-40R-2, 63–71 cm). B. Brecciated pillow rim veined and cemented by calcite (interval 185-801C-34R-2, 70–76 cm). C. Angular basalt breccia cemented by quartz and celadonite (interval 185-801C-36R-3, 85–98 cm). The quality of the image reflects the AMST source.

A



B



C



Figure F45. Sketch and photograph of a hand specimen from interval 185-801C-44R-3, 3–11 cm. The medium-grained diabase is cut by several generations of veins predominantly composed of saponite and carbonate. Alteration halos have developed around the earliest veins (A–D) that are filled with mostly saponite. No alteration halos formed around later irregular veins composed typically of carbonate. Crosscutting relationships constrain the following vein chronology: (1) Veins A, B, C, and D, originally thin and filled with saponite. Thin dark green alteration halos could be associated with these veins. (2) Carbonate veins E, F, and G, filling open fractures. No alteration halos formed along these veins. (3) Reactivation of the earliest veins with possible rotation or translation of blocks (A, B, and C). Reopening and carbonate filling is recorded in vein A and to a lesser degree in vein D. Overprinting of large, mixed brown and dark halos is observed. The quality of the image reflects the AMST source.

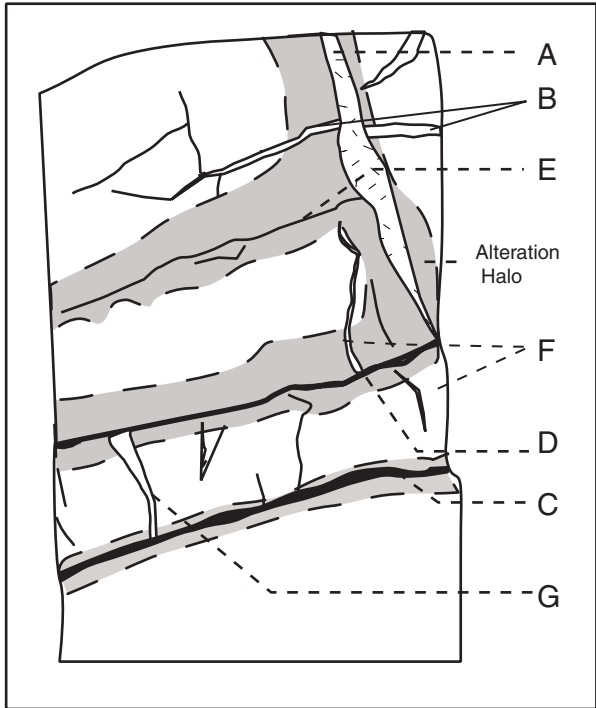


Figure F46. Mineral composition of interpillow material for each core.

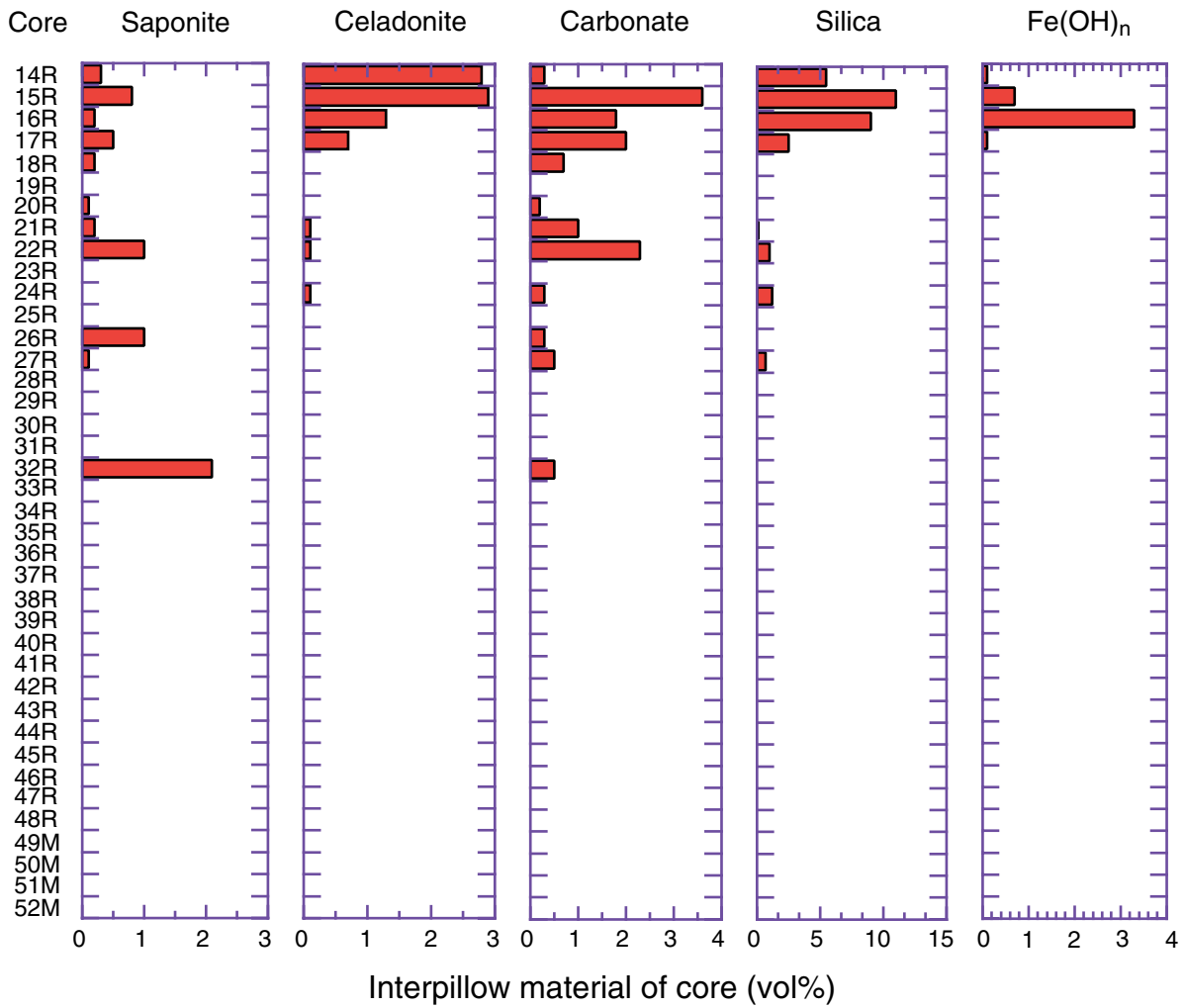


Figure F47. Photomicrographs of recrystallized and possibly hydrothermally altered interpillow sediment in thin section. **A.** Sample 185-801C-14R-2, 117–120 cm (plane-polarized light), showing a radiolarian replaced by calcite in a matrix of calcite and smectite. **B.** Sample 185-801C-5R-1, 7–8 cm (cross-polarized light), illustrating concentric zones within a calcite grain in a matrix of chalcedony. **C.** Sample 185-801C-15R-1, 7–8 cm (plane-polarized light), showing discrete celadonite crystals (green) and smectite (brown) in a matrix of calcite and chalcedony. **D.** Image (plane-polarized light) from Sample 185-801C-15R-1, 57–60 cm, displaying a radiolarian pseudomorph with a delicate honeycomb structure in an interpillow chert consisting of microcrystalline silica, chalcedony, and Fe oxyhydroxide. (Continued on next page.)

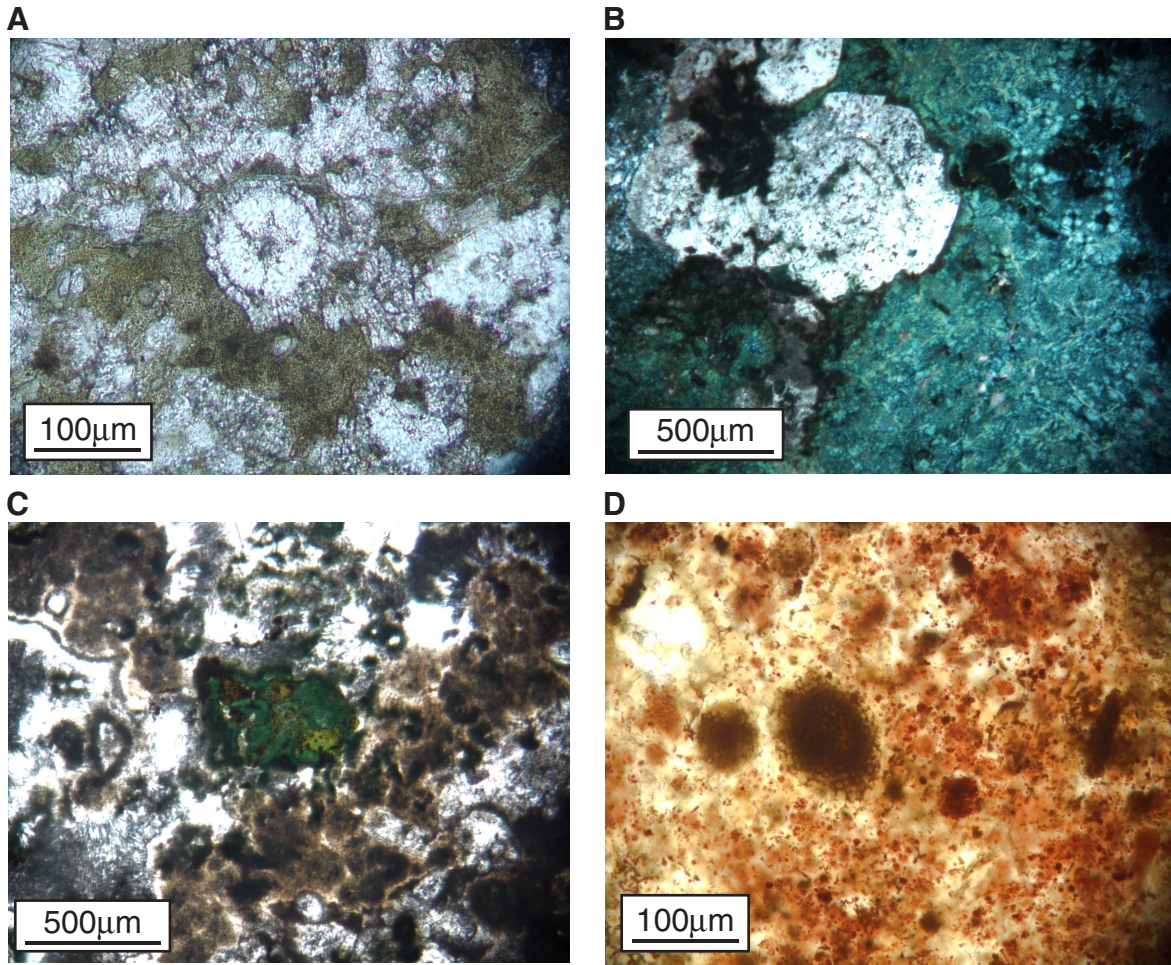
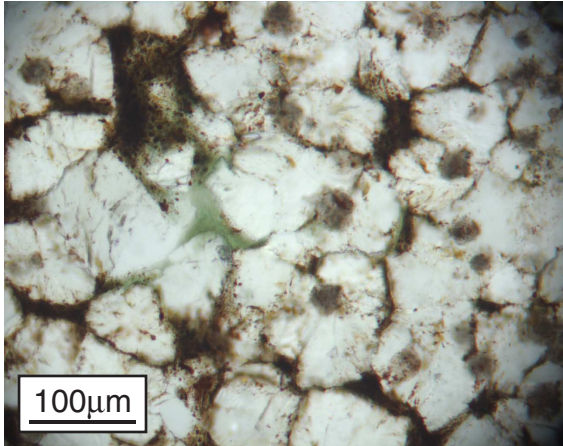
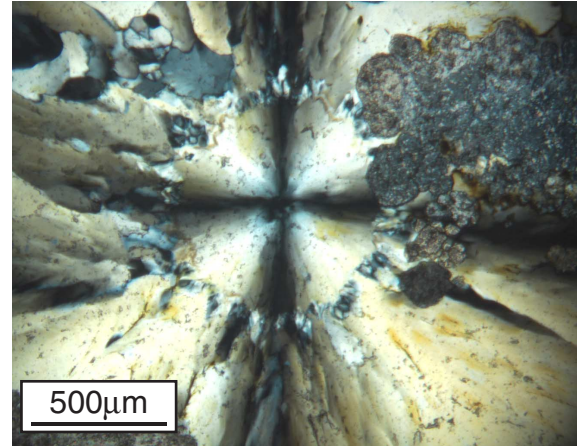


Figure F47 (continued). E. A recrystallized interpillow sediment (plane-polarized light) from Sample 185-801C-16R-3, 47–50 cm, comprised of close-packed spherical calcite in a matrix of Fe oxyhydroxides. These calcite crystals contain small seed opaque crystals. Green pore-filling material is probably celadonite. F. Image (cross-polarized light) from Sample 185-801C-22R-1 (Piece 4A, 44–47 cm) showing radial fibers of chalcedony rimmed with finely crystalline quartz. Mass of fine-grained calcite located in northeast quadrant. G. Sample 185-801C-22R-2 (Piece 1B, 18–21 cm) (plane-polarized light) showing botryoidal Fe oxyhydroxide (orange to brownish green) displaying “growth rings” in a matrix of calcite and minor chalcedony. H. Sample 185-801C-24R-1, 112–114 cm (cross-polarized light), illustrating a calcisphere in a matrix of calcite near a pillow margin.

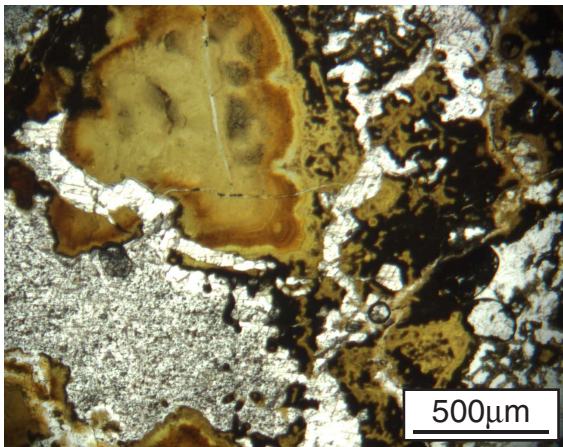
E



F



G



H



Figure F48. Depiction of the two types of interpillow sediment/lava interface. **A.** Interpillow sediment/pillow rim contact (interval 185-801C-14R-3 [Piece 10, 117–126 cm]) displaying a prominent chilled pillow margin. **B.** Flat contact between lava (below) and altered siliceous interpillow sediment (above) (interval 185-801C-17R-3 137–143 cm) suggesting that lava was injected within interpillow sediment horizon. The quality of the image reflects the AMST source.

A



B



Figure F49. Distribution of alteration types observed in Leg 185 Hole 801C. % = vol% of altered basalt.

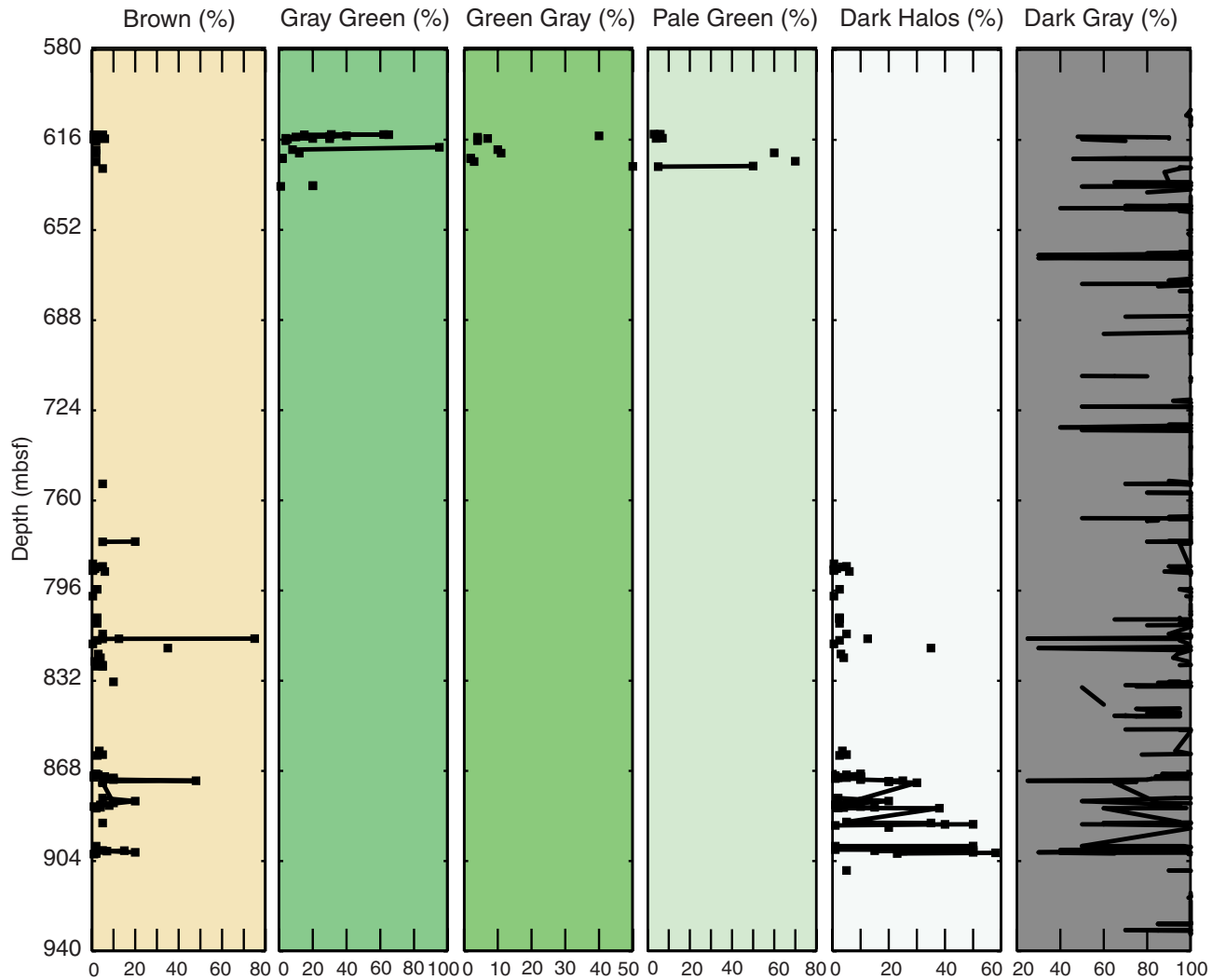


Figure F50. Pale green, green-gray, and gray-green alteration types in Section 185-801C-15R-7 and the gradational nature of the boundaries between these types; histogram showing modal mineralogy; and photomicrographs in plane- (left) and cross-polarized (right) light illustrate the various intensities of alteration.

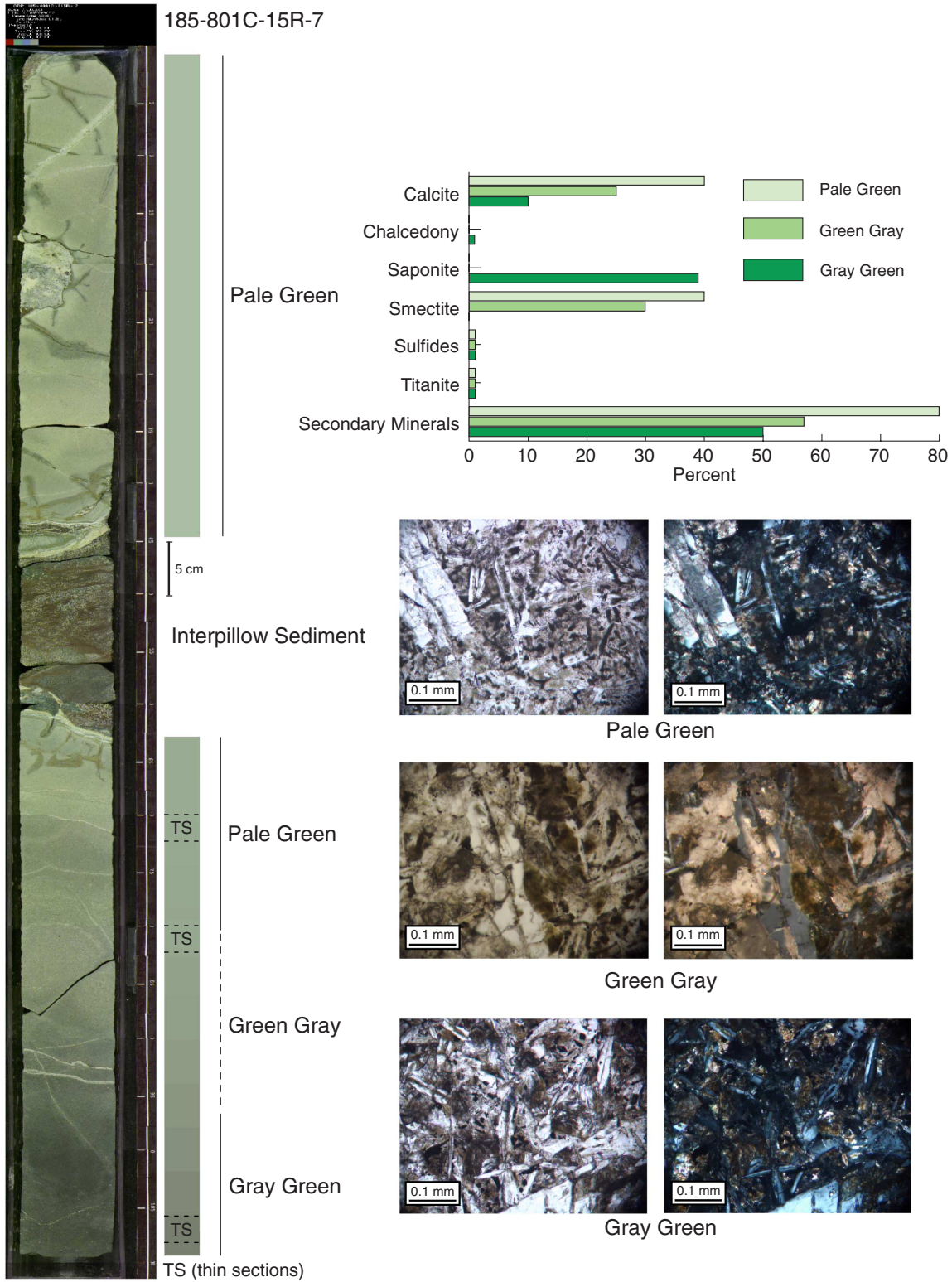


Figure F51. Alteration halos in volume percent per core. Several core numbers are indicated where peaks in halo volumes exist. See "Alteration Halos along Veins," p. 26, for descriptions.

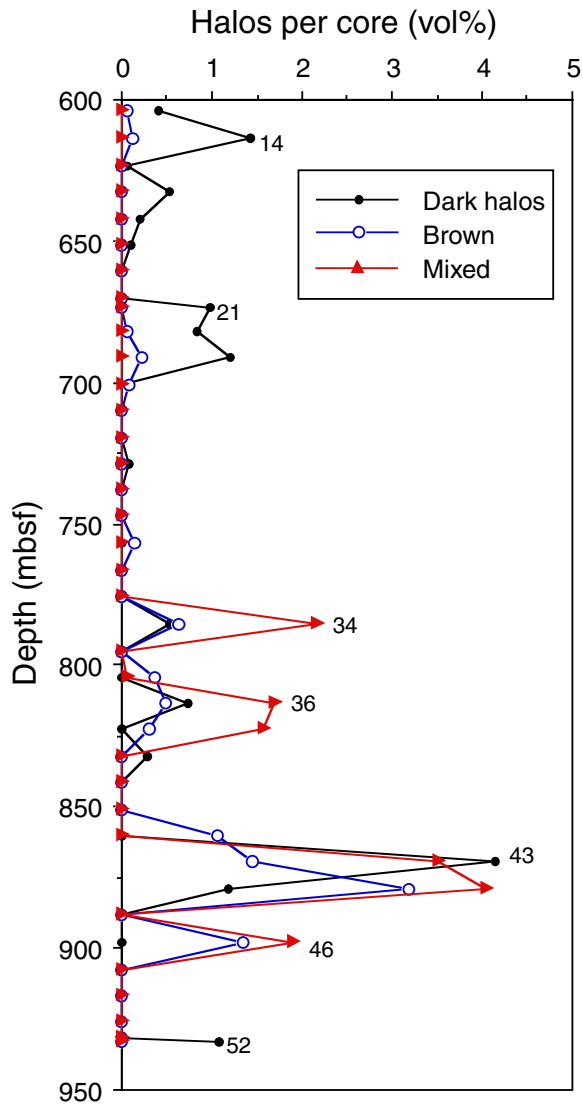


Figure F52. Plots of H₂O, Rb, CO₂, and K₂O vs. depth for Leg 185 Hole 801C. Data are from X-ray fluorescence analyses and Table T9, p. 202. Most basalts chosen for analysis were not highly altered, but were typical of the pervasive dark gray background alteration.

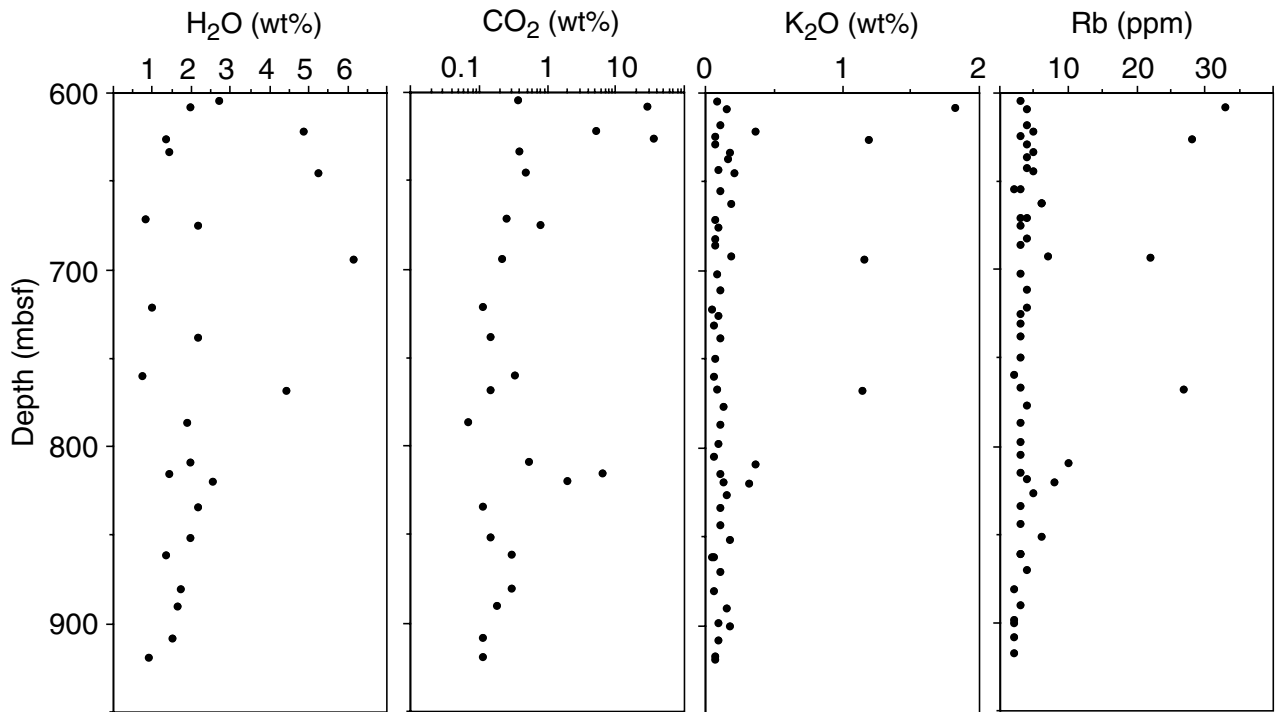


Figure F53. Chemical composition of intensely altered pale green sample (Sample 185-801C-15R-7, 72–74 cm). Sample composition is normalized to constant Ti and Al relative to mean least-altered rock from the same geochemical unit; plotted values are the ratio of the altered sample to the mean least-altered rock.

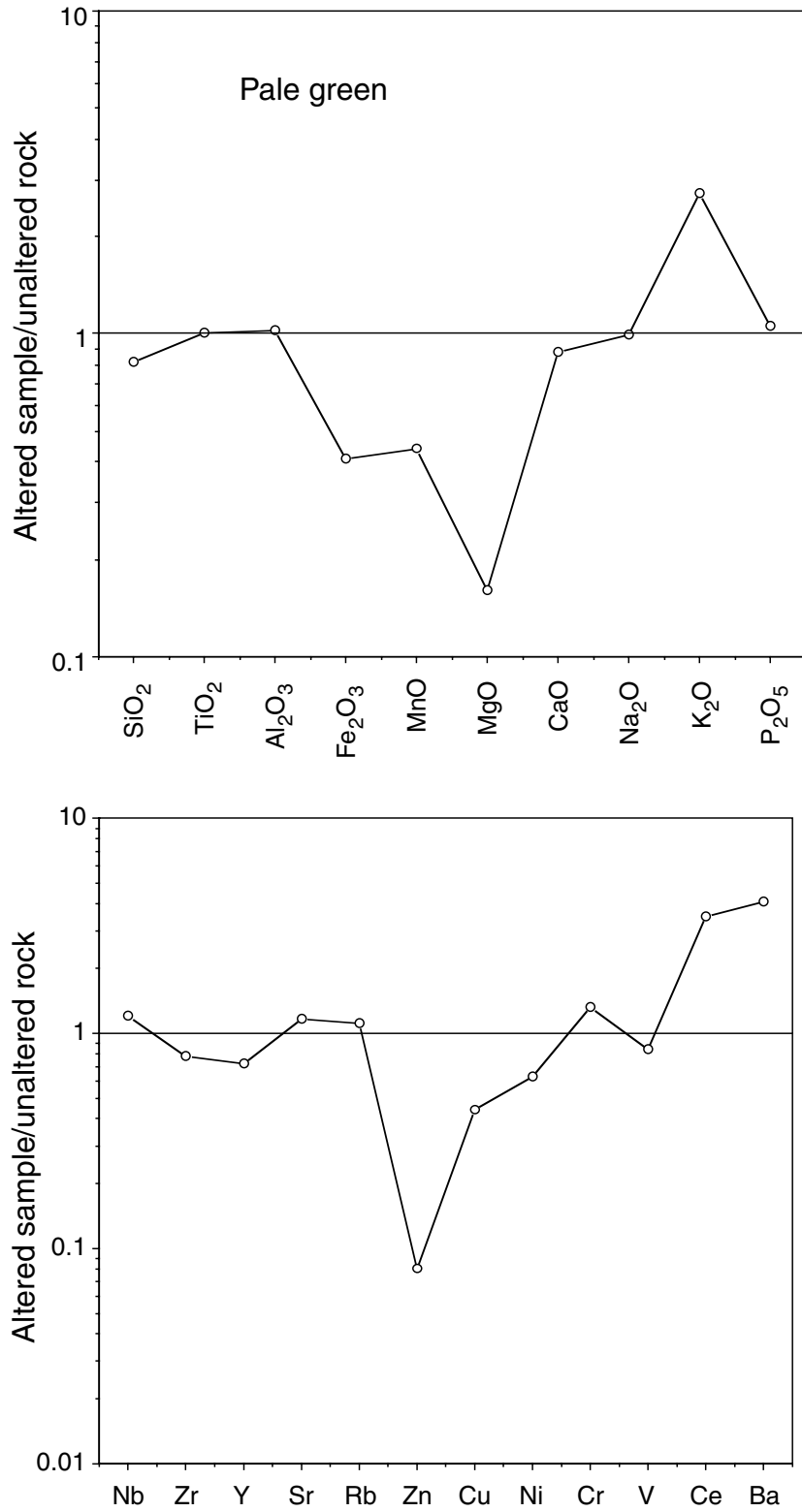


Figure F54. Chemical composition of altered hyaloclastite (Sample 185-801C-24R-2, 108–110 cm). Sample composition is normalized to constant Ti, Al, and Zr relative to mean least-altered rock from the same chemical unit, and plotted values are the ratio of the altered sample to the mean least-altered rock.

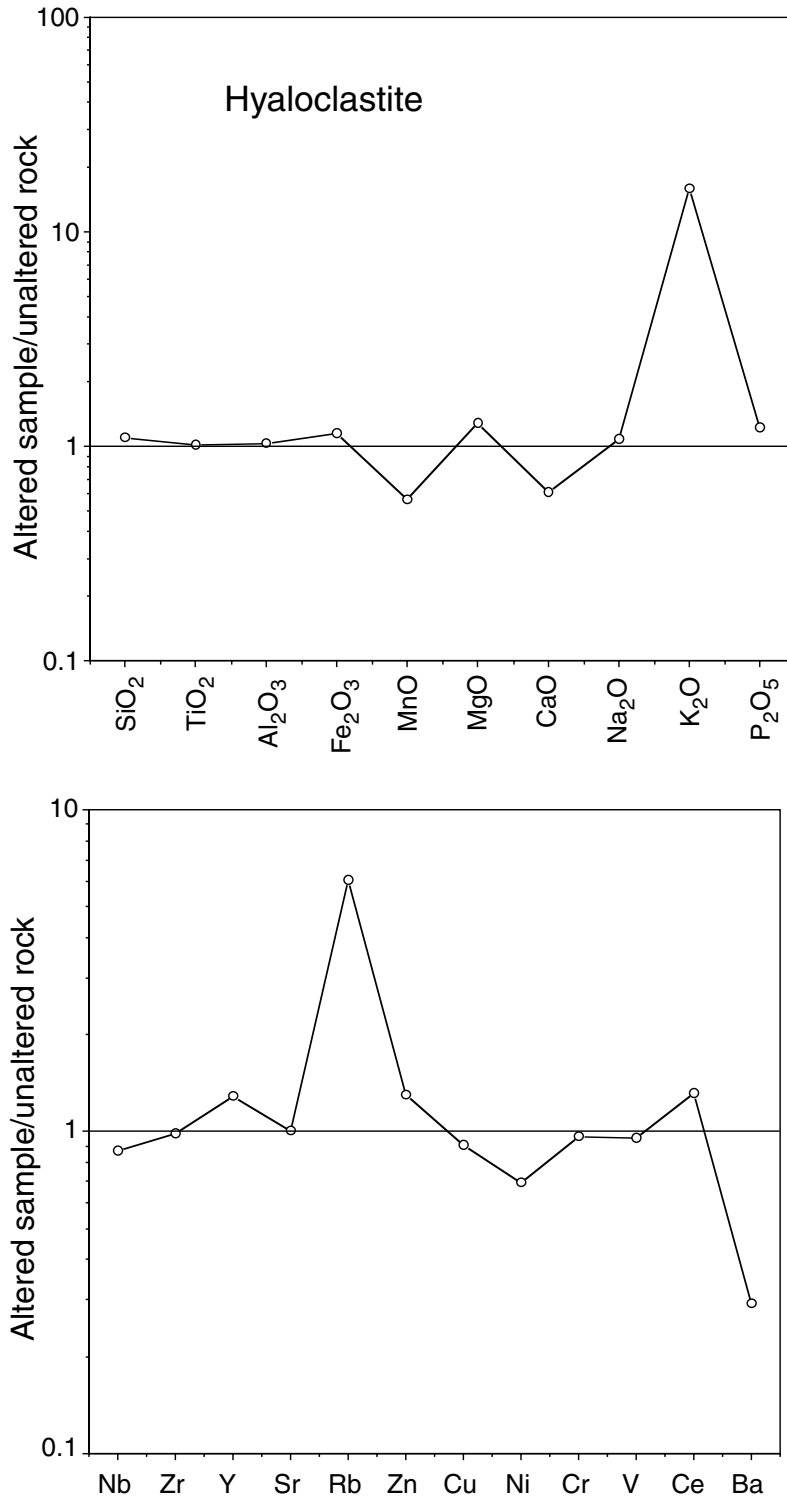


Figure F55. Chemical composition of a mixed brown + dark alteration halo along a vein (Sample 185-801C-36R-4, 112–114 cm). Sample composition is normalized to constant Ti, Al, and Zr relative to mean least-altered rock from the same chemical unit; plotted values are the ratio of the altered sample to the mean least-altered rock.

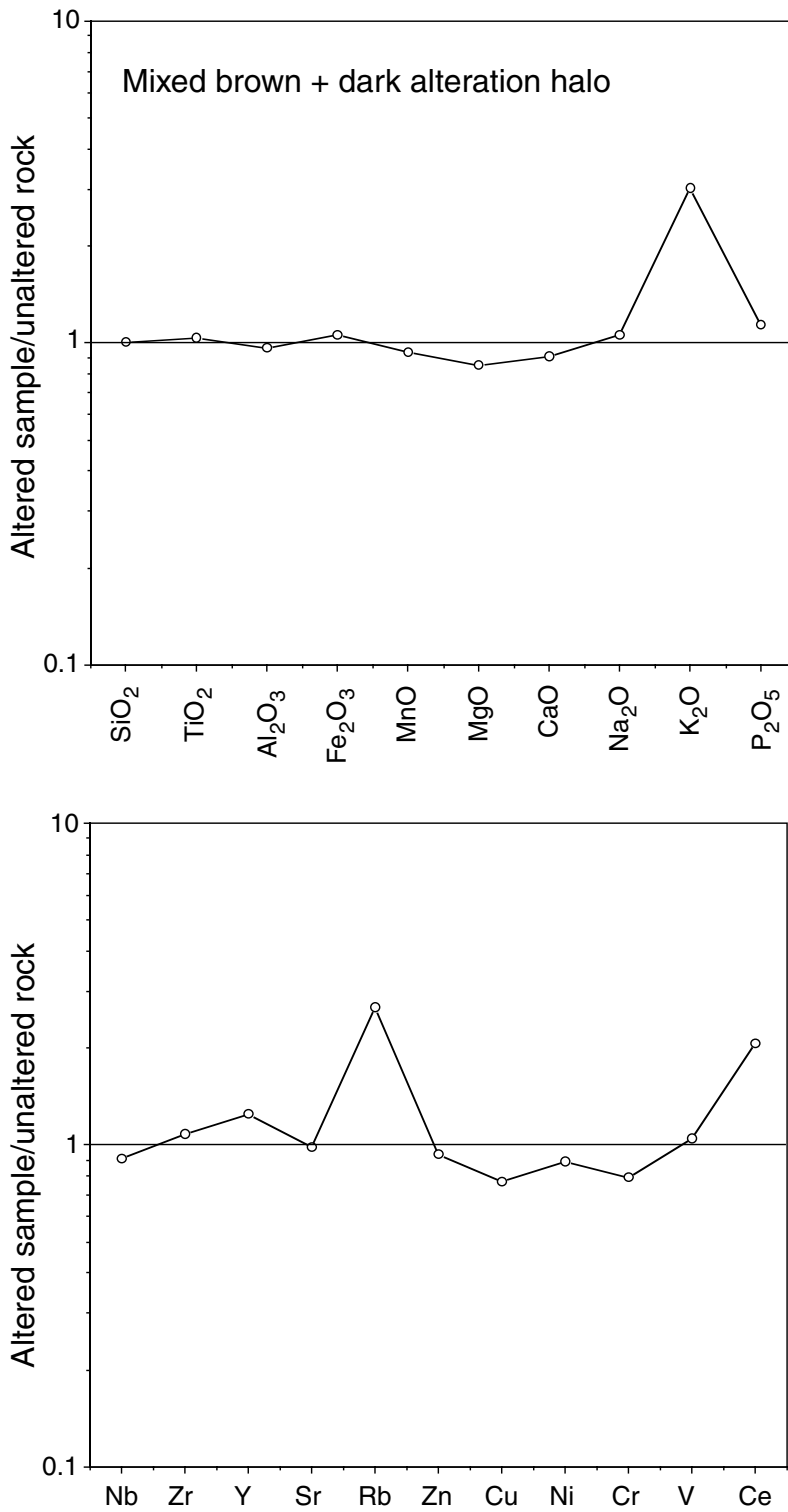


Figure F56. Chemical composition of a mixed brown + dark alteration halo. Sample (185-801C-37R-6, 33–35 cm) composition is normalized to constant Ti, Al, and Zr relative to mean least-altered rock from the same chemical unit. Plotted values are the ratio of the altered sample to the mean least-altered rock from the same chemical unit.

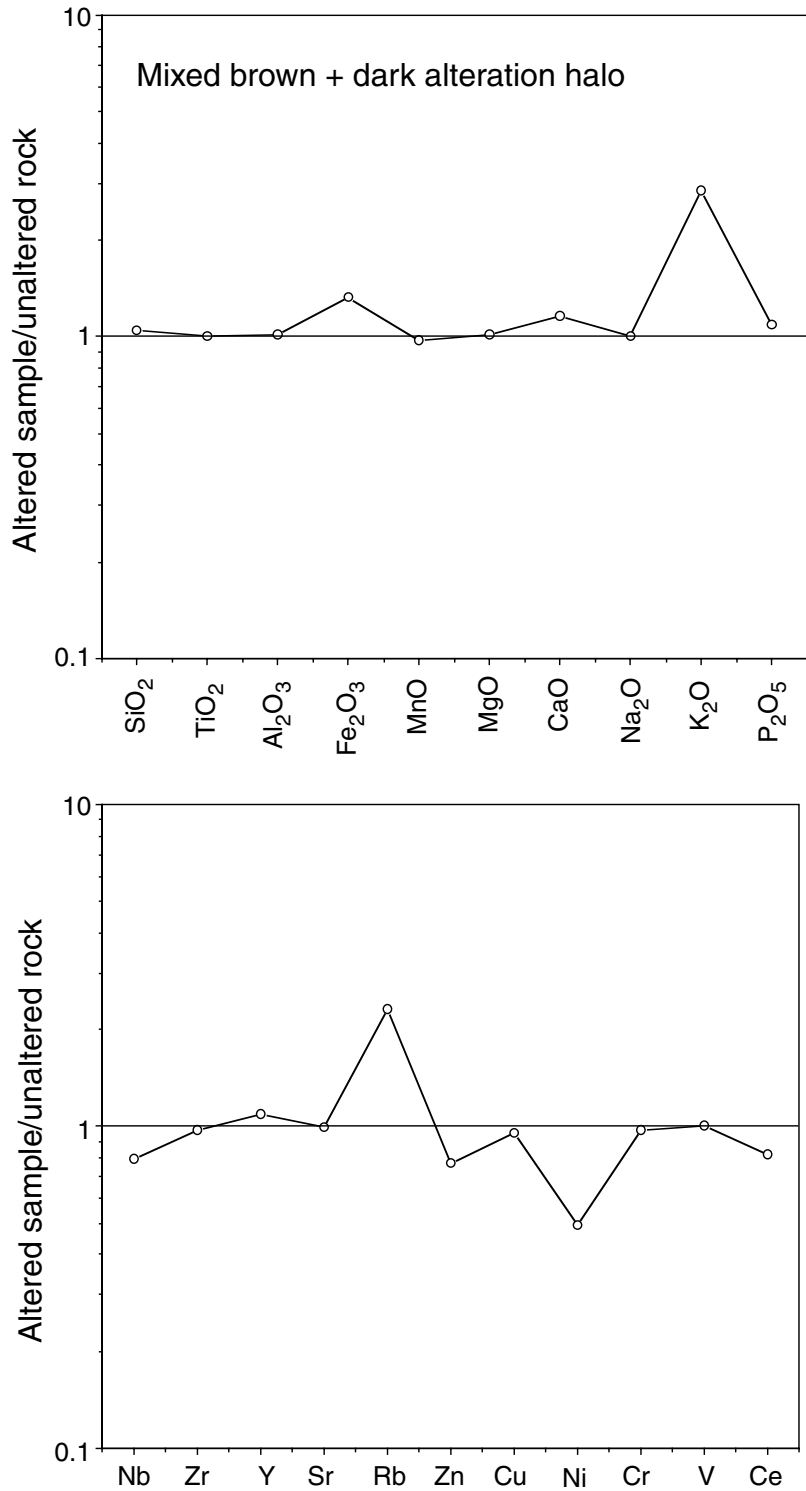


Figure F57. Interpolated curves of shipboard magnetic susceptibility measurements of the basaltic sequence in Hole 801C cored during Leg 185. Whole and half cores were measured with the MST and AMST instruments, respectively (see "Paleomagnetism," p. 27, in the "Explanatory Notes" chapter).

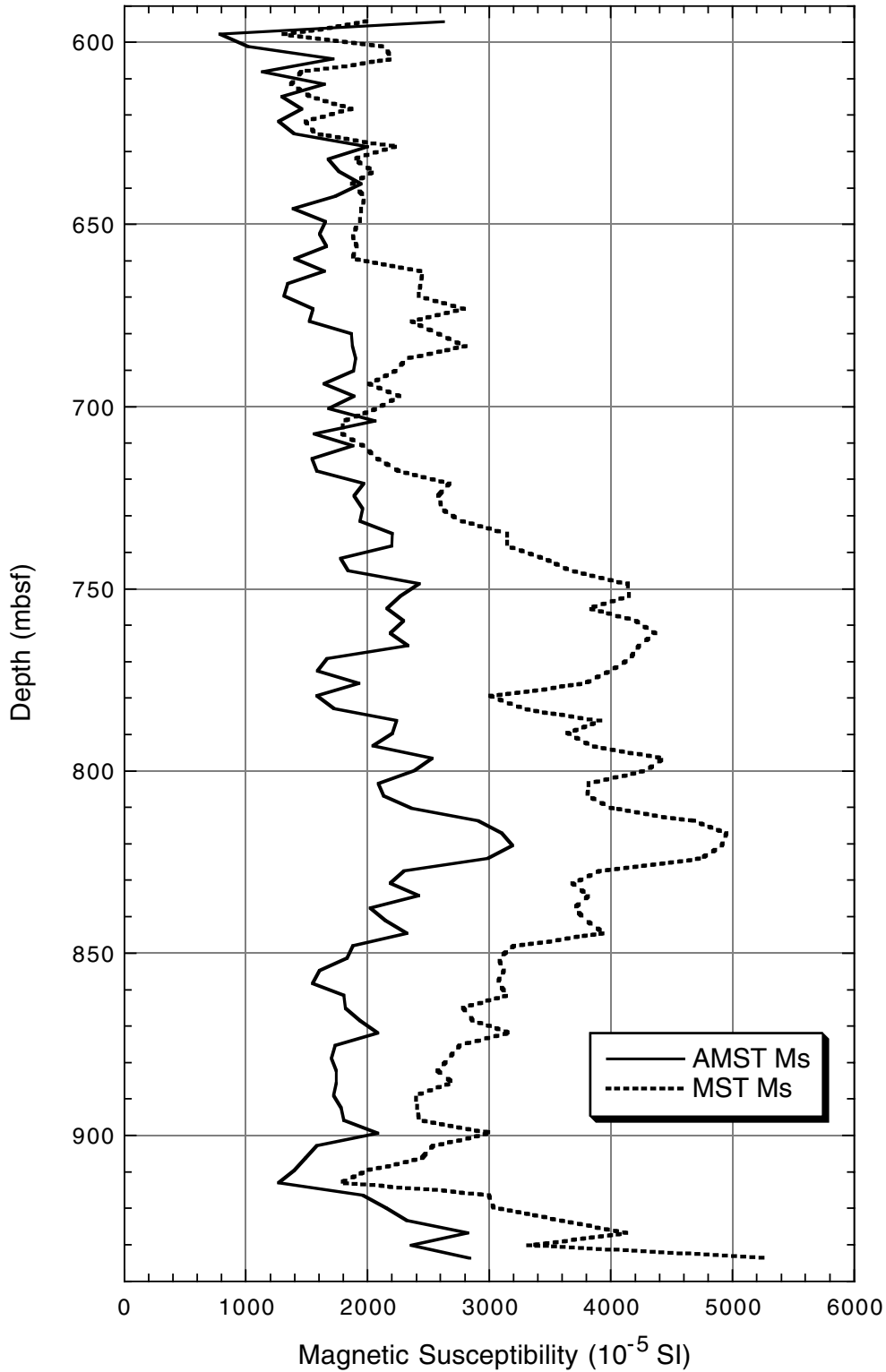


Figure F58. Intensities of natural remanent magnetization (NRM) measured before any laboratory treatment.

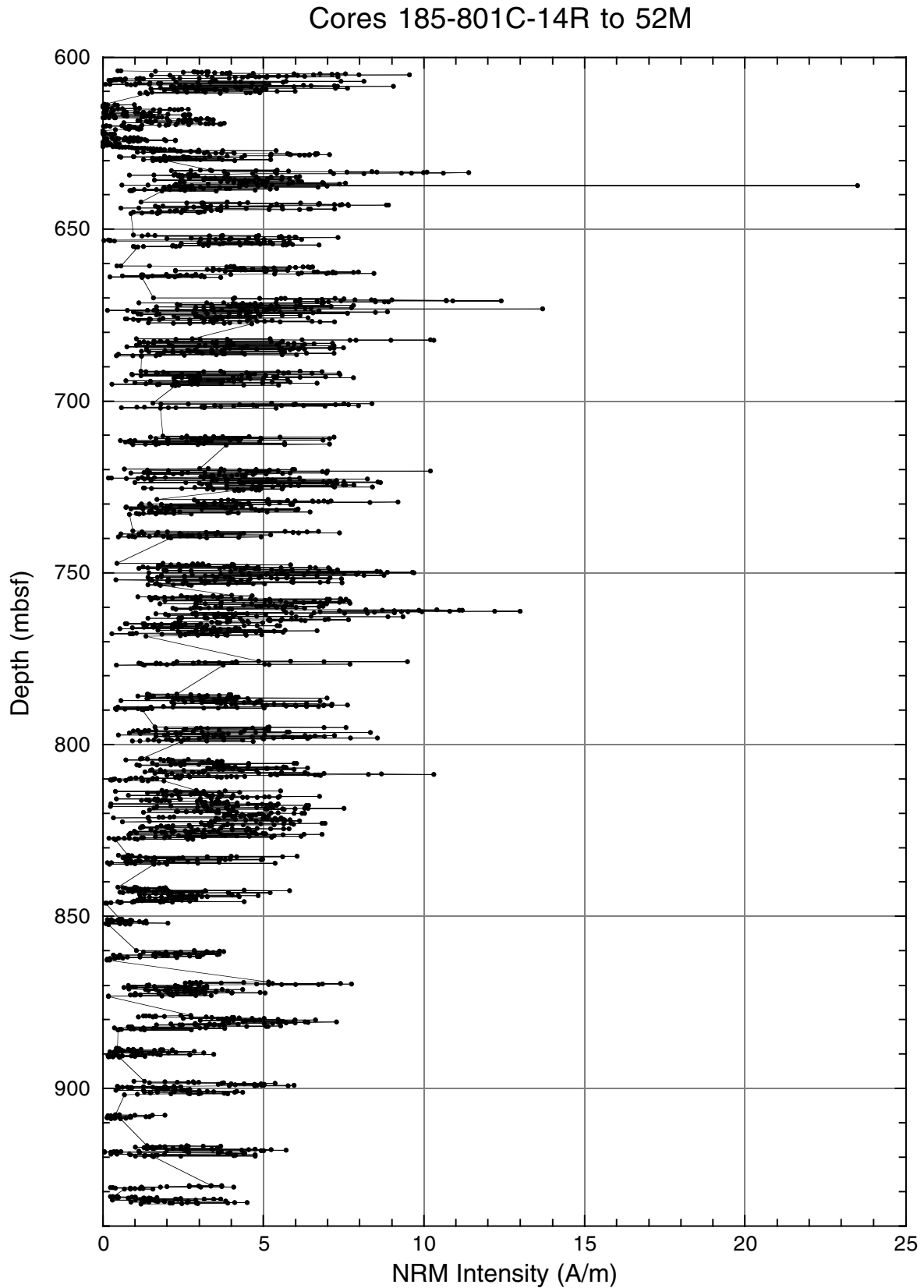


Figure F59. The inclination vector of the natural remanent magnetization prior to laboratory treatment.

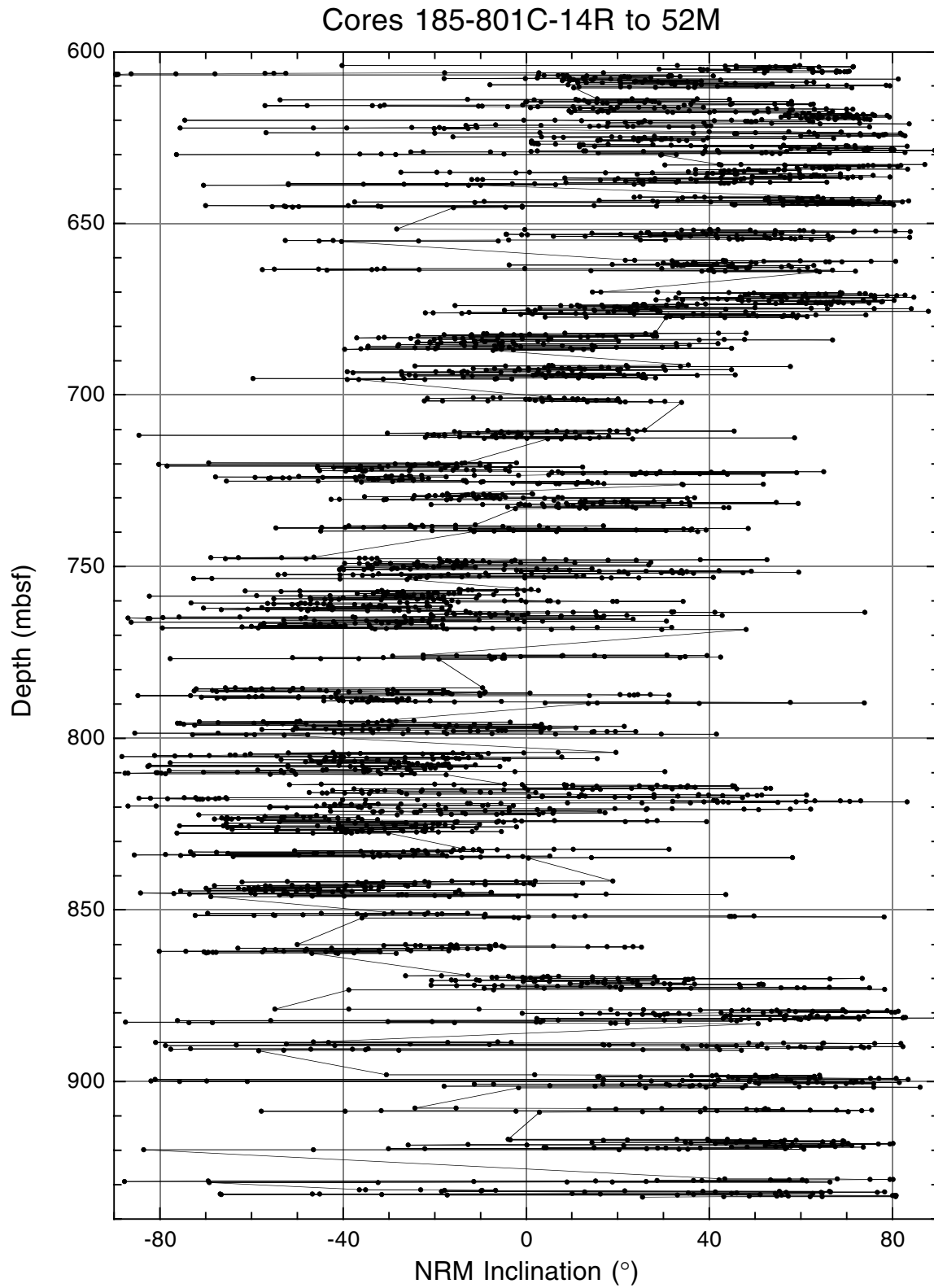


Figure F60. The inclination vector of the untreated remanent magnetization measured in the discrete samples from (mostly) the lower part of the recovered cores.

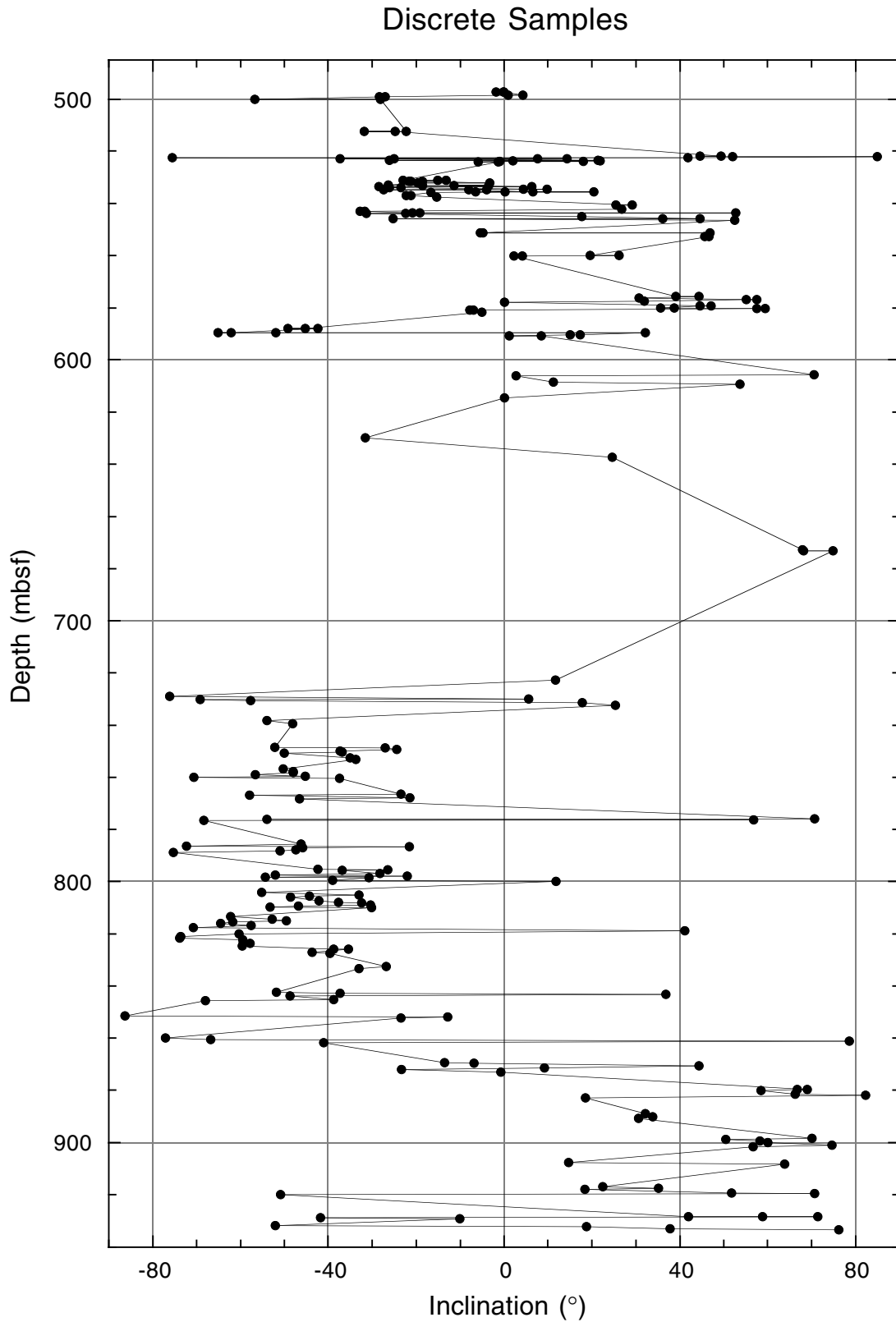


Figure F61. Demagnetization diagrams showing the effect of AF treatment. The J/J_{\max} diagram displays the demagnetized sample intensity normalized to the initial intensity for increasing strengths of the alternating field (plotted in milliteslas). The orthogonal axes diagram displays the change of intensity and direction for the vertical (open symbols) and horizontal (solid symbols) components of the magnetic vector. The stereographic projection displays the change in magnetic vector with increasing demagnetization on the upper (open symbols) or lower (solid symbols) hemispheres of an equal-area stereographic projection. **A.** Typical normal-direction samples. (Continued on next two pages.)

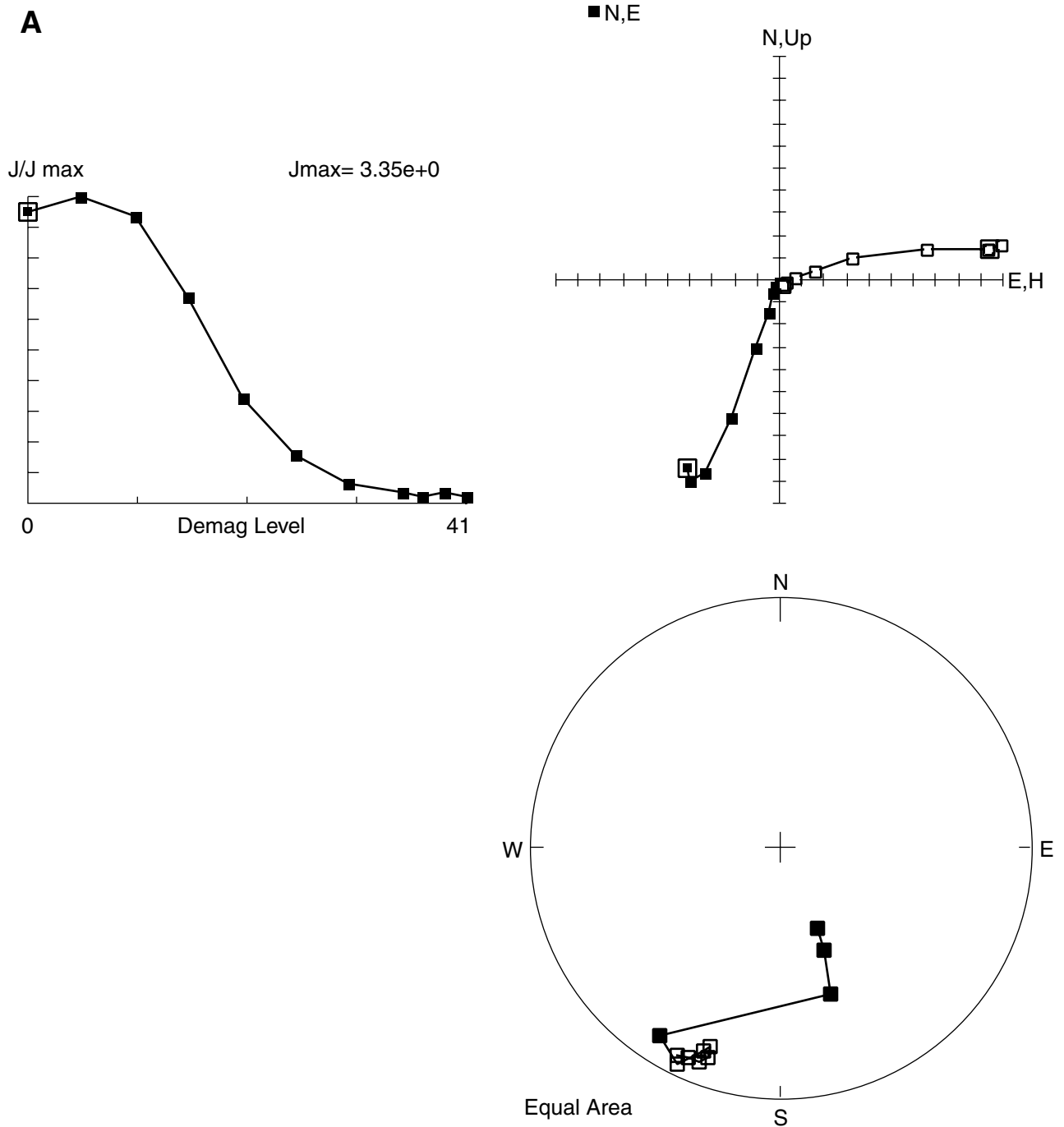


Figure F61 (continued). B. Reversed-direction samples.

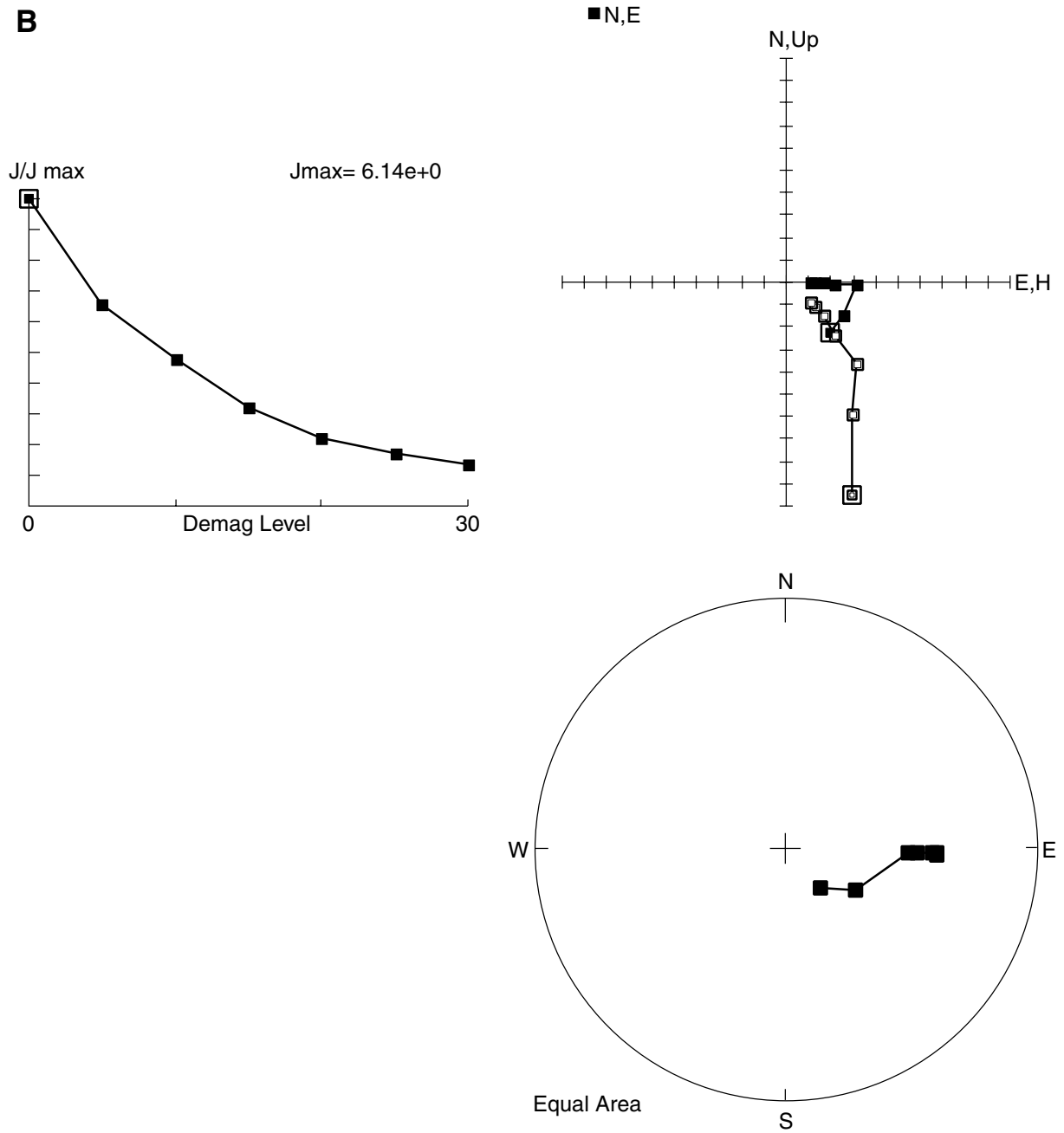


Figure F61 (continued). C. Transitional-direction samples.

C

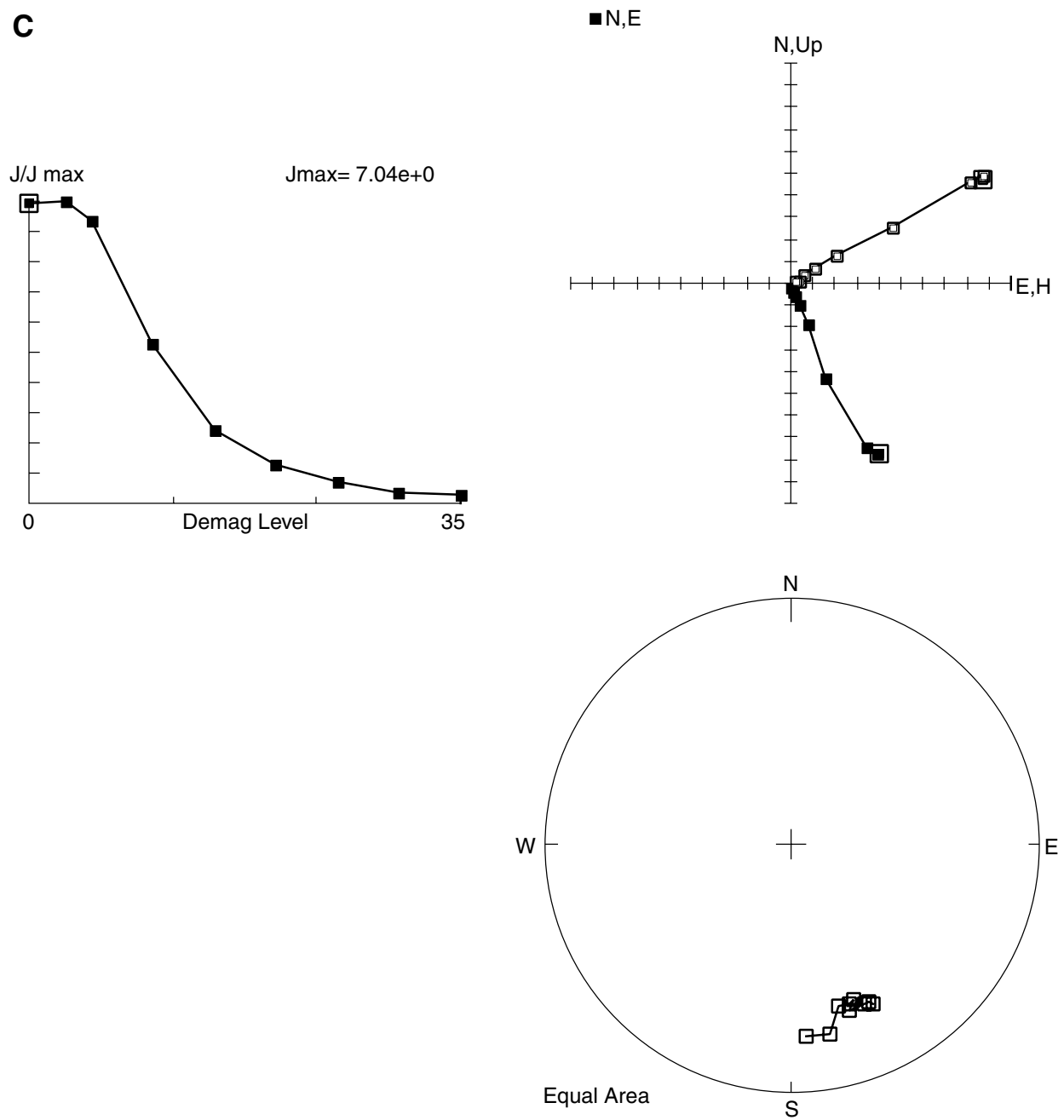


Figure F62. Inclinations plotted against depth below seafloor after demagnetization to 10 mT.

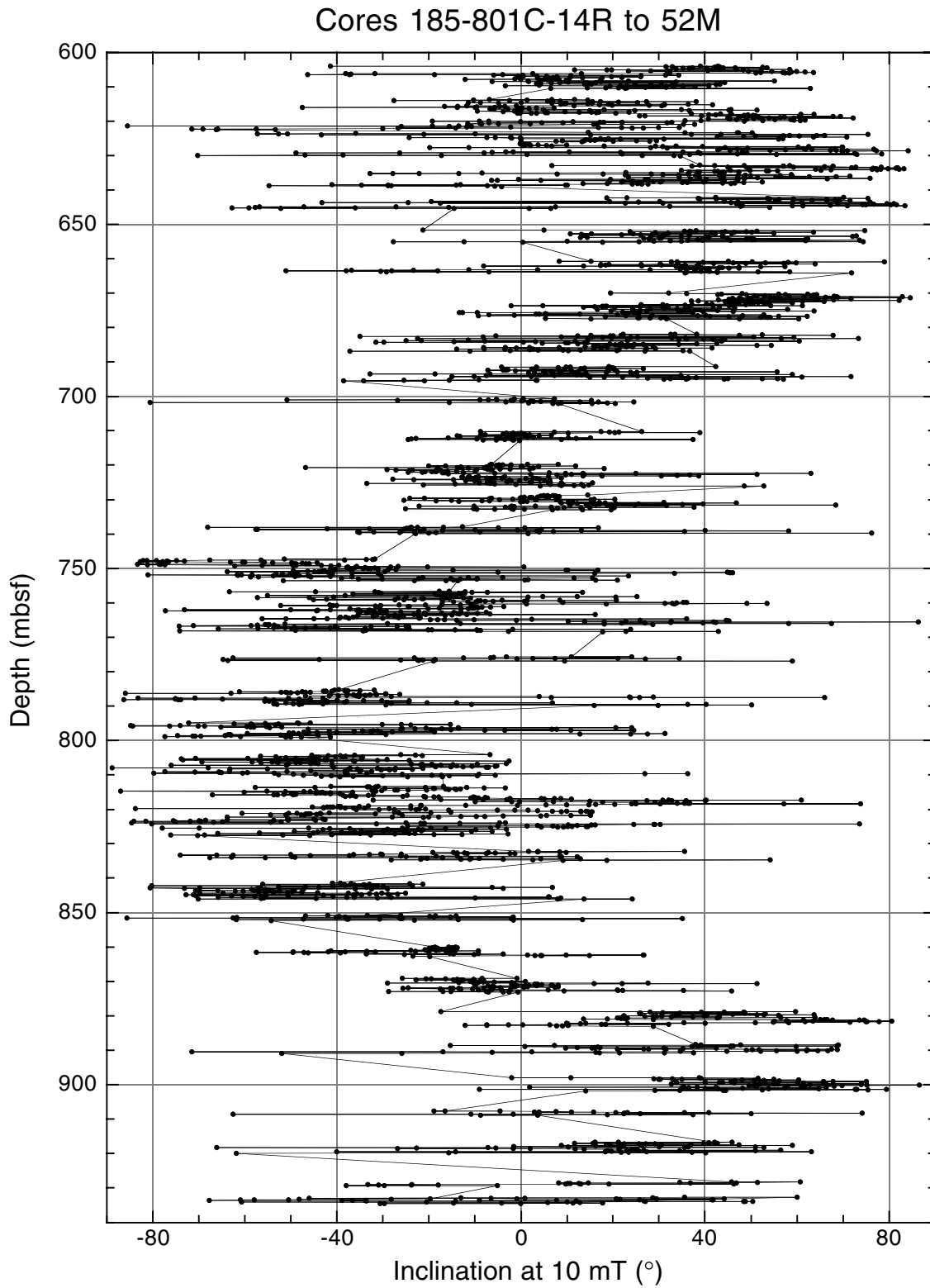


Figure F63. Index properties, compressional (P) wave velocities, and velocity anisotropy vs. depth in the igneous section cored at Site 801. P -wave velocities are measured in three directions on cubes with velocity in the x direction on split cores. Leg 129 data from tables 6 and 7 in the "Site 801" chapter of Lancelot, Larson, et al. (1990).

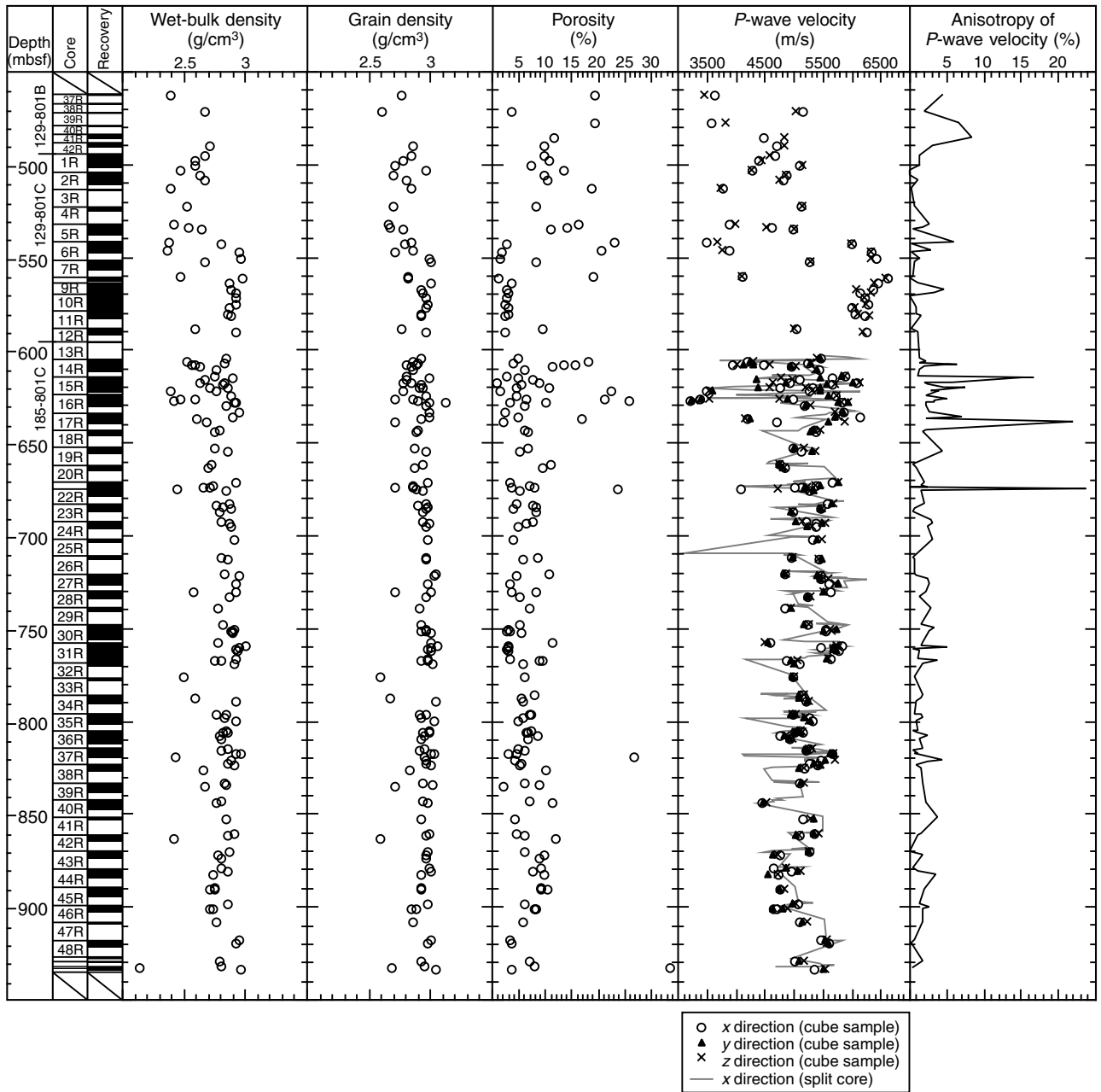


Figure F64. Crossplots of porosity, density, and average velocity from discrete samples in the igneous section cored at Site 801. Samples are coded according to lithology/structure type. Leg 129 data from tables 6 and 7 in the "Site 801" chapter of Lancelot, Larson, et al. (1990).

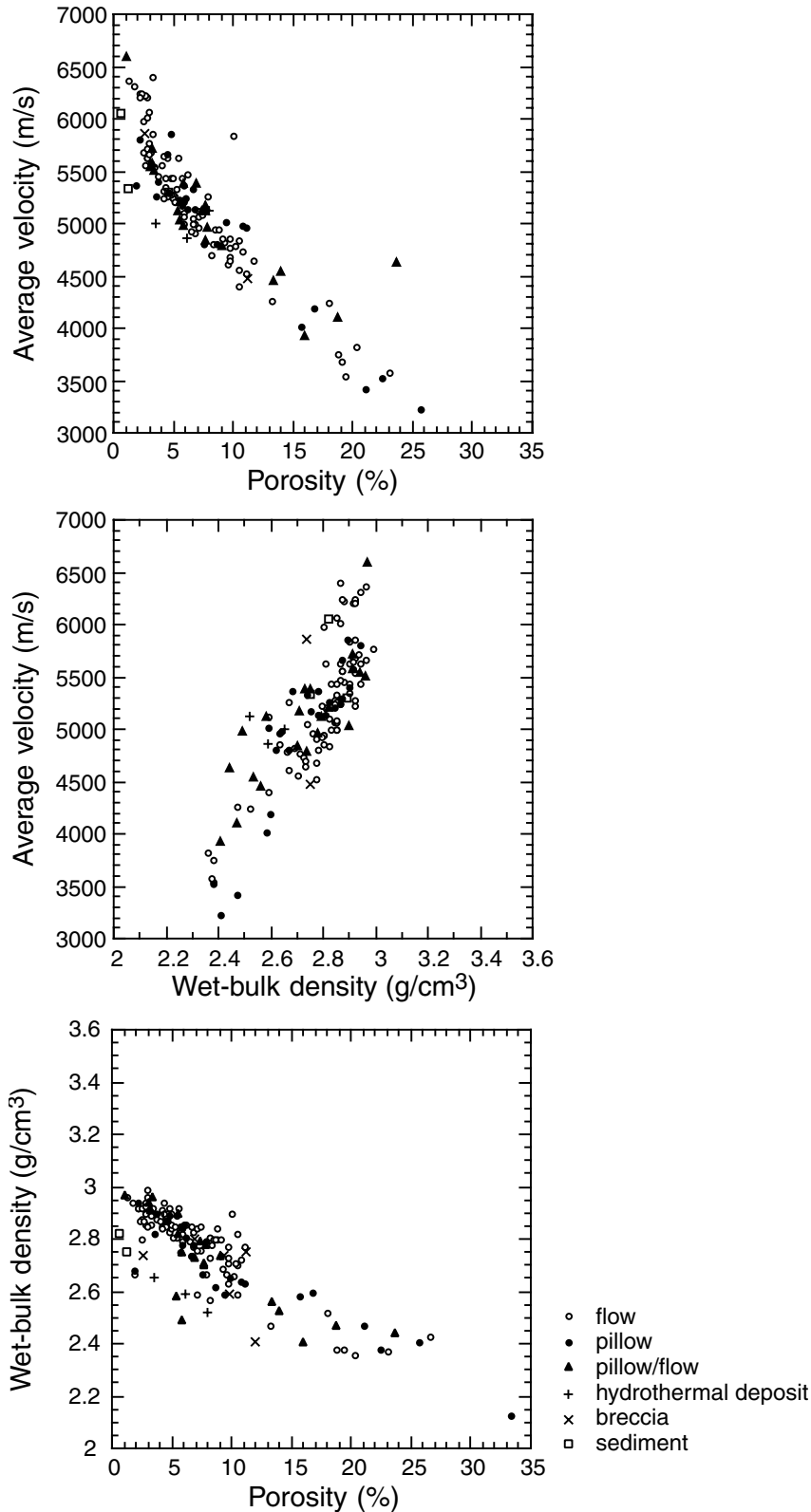


Figure F65. MST measurements vs. depth on whole cores obtained in Hole 801C during Leg 185 and on working-half cores in the tholeiitic section cored during Leg 129, but measured during Leg 185. Wet bulk densities measured on discrete samples using gravimetric methods are plotted as circles. Note: Measurements on half cores cannot be directly compared to those made on whole cores.

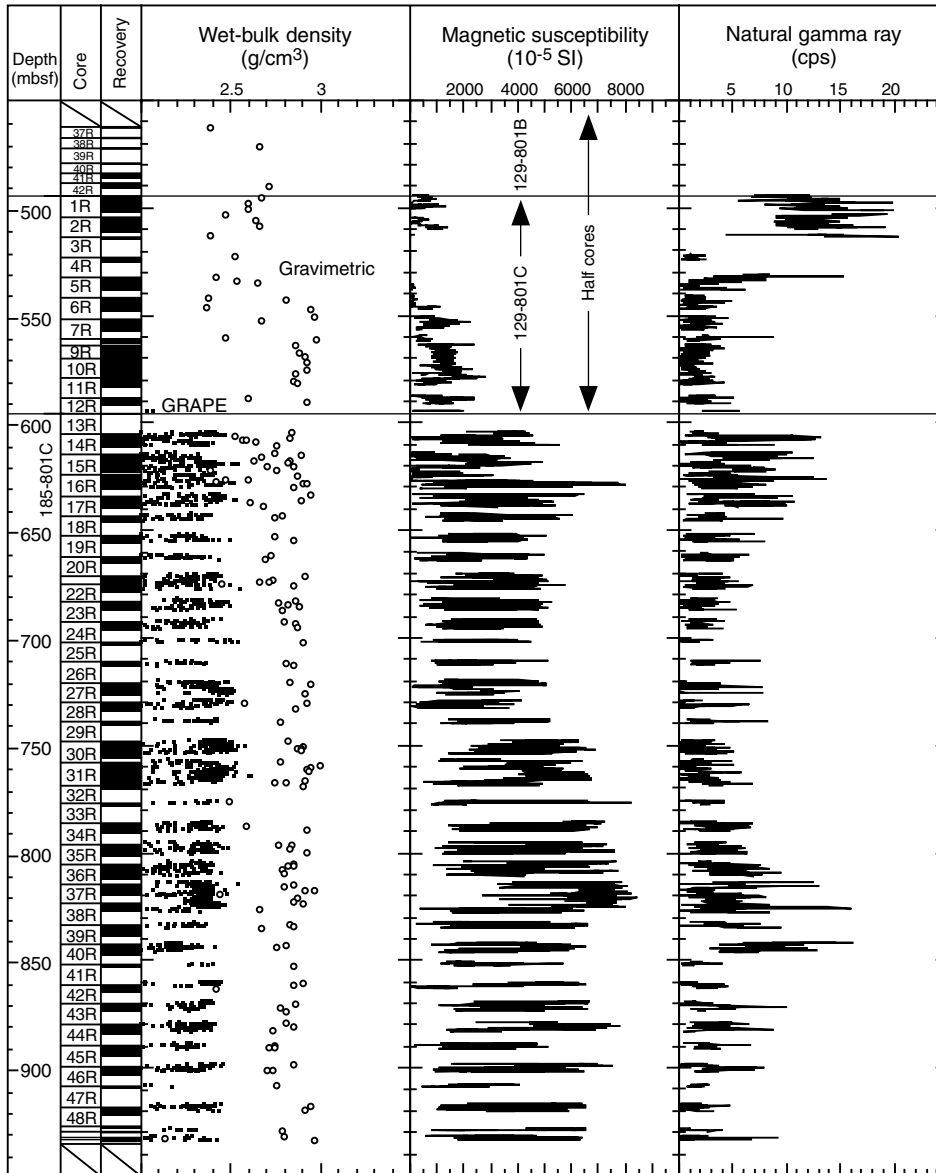


Figure F66. MST data for Hole 801D.

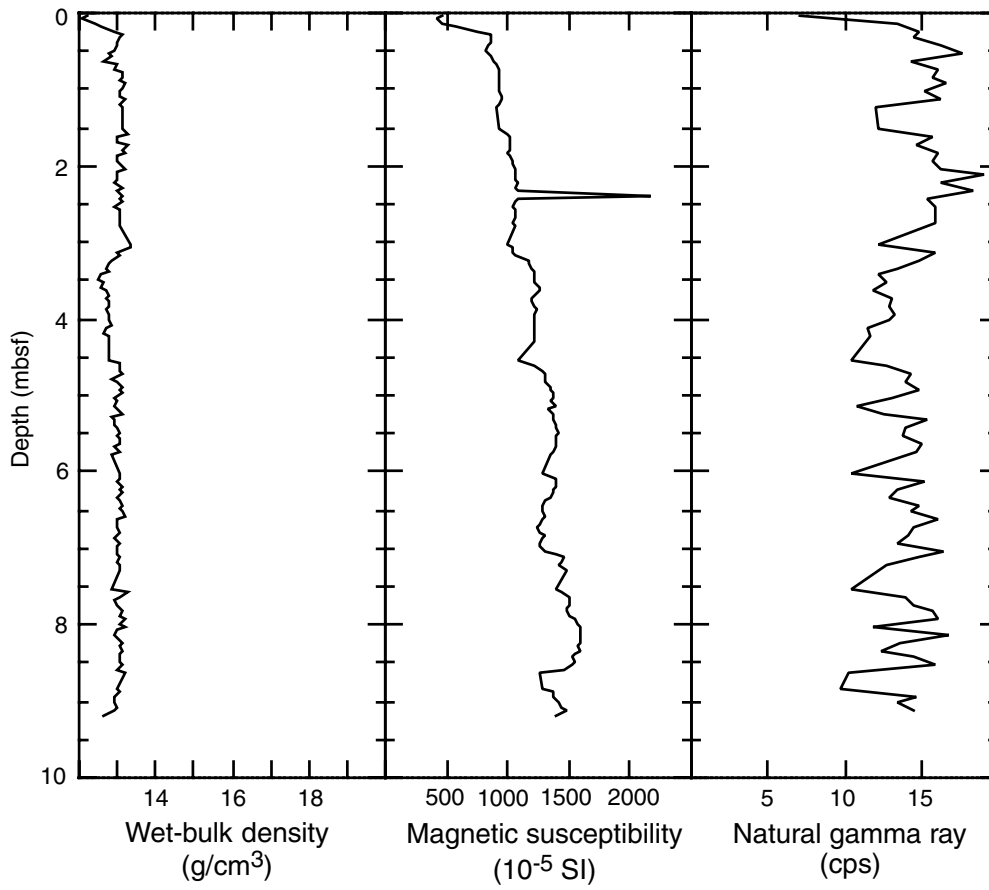


Figure F67. Thermal conductivity vs. depth for the igneous section cored during Legs 129 and 185 at Site 801. Leg 129 data from table 6 and 7 in the "Site 801" chapter of Lancelot, Larson et al. (1990).

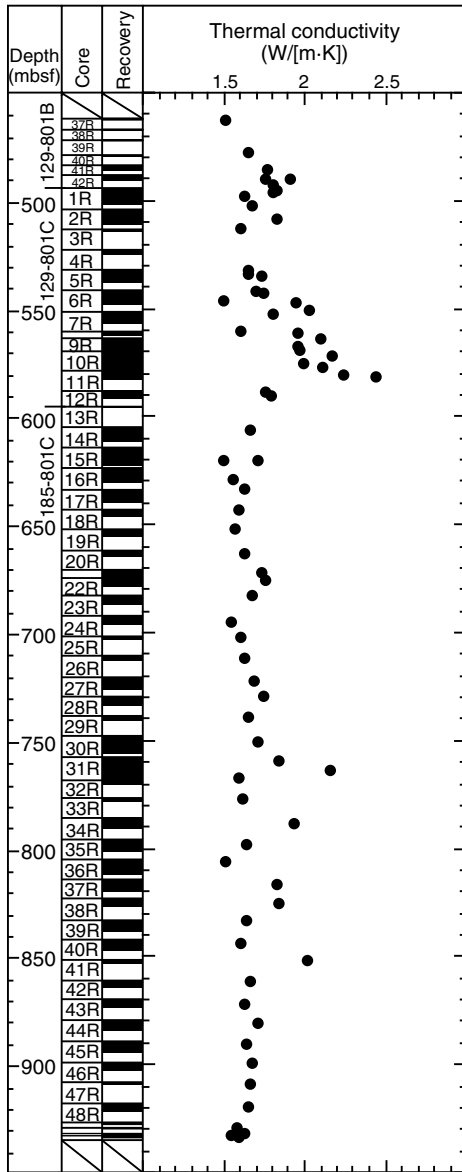


Figure F68. Cores and cored intervals correlated to logs by shifting the logs down 2 m from their originally recorded levels. Solid horizontal lines indicate the correlations of specific features observed in both the cores and logs after the logs were shifted down by 2 m relative to the cores. The dashed line above each solid line indicates the former position of these logged features relative to the cores before the downshift.

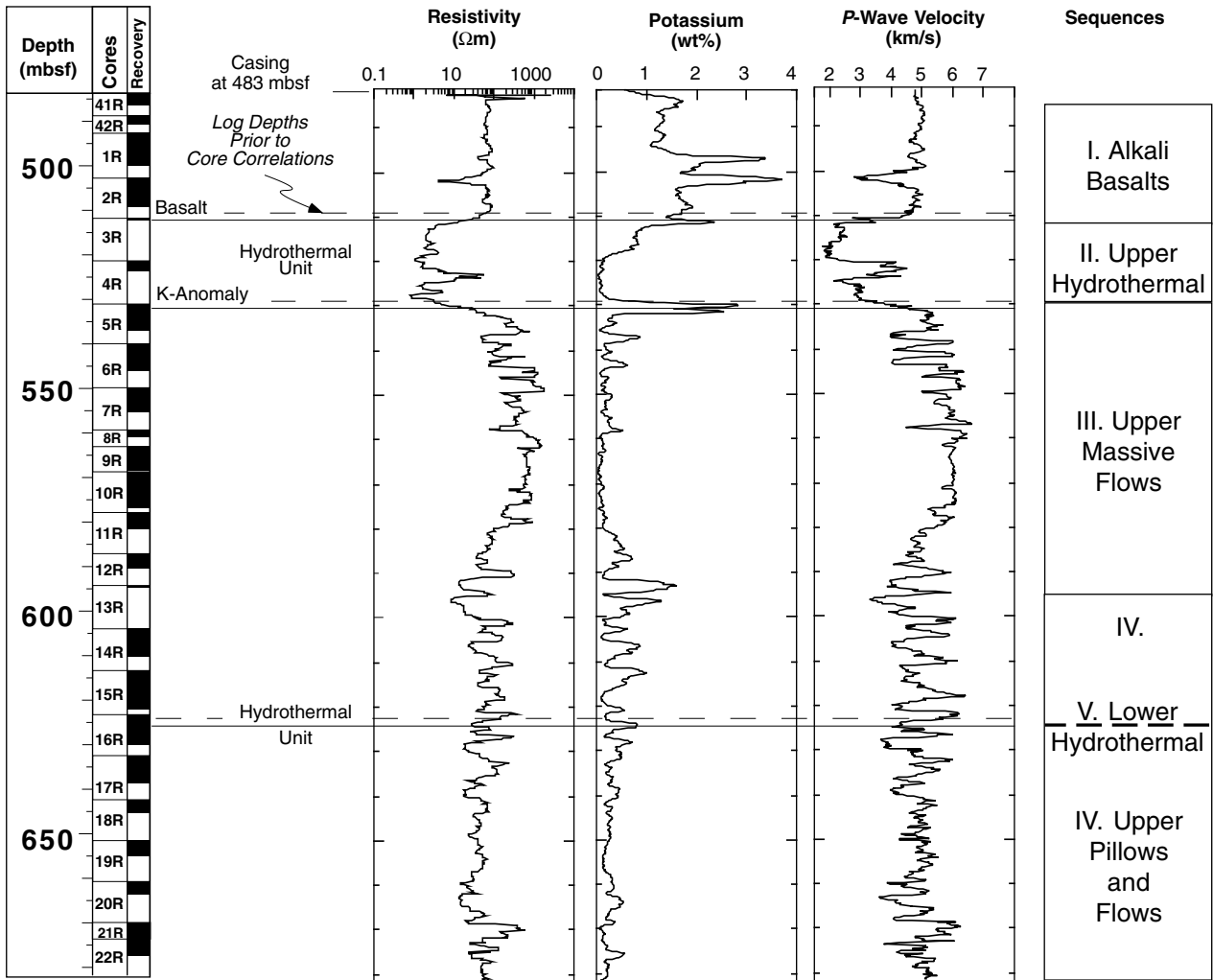


Figure F69. FMS microresistivity images correlated to specific features in Sections 185-801C-16R-1 to 16R-3. The hydrothermal unit and two large veins are identified in both the FMS and core images. The meters below seafloor scale on the FMS images shows the depth range of this interval after the 2-m downshift of the logs described in Figure F68, p. 141.

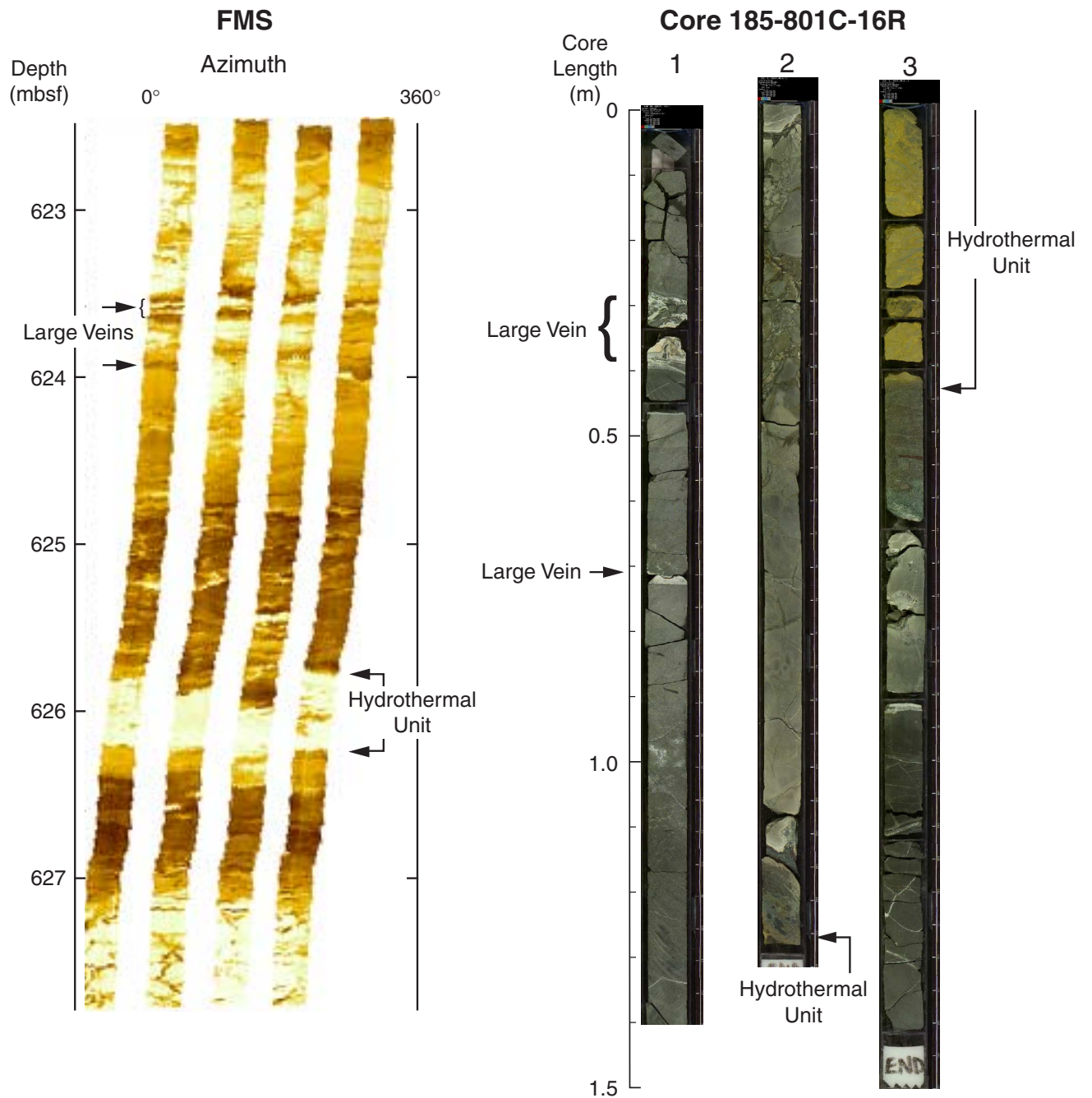


Figure F70. Radioactive element logging measurements in Jurassic basement in Hole 801C are shown with major lithologic sequences determined from core-log integration of Leg 129 and 185 data. The majority of the radioactive fraction seems to be concentrated in potassium. High gamma radiation values are located in the upper 50 m of the borehole. Other regions of high radioactivity are also observed below this shallow region.

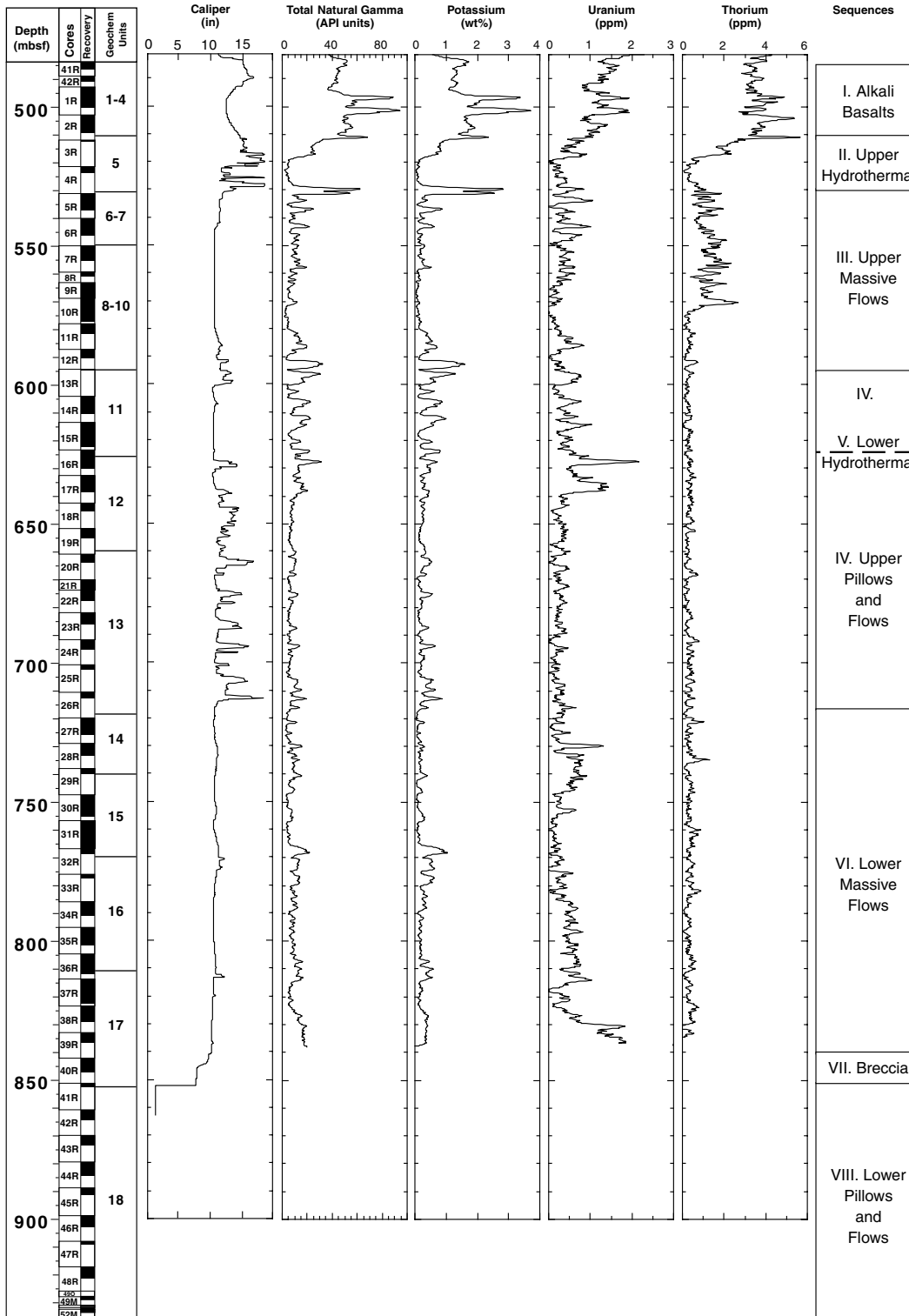


Figure F71. Geophysical logging measurements in Jurassic basement in Hole 801C are shown with major lithologic sequences determined from core-log integration of Leg 129 and 185 data. Resistivity, bulk density, and *P*-wave velocities exhibit very similar patterns of variation down the borehole. The largest resistivity and *P*-wave velocity values are within the massive flow units. Conversely, the lowest values are associated with the upper hydrothermal unit and the alternating pillow basalts, sediments, and breccias. Temperature anomalies at 520 and 710 mbsf are also observed and coincide with regions of low resistivity. (Figure shown on next page.)

Figure F71 (continued). (Caption on previous page.)

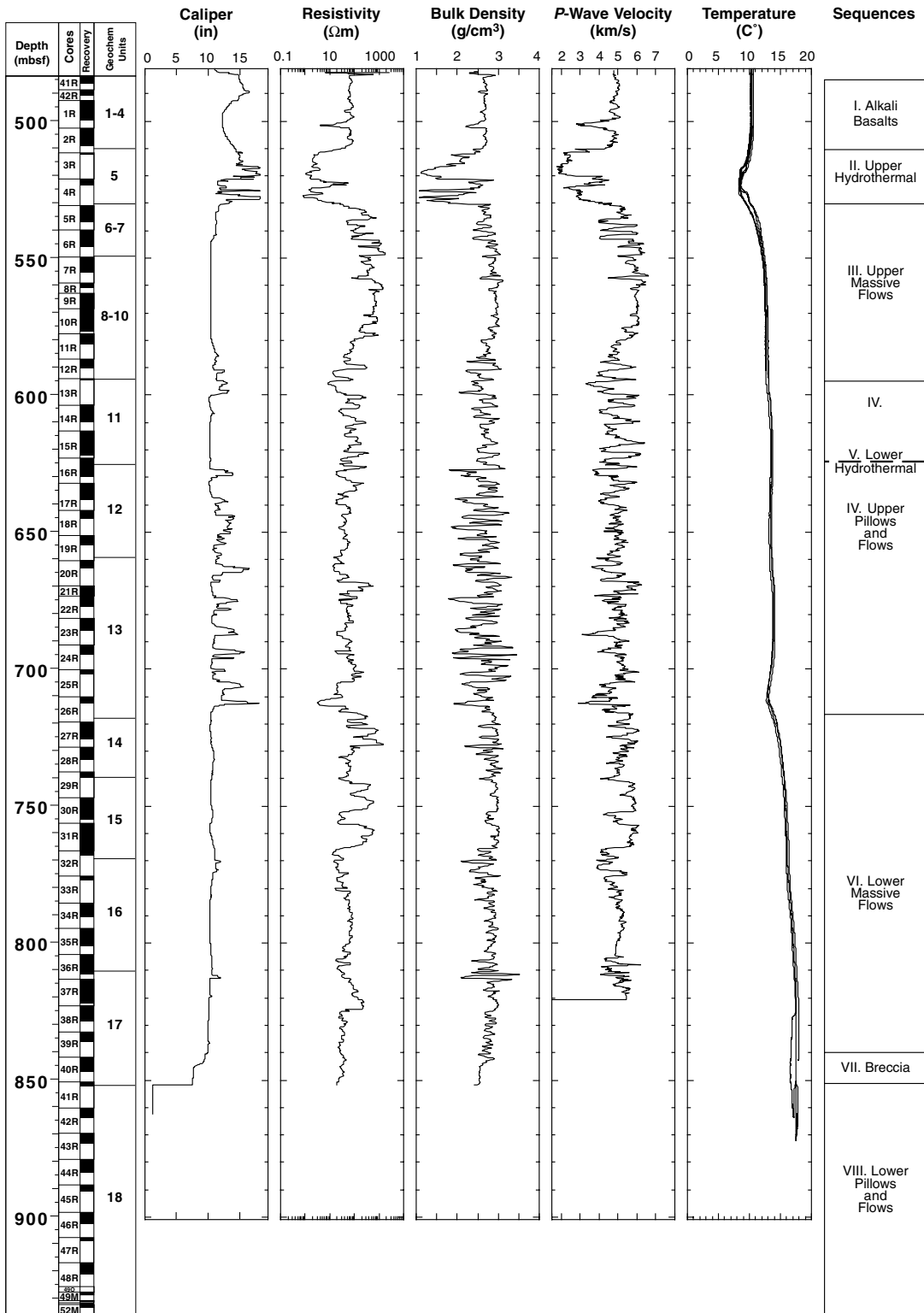


Figure F72. Magnetic measurements in Jurassic basement, deviation from true vertical, and the FMS caliper data for Hole 801C are shown with major lithologic sequences determined from core-log integration of Leg 129 and 185 data. Downhole magnetic intensity data exhibit similar patterns of variability in both the horizontal and vertical components. A large-amplitude variation at the top of the upper pillows and flows section marks the beginning of a long-wavelength variation in the total magnetic intensity.

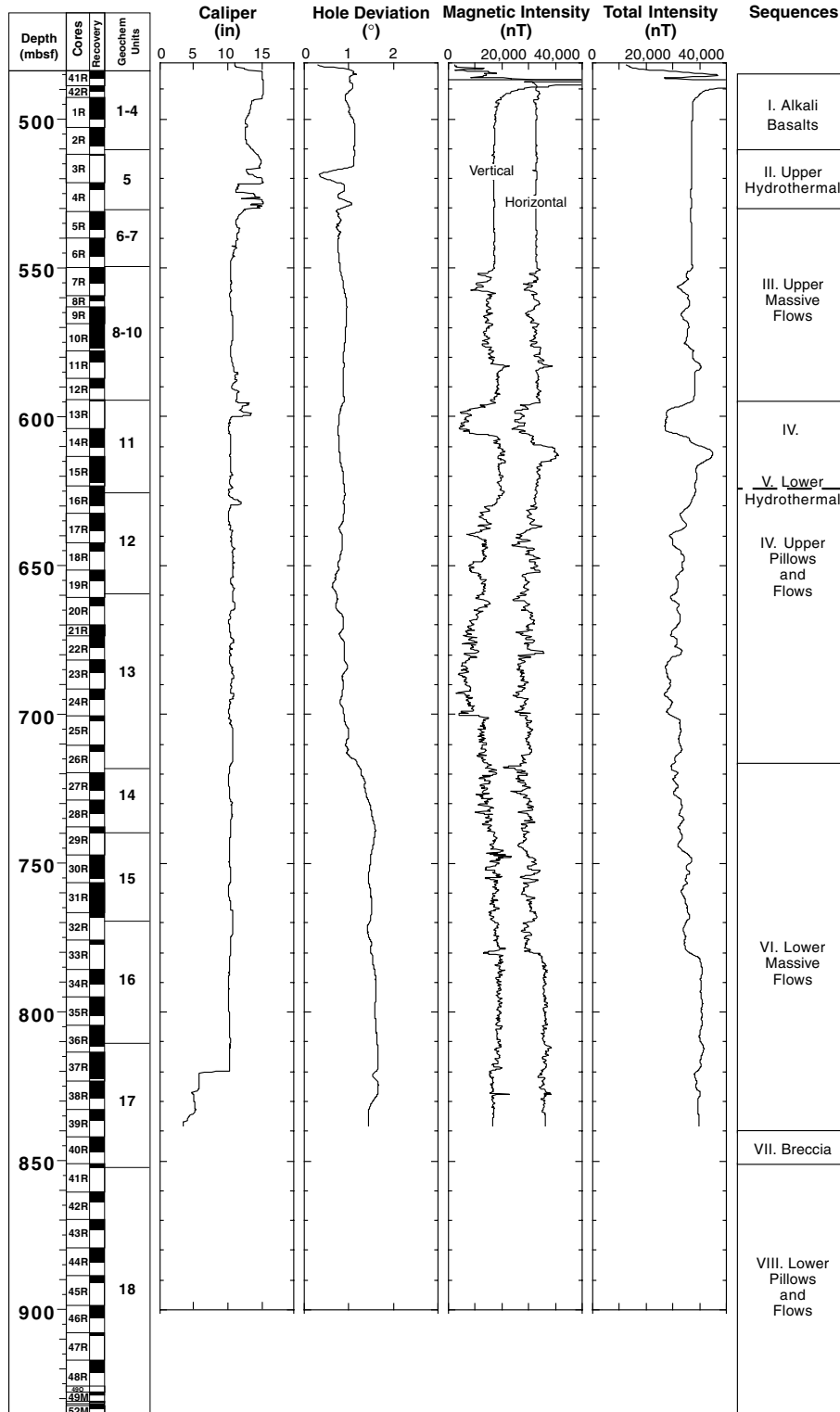


Figure F73. Downhole temperature and FMS data illustrating the correspondence of temperature anomalies with portions of the borehole with low resistivities. The solid dots at 480–590 mbsf are temperature measurements obtained from the WSTP before drilling. The solid black line is the temperature gradient measured during Leg 144 (Larson et al., 1993).

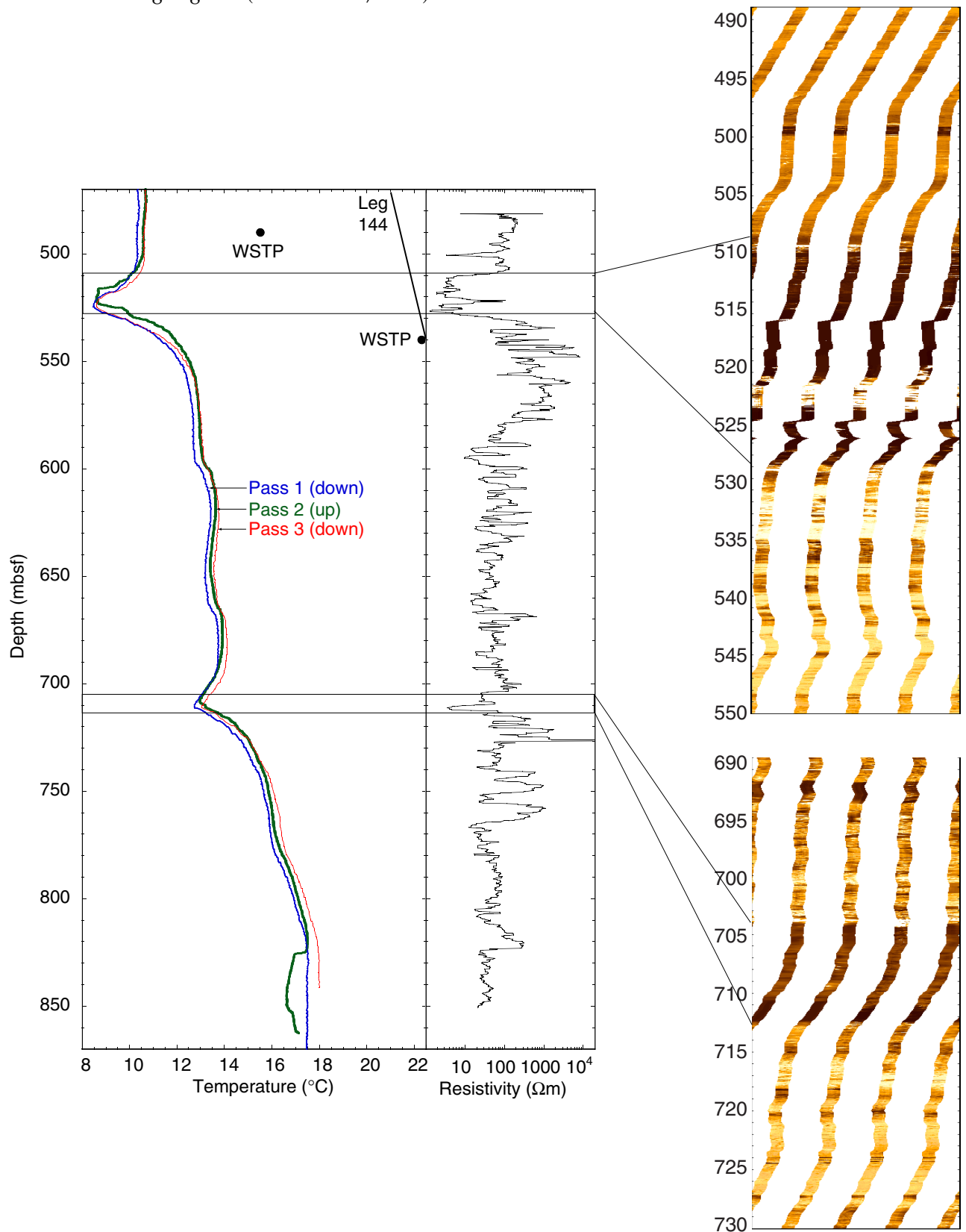


Figure F74. Concentration of perfluoro(methylcyclohexane) in the interior of igneous rock samples from Core 185-801C-37R (see Table T19, p. 216, for exact locations), treated by various handling procedures (Smith et al., 2000).

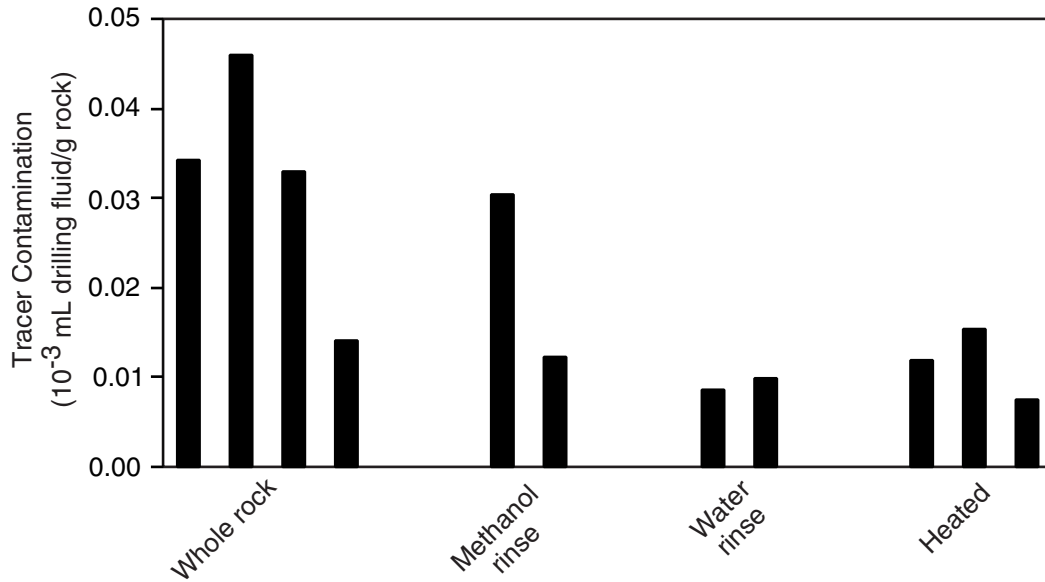


Figure F75. Concentration of perfluoro(methylcyclohexane) in the interior of igneous rock samples from Sections 185-801C-37R-6, and 185-1149C-9R-1 (Smith et al., in press).

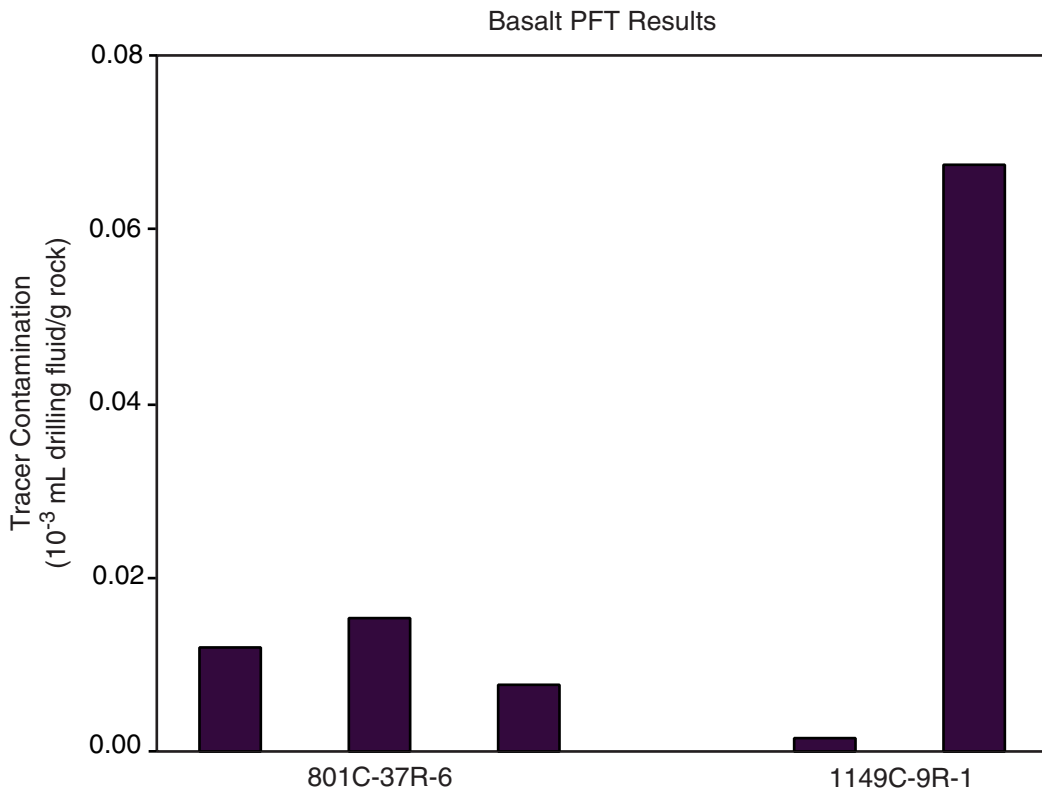


Figure F76. Close-up photograph of Sample 185-801C-14R-3 (Pieces 8 and 9, 103–110 cm). This core contains pillow basalts with interpillow material. The pillow basalt edges are white, the basalts are slightly reddish, and the interpillow material is black to dark green.

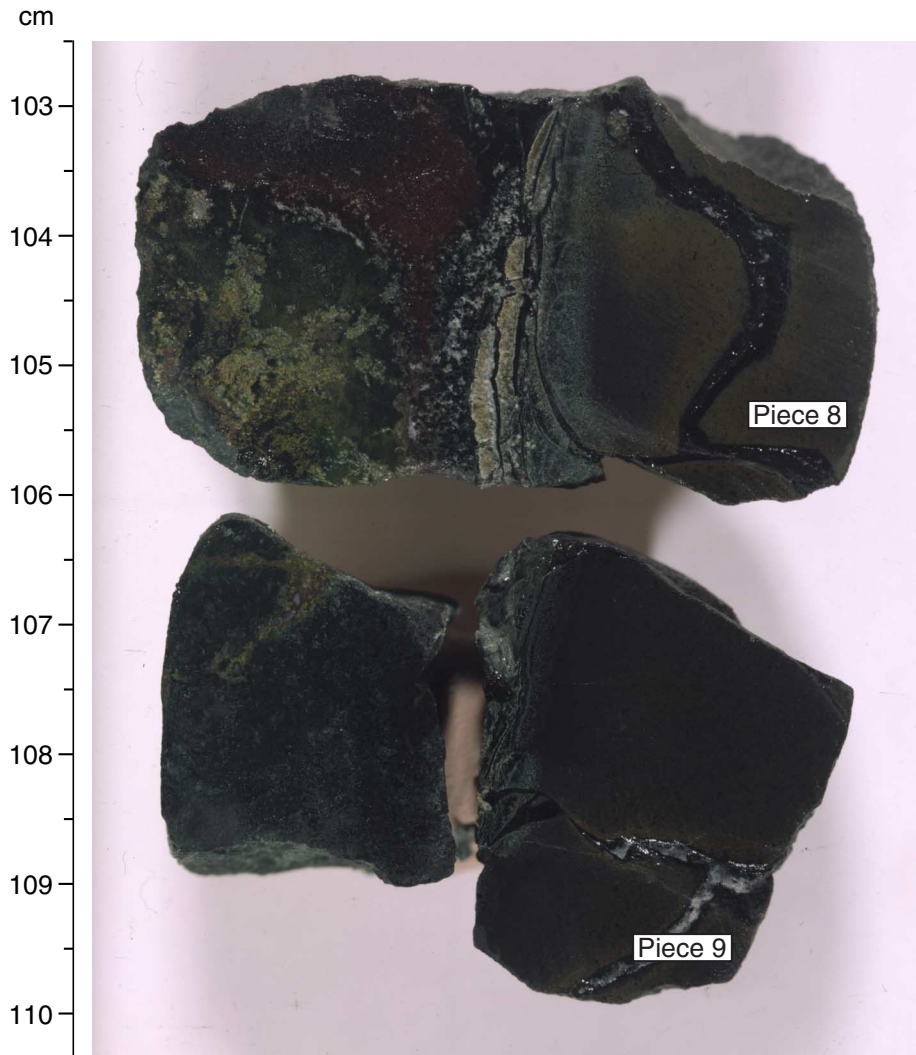


Figure F77. Photomicrograph of a glassy pillow rim in Sample 185-801C-14R-3, 120–122 cm. Brown feathery varioles surround laths of white plagioclase. The pale green is quenched glass that has been altered to clay. Three olivine grains (red) have been altered to a mixture of clay and iron oxides or iddingsite.

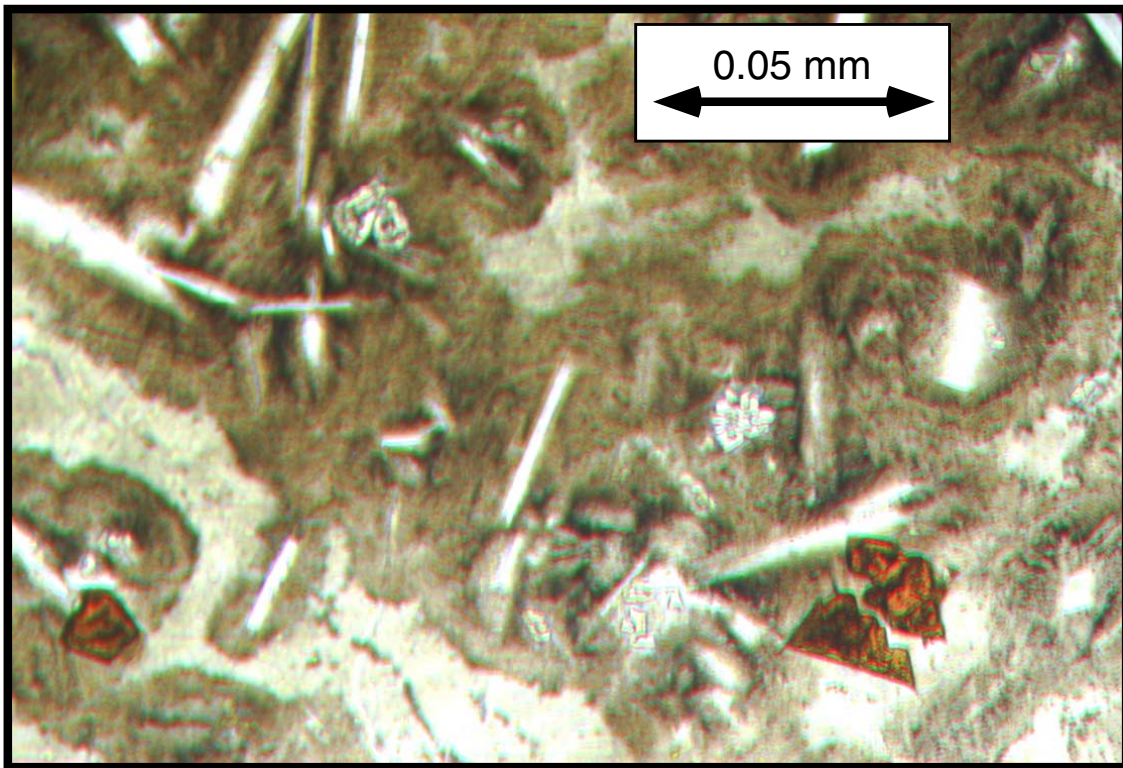


Figure F78. Close-up photograph of Sample 185-801C-16R-5 (Pieces 9 and 10, 72–86 cm) from which the second biological sample was taken. The pillow basalts are dark gray, which reflects the relatively small amount of alteration. Intrapillow breccia is a mixture of basalt fragments, dark clay, calcite, and quartz. Irregular, subrounded centimeter-sized voids are filled with calcite (white).

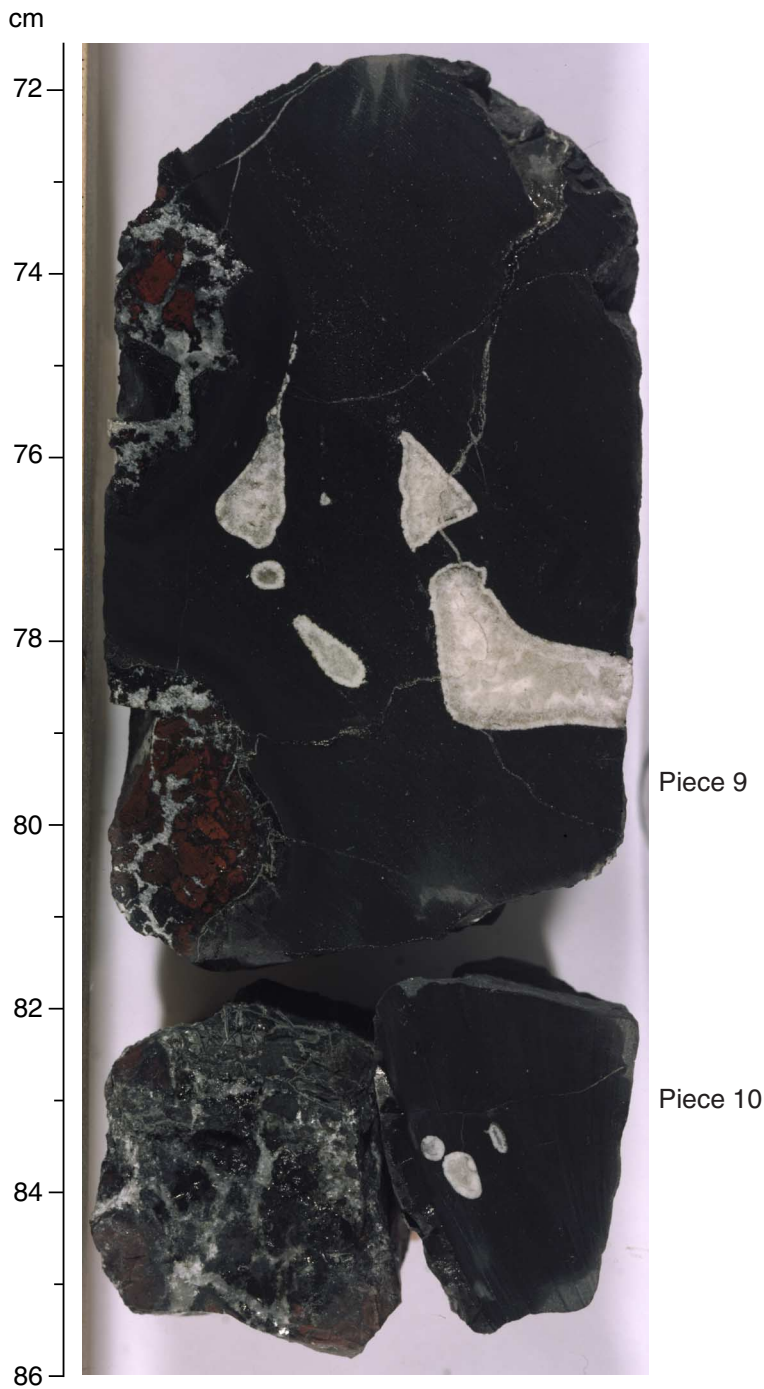


Figure F79. Photomicrograph of Sample 185-801C-16R-5, 107–110 cm. Glass, clay, and calcite are labeled. A 100- μm -long lath of plagioclase (white) is near the bottom of the picture. The glass at the contact with the clay is opaque black. Clay is gray to light brown, and the white region in the upper left is calcite. The crack from the center bottom to the upper right was probably created during the manufacture of the thin section. Photo was taken with a 20 \times objective lens in plane-polarized light.

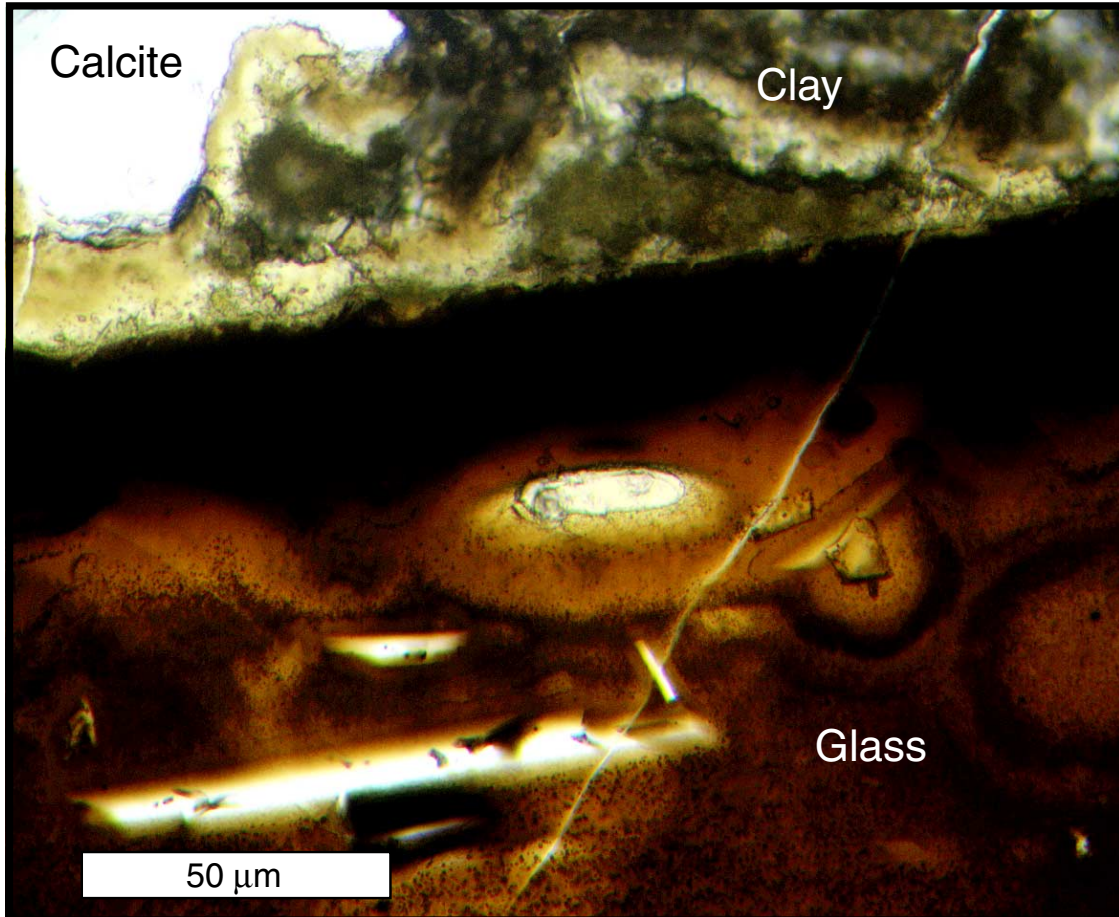


Figure F80. A biological sample taken from Sample 185-801C-23R-1 (Piece 10, 109–125 cm). This sample is a piece of a thick basalt flow with fractures and veins running through it. The veins are filled primarily with carbonate but also contain ~1% or 2% sulfide.

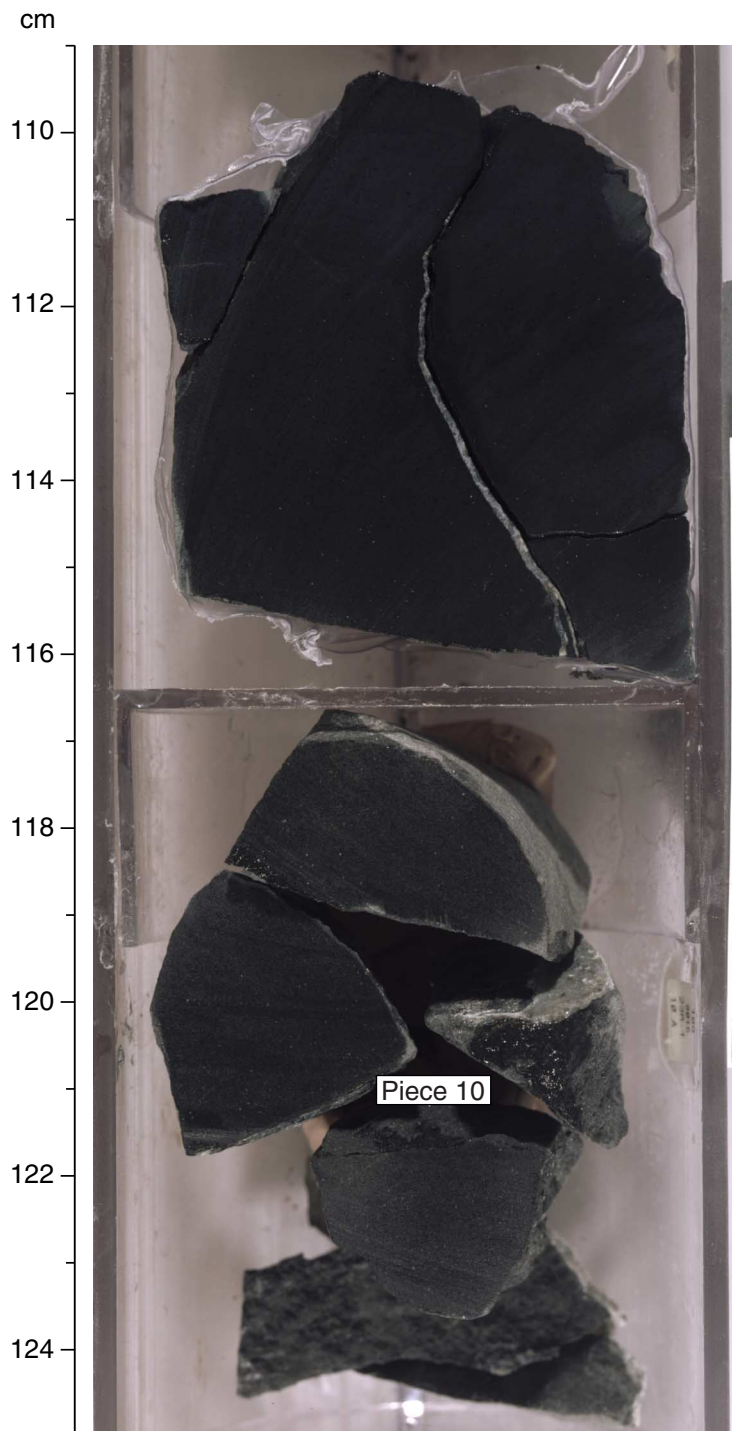


Figure F81. Photomicrograph taken in plane-polarized light of a typical area of Sample 185-801C-23R-1 (Piece 3, 27–28 cm). Representative plagioclase, pyroxene, and magnetite grains are labeled PL, PX, and MT, respectively. A round vesicle (V) ~50 μm in diameter is filled with smectite clay.

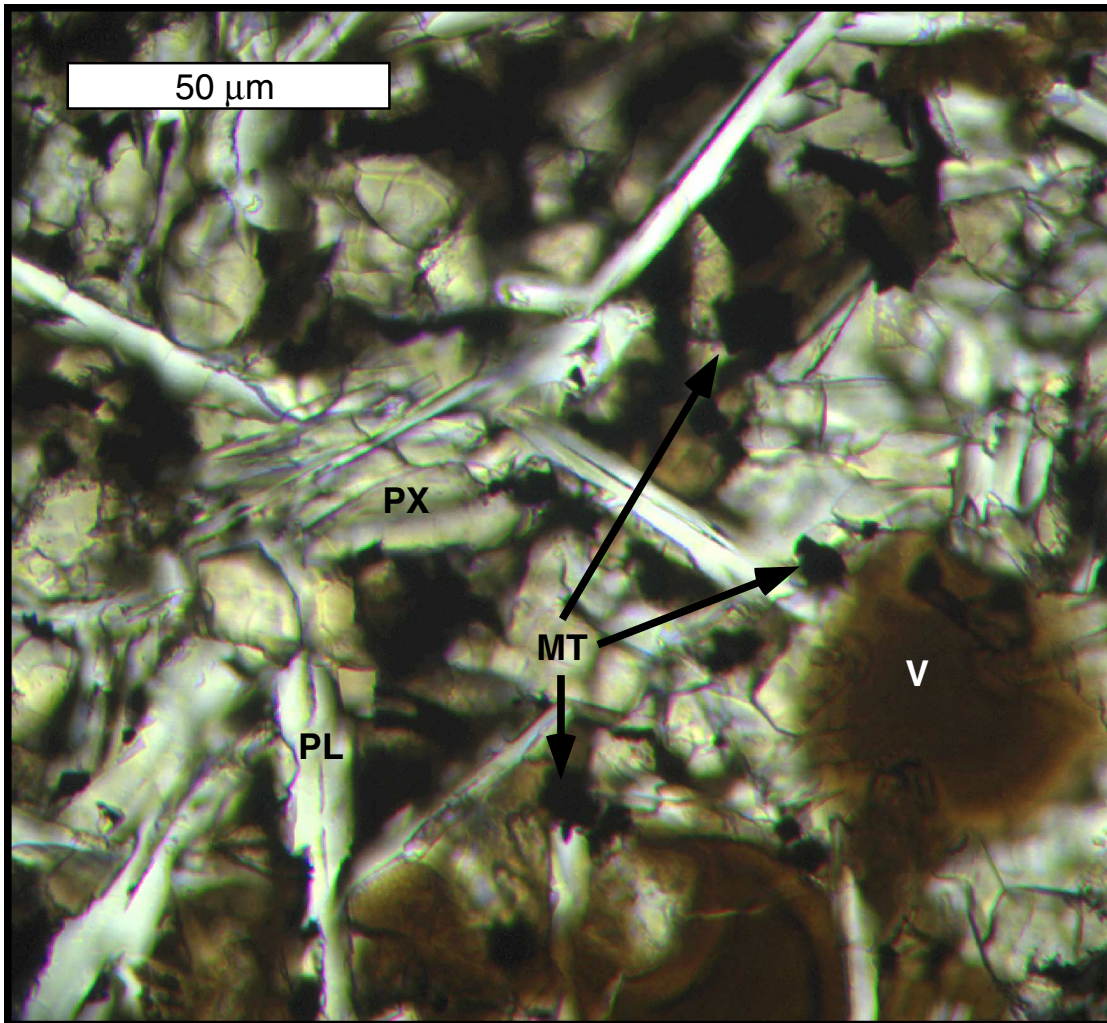


Figure F82. Close-up photograph of interval 185-801C-27R-3, 5–35 cm. The top end of Piece 5 was sampled for biological studies. Although the majority of Piece 5 is crystalline basalt, the top of it is similar to Pieces 2, 3, and 4. These pieces contain interpillow glass, carbonate, and clay (mottled dark and white areas). These areas contain fresh glass unlike the interpillow material sampled at intervals 185-801C-14R-3, 106–109 cm, and 16R-5, 84–87 cm, in which all of the glass was altered.

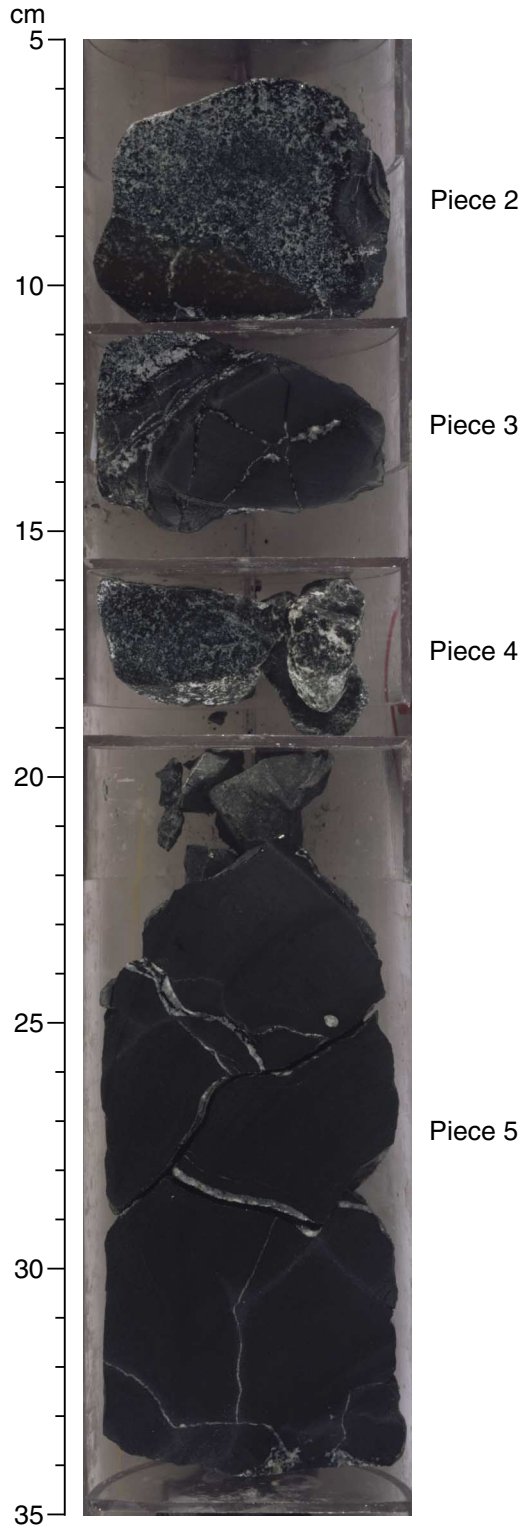


Figure F83. Photomicrograph of a thin section (from Piece 2 in Figure F82, p. 156) from Sample 185-801C-27R-3, 6–11 cm. This photograph shows the calcite matrix enclosing green clay and brown iron oxides. Photomicrograph is in plane-polarized light with a 20× objective lens.

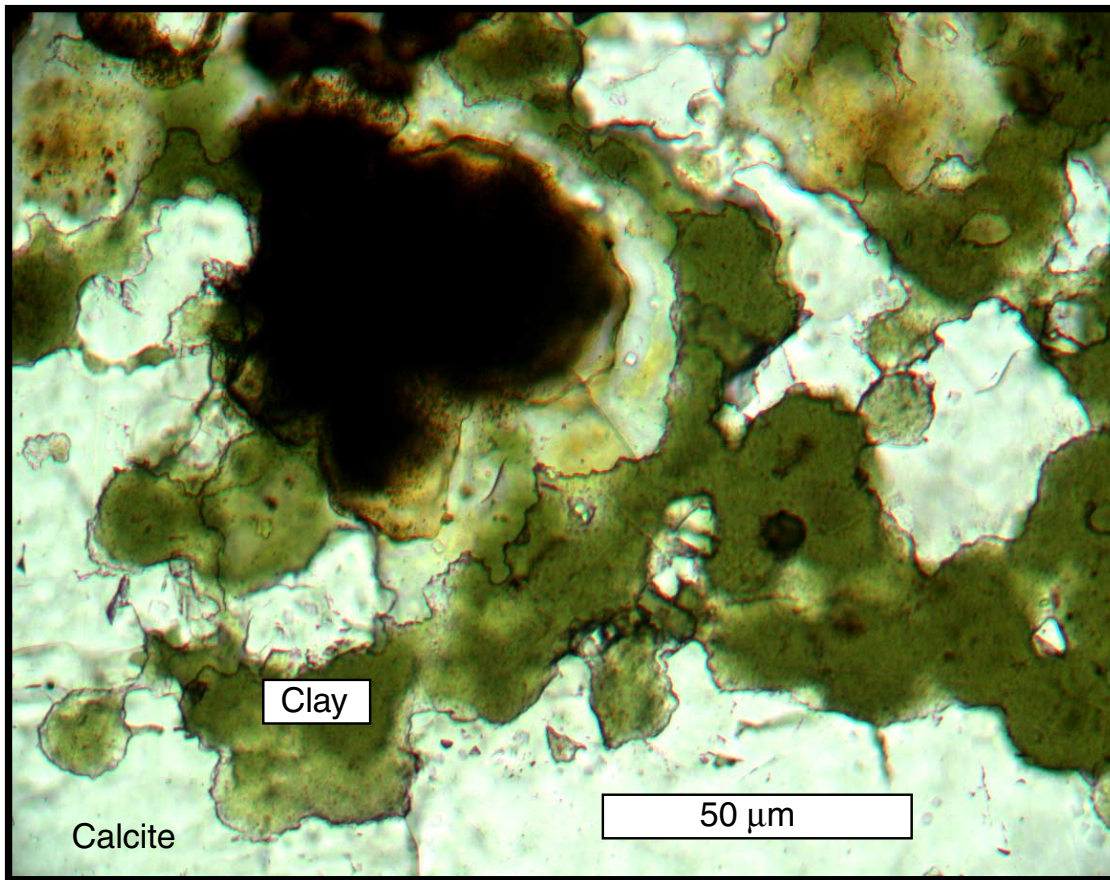


Figure F84. Interval 185-801C-37R-1, 26–38 cm, is from the top of a lava flow that is >10 m thick. The flow is cut by fractures that are filled with calcite, some of which are more than 1 cm thick. Part of the thick calcite vein shown here was used to inoculate cultures. A thin section taken from this piece shows bands of pyrite and brown alteration along the fractures. This suggests an episode of alteration sulfide formation followed by an episode of iron oxide formation.

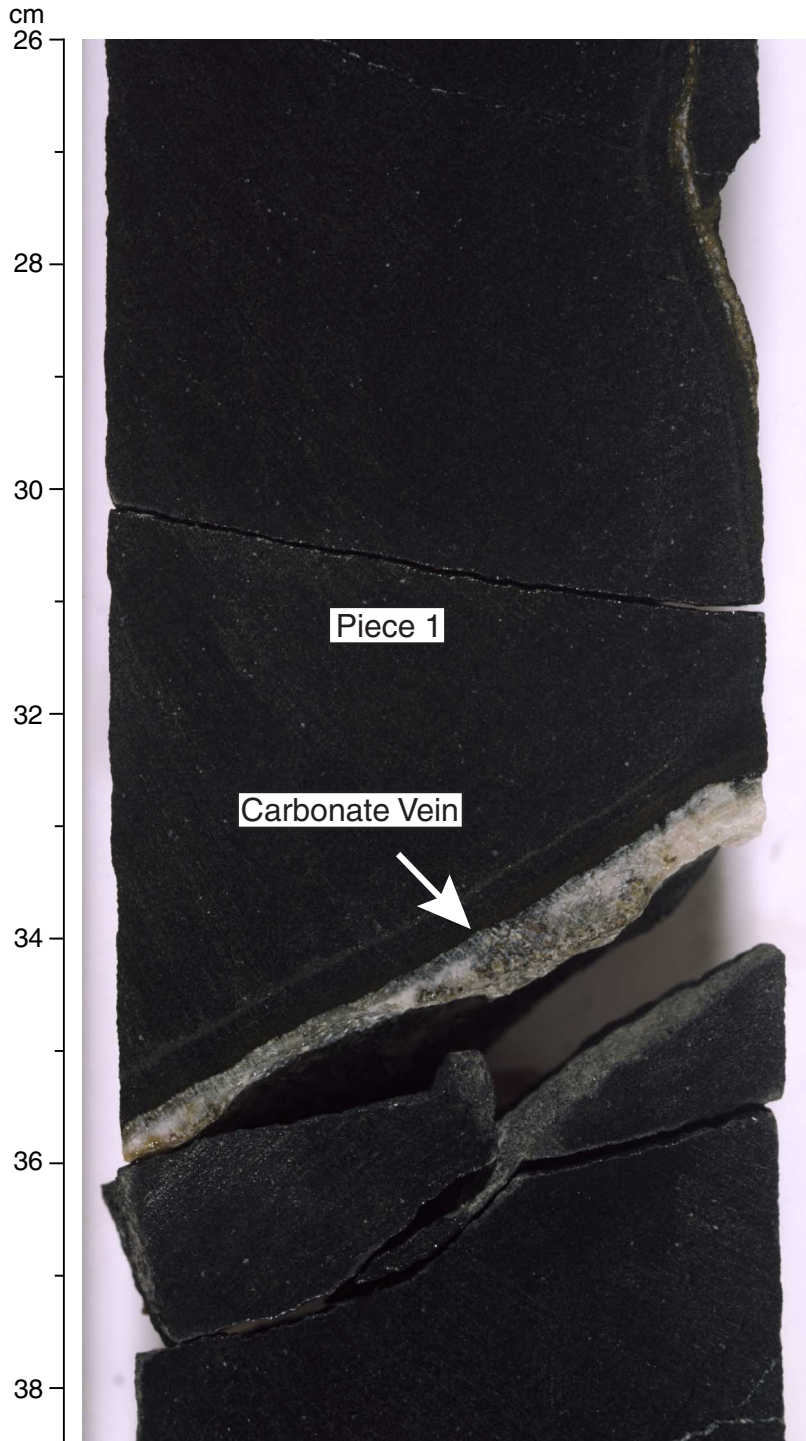


Figure F85. Sample 185-801C-37R-1, 27–29 cm, photographed in reflected light with a 20× objective lens. Shades of gray are identified as plagioclase (PL), pyroxene (PX), and titanomagnetite (MT), and representative examples are labeled. The white material on the right half of the photo is the secondary sulfide that is filling spaces between grains and pore space created by the alteration of interstitial material. A sharp boundary (10–20 μm wide) separates the area with sulfides from the area that is sulfide free.

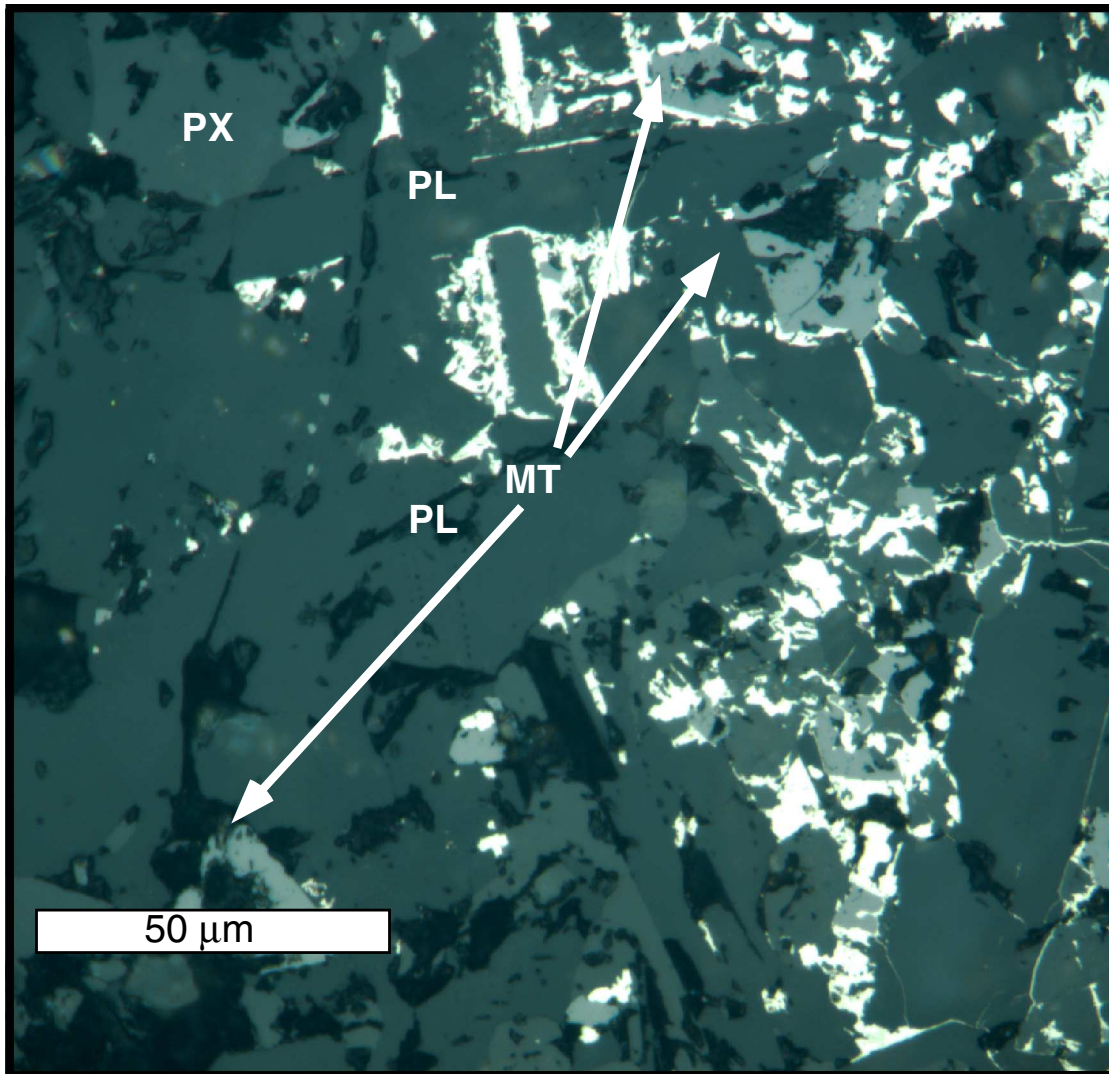


Figure F86. Photomicrograph of thin section from Sample 185-801C-50M-1, 43–45 cm. The groundmass is microcrystalline and is composed of plagioclase, pyroxene, traces of magnetite, and interstitial material. A fracture runs through the center of the photograph and is filled on one side by sulfide (S) and on the other by chalcedony (C). Secondary sulfides are also found in the groundmass near the fracture.

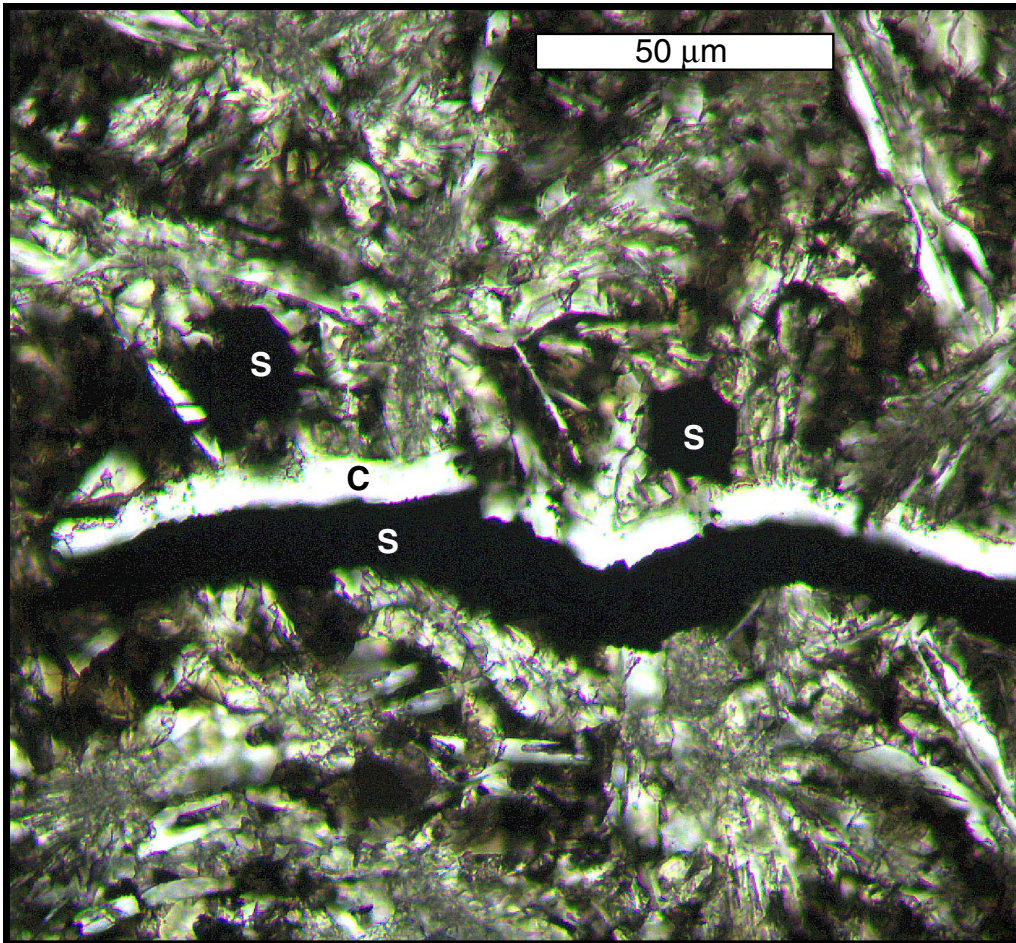


Figure F87. Photomicrographs of glass from Hole 801C viewed in plane-polarized light demonstrating microbial alteration textures. **A.** Sample 185-801C-12R-1, 85–89 cm, pillow margin. Brown variolitic (V) and clear glass with a single white plagioclase feldspar lath (P) in the lower right. A fine (5- μm wide) fracture extends into the glass in the center of the photograph from a fracture that lies along the edge of the feldspar. This 5- μm fracture is surrounded by delicate, hollow, ornamented channels that extend 5–10 μm from the fracture. These are similar to decorations found in a variety of subseafloor volcanic glasses that have been attributed to microbial activity. **B.** Sample 185-801C-17R-3, 85–91 cm, flow margin. This glass has parallel fractures and one of these lies at the bottom of the photograph and a second one is just beyond the top of the photograph. Surrounding the top fracture is a dense network of channels that extend 50–100 μm from the fracture and make the glass opaque. Some individual channels can be seen extending toward the center of the photograph. Where these intersect the surface of the thin section the channel cross section is $\sim 5 \mu\text{m}$. The fracture across the bottom of the photograph has not developed the dense network of channels. **C.** Sample 185-801C-48R-2, 121–123 cm. This photograph shows variolitic glass (V) and fresh glass (F), which are cut by a 100- μm -wide fracture. Near the bottom of the photograph, fresh glass is being replaced with clay and the boundary between them is irregular, much like the dark boundary in B. The glass next to the fracture is being converted to clay along an irregular alteration front. The box shows the location of D. **D.** Detail of Sample 185-801C-48R-2, 121–123 cm. Brown variolitic glass is around the edges of the photograph. The fracture is $\sim 20 \mu\text{m}$ wide and is filled with clay. The dark bands in the glass along the fracture contain irregular interconnected voids $\sim 1 \mu\text{m}$ across. This irregular texture is not preserved as the glass-to-clay alteration front advances. **E.** Sample 185-801C-801C-42R-2, 126–128 cm. Hyaloclastite thin section viewed in plane-polarized light. The white in the upper left corner is calcite. The glass is tan and contains a 500- μm white plagioclase feldspar (P). The outer 100–200 μm of the glass has been altered to clay that is the nearly same color as the glass. The glass is altered to clay along fractures. The area in the square is shown in F. **F.** Detail of Sample 185-801C-42R-2, 126–128 cm. The edge of the glass (upper left of photo) is scalloped and the edges of the fracture are irregular. In both areas the glass is being replaced by clay. **G.** Detail of Sample 185-801C-42R-2, 126–128 cm. The interior of a separate piece of glass from that shown in E and F. Three voids are labeled and 2- to 4- μm -diameter tunnels lead from the voids into the glass. The tunnels are 100–200 μm long and have irregular edges from which 1- μm tunnels branch. This is the only location in Hole 801C where this type of tunnel was observed. They are also similar to a style of tunneling seen in ocean floor basalts from other ODP holes. (Figure shown on next page.)

Figure F87 (continued). (Caption on previous page.)

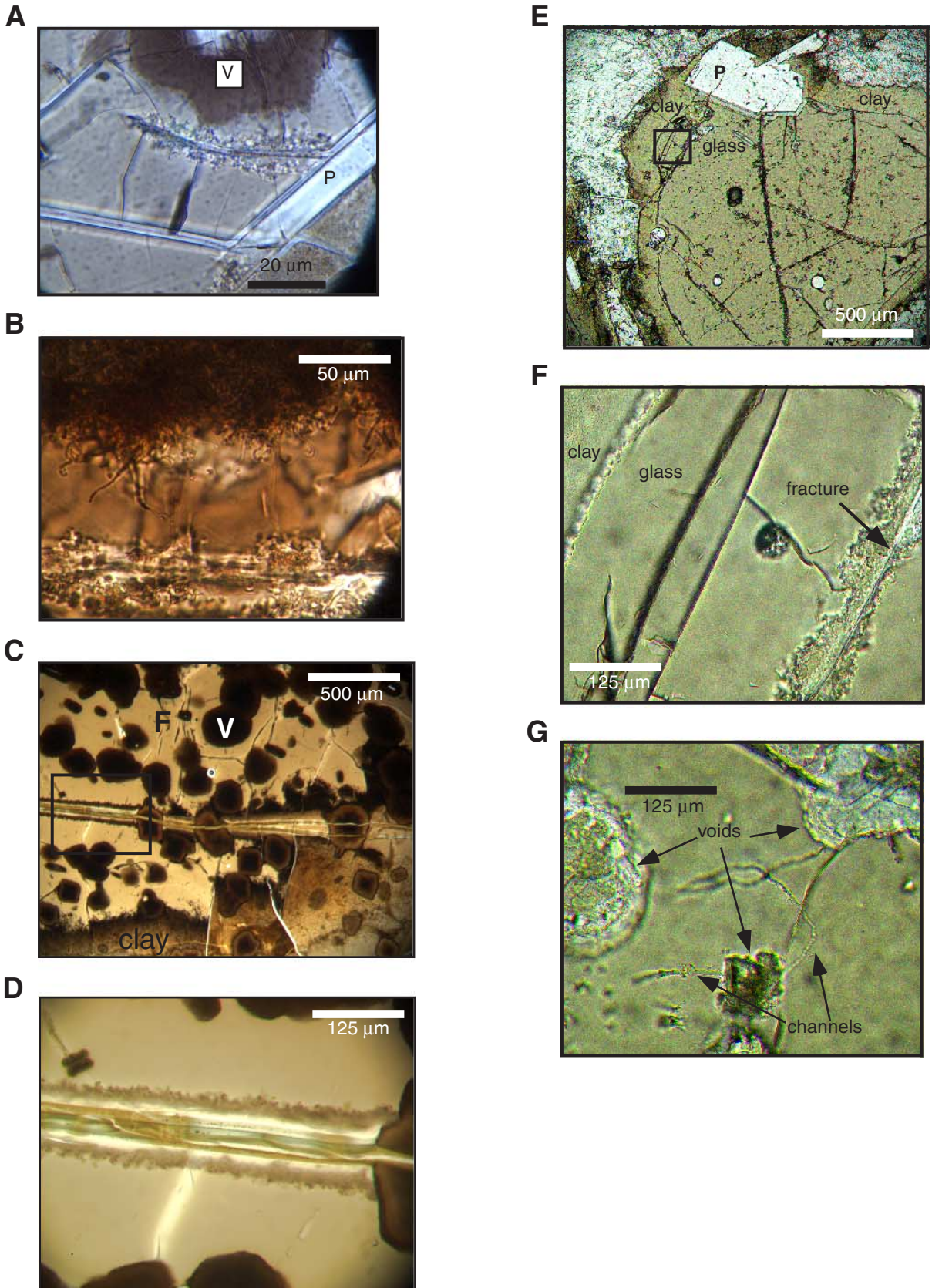


Figure F88. Photomicrographs of glass alteration fronts in three samples from Hole 801C showing the absence of microbial alteration. **A.** Sample 185-801C-16R-5, 107–110 cm. A sharp boundary between brown hydrated glass and greenish yellow clay runs across the top of the photograph. Smooth chemical boundaries within the glass and clay are indicated by color changes. This smooth zoning suggests pure chemical alteration, as microbes would produce localized zones of alteration. **B.** Sample 185-801C-17R-1, 35–38 cm. Two veins cut the glass. The white vein is filled with calcite and the brown vein cuts concentric bands of dark and light alteration. The dark alteration around the calcite vein appears to be homogeneous replacement of glass. The hydrated glass does not appear to have localized zones of alteration that could be attributed to microbes. **C.** Sample 185-801C-32R-1, 67–69 cm. Clay-filled fractures in hydrated glass. The glass around the fractures is darkened but there are no microbial alteration textures. Boundaries between clay and glass are smooth.

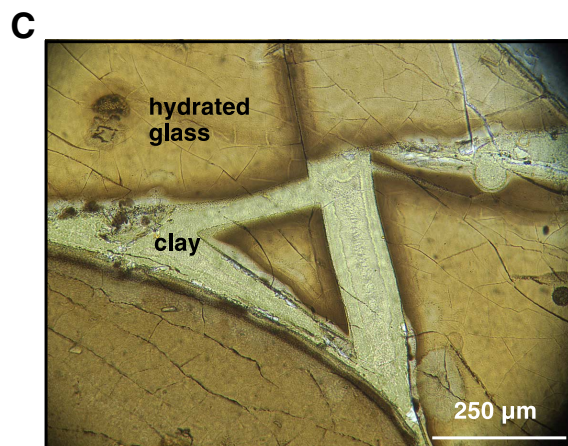
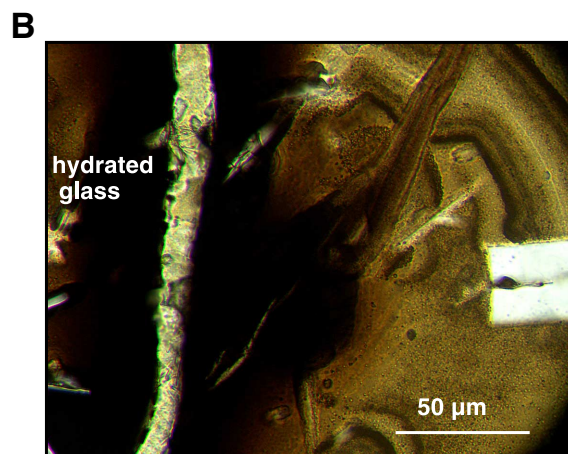
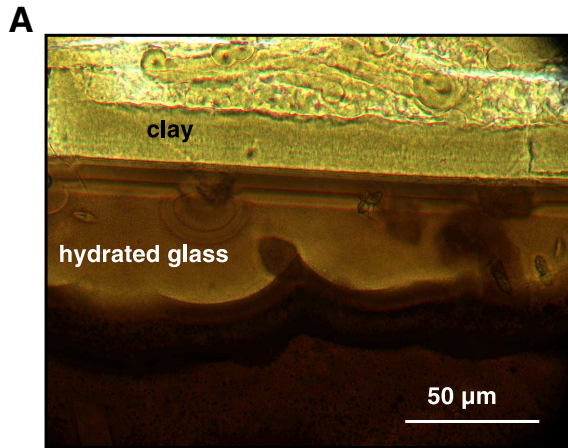


Figure F89. A. Time and temperature record of the first water sampling run. Near the seafloor (mudline) the temperature of the tool was allowed to stabilize for 10 min. The tool was then lowered into position in the bit (latch in). Then the whole drill string was advanced to 490 mbsf. After 10 min the drill string was raised and the tool released and brought back to the surface. B. Expanded view of the first run. C. The sequence of events for the second WSTP tool deployment were the same as for the first. Water was collected at 540 mbsf. D. Expanded view of the second run.

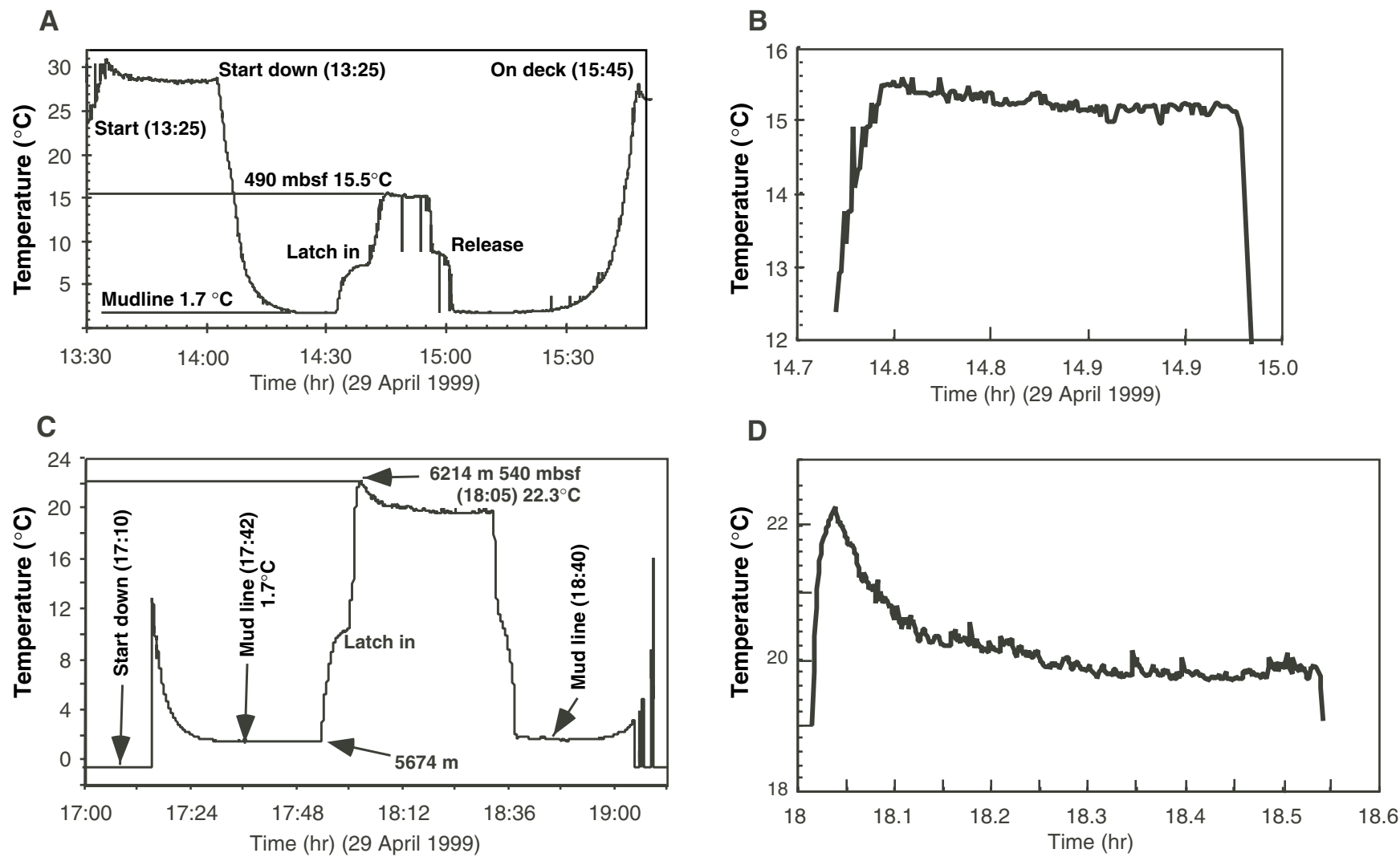


Figure F90. Water temperatures in Hole 801C before drilling during Leg 185. Temperatures of WSTP1 and WSTP2 were obtained with the drill string advancing ~30 m into undisturbed water with the WSTP tool latched into the end of the string. The solid line is that of Larson et al. (1993) for temperatures measured between 490 and 540 mbsf. The dashed straight line is drawn to 1.7°C at 0 mbsf (mudline) for WSTP2. The curved line is one possible representation of the temperature where cool water has been mixed with the warm water of the hole. This could have happened during the introduction of the drill string into the hole or by slow influx of bottom water into the hole and possibly into the hydrothermal zone (indicated by horizontal lines).

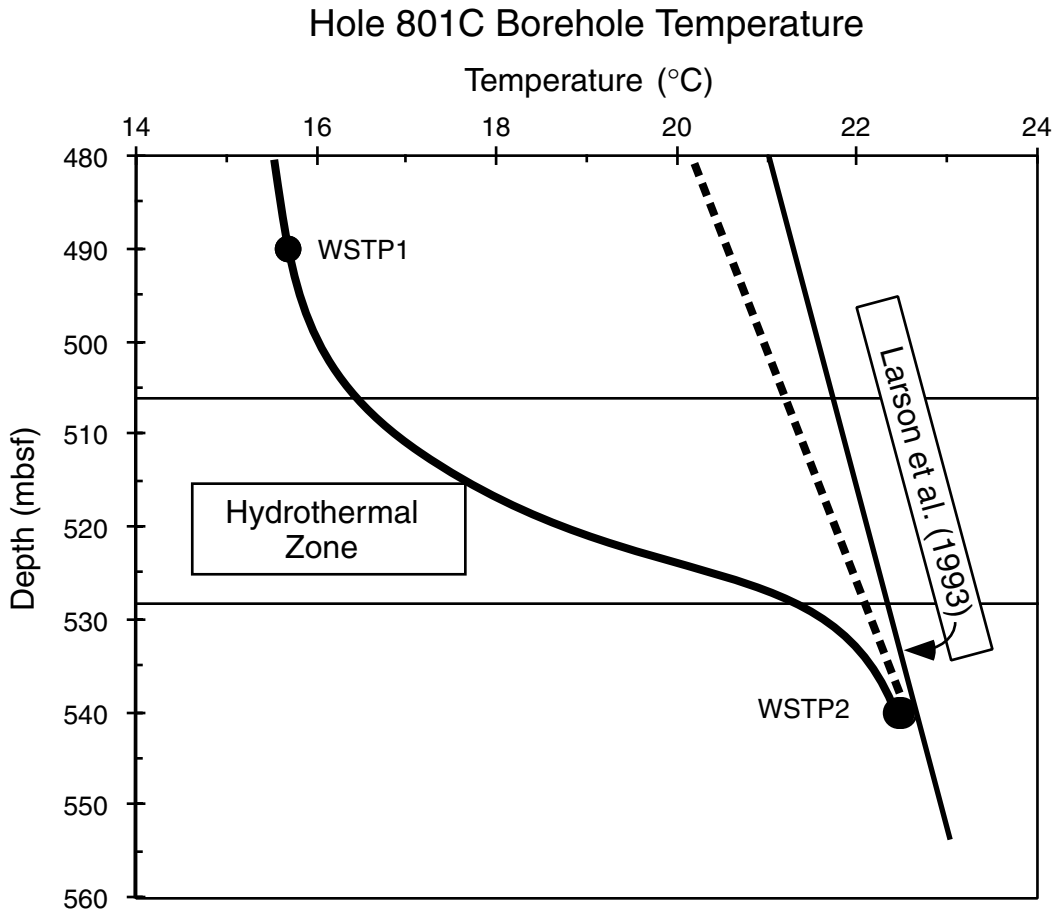


Figure F91. Comparison of MST-NGR data, K₂O measurements on core samples, MST-MS data, and down-hole gamma-ray logs for Core 185-801C-14R. The lithologic column on the left is schematic and not an actual core photo. Lines show the locations of sediment and precipitated interpillow material (IP), which correspond closely to the measured high K₂O values, high gamma-ray signals, and low MS measurements.

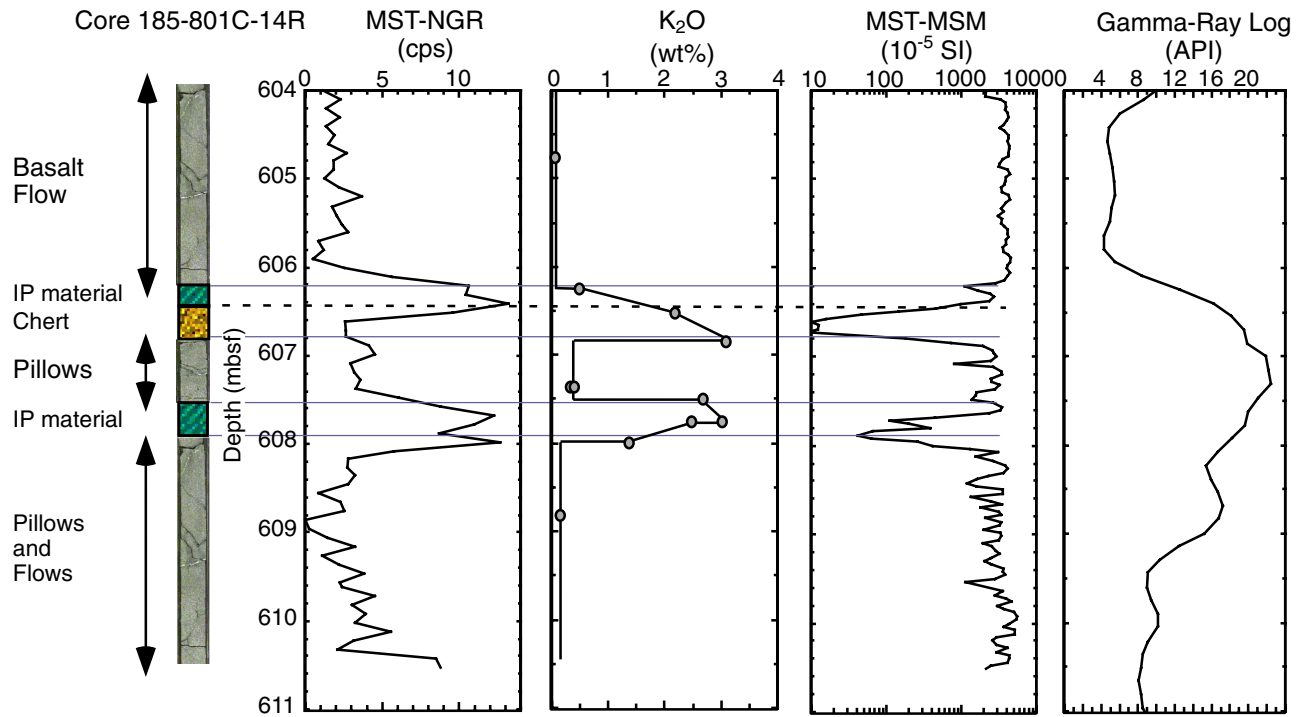


Figure F92. MST-NGR and core K_2O data for Section 185-801C-14R-3. Schematic lithologic column and section photo are on the left, with discrete AA samples indicated. **A.** Actual AA K_2O measurements are shown as large open circles (data in Table T23, p. 220). Interpolated K_2O (bars with diagonal fill) are calculated by apportioning discrete analyses over 10-cm intervals (see Table T24, p. 221, for proportions) such that they are comparable to the footprint of the MST measurements. **B.** Routine MST-NGR measurements (whole-round with 20-s readings every 10 cm). **C.** Half-round data for longer counting times. The striped bars are the average and standard deviation of two MST passes with 60-s readings every 10 cm, and the gray bars are the same for three MST passes with 20-s readings.

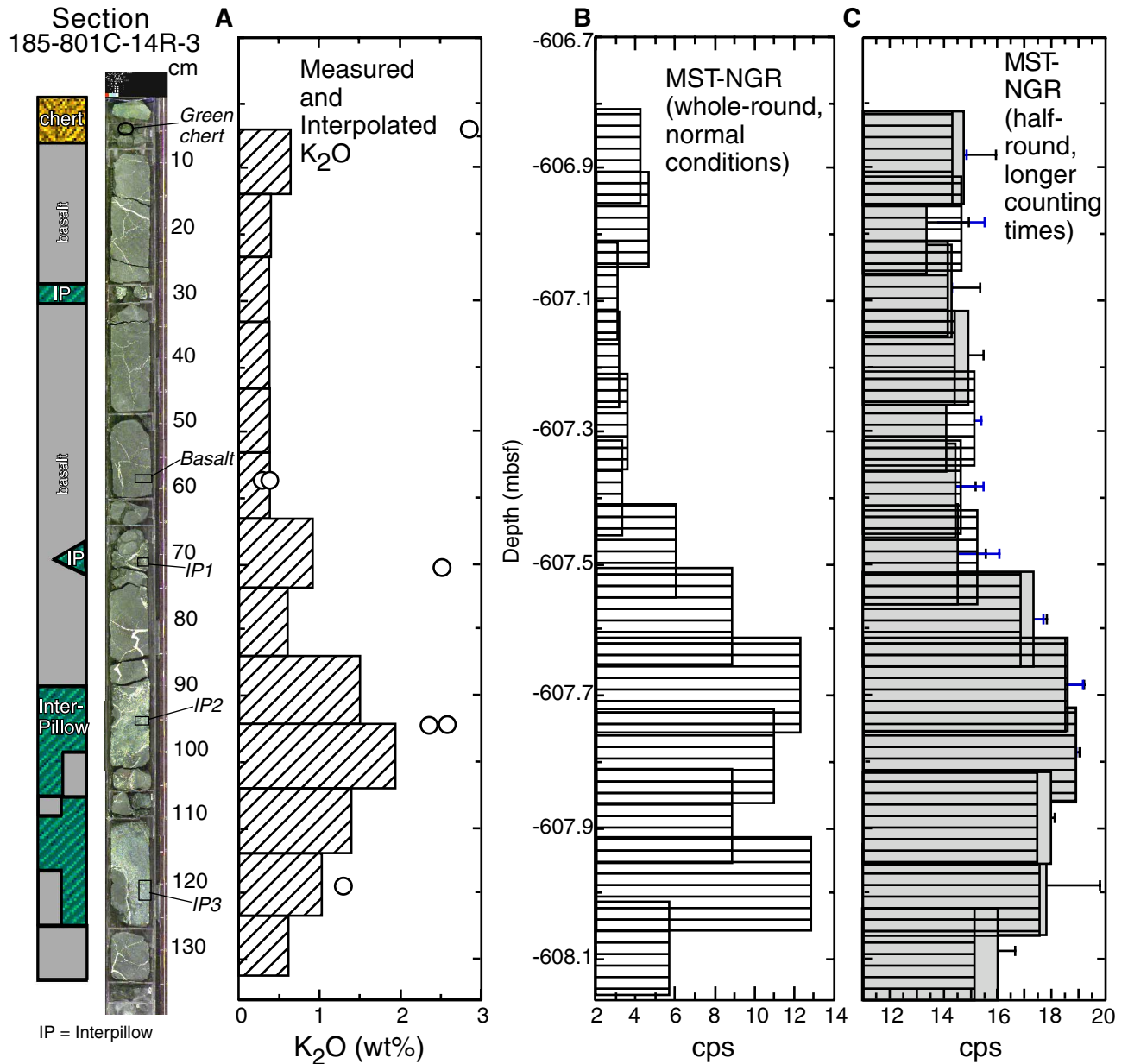


Figure F93. A. Relationship between whole-round and half-round core MST-NGR measurements on Section 185-801C-14R-3. The whole-round data are corrected for background counts (11.75 cps), whereas the half-round data are not. The equation for a best-fit line is given and used to correct half-round measurements to whole-round counts per second. **B.** Calibration of MST-NGR to K₂O concentration, based on data in Table T24, p. 221. Error bars on individual points are from 10% uncertainty in AA measurements and one standard deviation of the MST readings. Calibration assumes all natural gamma-ray counts are due to K₂O (and not U and Th). The linear regression is shown (thick line), including errors on the intercept (thinner lines) and slope (dashed lines). Uncertainties in regression are given in parentheses; the total uncertainty region is shown in the shaded area. At low count rates, most of the uncertainty is in the intercept. Point at 80 cm is excluded from the regression.

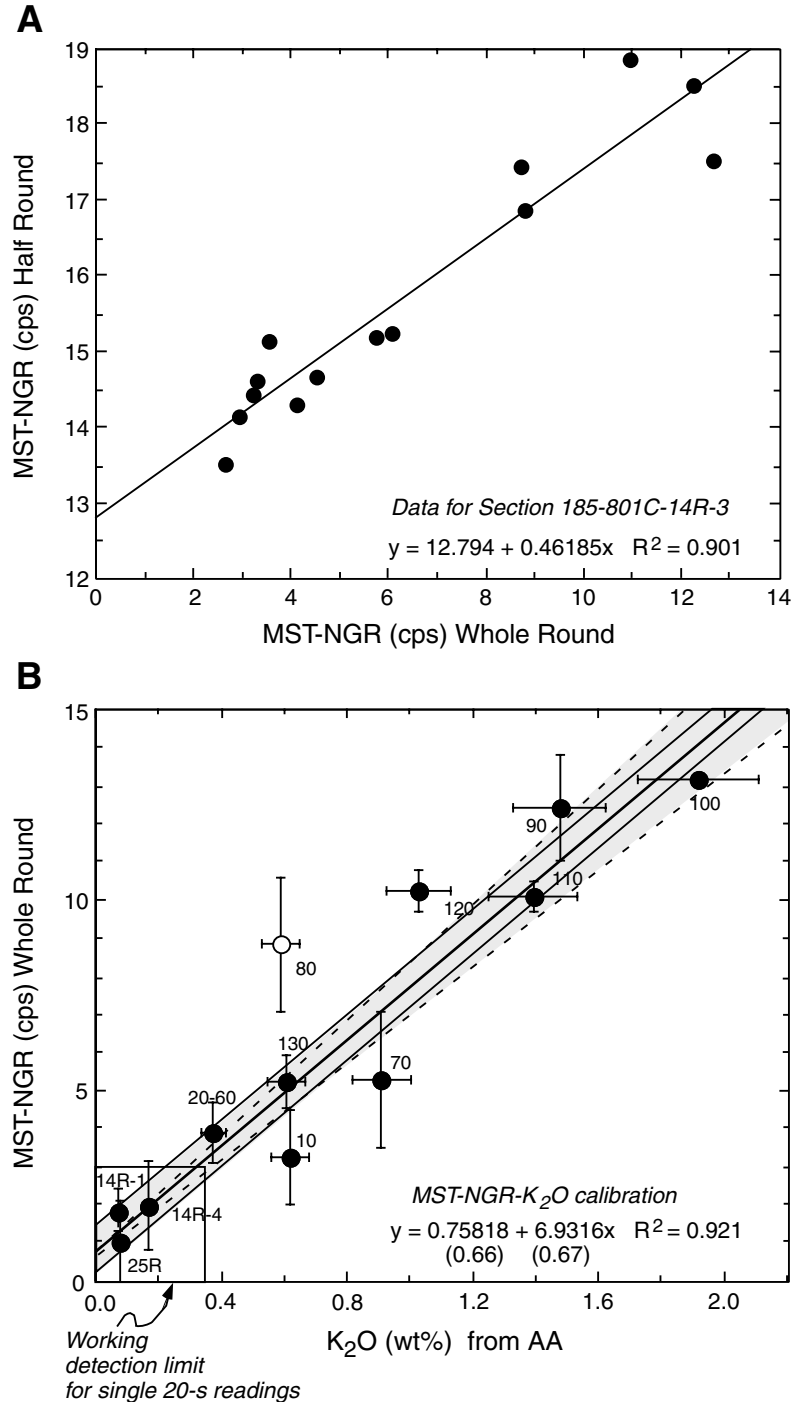


Figure F94. K_2O vs. depth in Hole 801C (tholeiitic section only). K_2O calculated from MST-NGR and calibration shown in Figure F91, p. 166, and plotted as the average of each core section. Three zones of high K_2O in the section are associated with the two Fe-Si hydrothermal units (HT Sequences II and V) and the breccia unit (VII). Low K_2O occurs around Core 185-801C-26R, where the section changes from pillows and flows (IV) to predominantly flows (VI). The average K_2O for the 400-m-thick tholeiitic section (dashed line) is $0.31 \text{ wt\% } K_2O$, significantly enriched by alteration over the primary magmatic value ($\sim 0.08 \text{ wt\% } K_2O$).

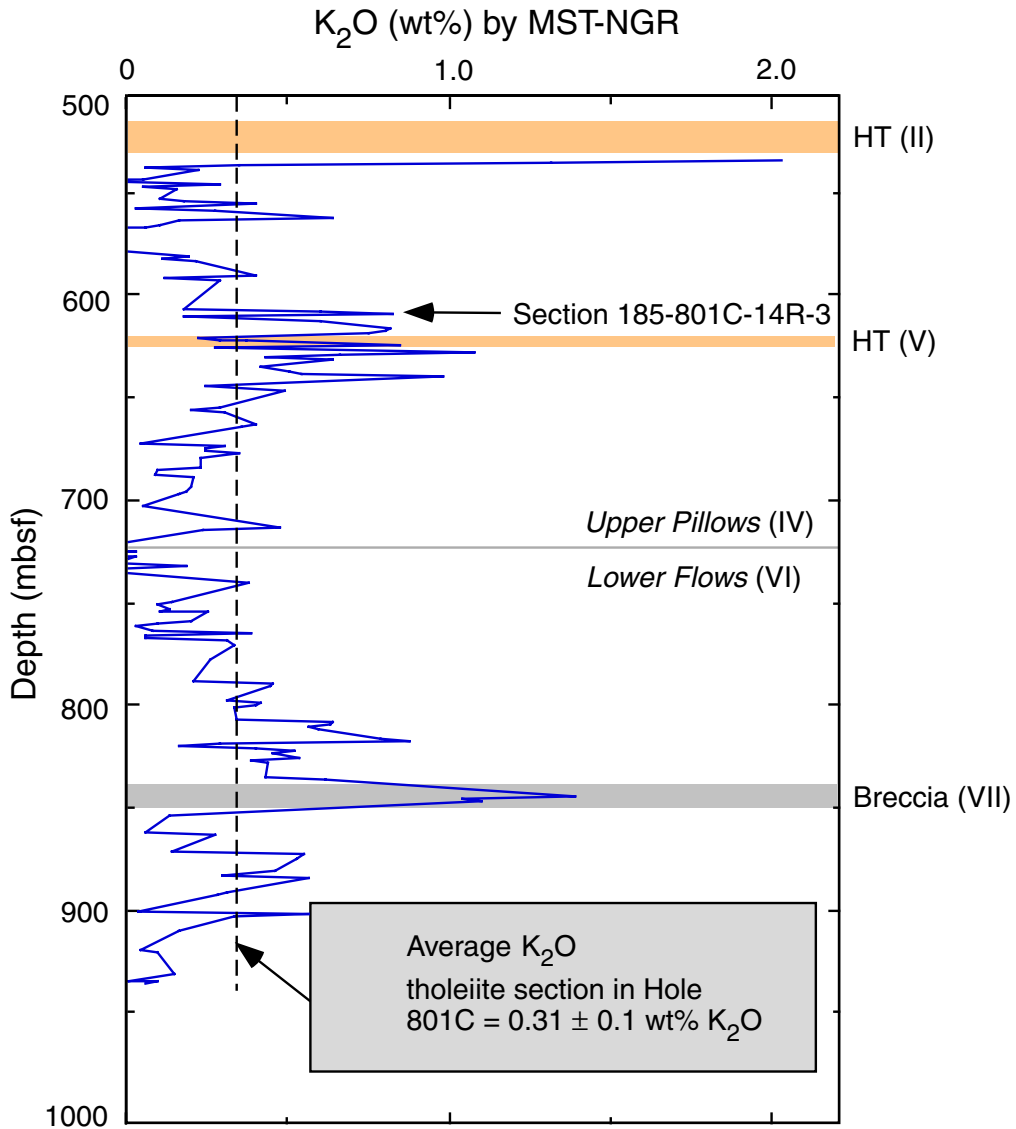


Table T1. Coring summary, Site 801.

Core	Date (1999)	Time (UTC)	Depth (mbsf)		Length (m)		Recovery (%)	Comments
			Top	Bottom	Cored	Recovered		
185-801C-								
13R	30 April	0530	594.3	604.0	9.7	0.36	3.71	
14R	30 April	1210	604.0	613.7	9.7	6.42	66.19	
15R	30 April	1910	613.7	623.3	9.6	8.54	88.96	
16R	1 May	0115	623.3	632.8	9.5	6.72	70.74	
17R	1 May	0715	632.8	642.2	9.4	5.78	61.49	
18R	1 May	1225	642.2	651.7	9.5	2.89	30.42	
19R	1 May	1755	651.7	660.7	9.0	3.54	39.33	
20R	1 May	2255	660.7	670.0	9.3	2.97	31.94	
21R	2 May	0355	670.0	673.6	3.6	3.63	100.83	
22R	4 May	0355	673.6	681.9	8.3	3.95	47.59	
23R	4 May	0905	681.9	691.3	9.4	4.25	45.21	
24R	4 May	1430	691.3	700.7	9.4	3.66	38.94	
25R	4 May	2140	700.7	710.2	9.5	1.67	17.58	
26R	5 May	0430	710.2	719.7	9.5	2.29	24.11	
27R	5 May	1305	719.7	728.7	9.0	6.06	67.33	
28R	5 May	2040	728.7	737.9	9.2	4.50	48.91	
29R	6 May	0510	737.9	747.3	9.4	1.98	21.06	
30R	6 May	1315	747.3	756.6	9.3	7.92	85.16	
31R	8 May	1945	756.6	766.3	9.7	10.64	109.69	
32R	9 May	0135	766.3	775.7	9.4	1.87	19.89	
33R	9 May	1020	775.7	785.3	9.6	1.46	15.21	
34R	9 May	1720	785.3	794.9	9.6	5.06	52.71	
35R	9 May	2350	794.9	804.1	9.2	5.87	63.80	
36R	10 May	0500	804.1	813.3	9.2	7.25	78.80	
37R	10 May	1125	813.3	822.8	9.5	8.74	92.00	
38R	10 May	1710	822.8	832.2	9.4	5.48	58.30	
39R	10 May	2210	832.2	841.5	9.3	3.70	39.78	
40R	11 May	0415	841.5	850.8	9.3	5.19	55.81	
41R	11 May	0920	850.8	860.0	9.2	1.50	16.30	
42R	11 May	1405	860.0	869.1	9.1	3.49	38.35	
43R	13 May	0610	869.1	878.8	9.7	3.83	39.48	
44R	13 May	1120	878.8	888.4	9.6	4.81	50.10	
45R	13 May	1655	888.4	898.0	9.6	2.42	25.21	
46R	13 May	2245	898.0	907.7	9.7	4.07	41.96	
47R	14 May	0520	907.7	916.7	9.0	1.02	11.33	
48R	14 May	1400	916.7	926.2	9.5	3.80	40.00	
Drilled from 926.2 to 928.3 mbsf								
49M	18 May	0110	928.3	931.5	3.2	1.01	31.56	
50M	18 May	0700	931.5	932.0	0.5	0.48	96.00	
51M	18 May	1215	932.0	932.8	0.8	0.80	100.00	
52M	18 May	2145	932.8	935.7	2.9	0.80	27.59	
Coring totals:					339.3	160.42	47.28	
185-801D-								
Drilled from 0.0 to 19.3 mbsf								
1W	29 April	815						Bead test for biological contamination study
Coring totals:					0.0	9.38	—	

Notes: UTC = Universal Time Coordinated. — = not applicable. This table is also available in [ASCII format](#).

Table T2. Expanded coring summary, Site 801. (See table notes. Continued on next four pages).

Hole 801C													
Latitude: 18.6422997° (18°38.53798'N)													
Longitude: 156.3598022° (156°21.58813'E)													
Depth (mbrf): 5685													
Core	Date (1999)	Time (UTC)	Depth (mbsf)		Length (m)		Recovery (%)	Section	Length (m)		Section (mbsf)		Comments
			Top	Bottom	Cored	Recovered			Liner	Curated	Top	Bottom	
185-801C-13R	30 April	0530	594.3	604.0	9.7	0.36	3.7	1	0.36	0.47	594.30	594.77	
								Totals:	0.36	0.47			
14R	30 April	1210	604.0	613.7	9.7	6.42	66.2	1	1.15	1.31	604.00	605.31	
								2	1.32	1.47	605.31	606.78	
								3	1.41	1.38	606.78	608.16	
								4	1.04	1.46	608.16	609.62	
								5	1.50	0.96	609.62	610.58	
								Totals:	6.42	6.58			
15R	30 April	1910	613.7	623.3	9.6	8.54	89.0	1	1.47	1.32	613.70	615.02	
								2	1.06	1.39	615.02	616.41	
								3	1.28	1.30	616.41	617.71	
								4	1.31	1.32	617.71	619.03	
								5	0.94	0.95	619.03	619.98	
								6	1.39	1.40	619.98	621.38	
								7	1.09	1.12	621.38	622.50	
Totals:	8.54	8.80											
16R	1 May	0115	623.3	632.8	9.5	6.72	70.7	1	2.18	1.44	623.30	624.74	
								2	0.75	1.28	624.74	626.02	
								3	1.10	1.41	626.02	627.43	
								4	1.28	1.46	627.43	628.89	
								5	1.41	1.28	628.89	630.17	
								Totals:	6.72	6.87			
17R	1 May	0715	632.8	642.2	9.4	5.78	61.5	1	0.17	1.48	632.8	634.28	
								2	1.31	1.5	634.28	635.78	
								3	1.42	1.44	635.78	637.22	
								4	1.41	1.4	637.22	638.62	
								5	1.47	0.35	638.62	638.97	
								Totals:	5.78	6.17			
18R	1 May	1225	642.2	651.7	9.5	2.89	30.4	1	0.93	1.5	642.2	643.70	
								2	1.41	1.5	643.7	645.20	
								3	0.55	0.25	645.2	645.45	
								Totals:	2.89	3.25			
19R	1 May	1755	651.7	660.7	9.0	3.54	39.3	1	1.12	1.49	651.70	653.19	
								2	0.92	1.20	653.19	654.39	
								3	1.50	0.87	654.39	655.26	
								Totals:	3.54	3.56			

Table T2 (continued).

Core	Date (1999)	Time (UTC)	Depth (mbsf)		Length (m)		Recovery (%)	Section	Length (m)		Section (mbsf)		Comments
			Top	Bottom	Cored	Recovered			Liner	Curated	Top	Bottom	
20R	1 May	2255	660.7	670.0	9.3	2.97	31.9	1	1.20	1.42	660.70	662.12	
								2	1.50	1.50	662.12	663.62	
								3	0.27	0.50	663.62	664.12	
								Totals:	2.97	3.42			
21R	2 May	0355	670.0	673.6	3.6	3.63	100.8	1	1.30	1.43	670.00	671.43	
								2	1.30	1.22	671.43	672.65	
								3	1.03	1.10	672.65	673.75	
								Totals:	3.63	3.75			
22R	4 May	0355	673.6	681.9	8.3	3.95	47.6	1	1.15	1.24	673.60	674.84	
								2	1.30	1.50	674.84	676.34	
								3	1.50	1.22	676.34	677.56	
								Totals:	3.95	3.96			
23R	4 May	0905	681.9	691.3	9.4	4.25	45.2	1	1.01	1.25	681.90	683.15	
								2	1.50	1.43	683.15	684.58	
								3	1.47	1.40	684.58	685.98	
								4	0.27	1.01	685.98	686.99	
								Totals:	4.25	5.09			
24R	4 May	1430	691.3	700.7	9.4	3.66	38.9	1	0.78	1.33	691.30	692.63	Pieces in interval from 100 cm to bottom of section may be out of order and unoriented; fell out of core catcher onto rig floor
								2	1.48	1.50	692.63	694.13	
								3	1.40	1.44	694.13	695.57	
								Totals:	3.66	4.27			
25R	4 May	2140	700.7	710.2	9.5	1.67	17.6	1	1.67	1.46	700.70	702.16	
								Totals:	1.67	1.46			
26R	5 May	0430	710.2	719.7	9.5	2.29	24.1	1	1.14	1.33	710.20	711.53	
								2	1.15	1.30	711.53	712.83	
								Totals:	2.29	2.63			
27R	5 May	1305	719.7	728.7	9.0	6.06	67.3	1	0.98	1.28	719.70	720.98	Pieces 2 through 5 are unoriented and may be out of order; fell out of core catcher onto rig floor
								2	1.43	1.50	720.98	722.48	
								3	1.25	1.30	722.48	723.78	
								4	1.50	1.44	723.78	725.22	
								5	0.90	0.90	725.22	726.12	
								Totals:	6.06	6.42			
28R	5 May	2040	728.7	737.9	9.2	4.5	48.9	1	1.50	1.34	728.70	730.04	
								2	1.50	1.50	730.04	731.54	
								3	1.50	1.50	731.54	733.04	
								Totals:	4.50	4.34			
29R	6 May	0510	737.9	747.3	9.4	1.98	21.1	1	0.82	1.45	737.90	739.35	

Table T2 (continued).

Core	Date (1999)	Time (UTC)	Depth (mbsf)		Length (m)		Recovery (%)	Section	Length (m)		Section (mbsf)		Comments
			Top	Bottom	Cored	Recovered			Liner	Curated	Top	Bottom	
30R	6 May	1315	747.3	756.6	9.3	7.92	85.2	2	1.16	0.54	739.35	739.89	
								Totals:	1.98	1.99			
								1	1.91	1.44	747.30	748.74	
								2	1.42	1.32	748.74	750.06	
								3	1.34	1.32	750.06	751.38	
								4	1.46	0.78	751.38	752.16	
31R	8 May	1945	756.6	766.3	9.7	10.64	109.7	5	1.42	1.50	752.16	753.66	Stuck in bit, fell onto deck after pipe trip, no orientations or correct positions of pieces within section Stuck in bit, fell onto deck, no orientations or correct positions of pieces within section
								6	0.37	0.45	753.66	754.11	
								Totals:	7.92	6.81			
								1	1.52	1.30	756.60	757.90	
								2	1.52	1.28	757.90	759.18	
								3	1.52	1.41	759.18	760.59	
32R	9 May	0135	766.3	775.7	9.4	1.87	19.9	4	1.52	1.45	760.59	762.04	
								5	1.52	1.30	762.04	763.34	
								6	1.52	1.40	763.34	764.74	
								7	1.52	1.50	764.74	766.24	
								Totals:	10.64	9.64			
								1	0.60	1.50	766.30	767.80	
33R	9 May	1020	775.7	785.3	9.6	1.46	15.2	2	1.27	0.63	767.80	768.43	
								Totals:	1.87	2.13			
34R	9 May	1720	785.3	794.9	9.6	5.06	52.7	1	1.00	1.29	775.70	776.99	
								2	0.46	0.47	776.99	777.46	
35R	9 May	2350	794.9	804.1	9.2	5.87	63.8	Totals:	1.46	1.76			
								1	1.58	1.24	785.30	786.54	
								2	1.50	1.47	786.54	788.01	
								3	1.38	1.50	788.01	789.51	
								4	0.60	0.30	789.51	789.81	
								Totals:	5.06	4.51			
36R	10 May	0500	804.1	813.3	9.2	7.25	78.8	1	1.27	1.37	794.90	796.27	
								2	1.29	1.35	796.27	797.62	
								3	1.06	1.50	797.62	799.12	
								4	1.25	1.50	799.12	800.62	
								5	1.00	0.00			
								Totals:	5.87	5.72			
36R	10 May	0500	804.1	813.3	9.2	7.25	78.8	1	1.72	1.34	804.10	805.44	
								2	1.39	1.33	805.44	806.77	
								3	1.45	1.42	806.77	808.19	
								4	1.30	1.48	808.19	809.67	
								5	1.39	0.95	809.67	810.62	
								Totals:	7.25	6.52			

Table T2 (continued).

Core	Date (1999)	Time (UTC)	Depth (mbsf)		Length (m)		Recovery (%)	Section	Length (m)		Section (mbsf)		Comments
			Top	Bottom	Cored	Recovered			Liner	Curated	Top	Bottom	
37R	10 May	1125	813.3	822.8	9.5	8.74	92.0						
								1	1.05	1.45	813.30	814.75	
								2	1.44	1.10	814.75	815.85	
								3	1.54	1.41	815.85	817.26	
								4	1.50	1.20	817.26	818.46	
								5	1.50	1.34	818.46	819.80	
								6	1.19	1.50	819.80	821.30	
								7	0.52	1.22	821.30	822.52	
Totals:	8.74	9.22											
38R	10 May	1710	822.8	832.2	9.4	5.48	58.3						
								1	1.24	1.46	822.80	824.26	
								2	1.38	1.50	824.26	825.76	
								3	1.36	1.50	825.76	827.26	
								4	1.50	0.55	827.26	827.81	
Totals:	5.48	5.01											
39R	10 May	2210	832.2	841.5	9.3	3.7	39.8						
								1	1.85	1.47	832.20	833.67	
								2	1.85	1.22	833.67	834.89	
Totals:	3.70	2.69											
40R	11 May	0415	841.5	850.8	9.3	5.19	55.8						
								1	1.26	1.48	841.50	842.98	
								2	1.24	1.41	842.98	844.39	
								3	1.46	1.46	844.39	845.85	
								4	1.23	0.39	845.85	846.24	
Totals:	5.19	4.74											
41R	11 May	920	850.8	860.0	9.2	1.5	16.3						
								1	1.50	1.50	850.80	852.30	
Totals:	1.50	1.50											
42R	11 May	1405	860.0	869.1	9.1	3.49	38.4						
								1	1.37	1.21	860.00	861.21	
								2	1.37	1.50	861.21	862.71	
								3	0.75	0.29	862.71	863.00	
Totals:	3.49	3.00											
43R	13 May	0610	869.1	878.8	9.7	3.83	39.5						
								1	0.95	1.46	869.10	870.56	
								2	1.36	1.36	870.56	871.92	
								3	1.52	1.36	871.92	873.28	
Totals:	3.83	4.18											
44R	13 May	1120	878.8	888.4	9.6	4.81	50.1						
								1	1.50	1.26	878.80	880.06	
								2	1.87	1.50	880.06	881.56	
								3	1.44	1.50	881.56	883.06	
Totals:	4.81	4.26											
45R	13 May	1655	888.4	898.0	9.6	2.42	25.2						
								1	1.42	1.36	888.40	889.76	
								2	1.00	1.24	889.76	891.00	
Totals:	2.42	2.60											
46R	13 May	2245	898.0	907.7	9.7	4.07	42.0						
								1	1.42	1.42	898.00	899.42	
2	1.15	1.29	899.42	900.71									

Table T2 (continued).

Core	Date (1999)	Time (UTC)	Depth (mbsf)		Length (m)		Recovery (%)	Section	Length (m)		Section (mbsf)		Comments	
			Top	Bottom	Cored	Recovered			Liner	Curated	Top	Bottom		
47R	14 May	0520	907.7	916.7	9.0	1.02	11.3	3	1.50	1.14	900.71	901.85		
								Totals:	4.07	3.85				
48R	14 May	1400	916.7	926.2	9.5	3.8	40.0	1	1.02	1.32	907.70	909.02		
								Totals:	1.02	1.32				
49M	18 May	0110	928.3	931.5	3.2	1.01	31.6	1	1.00	1.30	916.70	918.00		
								Totals:	3.80	3.24				
				Drilled from 926.2 to 928.3 mbsf										
50M	18 May	0700	931.5	932.0	0.5	0.48	96.0	1	1.01	1.12	928.30	929.42		
								Totals:	1.01	1.12				
51M	18 May	1215	932.0	932.8	0.8	0.8	100	1	0.48	0.57	931.50	932.07		
								Totals:	0.48	0.57				
52M	18 May	2145	932.8	935.7	2.9	0.8	27.6	1	0.80	0.87	932.00	932.87		
								Totals:	0.80	0.87				
Coring totals:					339.3	160.42	47.28							
Drilled:					2.1									
Total:					341.4									
Hole 801D														
Latitude: 18.6422997° (18° 38.53798' N)														
Longitude: 156.3598022° (156° 21.58813' E)														
Depth (mbrf): 5685														
Core	Date (1999)	Time (UTC)	Depth (mbsf)		Length (m)		Recovery (%)	Section	Length (m)		Section (mbsf)		Comments	
			Top	Bottom	Cored	Recovered			Liner	Curated	Top	Bottom		
185-801D-1W	29 April	0815	***Drilled from 0.0 to 19.3 mbsf***											
			1	1.50	1.50	0.00	1.50							
			2	1.50	1.50	1.50	3.00							
			3	1.50	1.50	3.00	4.50							
			4	1.50	1.50	4.50	6.00							
			5	1.50	1.50	6.00	7.50							
			6	1.30	1.30	7.50	8.80							
			7	0.43	0.43	8.80	9.23							
			CC(w/7)	0.15	0.15	9.23	9.38							
			Totals:	9.38	9.38									
Totals:					0.0	9.38	—							

Notes: UTC = Universal Time Coordinated. — = not applicable. This table is also available in [ASCII format](#).

Table T3. Radiolarians from Samples 129-801B-39R-1, 8–11 cm, and 37R-1, 0–6 cm.

RADIOLARIAN TAXA	129-801B-39R-1, 8-11 cm	129-801B-37R-1, 0-6 cm
<i>Guexella nudata</i> (Koehler)	X	X
<i>Stichocapsa robusta</i> Matsuoka	X	X
<i>Williriedellum</i> sp. A sensu Matsuoka	X	X
<i>Saitoum levium</i> De Wever	X	X
<i>Ristola</i> (?) <i>turpicula</i> Pessagno and Whalen	X	
<i>Dictyomitrella</i> (?) <i>kamoensis</i> Mizutani and Kido	X	X
<i>Parvicingula dhimenaensis</i> s.l. Baumgartner	X	X
<i>Tricolocapsa</i> (?) sp. aff. <i>T. fusiformis</i> Yao	X	X
<i>Orbiculiforma</i> (?) sp. X	X	X
<i>Homeoparonaella elegans</i> (Pessagno)	X	X
<i>Acaeniotylopsis variatus triacanthus</i> Kito and De Wever		X
<i>Emiluvia chica</i> s.l. Foreman		X
<i>Archaeohagiastrum longipes</i> Baumgartner		X
<i>Higumastra imbricata</i> (Ozoldova)		X
<i>Emiluvia premyogii</i> Baumgartner		X
<i>Tetraditryma corralitosensis corralitosensis</i> (Pessagno)		X
<i>Perispyridium ordinarium</i> gr. (Pessagno)		X
<i>Archaeohagiastrum munitum</i> Baumgartner		X
<i>Amphipyndax durisaeptum</i> Aita		X
<i>Napora pyramidalis</i> Baumgartner		X
<i>Haliodyctya</i> (?) <i>hojnosi</i> Riedel and Sanfilippo		X
<i>Bernoullius rectispinus delnortensis</i> Pessagno, Blome and Hull		X
<i>Hexasaturnalis tetraspinus</i> (Yao)		X
<i>Acanthocircus suboblongus suboblongus</i> (Yao)		X
<i>Haliodyctya</i> (?) <i>antiqua</i> s.l. (Rüst)		X
<i>Leugeo hexacubicus</i> (Baumgartner)		X
<i>Palinandromeda podbielensis</i> (Ozoldova)		X
<i>Podobursa helvetica</i> (Rüst)		X
<i>Mirifusus fragilis</i> s.l. Baumgartner		X
<i>Linaresia beniderkoulensis</i> El Kadiri		X
<i>Transsuum maxwelli</i> gr. (Pessagno)		X
<i>Eucyrtidiellum unumaense</i> s.l. (Yao)		X
<i>Spongocapsula perampla</i> (Rüst)		X
<i>Stichocapsa convexa</i> Yao		X
<i>Eucyrtidiellum unumaense pustulatum</i> Baumgartner		X
<i>Tricolocapsa conexa</i> Matsuoka		X

Note: Taxonomy is according to INTERRAD Jurassic-Cretaceous working group (1995).

Table T4. Igneous core description log, Hole 801C. (See table notes. Continued on next 16 pages.)

Core, section	Piece	Analysis*	Depth (mbsf)		Interval (cm)	Length (cm)			Unit, subunit	Lithology	Texture	Structure	Color	Comments	Chilled margin present	
			Top	Bottom		Interval	Unit	Subunit							Top	Base
129-801C-																
1R-1	1A-2G	3	493.70	494.94	0-124	124	361	—	1	Alkali aphyric microdolerite, sparsely plagioclase phyric basalt	Medium to fine grained	Sill	White, speckled gray to black	Massive unit no contacts, sparse plagioclase phenocrysts, no vesicles	N	Y
1R-2	1A-3F	1	494.94	496.30	0-136	136	361	—	1	Same as above	Same as above		Same as above	—	N	Y
1R-3	1A-1G	1	496.30	497.31	0-101	101	361	—	1	Same as above	Same as above		Same as above	—	N	Y
1R-3	2	1	497.31	497.40	101-110	9	398	—	2	Sparsely plagioclase, olivine microphyric, aphyric basalt	Fine to medium grained, massive		Brown/gray to speckled gray	Diffuse contacts, grain size changes, mineral accumulation	N	Y
1R-4	1-2D	1	497.40	498.55	0-115	115	398	—	2	Same as above	Same as above	Sill	Same as above	—	N	Y
1R-5	1A-4B	2	498.55	499.97	0-142	142	398	—	2	Same as above	Same as above		Same as above	—	N	Y
1R-6	1-5	1	499.97	501.29	0-132	132	398	—	2	Same as above	Same as above		Same as above	—	N	Y
2R-1	1A-1F	2	503.00	504.38	0-138	138	344	—	3	Sparsely plagioclase phyric to aphyric alkali basalt	Fine to glassy, massive		Gray brown to speckled gray	Diffuse contacts, devitrified glassy rim, grain size coarsening downward	Y	N
2R-2	1A-1G	1	504.38	505.82	0-144	144	344	—	3	Same as above	Same as above	Sill	Same as above	—	Y	N
2R-3	1A-1D	—	505.82	506.44	0-62	62	344	—	3	Same as above	Same as above		Same as above	—	Y	N
2R-3	2A-2D	1	506.44	506.93	62-111	49	49	—	4	Moderately plagioclase phyric, aphyric alkali basalt	Fine to glassy, massive	Sill	Gray brown to speckled gray	Diffuse/irregular contacts	Y	Y
2R-3	3	—	506.93	506.97	111-115	4	4	—	5	Aphyric alkali basalt	Fine-grained unit	Sill	Gray	Inclined contacts, thin sliver of lava flow, between intrusion of Units 4 and 6	Y	Y
2R-3	3	1	506.97	507.06	115-124	9	266	—	6	Sparsely plagioclase phyric, aphyric basalt or microdolerite	Fine to medium grained, massive	Sill	Gray speckled	Contacts diffuse and inclined, defined by grain-size decrease, no glass	Y	N
2R-4	1A-1B	1	507.06	508.44	0-138	138	266	—	6	Same as above	Same as above		Same as above	—	Y	N
2R-5	1-2	1	508.44	509.63	0-119	119	266	—	6	Same as above	Same as above		Same as above	—	Y	N
3R-1	1-3B	2	512.20	513.18	0-98	98	98	—	7	Aphyric alkali basalt	Fine grained, massive	Sill	Purple gray/brown	Diffuse contacts, quench textured, some plagioclase microphenocrysts at base	Y	Y
4R-1	1-12	1	521.70	523.07	0-137	137	266	—	8	Hydrothermal deposit	Fine grained and wavy lamination	Hydrothermal	Red brown and yellow	Silicified red and yellow breccia, chemical Fe-Si deposit	N	N
4R-2	1A-15	—	523.07	524.36	0-129	129	266	—	8	Same as above	Same as above		Same as above	—	N	N
5R-1	1-2	—	531.20	531.54	0-34	34	232	34	9-1	Interflow material or sediment	Fine to medium grained	Sediment	Pale brown or greenish gray	Interflow sediment or very highly altered basalt	N	N
5R-1	2-4	3	531.54	532.46	34-126	92	232	222	9-2	Highly to moderately plagioclase megaphyric basalt	Fine to medium grained, spherulitic, thin flow/pile of pillows	Pillow breccia	Greenish gray	Brecciated pillows, highly altered, no vesicles, highly altered at top	Y	Y
5R-2	1A-2E	3	532.46	533.76	0-130	130	232	222	9-2	Same as above	Same as above		Same as above	—	Y	Y
5R-3	1A-1F	3	533.76	534.44	0-68	68	232	68	9-3	Moderately plagioclase megaphyric basalt	Fine grained	Pillow/flow	Spotted light fawn to greenish gray	Some recrystallized interpillow sediments	Y	Y
5R-3	2-4A	1	534.44	534.79	68-103	35	35	—	10	Moderately plagioclase megaphyric basalt	Fine grained	Pillow	Spotted light fawn to greenish gray	Some recrystallized interpillow sediments	Y	Y

Table T4 (continued).

Core, section	Piece	Analysis*	Depth (mbsf)		Interval (cm)	Length (cm)			Unit, subunit	Lithology	Texture	Structure	Color	Comments	Chilled margin present	
			Top	Bottom		Interval	Unit	Subunit							Top	Base
5R-3	4B-6	—	534.79	534.91	103-115	12	47	12	11-1	Interflow material or sediment	Fine to medium grained	Sediment	Grayish green/brown	Interflow material or sediment	N	N
5R-3	6-9	1	534.91	535.26	115-150	35	47	35	11-2	Sparsely plagioclase-olivine microphyric basalt	Fine grained	Pillow	Grayish green blackish rim	Trace vesicles, 0.5 mm maximum size	Y	Y
5R-4	1-3B	—	535.26	535.58	0-32	32	32	—	12	Highly calcified interpillow materials	Fine-grained interpillow sediment	Sediment	Weak red, gray, green, orange	Basalt fragments, hydrothermal precipitates, claystone and calcareous sediments	N	Y
5R-4	3C-9C	1	535.58	536.68	32-142	110	211	110	13-1	Moderately plagioclase-olivine phyric, aphyric basalt	Fine grained	Pillow/flow	Light to fine-speckled gray	—	Y	Y
5R-5	1A-6	3	536.68	537.69	0-101	101	211	101	13-1	Same as above	Same as above	Sediment	Same as above	—	Y	Y
5R-5	6-9	—	537.69	537.98	101-130	29	211	29	13-2	Interpillow material and sediment	Fine-grained interpillow sediment	Sediment	Olive green, brown	Recrystallized interpillow sediments	N	N
5R-5	10	—	537.98	538.09	130-141	11	11	—	14	Aphyric basalt	Fine grained	Pillow	Fine-speckled gray	Base of unit contains void space that has been filled with carbonate	Y	N
6R-1	1-4	—	540.50	540.88	0-38	38	97	38	15-1	Basalt fragments, unverified ordering and orientation	Fine grained	Pillow	Grays with greenish tinge	—	N	N
6R-1	4-8	—	540.88	541.47	38-97	59	97	59	15-2	Basalt fragments, unverified ordering and orientation	Fine grained	Pillow/flow	Grays with greenish tinge	Small amount of interpillow material observed between Subunits 15-1 and 15-2	N	N
6R-1	9-11	—	541.47	541.80	97-130	33	168	—	16	Sparsely plagioclase, olivine phyric, aphyric basalt	Fine grained, sheet flow	Flow	Speckled gray, greenish gray	Alteration of phenocrysts is banded, some layers altered white, others dark green	Y	Y
6R-2	1A-2F	2	541.80	543.15	0-135	135	168	—	16	Same as above	Same as above	Sediment	Same as above	—	Y	Y
6R-2	2G	—	543.15	543.30	135-150	15	15	—	17	Moderately olivine, plagioclase phyric basalt	Fine grained	Pillow	Dark greenish gray and black	Glassy rims on contacts, veins have black halos	Y	Y
6R-3	1	1	543.30	543.45	0-15	15	15	—	18	Moderately olivine, plagioclase phyric basalt	Fine grained	Pillow	Greenish gray	—	Y	N
6R-3	2-4	—	543.45	543.64	15-34	19	19	—	19	Aphyric basalt	Fine grained	Pillow	Greenish gray	3-4 cm of altered interpillow sediments at top of unit	Y	N
6R-3	5-10	2	543.64	544.75	34-145	111	271	227	20-1	Moderately to sparsely olivine, plagioclase phyric patches	Cryptocrystalline, sheet flow	Flow	Greenish gray to speckled gray	Cr-rich basalt, 2% vesicles at base	Y	N
6R-4	1A-4	1	544.75	545.91	0-116	116	271	—	20-1	Same as above	Same as above	Sediment	Same as above	—	Y	N
6R-4	4-5	—	545.91	546.12	116-137	21	271	65	20-2	Moderately-sparsely olivine-plagioclase phyric patches	Cryptocrystalline, sheet flow	Pillow/flow	Greenish gray to speckled gray	Cr-poor basalt, microcrystalline at top	Y	N
6R-5	1A-2	—	546.12	546.56	0-44	44	271	—	20-2	Same as above	Same as above	Sediment	Same as above	—	Y	N
6R-5	3A-8	2	546.56	547.22	44-110	66	195	—	21	Aphyric basalt	Fine grained, sheet flow	Flow	Medium gray	<1% vesicles, rare pyrite, carbonate veinlets	N	N
7R-1	1-9B	3	550.10	551.39	0-129	129	195	—	21	Same as above	Same as above	Sediment	Same as above	—	N	N

Table T4 (continued).

Core, section	Piece	Analysis*	Depth (mbsf)		Interval (cm)	Length (cm)			Unit, subunit	Lithology	Texture	Structure	Color	Comments	Chilled margin present	
			Top	Bottom		Interval	Unit	Subunit							Top	Base
7R-1	10A-10B	—	551.39	551.54	129-144	15	158	—	22	Aphyric basalt	Fine grained, sheet flow	Flow	Medium gray	2% vesicles up to 0.5 mm	N	N
7R-2	1A-5	1	551.54	552.97	0-143	143	158	—	22	Same as above	Same as above		Same as above	—	N	N
7R-3	1A-6	4	552.97	554.42	0-145	145	381	—	23	Aphyric basalt	Fine grained, sheet flow		Medium gray	Hydrothermal breccia zone toward top of unit, up to 5% vesicles	N	Y
7R-4	1-12	2	554.42	555.92	0-150	150	381	—	23	Same as above	Same as above	Flow	Same as above	—	N	Y
7R-5	1-9	—	555.92	556.45	0-53	53	381	—	23	Same as above	Same as above		Same as above	—	N	Y
8R-1	1-4B	1	559.50	559.83	0-33	33	381	—	23	Same as above	Same as above		Same as above	—	N	Y
8R-1	5-7	1	559.83	560.30	33-80	47	220	47	24-1	Aphyric basalt	Fine grained	Pillow	Gray to greenish gray	Top portion of unit is brecciated, up to 2% vesicles	Y	Y
8R-1	7-8B	1	560.30	560.56	80-106	26	220	26	24-2	Aphyric basalt	Fine grained		Gray to greenish gray	Interpillow material observed between Subunits 24-1 and 24-2	Y	Y
8R-2	1A-18	5	560.56	561.98	0-142	142	220	173	24-3	Aphyric basalt	Fine grained		Flow	Gray to greenish gray	—	Y
9R-1	1A-3	—	563.20	563.51	0-31	31	220	173	24-3	Same as above	Same as above	Flow	Same as above	—	Y	Y
9R-1	4-8D	1	563.51	564.60	31-140	109	1352	—	25	Aphyric, patches of sparsely plagioclase pyritic basalt	Fine grained		Gray with dark green spots	Concentration of pyrite near top margin as vein infilling and replacement material	Y	Y
9R-2	1A-1L	2	564.60	565.94	0-134	134	1352	—	25	Same as above	Same as above		Same as above	—	Y	Y
9R-3	1A-1M	2	565.94	567.20	0-126	126	1352	—	25	Same as above	Same as above		Same as above	—	Y	Y
9R-4	1A-1G	1	567.20	568.60	0-140	140	1352	—	25	Same as above	Same as above	Flow	Same as above	—	Y	Y
9R-5	1A-1E	2	568.60	569.10	0-50	50	1352	—	25	Same as above	Same as above		Same as above	—	Y	Y
10R-1	1A-1U	1	569.00	570.47	0-147	147	1352	—	25	Same as above	Same as above		Same as above	—	Y	Y
10R-2	1A-2O	3	570.47	571.87	0-140	140	1352	—	25	Same as above	Same as above		Same as above	—	Y	Y
10R-3	1A-4A	—	571.87	573.37	0-150	150	1352	—	25	Same as above	Same as above		Same as above	—	Y	Y
10R-4	1A-2O	1	573.37	574.84	0-147	147	1352	—	25	Same as above	Same as above		Same as above	—	Y	Y
10R-5	1A-2I	3	574.84	576.18	0-134	134	1352	—	25	Same as above	Same as above		Same as above	—	Y	Y
10R-6	1A-2	3	576.18	576.93	0-75	75	1352	—	25	Same as above	Same as above		Same as above	—	Y	Y
10R-6	3A-3E	1	576.93	577.52	75-134	59	76	—	26	Moderately olivine, plagioclase microphyric basalt	Microcrystalline to fine grained	Pillow/flow	Medium to dark gray	5-10% veins and fractures infilled with carbonate and smectite	Y	N
11R-1	1A-1E	—	577.90	578.07	0-17	17	76	—	26	Same as above	Same as above		Same as above	—	Y	N
11R-1	1F-4D	2	578.07	579.29	17-139	122	247	—	27	Sparsely plagioclase, olivine microphyric basalt	Cryptocrystalline		Dark gray to gray	Veins have well-developed halos containing disseminated fine pyrite	Y	Y
11R-2	1A-8	1	579.29	580.54	0-125	125	247	—	27	Same as above	Same as above	Flow	Same as above	—	Y	Y
11R-2	9A-9B	1	580.54	580.79	125-150	25	84	—	28	Aphyric basalt	Hypocrystalline		Dark gray	Bottom contact is a carbonate veinlet with green clay and pyrite	Y	N
11R-3	1A-1D	1	580.79	581.38	0-59	59	84	—	28	Same as above	Same as above		Same as above	—	Y	N
11R-3	2A-9	2	581.38	582.29	59-150	91	106	—	29	Aphyric basalt	Hypocrystalline fine grained	Flow	Dark gray to blackish	Veins have well-developed halos containing clays and pyrite	Y	Y
11R-4	1	—	582.29	582.38	0-9	9	106	—	29	Same as above	Same as above		Same as above	—	Y	Y
12R-1	1A-1B	—	587.30	587.36	0-6	6	106	—	29	Same as above	Same as above		Same as above	—	Y	Y

Table T4 (continued).

Core, section	Piece	Analysis*	Depth (mbsf)		Interval (cm)	Length (cm)			Unit, subunit	Lithology	Texture	Structure	Color	Comments	Chilled margin present	
			Top	Bottom		Interval	Unit	Subunit							Top	Base
12R-1	2-9A	1	587.36	587.79	6-49	43	43	—	30	Aphyric basalt	Cryptocrystalline	Pillow	Dark gray	Top 12 cm interpillow carbonate and clay sediments present	Y	Y
12R-1	9B-23	1	587.79	588.80	49-150	101	101	—	31	Moderately olivine, plagioclase microphyric basalt	Cryptocrystalline fine grained	Flow	Dark gray		Y	Y
12R-2	1A-11B	2	588.80	590.24	0-144	144	236	—	32	Aphyric basalt	Hypocrystalline fine grained	Flow	Medium gray		N	N
12R-3	1A-5B	3	590.24	591.16	0-92	92	236	—	32	Same as above	Same as above		Same as above	—	N	N
185-801C-13R-1	1-8	—	594.30	594.77	0-47	47	47	—	33	Rubble unit, mixed debris from overlying section		Rubble		Rubble unit, debris from overlying section that dropped into the hole	N	N
14R-1	1-2	XRF, PP, TSB	604.00	605.30	0-130	130	221	—	34	Aphyric basalt	Fine grained, single flow	Flow	Gray to dark gray	This unit is similar to 129-801C-12R-3 (Unit 32) above	N	Y
14R-2	1	PP	605.30	606.21	0-91	91	221	—	34	Aphyric basalt	Fine grained, single flow		Gray to dark gray	—	N	Y
14R-2	2A-2C	PP, TSB*2	606.21	606.55	91-125	34	34	—	35	Aphyric basalt	Fine grained, pillow with interpillow sediment	Pillow	Very dark gray, green brown, red	Pillow margins are altered glass, irregular curved margin 14R-2, 112 cm	N	Y
14R-2	3-7	TSB	606.55	606.76	125-146	21	27	—	36	Cherty interpillow sediments	Fine grained and banded	Sediment	Dark brown, yellow, green	Bedding observed perpendicular to color banding, contains radiolarians	N	N
14R-3	1-2	—	606.76	606.82	0-6	6	27	—	36	Cherty interpillow sediments	Fine grained and banded		Dark brown, yellow, green	—	N	N
14R-3	3	—	606.82	607.04	6-28	22	158	22	37-1	Aphyric basalt	Fine grained, pillow with interpillow sediment	Pillow	Very dark gray, interpillow green yellow, red	MST log results suggest high K and low magnetic susceptibility in interpillow zones	N	N
14R-3	4-5B	PP	607.04	607.23	28-47	19	—	19	37-2	Aphyric basalt	Fine-grained pillow or maybe thin flow	Pillow	Very dark gray	—	Y	Y
14R-3	6-8B	—	607.23	607.46	47-70	23	—	23	37-3	Aphyric basalt	Fine-grained pillow or maybe thin flow	Pillow	Very dark gray	—	Y	Y
14R-3	8C-8D	—	607.46	607.66	70-90	20	—	20	37-4	Aphyric basalt	Fine-grained pillow or maybe thin flow	Pillow	Very dark gray	—	Y	Y
14R-3	8D-10	XRF, PP, TSB	607.66	608.02	90-126	36	—	36	37-5	Aphyric basalt	Fine grained, small pillows and interpillow material	Pillow	Very dark gray	Curved chilled pillow margins	Y	Y
14R-3	11-12	—	608.02	608.13	126-137	11	—	11	37-6	Aphyric basalt	Fine grained	Pillow	Very dark gray	—	N	N
14R-4	1A-3	PP	608.13	608.40	0-27	27	—	27	37-7	Aphyric basalt	Fine grained	Pillow	Very dark gray	—	Y	N
14R-4	4-10	XRF	608.40	609.08	27-95	68	213	68	38-1	Aphyric basalt	Fine grained, varying grain size	Pillow/flow	Very dark gray to gray	MST log shows differences in K and magnetic susceptibility between sections 4 and 5	N	N
14R-4	11-15	—	609.08	609.58	95-145	50	—	50	38-2	Aphyric basalt	Fine margins, coarser center	Pillow/flow	Gray	—	Y	N
14R-5	1A-2A	—	609.58	609.79	0-21	21	—	21	38-3	Aphyric basalt	Fine grained	Pillow	Dark gray	No contact observed	N	N
14R-5	3A-4A	PP	609.79	610.14	21-56	35	—	35	38-4	Aphyric basalt	Fine grained	Pillow	Dark gray	—	Y	N
14R-5	5-8A	—	610.14	610.53	56-95	39	—	39	38-5	Aphyric basalt	Fine grained	Pillow	Dark gray	No contact observed	N	N

Table T4 (continued).

Core, section	Piece	Analysis*	Depth (mbsf)		Interval (cm)	Length (cm)			Unit, subunit	Lithology	Texture	Structure	Color	Comments	Chilled margin present	
			Top	Bottom		Interval	Unit	Subunit							Top	Base
15R-1	1A-6	PP, TSB*2	613.70	614.13	0-43	43	43	—	39	Aphyric basalt	Fine grained, varying grain size, pillows and interpillow breccia	Breccia	Pale gray to green, white brown, red	Highly variable color, interpillow fill mostly green and white	Y	Y
15R-1	7-14	PP, TSB	614.13	614.50	43-80	37	37	—	40	Interpillow material and sediment (black chert)	Sometimes brecciated sedimentary fill material	Sediment	Reddish strong brown, green	Red zone of sedimentation between flows/pillows	N	N
15R-1	15-16B	—	614.50	614.75	80-105	25	107	25	41-1	Aphyric basalt	Fine grained, varying grain size, pillows and interpillow breccia	Breccia	Green to dark gray, white brown, red	Highly variable, fill is red and white, red is similar to overlying fill unit	Y	Y
15R-1	17A-18	—	614.75	615.02	105-132	27	—	27	41-2	Aphyric basalt	Fine grained	Pillow	Dark gray	—	Y	N
15R-2	1A-1D	PP*2	615.02	615.43	0-41	41	—	41	41-3	Aphyric basalt	Fine grained	Pillow	Dark gray	—	N	Y
15R-2	2	—	615.43	615.57	41-55	14	—	14	41-4	Aphyric basalt	Fine grained	Pillow	Dark gray	—	Y	Y
15R-2	3-4	TSB	615.57	615.64	55-62	7	39	7	42-1	Chert, aphyric basalt and interpillow material	Fine grained, polyimict interpillow sediments and breccia	Sediment	Greenish gray, brown, red	Fill material red and yellow, similar to above	N	N
15R-2	5-7A	—	615.64	615.96	62-94	32	—	32	42-2	Aphyric basalt	Fine grained, varying grain size, pillows and interpillow breccia	Breccia	Greenish gray	—	N	Y
15R-2	7A-7B	—	615.96	616.27	94-125	31	174	31	43-1	Aphyric basalt	Fine grained, varying grain size, pillows and interpillow breccia	Breccia	Dark green gray, green and red	Curved or irregular chilled margins to the pillows	Y	Y
15R-2	7B-7C	—	616.27	616.38	125-136	11	—	11	43-2	Aphyric basalt	Fine grained	Pillow	Dark gray to greenish gray	—	Y	Y
15R-3	1A	—	616.38	616.49	0-11	11	—	11	43-3	Aphyric basalt	Fine grained	Pillow	Dark gray to greenish gray	—	N	Y
15R-3	1A	—	616.49	616.60	11-22	11	—	11	43-4	Aphyric basalt	Fine grained	Pillow	Dark gray to greenish gray	—	Y	Y
15R-3	1A-1B	PP	616.60	616.92	22-54	32	—	32	43-5	Aphyric basalt	Fine grained	Pillow	Dark gray to greenish gray	—	Y	Y
15R-3	1B-2	—	616.92	617.10	54-72	18	—	18	43-6	Aphyric basalt	Fine grained	Pillow	Dark gray to greenish gray	Curved or irregular chilled margins to the pillows	Y	Y
15R-3	2-3B	—	617.10	617.51	72-113	41	—	41	43-7	Aphyric basalt	Fine grained	Pillow	Dark gray to greenish gray	—	Y	N
15R-3	3C-5	PP, TSB	617.51	617.68	113-130	17	—	19	43-8	Aphyric basalt	Medium-grained interpillow material	Sediment	Gray and brownish red	—	N	N
15R-4	1	—	617.68	617.70	0-2	2	—	19	43-8	Aphyric basalt	Medium-grained interpillow material	Sediment	Gray and brownish red	—	N	N
15R-4	1	XRF, PP, TSB	617.70	619.00	2-132	130	225	—	44	Aphyric basalt with small vesicles	Fine-grained single flow	Flow	Gray	Red interflow material at the bottom margin 15R-4, 91-97 cm	Y	Y
15R-5	1A	PP	619.00	619.95	0-95	95	225	—	44	Aphyric basalt with small vesicles	Fine-grained single flow	Flow	Gray	—	Y	Y
15R-6	1A-1C	PP	619.95	621.07	0-112	112	112	—	45	Aphyric to plagioclase, clinopyroxene phyrlic basalt at base	Fine-grained single flow	Flow	Dark gray	Red interpillow material and basalt chunk at the top of flow 15R-6, 0-3 cm	Y	Y
15R-6	1C-1E	—	621.07	621.20	112-125	13	138	13	46-1	Aphyric basalt with interpillow material	Fine grained, small pillows and breccia	Breccia	Greenish dark gray, brown red	—	Y	Y
15R-6	1E-1G	—	621.20	621.35	125-140	15	—	60	46-2	Aphyric basalt	Fine grained	Pillow/flow	Dark gray	—	Y	Y
15R-7	1A-1B	PP	621.35	621.80	0-45	45	—	60	46-2	Aphyric basalt	Fine grained	Pillow/flow	Dark gray	—	Y	Y

Table T4 (continued).

Core, section	Piece	Analysis*	Depth (mbsf)		Interval (cm)	Length (cm)			Unit, subunit	Lithology	Texture	Structure	Color	Comments	Chilled margin present	
			Top	Bottom		Interval	Unit	Subunit							Top	Base
15R-7	1C-1D	PP	621.80	621.98	45-63	18	—	18	46-3	Interpillow material	Medium-grained interpillow material	Sediment	Brownish red	—	N	N
15R-7	1E-1F	XRF, TSB*2	621.98	622.45	63-110	47	—	47	46-4	Aphyric basalt	Fine grained	Pillow	Dark gray	—	Y	N
16R-1	1-2F	—	623.30	623.57	0-27	27	270	27	47-1	Aphyric basalt to sparsely plagioclase aphyric	Fine grained microcrystalline	Pillow	Gray to pale green at base	—	N	Y
16R-1	2F-3	—	623.57	623.67	27-37	10	—	10	47-2	Aphyric basalt	Fine-grained interpillow breccia with pillows	Breccia	Gray green	—	N	N
16R-1	3-4G	XRF, PP, TSB	623.67	624.74	37-144	107	—	111	47-3	Aphyric basalt	Fine grained	Flow	Gray	—	Y	Y
16R-2	1A	—	624.74	624.78	0-4	4	—	111	47-3	Aphyric basalt	Fine grained	Flow	Gray	—	Y	Y
16R-2	1A-1B	—	624.78	625.14	4-40	36	—	36	47-4	Aphyric basalt	Fine-grained interpillow breccia with pillows	Breccia	Gray green	Pale green altered small pillows and breccia	N	N
16R-2	1B-1D	PP, TSB	625.14	625.86	40-112	72	—	72	47-5	Aphyric basalt	Fine grained	Pillow/flow	Pale green, grayish green	—	Y	Y
16R-2	1E-1F	—	625.86	626.00	112-126	14	—	14	47-6	Interflow sediment	Medium-grained granular recrystallized sediments	Sediment	Olive green to red brown	Recrystallized sediment	N	N
16R-2	1F	—	626.00	626.03	126-129	3	46	—	48	Hydrothermal deposit	Medium grained	Hydrothermal	Olive yellow to olive brown	Silicified yellow brown breccia, chemical Fe-Si deposit	N	N
16R-3	1-4	PP, TSB	626.03	626.46	0-43	43	46	—	48	Hydrothermal deposit	Medium grained	Hydrothermal	Olive yellow to olive brown	—	N	N
16R-3	5	XRF, TSB	626.46	626.67	43-64	21	817	21	49-1	Interflow sediment	Medium-grained granular recrystallized sediments	Sediment	Olive green to red brown	Recrystallized sediment	N	N
16R-3	6A-6B	PP	626.67	626.93	64-90	26	—	26	49-2	Aphyric basalt	Fine grained	Pillow	Greenish gray	—	Y	Y
16R-3	7A-8B	—	626.93	627.44	90-141	51	—	198	49-3	Aphyric basalt	Fine grained	Pillow	Dark gray	—	Y	Y
16R-4	1A-9	XRF, PP*2, TSB	627.44	628.91	0-147	147	—	198	49-3	Aphyric basalt	Fine grained	Flow	Dark gray	—	Y	Y
16R-5	1A-2A	—	628.91	629.06	0-15	15	—	15	49-4	Interflow sediment	Medium-grained interpillow material	Sediment	Green and white	Rubble pieces and recrystallized interpillow sediment, olive green and red brown	N	N
16R-5	3A-6B	PP	629.06	629.47	15-56	41	—	41	49-5	Aphyric basalt	Fine grained	Pillow	Dark gray	—	Y	N
16R-5	7A-15	TSB	629.47	630.20	56-129	73	—	118	49-6	Pillows and interflow sediment	Medium grained	Breccia	Red and white basalt breccia	Small pillows with vugs and interpillow fill, carbonate and red chert	N	N
17R-1	1-7A	TSB	632.80	633.25	0-45	45	—	118	49-6	Pillows and interpillow sediment	Medium grained	Sediment	Red and white basalt breccia	Small pillows, rims and basalt clasts with recrystallized red and white interpillow material	N	N
17R-1	7A-9B	XRF, PP, TSB	633.25	634.29	45-149	104	—	104	49-7	Aphyric basalt	Fine grained	Flow	Dark gray	—	Y	Y
17R-2	1-5	—	634.29	634.64	0-35	35	—	35	49-8	Aphyric basalt	Fine grained	Pillow	Very dark gray	—	Y	N
17R-2	6-9	—	634.64	635.30	35-101	66	—	66	49-9	Aphyric basalt	Fine grained	Pillow/flow	Very dark gray	—	Y	N
17R-2	10-12	—	635.30	635.69	101-140	39	—	39	49-10	Aphyric basalt	Fine grained	Pillow	Very dark gray	—	Y	N
17R-2	13	—	635.69	635.78	140-149	9	—	96	49-11	Aphyric basalt	Fine grained	Pillow/flow	Very dark gray	—	Y	N
17R-3	1-5	PP	635.78	636.65	0-87	87	—	96	49-11	Aphyric basalt	Fine grained	Pillow/flow	Very dark gray	—	Y	N

Table T4 (continued).

Core, section	Piece	Analysis*	Depth (mbsf)		Interval (cm)	Length (cm)			Unit, subunit	Lithology	Texture	Structure	Color	Comments	Chilled margin present	
			Top	Bottom		Interval	Unit	Subunit							Top	Base
17R-3	6-9	XRF, TSB	636.65	636.95	87-117	30	—	30	49-12	Aphyric basalt	Fine grained	Pillow	Very dark gray	—	Y	N
17R-3	10	PP	636.95	637.15	117-137	20	—	20	49-13	Aphyric basalt	Fine grained	Pillow	Very dark gray	—	Y	Y
17R-3	10	—	637.15	637.23	137-145	8	—	8	49-14	Interpillow sediment	Variable grain size, granular appearance		Green and white	Interpillow material, both contacts with basalt are observed	N	N
17R-4	1	—	637.23	637.28	0-5	5	4308	5	50-1	Cherty interpillow sediments	Variable grain size		Dark gray to green	Single piece of cherty sediment	N	N
17R-4	2-4B	—	637.28	637.70	5-47	42	—	42	50-2	Aphyric basalt	Fine grained, very thin lows and interflow breccia	Breccia	Very dark gray and dark green	Seven chills, some are exceptionally straight dark green interpillow material	Y	Y
17R-4	4B-5A	—	637.70	637.90	47-67	20	—	20	50-3	Aphyric basalt	Fine grained	Pillow	Gray to dark gray	—	Y	Y
17R-4	5B	—	637.90	638.08	67-85	18	—	18	50-4	Aphyric basalt	Fine grained	Pillow	Gray to dark gray	—	Y	Y
17R-4	6-9	PP	638.08	638.63	85-140	55	—	90	50-5	Aphyric basalt	Fine grained	Pillow/flow	Gray to dark gray	Brecciated flow top	N	Y
17R-5	1-4	—	638.63	638.98	0-35	35	—	90	50-5	Aphyric basalt	Fine grained		Gray to dark gray	—	N	Y
18R-1	1-5	—	642.20	642.51	0-31	31	—	31	50-6	Aphyric basalt	Fine grained	Pillow	Gray to dark gray	—	Y	Y
18R-1	6-9	—	642.51	642.70	31-50	19	—	19	50-7	Aphyric basalt	Fine grained	Pillow	Gray to dark gray	—	Y	Y
18R-1	10-11	XRF, PP, TSB	642.70	643.24	50-104	54	—	54	50-8	Aphyric basalt	Fine grained	Pillow/flow	Gray to dark gray	—	Y	Y
18R-1	12-14	—	643.24	643.34	104-114	10	—	10	50-9	Volcaniclastic breccia	Variable grain size	Pillow	Gray, green and white	—	N	N
18R-1	15-18	—	643.34	643.70	114-150	36	—	108	50-10	Aphyric basalt	Fine grained	Flow	Dark gray	Glass on several pieces	Y	Y
18R-2	1-6	PP	643.70	644.42	0-72	72	—	108	50-10	Aphyric basalt	Fine grained		Dark gray	—	Y	Y
18R-2	6-7	XRF	644.42	644.85	72-115	43	—	43	50-11	Aphyric basalt	Fine grained, thin flow or pillow	Pillow	Gray to dark gray	—	Y	Y
18R-2	8-10	—	644.85	645.04	115-134	19	—	19	50-12	Aphyric basalt	Fine grained, thin flow or pillow	Pillow	Gray to dark gray	—	Y	Y
18R-2	11-13	—	645.04	645.19	134-149	15	—	39	50-13	Aphyric basalt	Fine grained, thin flow or pillow	Pillow	Gray to dark gray	Small fragments, no chills	N	N
18R-3	1-4	—	645.19	645.43	0-24	24	—	39	50-13	Aphyric basalt	Fine grained, thin flow or pillow		Gray to dark gray	—	N	N
19R-1	1-4	PP	651.70	652.56	0-86	86	—	86	50-14	Aphyric basalt	Fine grained, thin flow or pillow	Pillow/flow	Gray to dark gray	—	N	Y
19R-1	5-13	—	652.56	653.20	86-150	64	—	64	50-15	Aphyric basalt	Fine grained, thin flow or pillow	Pillow/flow	Gray to dark gray	—	N	Y
19R-2	1-4	—	653.20	653.48	0-28	28	—	28	50-16	Volcaniclastic breccia	Fine grained, thin flow or pillow	Pillow	Black, green, and white	—	N	N
19R-2	5-7	—	653.48	653.91	28-71	43	—	43	50-17	Aphyric basalt	Fine grained, thin flow or pillow	Pillow	Gray to dark gray	—	N	Y
19R-2	8-10	—	653.91	654.39	71-119	48	—	89	50-18	Aphyric basalt	Fine grained, thin flow or pillow	Pillow/flow	Gray to dark gray	—	Y	Y
19R-3	1	XRF, PP, TSB	654.39	654.80	0-41	41	—	89	50-18	Aphyric basalt	Fine grained, thin flow or pillow		Gray to dark gray	—	Y	Y
19R-3	2-5	—	654.80	655.26	41-87	46	—	46	50-19	Aphyric basalt	Fine grained, thin flow or pillow	Pillow	Gray to dark gray	Small fragments, no chills	N	N
20R-1	1-5	—	660.70	660.88	0-18	18	—	18	50-20	Aphyric basalt	Fine grained, thin flow or pillow	Pillow	Gray to dark gray	—	Y	Y
20R-1	6-7C	PP	660.88	661.37	18-67	49	—	49	50-21	Aphyric basalt	Fine grained, thin flow or pillow	Pillow	Gray to dark gray	Thick vein at base of unit	Y	Y

Table T4 (continued).

Core, section	Piece	Analysis*	Depth (mbsf)		Interval (cm)	Length (cm)			Unit, subunit	Lithology	Texture	Structure	Color	Comments	Chilled margin present	
			Top	Bottom		Interval	Unit	Subunit							Top	Base
20R-1	8-11	—	661.37	661.74	67-104	37	—	37	50-22	Aphyric basalt	Fine grained, thin flow or pillow	Pillow	Gray to dark gray	—	N	Y
20R-1	12-17	—	661.74	662.11	104-141	37	—	37	50-23	Aphyric basalt	Fine grained, thin flow or pillow	Pillow	Gray to dark gray	—	Y	Y
20R-2	1	XRF, PP	662.11	663.18	0-107	107	—	107	50-24	Aphyric basalt	Fine grained, thin flow or pillow	Flow	Gray to dark gray	—	Y	Y
20R-2	2-10	—	663.18	663.59	107-148	41	—	90	50-25	Aphyric basalt	Fine grained, small pillows and breccia	Breccia	Gray to dark gray	Glassy pillow rims and interpillow material, brecciated pillow fragments	Y	Y
20R-3	1-7	TSB	663.59	664.08	0-49	49	—	90	50-25	Aphyric basalt	Fine grained, small pillows and breccia	Pillow	Gray to dark gray	Various glassy chills, basalt and breccia fragments, rubbly section	Y	Y
21R-1	1-6E	XRF, PP, TSB	670.00	671.41	0-141	141	—	210	50-26	Aphyric basalt	Fine grained, flow or thick pillow	Flow	Dark gray	More massive unit, some olivine present with plagioclase	Y	N
21R-2	1-5	—	671.41	672.10	0-69	69	—	210	50-26	Aphyric basalt	Fine grained, flow or thick pillow	Flow	Dark gray	—	Y	N
21R-2	6	PP, TSB	672.10	672.63	69-122	53	—	129	50-27	Aphyric basalt	Fine grained, flow or thick pillow	Flow	Dark gray	5 cm breccia/sediment at top	Y	Y
21R-3	1	PP	672.63	673.39	0-76	76	—	129	50-27	Aphyric basalt	Fine grained, flow or thick pillow	Flow	Dark gray	>100% recovery so there is a 13-cm overlap on depth calculation in 21R	Y	Y
21R-3	2-8	TSB	673.39	673.73	76-110	34	—	34	50-28	Aphyric basalt and interpillow material	Fine grained, pillows/basalt breccia and interpillow stuff	Breccia	Dark gray, green and white	Small pillows and basalt clasts with recrystallized white interpillow material	N	N
22R-1	1-3	PP	673.60	673.99	0-39	39	—	39	50-29	Aphyric basalt	Fine-grained thin flow or pillow	Pillow	Dark gray	Top 10 cm is hydrothermal deposit rubble from above	N	Y
22R-1	4A	TSB	673.99	674.06	39-46	7	—	7	50-30	Interflow recrystallized sediment pale colored	Medium grained, granular appearance	Sediment	Yellow green and white	Chilled contacts to units above and below suggest it is recrystallized interflow sediment	N	N
22R-1	4B-4C	—	674.06	674.26	46-66	20	—	20	50-31	Aphyric basalt	Fine-grained thin flow or pillow	Pillow	Dark gray	—	Y	Y
22R-1	4D-4F	—	674.26	674.43	66-83	17	—	17	50-32	Aphyric basalt	Fine-grained thin flow or pillow	Pillow	Dark gray	—	Y	Y
22R-1	4F-4G	—	674.43	674.54	83-94	11	—	11	50-33	Aphyric basalt	Fine-grained thin flow or pillow	Pillow	Dark gray	—	Y	Y
22R-1	4G-5	—	674.54	674.66	94-106	12	—	12	50-34	Aphyric basalt	Fine-grained thin flow or pillow	Pillow	Dark gray	—	Y	Y
22R-1	6	—	674.66	674.70	106-110	4	—	4	50-35	Interflow recrystallized sediments layered and greenish brown	Medium grained, banded	Sediment	Greenish brown to olive green	Occurs as an individual piece, no contacts, may originally have been more	N	N
22R-1	7	PP	674.70	674.81	110-121	11	—	11	50-36	Aphyric basalt	Fine-grained thin flow or pillow	Pillow	Dark gray	—	N	Y

Table T4 (continued).

Core, section	Piece	Analysis*	Depth (mbsf)		Interval (cm)	Length (cm)			Unit, subunit	Lithology	Texture	Structure	Color	Comments	Chilled margin present	
			Top	Bottom		Interval	Unit	Subunit							Top	Base
22R-1	8	—	674.81	674.84	121-124	3	—	21	50-37	Aphyric basalt	Fine-grained thin flow or pillow		Dark gray	Top 4 cm is interflow sediment, like that observed in Subunit 50-30	Y	Y
22R-2	1A-1B	—	674.84	675.02	0-18	18	—	21	50-37	Aphyric basalt	Fine-grained thin flow or pillow	Pillow	Dark gray	Rubble and glass at the base of the unit	Y	Y
22R-2	1B	TSB	675.02	675.07	18-23	5	—	5	50-38	Interflow recrystallized sediment pale colored	Medium grained, granular	Sediment	Olive green and white	Chilled contacts to units above and below suggest it is recrystallized interflow sediment	N	N
22R-2	1B-4	XRF, PP*2	675.07	676.33	23-149	126	—	126	50-39	Aphyric basalt	Fine margins medium center of thicker flow	Flow	Gray to dark gray	Glassy margins	Y	Y
22R-3	1-3	—	676.33	676.63	0-30	30	—	30	50-40	Aphyric basalt	Fine-grained thin flow or pillow	Pillow	Gray to dark gray	—	Y	Y
22R-3	4A-11	—	676.63	677.55	30-122	92	—	92	50-41	Aphyric basalt	Fine margins, medium center, thicker flow	Pillow/flow	Gray to dark gray	—	N	Y
23R-1	1-2	—	681.90	682.00	0-10	10	—	10	50-42	Aphyric basalt	Fine-grained thin flow or pillow	Pillow	Gray to dark gray	—	N	Y
23R-1	2-7	—	682.00	682.90	10-100	90	—	90	50-43	Aphyric basalt	Fine margins, medium center, thicker flow	Pillow/flow	Gray to dark gray	—	Y	Y
23R-1	7-10	TSB	682.90	683.16	100-126	26	—	92	50-44	Aphyric basalt	Fine margins, medium center, thicker flow	Pillow/flow	Gray to dark gray	—	Y	Y
23R-2	1-4	PP	683.16	683.82	0-66	66	—	92	50-44	Aphyric basalt	Fine margins, medium center, thicker flow		Gray to dark gray	—	Y	Y
23R-2	4-12	—	683.82	684.58	66-142	76	—	131	50-45	Aphyric basalt	Fine margins, medium center, thicker flow	Flow	Gray to dark gray	—	Y	Y
23R-3	1-4	PP	684.58	685.13	0-55	55	—	131	50-45	Aphyric basalt	Fine margins, medium center, thicker flow		Gray to dark gray	—	Y	Y
23R-3	5-7	—	685.13	685.48	55-90	35	—	35	50-46	Aphyric basalt	Fine margins, medium center, flow or larger pillow	Pillow	Gray to dark gray	—	Y	Y
23R-3	8-12	—	685.48	685.98	90-140	50	—	50	50-47	Aphyric basalt	Fine margins, medium center, flow or larger pillow	Pillow	Gray to dark gray	—	Y	Y
23R-4	1-4	XRF, PP	685.98	686.78	0-80	80	—	80	50-48	Aphyric basalt	Fine margins, medium center, flow or larger pillow	Pillow/flow	Gray to dark gray	—	Y	Y
23R-4	5-6	—	686.78	686.96	80-98	18	—	18	50-49	Aphyric basalt	Fine margins, medium center	Pillow	Gray to dark gray	—	Y	Y
24R-1	1-2	—	691.30	691.52	0-22	22	—	22	50-50	Aphyric basalt	Fine margins, medium center	Pillow	Gray to dark gray	—	Y	Y
24R-1	3-10	PP	691.52	692.27	22-97	75	—	75	50-51	Aphyric basalt	Fine margins, medium center	Pillow/flow	Gray to dark gray	—	Y	Y
24R-1	11-12	XRF, TSB*2	692.27	692.44	97-114	17	—	17	50-52	Aphyric basalt	Thin microcrystalline unit	Pillow	Dark gray	Recrystallized interpillow material at the base of this thin subunit	Y	Y
24R-1	13-14	—	692.44	692.63	114-133	19	—	19	50-53	Aphyric basalt	Thin microcrystalline unit	Pillow	Dark gray	Recrystallized interpillow material at the top of this thin subunit	Y	N
24R-2	1	—	692.63	692.87	0-24	24	—	24	50-54	Aphyric basalt	Thin microcrystalline unit	Pillow	Dark gray	—	Y	Y

Table T4 (continued).

Core, section	Piece	Analysis*	Depth (mbsf)		Interval (cm)	Length (cm)			Unit, subunit	Lithology	Texture	Structure	Color	Comments	Chilled margin present	
			Top	Bottom		Interval	Unit	Subunit							Top	Base
24R-2	2	PP	692.87	693.47	24-84	60	—	60	50-55	Aphyric basalt	Fine margins, medium center	Pillow/flow	Dark gray	—	Y	Y
24R-2	3-10	XRF, PP	693.47	693.88	84-125	41	—	41	50-56	Rubbly brecciated pillow, dark cement	Fine-grained and glassy pillow breccia	Breccia	Dark to very dark gray or black	Various glassy fragments, chilled pillow rims and fragmented basalt breccia	Y	Y
24R-2	11-15	—	693.88	694.13	125-150	25	—	91	50-57	Aphyric basalt	Fine margins, medium center	Pillow/flow	Dark gray	2-3 cm of interpillow material at base of unit	Y	Y
24R-3	1-5	PP, TSB	694.13	694.79	0-66	66	—	91	50-57	Aphyric basalt	Fine margins, medium center	Pillow/flow	Dark gray	—	Y	Y
24R-3	6A-9	—	694.79	695.09	66-96	30	—	30	50-58	Aphyric basalt	Fine grained	Pillow	Dark gray	—	Y	Y
24R-3	10-14	—	695.09	695.53	96-140	44	—	44	50-59	Aphyric basalt	Fine grained	Pillow	Dark gray	—	N	N
25R-1	1A-6	—	700.70	701.20	0-50	50	—	50	50-60	Aphyric basalt	Fine grained	Pillow	Dark gray	—	Y	N
25R-1	7A-11	PP	701.20	701.82	50-112	62	—	62	50-61	Aphyric basalt	Fine grained	Pillow/flow	Dark gray	—	N	N
25R-1	12-15	XRF	701.82	702.16	112-146	34	—	34	50-62	Aphyric basalt	Fine grained	Pillow	Dark gray	—	Y	N
26R-1	1-4A	PP, TSB	710.20	710.50	0-30	30	—	30	50-63	Aphyric basalt breccia and green recrystallized interflow material	Fine grained, thin 4-10 cm flows and basalt clasts	Breccia	Dark gray, dark green and white	Basalt and recrystallized interflow material, saponite, celadonite, and carbonate	Y	Y
26R-1	4B-5	—	710.50	710.88	30-68	38	—	38	50-64	Aphyric basalt	Fine-grained sheet flow	Pillow	Dark gray	—	Y	N
26R-1	6-12	XRF, PP, TSB	710.88	711.52	68-132	64	—	103	50-65	Aphyric basalt	Fine-grained sheet flow	Flow	Dark gray	—	Y	Y
26R-2	1-2	—	711.52	711.91	0-39	39	—	103	50-65	Aphyric basalt	Fine-grained sheet flow	Flow	Dark gray	—	Y	Y
26R-2	3-11	PP	711.91	712.82	39-130	91	—	91	50-66	Aphyric basalt	Fine-grained sheet flow	Pillow/flow	Dark gray	—	N	Y
27R-1	1-3	—	719.70	720.20	0-50	50	—	50	50-67	Aphyric basalt	Fine-grained sheet flow	Pillow	Dark gray	—	N	Y
27R-1	4-7	PP	720.20	720.96	50-126	76	—	76	50-68	Aphyric basalt	Fine-grained sheet flow	Pillow/flow	Dark gray	Top 5 cm and bottom 2 cm are brecciated interflow material	Y	Y
27R-2	1-6	XRF, PP	720.96	722.45	0-149	149	—	149	50-69	Aphyric basalt	Fine-grained sheet flow	Flow	Dark gray	Brecciated base (bottom 10 cm)	N	Y
27R-3	1-4	TSB	722.45	722.65	0-20	20	—	20	50-70	Interflow material and hyaloclastite breccia	Fine-grained interpillow recrystallized sediments	Sediment	Dark gray	Various glassy rims, some hyaloclastite and recrystallized interflow material	Y	Y
27R-3	5-9	PP	722.65	723.75	20-130	110	—	447	50-71	Aphyric basalt	Fine margins, medium center, thick massive sheet flow	Flow	Gray	Top 30-40 cm is brecciated	Y	Y
27R-4	1	PP	723.75	725.17	0-142	142	—	447	50-71	Aphyric basalt	Fine margins, medium center, thick massive sheet flow	Flow	Gray	—	Y	Y
27R-5	1-8	XRF, TSB	725.17	726.07	0-90	90	—	447	50-71	Aphyric basalt	Fine margins, medium center, thick massive sheet flow	Flow	Gray	—	Y	Y
28R-1	1A-3	PP	728.70	729.75	0-105	105	—	447	50-71	Aphyric basalt	Fine margins, medium center, thick massive sheet flow	Flow	Gray	—	Y	Y
28R-1	4-7	—	729.75	730.04	105-134	29	—	95	50-72	Aphyric basalt	Fine margins, medium center, sheet flow	Pillow/flow	Gray	Brecciated flow top and base	Y	Y
28R-2	1A-1C	XRF, PP	730.04	730.70	0-66	66	—	95	50-72	Aphyric basalt	Fine margins, medium center, sheet flow	Pillow/flow	Gray	—	Y	Y

Table T4 (continued).

Core, section	Piece	Analysis*	Depth (mbsf)		Interval (cm)	Length (cm)			Unit, subunit	Lithology	Texture	Structure	Color	Comments	Chilled margin present	
			Top	Bottom		Interval	Unit	Subunit							Top	Base
28R-2	1C-8	—	730.70	731.19	66-115	49	—	49	50-73	Interpillow basalt breccia, glassy in places	Fine-grained interflow breccia, carbonate cement	Breccia	Dark gray	Various glassy fragments, chilled pillow rims, and fragmented basalt breccia	Y	Y
28R-2	9-10	—	731.19	731.54	115-150	35	—	72	50-74	Aphyric basalt	Fine rims, medium-grained center, sheet flow		Dark gray	Brecciated flow top and base	Y	Y
28R-3	1	—	731.54	731.91	0-37	37	—	72	50-74	Aphyric basalt	Fine rims, medium-grained center, sheet flow	Pillow/flow	Dark gray	—	Y	Y
28R-3	2-5	—	731.91	732.21	37-67	30	—	30	50-75	Glassy hyaloclastite breccia	Fine-grained breccia, hyaloclastite fragments	Hyaloclastite	Dark gray, silver alteration	Fresh glass and 0.5- to 4-cm shards, fragments of pillow edges	Y	Y
28R-3	6-9	—	732.21	732.44	67-90	23	—	23	50-76	Aphyric basalt	Fine-grained sheet flow	Pillow	Gray to dark gray	—	Y	Y
28R-3	10-16	PP	732.44	733.04	90-150	60	1943	60	51-1	Sparsely olivine phyric basalt	Fine- to medium-grained sheet flow	Pillow/flow	Gray	More massive unit, coarser, and contains many small vesicles	N	N
29R-1	1-2	XRF	737.90	738.20	0-30	30	—	700	51-2	Sparsely olivine phyric basalt	Medium grained, thick massive flow		Gray	More massive unit, coarser, and contains many vesicles varying in size to 2 mm	N	N
29R-1	3-14	PP	738.20	739.35	30-145	115	—	700	51-2	Sparsely olivine phyric basalt	Medium grained, thick massive flow		Gray	—	N	N
29R-2	1-5	—	739.35	739.90	0-55	55	—	700	51-2	Sparsely olivine phyric basalt	Medium grained, thick massive flow		Gray	—	N	N
30R-1	1-2	PP	747.30	748.79	0-149	149	—	700	51-2	Sparsely olivine phyric basalt	Medium grained, thick massive flow	Flow	Gray	—	N	N
30R-2	1-3	XRF, PP, TSB	748.79	750.20	0-141	141	—	700	51-2	Sparsely olivine phyric basalt	Medium grained, thick massive flow		Gray	—	N	N
30R-3	1-6	PP	750.20	751.52	0-132	132	—	700	51-2	Sparsely olivine phyric basalt	Medium grained, thick massive flow		Gray	—	N	N
30R-4	1-4	PP	751.52	752.30	0-78	78	—	700	51-2	Sparsely olivine phyric basalt	Medium grained, thick massive flow		Gray	—	N	N
30R-5	1A-3A	PP, TSB	752.30	753.24	0-94	94	—	94	51-3	Sparsely olivine phyric basalt	Medium grained, thick massive flow	Pillow/flow	Gray	More massive unit, coarser, and contains many small vesicles	N	Y
30R-5	4A-5A	TSB	753.24	753.57	94-127	33	—	33	51-4	Sparsely olivine phyric basalt	Medium-grained sheet flow	Pillow	Gray	Contains many small vesicles	Y	Y
30R-5	6A-7A	—	753.57	753.77	127-147	20	—	121	51-5	Sparsely olivine phyric basalt	Medium-grained sheet flow		Gray	Contains many small vesicles	N	N
30R-6	1-6	—	753.77	754.22	0-45	45	—	121	51-5	Sparsely olivine phyric basalt	Medium-grained sheet flow	Flow	Gray	—	N	N
31R-1	1-8	PP	756.60	757.16	0-56	56	—	121	51-5	Sparsely olivine phyric basalt	Medium-grained sheet flow		Gray	—	N	N

Table T4 (continued).

Core, section	Piece	Analysis*	Depth (mbsf)		Interval (cm)	Length (cm)			Unit, subunit	Lithology	Texture	Structure	Color	Comments	Chilled margin present	
			Top	Bottom		Interval	Unit	Subunit							Top	Base
31R-1	9A-10C	—	757.16	757.89	56-129	73	—	935	51-6	Sparsely olivine phyric basalt	Medium grained, thick massive flow		Gray	Thick continuous subunit, good recovery and slow drilling rate in 31R	N	Y
31R-2	1-3B	PP	757.89	759.15	0-126	126	—	935	51-6	Sparsely olivine phyric basalt	Medium grained, thick massive flow		Gray	—	N	Y
31R-3	1A-7	XRF, PP, TSB	759.15	760.55	0-140	140	—	935	51-6	Sparsely olivine phyric basalt	Medium grained, thick massive flow		Gray	—	N	Y
31R-4	1A-3F	PP	760.55	762.00	0-145	145	—	935	51-6	Sparsely olivine phyric basalt	Medium grained, thick massive flow		Gray	—	N	Y
31R-5	1A-2I	PP, TSB	762.00	763.32	0-132	132	—	935	51-6	Sparsely olivine phyric basalt	Medium grained, thick massive flow	Flow	Gray	Coarser veins in this section	N	Y
31R-6	1A-1H	—	763.32	764.72	0-140	140	—	935	51-6	Sparsely olivine phyric basalt	Medium grained, thick massive flow		Gray	—	N	Y
31R-7	1A-7	PP	764.72	766.21	0-149	149	—	935	51-6	Sparsely olivine phyric basalt	Medium to fine grained, thick massive flow		Gray	0.5- to 1.5-cm-thick, 40-cm-long vein in this section, fine grained at base	N	Y
32R-1	1	XRF, PP	766.30	766.60	0-30	30	—	935	51-6	Sparsely olivine phyric basalt	Fine grained, thick massive flow		Gray	—	N	Y
32R-1	2-8	PP, TSB	766.60	767.13	30-83	53	243	53	52-1	Aphyric basalt	Fine-grained fractured pillow	Pillow	Dark gray	Fragmented small aphyric or sparsely phyric pillows, breccia	Y	Y
32R-1	9-15	—	767.13	767.79	83-149	66	—	66	52-2	Aphyric basalt	Fine-grained brecciated pillows, interpillow	Breccia	Dark gray and blue green	Some interpillow material, basalt fractured with unusual cavity fills and halos	Y	Y
32R-2	1-3	XRF	767.79	768.15	0-36	36	—	36	52-3	Aphyric basalt	Fine-grained fractured pillow	Pillow	Dark gray	Fragmented small aphyric or sparsely phyric pillows, breccia	Y	Y
32R-2	3-6	PP	768.15	768.43	36-64	28	—	88	52-4	Aphyric basalt	Fine-grained basalt fragments	Pillow/flow	Dark gray	Unordered and unoriented basalt pieces	N	N
33R-1	1-3	PP	775.70	776.30	0-60	60	—	88	52-4	Aphyric basalt	Fine-grained basalt fragments		Dark gray	—	N	N
33R-1	4-12	XRF, TSB	776.30	777.00	60-130	70	1760	94	53-1	Aphyric basalt	Fine-grained pillow or thin flow		Gray	Rubble basalt pieces at the top of the unit, more vesicles	Y	Y
33R-2	1-5	—	777.00	777.24	0-24	24	—	94	53-1	Aphyric basalt	Fine-grained pillow or thin flow		Gray	—	Y	Y
33R-2	6-7	—	777.24	777.47	24-47	23	—	146	53-2	Aphyric basalt	Fine-grained pillow or thin flow		Gray	Finer grained at upper margin but no chill observed	N	Y
34R-1	1A-3	PP	785.30	786.53	0-123	123	—	146	53-2	Aphyric basalt	Fine-grained pillow or thin flow		Gray	—	N	Y
34R-2	1A-1G	XRF, PP, TSB*2	786.53	787.23	0-70	70	—	70	53-3	Aphyric basalt	Fine rims, medium-grained center	Pillow/flow	Dark gray to gray	—	Y	Y
34R-2	2A-2B	—	787.23	787.59	70-106	36	—	36	53-4	Aphyric basalt	Fine rims, medium-grained center	Pillow	Dark gray to gray	Veins with red brown alteration halos	Y	Y
34R-2	3A-3D	—	787.59	787.99	106-146	40	—	80	53-5	Aphyric basalt	Fine rims, medium grained center		Dark gray to gray	—	Y	Y
34R-3	1A-3B	—	787.99	788.39	0-40	40	—	80	53-5	Aphyric basalt	Fine rims, medium grained center	Pillow/flow	Dark gray to gray	—	Y	Y

Table T4 (continued).

Core, section	Piece	Analysis*	Depth (mbsf)		Interval (cm)	Length (cm)			Unit, subunit	Lithology	Texture	Structure	Color	Comments	Chilled margin present	
			Top	Bottom		Interval	Unit	Subunit							Top	Base
34R-3	4-5	TSB	788.39	788.95	40-96	56	—	56	53-6	Aphyric basalt	Fine rims, medium grained center	Pillow/flow	Dark gray to gray	Veins with red green alteration halos	Y	Y
34R-3	7-8	PP	788.95	789.47	96-148	52	—	139	53-7	Aphyric basalt	Fine rims, medium grained center		Dark gray to gray	—	Y	Y
34R-4	1-3	—	789.47	789.77	0-30	30	—	139	53-7	Aphyric basalt	Fine rims, medium grained center	Flow	Dark gray to gray	—	Y	Y
35R-1	1-5	—	794.90	795.47	0-57	57	—	139	53-7	Aphyric basalt	Fine rims, medium grained center		Gray	—	Y	Y
35R-1	6-7	PP	795.47	796.27	57-137	80	—	129	53-8	Aphyric basalt	Fine rims, medium grained center		Gray	—	Y	Y
35R-2	1A-2	PP	796.27	796.76	0-49	49	—	129	53-8	Aphyric basalt	Fine rims, medium grained center	Flow	Gray	—	Y	Y
35R-2	3-6	XRF, PP, TSB	796.76	797.64	49-137	88	—	88	53-9	Aphyric basalt	Fine rims, medium grained center	Pillow/flow	Dark gray to gray	—	Y	Y
35R-3	1-2	—	797.64	797.96	0-32	32	—	32	53-10	Aphyric basalt	Fine rims, medium grained center	Pillow	Dark gray to gray	—	Y	Y
35R-3	3-4	—	797.96	798.42	32-78	46	—	46	53-10	Aphyric basalt	Fine rims, medium grained center	Pillow	Dark gray to gray	—	Y	Y
35R-3	5-6D	—	798.42	799.14	78-150	72	—	146	53-12	Aphyric basalt	Fine rims, medium grained center		Dark gray to gray	—	Y	Y
35R-4	1A-2	PP	799.14	799.88	0-74	74	—	146	53-12	Aphyric basalt	Fine rims, medium grained center	Flow	Dark gray to gray	—	Y	Y
35R-4	3-7	—	799.88	800.64	74-150	76	—	76	53-13	Aphyric basalt	Fine rims, medium grained center	Pillow/flow	Dark gray to gray	—	N	N
36R-1	1-5	XRF, PP*2	804.10	805.44	0-134	134	—	134	53-14	Aphyric basalt	Microcrystalline, hypocrySTALLINE at top	Flow	Gray to dark gray	Brecciated top, hypocrySTALLINE at top and base, coarser in center, no chills	N	N
36R-2	1-2	PP	805.44	805.90	0-46	46	—	46	53-15	Aphyric basalt	Microcrystalline, hypocrySTALLINE at top	Pillow	Gray	—	N	Y
36R-2	3-4	—	805.90	806.77	46-133	87	—	172	53-16	Aphyric basalt	Microcrystalline, hypocrySTALLINE at top		Dark gray	—	Y	Y
36R-3	1-3	PP	806.77	807.62	0-85	85	—	172	53-16	Aphyric basalt	Microcrystalline, hypocrySTALLINE at top	Flow	Dark gray	—	Y	Y
36R-3	4-8	—	807.62	807.83	85-106	21	—	21	53-17	Aphyric basalt, small angular fragments up to 5 cm	Microcrystalline, celadonite and carbonate cement	Breccia	Dark gray and very dark patches	Fragmented angular basalt pieces up to 5 cm, in green and white breccia cement	Y	N
36R-3	9-10	—	807.83	808.19	106-142	36	—	36	53-18	Aphyric basalt	Microcrystalline, hypocrySTALLINE at top	Pillow	Dark gray and very dark patches	—	Y	N
36R-4	1-4A	XRF, PP	808.19	809.64	0-145	145	—	213	53-19	Aphyric basalt	Microcrystalline margins, fine-grained center		Dark gray to gray	Fractured at the base and rubbly	Y	N
36R-5	1-4	—	809.64	810.32	0-68	68	—	213	53-19	Aphyric basalt	Microcrystalline margins, fine-grained center	Flow	Dark gray to gray	—	Y	N

Table T4 (continued).

Core, section	Piece	Analysis*	Depth (mbsf)		Interval (cm)	Length (cm)			Unit, subunit	Lithology	Texture	Structure	Color	Comments	Chilled margin present	
			Top	Bottom		Interval	Unit	Subunit							Top	Base
36R-5	6-8	—	810.32	810.59	68-95	27	1204	—	54	Aphyric basalt			Dark gray to gray	Top of flow rubbly and fractured, no contact observed at top	N	Y
37R-1	1A-1H	PP, TSB*3	813.30	814.73	0-143	143	1204	—	54	Aphyric basalt			Gray	Vesicles up to 0.5 cm, abundance increases toward base of section	N	Y
37R-2	1A-1B	XRF, PP, TSB	814.73	815.80	0-107	107	1204	—	54	Aphyric basalt			Gray	Abundant smectite- and saponite-filled vesicles up to 0.5 cm.	N	Y
37R-3	1A-1D	PP, TSB	815.80	817.18	0-138	138	1204	—	54	Aphyric basalt			Speckled gray	40-cm-long, thick vein and vesicles at top, alteration fronts along veins	N	Y
37R-4	1A-1D	PP	817.18	818.37	0-119	119	1204	—	54	Aphyric basalt			Speckled dark gray	Homogeneous section	N	Y
37R-5	1A-1E	XRF, PP, TSB*3	818.37	819.70	0-133	133	1204	—	54	Aphyric basalt	Flow		Dark to very dark speckled gray	Interval 60-130 cm has dark green gray, brown yellow alteration and miarolitic cavities	N	Y
37R-6	1A-1D	XRF, PP, TSB	819.70	821.14	0-144	144	1204	—	54	Aphyric basalt			Speckled dark gray to gray	—	N	Y
37R-7	1A-1B	PP	821.14	822.24	0-110	110	1204	—	54	Aphyric basalt			Speckled dark gray to gray	Altered zone at interval 20-40 cm	N	Y
38R-1	1A-1D	PP	822.80	824.26	0-146	146	1204	—	54	Aphyric basalt			Dark bluish gray	—	N	Y
38R-2	1A-1G	PP	824.26	825.63	0-137	137	1204	—	54	Aphyric basalt			Dark to very dark gray at base	Chilled contact at base against dark fractured pillow basalts	N	Y
38R-2	2-3	PP	825.63	825.75	137-149	12	458	12	55-1	Aphyric basalt	Pillow		Very dark gray	Glassy margins	Y	Y
38R-3	1-3	—	825.75	826.00	0-25	25	—	25	55-2	Aphyric basalt	Pillow		Dark to very dark gray	—	Y	Y
38R-3	3-6	—	826.00	826.30	25-55	30	—	30	55-3	Aphyric basalt	Pillow		Dark to very dark gray	—	Y	Y
38R-3	7-15	XRF	826.30	827.25	55-150	95	—	149	55-4	Aphyric basalt			Dark to very dark gray	Rubble basalt pieces at the base of the unit	Y	N
38R-4	1-4	—	827.25	827.79	0-54	54	—	149	55-4	Aphyric basalt	Flow		Dark to very dark gray	—	Y	N
39R-1	1-7	—	832.20	833.00	0-80	80	—	80	55-5	Aphyric basalt	Pillow/flow		Gray to dark gray	Hyaloclastite at top 10 cm, glassy and hypocrySTALLINE	Y	Y
39R-1	8-9	PP	833.00	833.65	80-145	65	—	162	55-6	Aphyric basalt			Greenish gray and gray to dark gray	Top 5 cm is hyaloclastite	Y	N
39R-2	1-9	XRF, PP*2, TSB	833.65	834.62	0-97	97	—	162	55-6	Aphyric basalt	Flow		Gray to dark gray	No contact, but highly fractured basalt fragments at base	N	N

Table T4 (continued).

Core, section	Piece	Analysis*	Depth (mbsf)		Interval (cm)	Length (cm)			Unit, subunit	Lithology	Texture	Structure	Color	Comments	Chilled margin present	
			Top	Bottom		Interval	Unit	Subunit							Top	Base
39R-2	10-11	—	834.62	834.87	97-122	25	591	—	56	Aphyric basalt breccia with carbonate-dominated cement	Microcrystalline basalt fragments in variable cement		Gray to dark gray basalt clasts	Cement is dark greenish black and white	N	N
40R-1	1A-8	PP, TSB	841.50	842.99	0-149	149	591	—	56	Aphyric basalt breccia with carbonate-dominated cement	Microcrystalline basalt fragments in variable cement		Gray to dark gray	Carbonate in breccia cement decreases toward the base of the unit	N	N
40R-2	1-3C	XRF, PP	842.99	844.40	0-141	141	591	—	56	Aphyric basalt breccia with carbonate-dominated cement	Microcrystalline basalt fragments in variable cement	Breccia	Gray	Basalt clasts are generally angular, some are subangular, variable sizes <1-40 cm	N	N
40R-3	1-12	PP	844.40	845.87	0-147	147	591	—	56	Aphyric basalt breccia with carbonate-dominated cement	Microcrystalline basalt fragments in variable cement		Dark gray, gray to greenish gray	Some pieces are glassy, larger clasts, less carbonate in cement	N	N
40R-4	1-3	—	845.87	846.26	0-39	39	591	—	56	Aphyric basalt breccia with dark cement	Microcrystalline basalt fragments in variable cement		Dark to very dark gray	Cement becomes darker and greenish black toward base, more fragmented	N	N
41R-1	1-11	XRF	850.80	851.70	0-90	90	591	—	56	Fragmented aphyric basalt pieces	Microcrystalline basalt fragments	Pillow/flow	Gray to dark gray	Rubby section, containing broken basalt pieces, until top of flow	N	N
41R-1	12-17	PP	851.70	852.30	90-150	60	238	—	57	Aphyric basalt	Microcrystalline		Gray	No chill, but microcrystalline at margins and coarser in the center	N	N
42R-1	1A-1J	PP	860.00	861.20	0-120	120	238	—	57	Aphyric basalt	Microcrystalline to fine grained	Flow	Gray	—	N	N
42R-2	1A-1C	XRF*2, PP, TSB	861.20	861.78	0-58	58	238	—	57	Aphyric basalt	Microcrystalline		Gray	—	N	N
42R-2	3-12	PP, TSB	861.78	862.48	58-128	70	517	99	58-1	Hyaloclastite with aphyric basalt pillow fragments	Glassy, hypocrySTALLINE to microcrystalline	Hyaloclastite	Dark gray, green to black cement	Fresh glass in several pieces	N	N
42R-3	1-3	—	862.48	862.77	0-29	29	517	99	58-1	Gravel and aphyric basalt pillow fragments	Glassy, hypocrySTALLINE to microcrystalline	Pillow	Dark gray, green to black cement	Rubble and gravel at the base	N	N
43R-1	1-4C	—	869.10	869.90	0-80	80	—	80	58-2	Aphyric basalt	Microcrystalline to fine grained		Gray to dark gray	No chills or contacts, but microcrystalline at margins and coarser in the center	N	N
43R-1	5	XRF, PP, TSB	869.90	870.33	80-123	43	—	43	58-3	Aphyric basalt	Microcrystalline to fine grained	Pillow	Gray to dark gray	—	N	N
43R-1	6-9	—	870.33	870.56	123-146	23	—	295	58-4	Aphyric basalt	Microcrystalline to fine grained		Gray	Celadonite veins with red brown and green halos	N	N
43R-2	1-6	PP	870.56	871.92	0-136	136	—	295	58-4	Aphyric basalt	Microcrystalline to fine grained	Flow	Gray	—	N	N
43R-3	1A-7	PP	871.92	873.28	0-136	136	—	295	58-4	Aphyric basalt	Microcrystalline to fine grained		Gray	Brecciated interval at top 20 cm, rubble and microcrystalline at base	N	N

Table T4 (continued).

Core, section	Piece	Analysis*	Depth (mbsf)		Interval (cm)	Length (cm)			Unit, subunit	Lithology	Texture	Structure	Color	Comments	Chilled margin present	
			Top	Bottom		Interval	Unit	Subunit							Top	Base
44R-1	1-2	PP	878.80	880.05	0-125	125	330	—	59	Aphyric basalt	Microcrystalline to fine grained		Gray	Contains many small vesicles, halos along veins	N	N
44R-2	1A-1G	XRF, PP, TSB	880.05	881.52	0-147	147	330	—	59	Aphyric basalt	Microcrystalline to fine grained	Flow	Gray to dark gray	70-cm-long carbonate vein, vesicles decrease toward base of section	N	N
44R-3	1A-2B	PP	881.52	882.10	0-58	58	330	—	59	Aphyric basalt	Microcrystalline to fine grained		Dark gray	Brown and green halos, microcrystalline base, but no chills	N	N
44R-3	3-10	—	882.10	883.02	58-150	92	1523	99	60-1	Aphyric basalt	Microcrystalline	Pillow/flow	Dark gray	Rubby microcrystalline top	N	Y
45R-1	1-2	—	888.40	888.47	0-7	7	—	99	60-1	Aphyric basalt	Microcrystalline		Dark gray	—	N	Y
45R-1	2-7	PP	888.47	889.02	7-62	55	—	55	60-2	Aphyric basalt	Microcrystalline	Pillow/flow	Dark gray	Glassy margins	Y	Y
45R-1	8-13	TSB	889.02	889.42	62-102	40	—	40	60-3	Aphyric basalt	Microcrystalline	Pillow	Dark gray to dark greenish gray	Hyaloclastite at base, glassy and hypocrySTALLINE	Y	Y
45R-1	13-15	—	889.42	889.74	102-134	32	—	94	60-4	Aphyric basalt	Microcrystalline to fine grained		Gray	Rubby base with glassy chills	Y	Y
45R-2	1A-1D	XRF, PP, TSB	889.74	890.36	0-62	62	—	94	60-4	Aphyric basalt	Microcrystalline to fine grained	Pillow/flow	Gray	—	Y	Y
45R-2	2-4	PP	890.36	890.98	62-124	62	—	115	60-5	Aphyric basalt	Microcrystalline to fine grained		Gray	Rubby basalt pieces, celadonite in some pieces	Y	Y
46R-1	1-3	XRF, PP, TSB	898.00	898.53	0-53	53	—	115	60-5	Aphyric basalt	Microcrystalline to fine grained	Flow	Gray	Glassy chill at base	Y	Y
46R-1	4	—	898.53	899.40	53-140	87	—	99	60-6	Aphyric basalt	Microcrystalline to fine grained		Gray	Microcrystalline top	N	Y
46R-2	1	—	899.40	899.52	0-12	12	—	99	60-6	Aphyric basalt	Microcrystalline to fine grained	Pillow/flow	Gray	—	N	Y
46R-2	2A-6D	XRF, PP, TSB	899.52	900.55	12-115	103	—	103	60-7	Aphyric basalt	Microcrystalline to fine grained	Flow	Dark greenish gray	30-cm brecciated interval containing carbonate and celadonite	N	Y
46R-2	7-8	—	900.55	900.66	115-126	11	—	61	60-8	Aphyric basalt	Microcrystalline	Pillow/flow	Dark gray	Red brown and green halos surrounding veins	Y	Y
46R-3	1-2A	PP	900.66	901.16	0-50	50	—	61	60-8	Aphyric basalt	Microcrystalline		Dark gray	—	Y	Y
46R-3	3-10	—	901.16	901.80	50-114	64	—	64	60-9	Aphyric basalt	Microcrystalline	Pillow/flow	Gray	—	Y	N
47R-1	1-3	—	907.70	907.93	0-23	23	—	23	60-10	Aphyric basalt	Microcrystalline	Pillow	Dark gray	—	N	Y
47R-1	4-10	XRF, PP	907.93	908.32	23-62	39	—	39	60-11	Aphyric basalt	Microcrystalline	Pillow	Dark gray	Rubby basalt pieces	N	Y
47R-1	10-19	—	908.32	909.01	62-131	69	—	69	60-12	Aphyric basalt	Microcrystalline	Pillow/flow	Gray	Rubby basalt pieces	Y	N
48R-1	1A-2D	XRF, PP, TSB	916.70	917.58	0-88	88	—	88	60-13	Aphyric basalt	Fine grained to microcrystalline with glassy chill	Pillow/flow	Gray	—	N	Y
48R-1	3-4	—	917.58	918.01	88-131	43	—	105	60-14	Aphyric basalt	Microcrystalline to fine grained		Dark gray to gray	Miarolitic cavities toward base of unit	Y	Y
48R-2	1-6	—	918.01	918.63	0-62	62	—	105	60-14	Aphyric basalt	Microcrystalline to fine grained	Flow	Dark gray to gray	—	Y	Y
48R-2	7-12	PP	918.63	919.21	62-120	58	—	58	60-15	Aphyric basalt	Microcrystalline to fine grained	Pillow/flow	Gray	—	Y	Y
48R-2	13-14	TSB	919.21	919.48	120-147	27	—	27	60-16	Aphyric basalt	Microcrystalline	Pillow	Dark gray to gray	—	Y	N
48R-3	1-4	XRF	919.48	919.92	0-44	44	—	44	60-17	Aphyric basalt	Microcrystalline to fine grained	Pillow	Gray	—	Y	N
49M-1	1-3	PP, TSB*2	928.30	928.79	0-49	49	—	49	60-18	Aphyric basalt	Microcrystalline to hypocrySTALLINE	Pillow	Dark gray	Finer grained at upper and lower margins, but no chills observed	N	N

Table T4 (continued).

Core, section	Piece	Analysis*	Depth (mbsf)		Interval (cm)	Length (cm)			Unit, subunit	Lithology	Texture	Structure	Color	Comments	Chilled margin present	
			Top	Bottom		Interval	Unit	Subunit							Top	Base
49M-1	4-7	—	928.79	929.06	49-76	27	—	27	60-19	Aphyric basalt	Microcrystalline to hypocrySTALLINE with glassy chill	Pillow	Dark gray to gray	Glassy piece at top	Y	Y
49M-1	7-12	PP	929.06	929.40	76-110	34	—	34	60-20	Aphyric basalt	Microcrystalline to hypocrySTALLINE with glassy chill	Pillow	Dark gray to gray	Glassy pillow rims	Y	Y
50M-1	1-3	TSB	931.50	931.76	0-26	26	—	26	60-21	Aphyric basalt	Microcrystalline to hypocrySTALLINE with glassy chill	Pillow	Dark gray to gray	Glassy pillow rim at base	N	Y
50M-1	3-6	XRF, PP, TSB	931.76	932.08	26-58	32	—	32	60-22	Aphyric basalt	Microcrystalline to hypocrySTALLINE with glassy chill	Pillow	Dark gray to gray	—	Y	N
51M-1	1	PP	932.00	932.39	0-39	39	—	39	60-23	Aphyric basalt	Microcrystalline to hypocrySTALLINE with glassy chill	Pillow	Dark gray to gray	Glassy pillow rim at base	N	Y
51M-1	2-4	—	932.39	932.67	39-67	28	—	28	60-24	Aphyric basalt	Microcrystalline to hypocrySTALLINE with glassy chill	Pillow	Dark gray to gray	Glassy rim at base	Y	Y
51M-1	4-5	—	932.67	932.87	67-87	20	—	20	60-25	Aphyric basalt	Microcrystalline to hypocrySTALLINE with glassy chill	Pillow	Dark gray to gray	Glassy rim at top	Y	N
52M-1	1-4	XRF, PP, TSB	932.80	933.65	0-85	85	—	85	60-26	Aphyric basalt	Microcrystalline to hypocrySTALLINE at base	Pillow/flow	Dark gray to gray	—	N	N

Notes: * = XRF analysis from Castillo et al. (1992), includes number of analyses per section; — = no data, Y = yes, N = no, XRF = X-ray fluorescence, PP = physical properties, TSB = thin-section billet, *2 = two samples. Cores 129-801C-1R to 12R were described in the "Site 801" chapter of the Leg 129 *Initial Reports* volume (Shipboard Scientific Party, 1990) and modified for consistency downhole during Leg 185 to include some subunits within the existing units. Cores 185-801C-13R to 52M are described in this chapter. This table is also available in [ASCII format](#).

Table T5. Location of volcanic glass, Hole 801C. (See table note. Continued on next page.)

Core	Section	Location (cm)	Piece	Unit	Comment
129-801C-					
5R	3	101	4A	12	
5R	4	36	2B	12	Glass in carbonate
5R	4	37	3C	12	Glass in carbonate
12R	1	60	11C	31	Thin section billet with 1-mm-thick glass zone under glass altered to clay
12R	1	75	13	31	Thin section billet with 1-mm-thick glass zone under glass altered to clay
12R	1	85	15		Thin section with volcanic glass
12R	1	150	23	31	
12R	2	90	16	31	
12R	2	22	2	32	
12R	2	85	15		Thin section with volcanic glass
185-801C-					
14R	4	140	14B		Glass at bottom of piece
15R	1	27	4		Thin section with volcanic glass
15R	5	107			Thin section with volcanic glass
16R	4	39	8	50	
16R	5	73	9	50	
17R	1	24	5		
17R	1	35			Thin section with volcanic glass
17R	2	9	3		
17R	3	83	6		Thin section with volcanic glass
17R	5	111	13		
18R	1	32	6		
18R	1	44	8		
18R	1	48	9		
18R	1	105	12		
18R	1	108	13		
18R	1	114	14	50	
18R	1	148	18		
18R	2	0	1		
19R	3	41	1	50	
20R	2	107	10	50	
20R	2	148	10	50	
22R	3	0-15	1,2,3	50	
23R	1	13	3	50	
23R	1	110	9	50	
23R	3	53	4	50	
23R	4	0	1	50	
24R	1	96	10	50	
25R	1	0	1A	50	
27R	3	0	1	50	
27R	3	10	2	50	
27R	3	13	3	50	Glass will be difficult to extract
28R	1	95	2	50	Three pieces with 50, 50, and 100 mg of glass, respectively
28R	1	112	5	50	Difficult to separate glass from alteration
28R	2	67	2	50	Difficult to estimate the amount
28R	2	79	3	50	
28R	2	83	4	50	
28R	2	102	7	50	Glass is in breccia surrounded with carbonate
28R	2	120	9	50	Glass is in breccia surrounded with carbonate
28R	2	150	10	50	
28R	3	0	1	50	
28R	3	40	2	50	
28R	3	50	3	50	
28R	3	56	4	50	
28R	3	63	5	50	
28R	3	70	6	50	
28R	3	92	9	50	Two pieces with 100 mg and 200 mg of glass, respectively
29R	1	25	2	51	
34R	2	68	1	53	
34R	2	72	2	53	
34R	3	103	6	53	
35R	3	32	1	53	Piece and vial with 200 mg of chips
35R	4	70	2	53	
42R	2	60	2	58	
42R	2	64	3	58	
42R	2	80	4	58	

Table T5 (continued).

Core	Section	Location (cm)	Piece	Unit	Comment
42R	2	90	5	58	
42R	2	96	6	58	
42R	2	103	7	58	
42R	2	107	8	58	
42R	2	111	9	58	
42R	2	117	10	58	
42R	2	124	11	58	Thin section with volcanic glass
42R	2	133	12	58	
45R	1	64	8	60	Thin section with volcanic glass
46R	1	48	3	60	
48R	1	86	2	60	
48R	2	6	6	60	Thin section with volcanic glass
48R	2	121	12	60	Thin section with volcanic glass

Note: This table is also available in [ASCII format](#).

Table T6 (continued).

Thin section	Core, section, interval (cm)	Piece	Depth	Unit	Phenocrysts						Groundmass										
					Plagioclase		Olivine		Pyroxene		Plagioclase		Pyroxene		Olivine		Oxides		Vesicles		
					Size (vol%)	Size (mm)	Glass (vol%)	Size (vol%)	Size (mm)												
53	34R-2, 21-23	1C	786.74	53						50	0.2	30	0.1			4	0.05	16	0.5	0.4	
54	34R-2, 52-55	1F	787.03	53						50	0.3	35	0.1			5	0.05	10	1	0.1	
55	34R-3, 55-58	4	788.54	53						35	0.15	7	0.1	1	0.15	4	0.03	53	1	0.2	
57	35R-2, 98-100	5	797.25	53						50	0.4	25	0.1			5	0.02	20	1	0.2	
58	37R-1, 29-32	1A	813.59	54						50	0.25	36	0.07			6		8	0.5	0.2	
59	37R-1, 66-68	1D	813.96	54						50	0.45	43	0.1			2	0.1	5	1	0.4	
60	37R-1, 34-38	1F	814.24	54						50	0.4	43	0.2			5		2	1	0.8	
61	37R-2, 25-28		814.98	54						52	0.6	35	0.3			7		6	10	2	
62	37R-3, 37-40	1A	817.55	54						51	0.6	35	0.3			6		8	0.5	0.6	
63	37R-5, 37-40	1A	818.74	54						50	1.4	37	1	2	0.4	5		7	0.5	1	
64	37R-5, 109-114	1D	819.46	54						55	1	38	0.4			7					
65	37R-6, 29-33		819.99	54						45	1	20	0.6			5		30			
66	39R-2, 25-28	3	833.92	55	0.3	0.6				52	0.15	32	0.08	3	0.1	3		10	1	0.2	
69	40R-1, 65-67	1F	841.57	56						54	0.08	30	0.04	1	0.04	5		10			
67	42R-2, 8-11	1B	861.28	57						52	0.15	39	0.07	1	0.1	4		4	0.5	0.15	
68	42R-2, 126-128	11	862.46	58	2	0.2	1	0.1	0.5	0.55								96			
70	43R-1, 102-104	5	870.12	58						50	0.3	30	0.08	2	0.2	3		15	1	0.12	
71	44R-2, 59-61	1B	879.39	59						50	0.4	30	0.2	1	0.08	1	0.05	18			
72	45R-1, 64-65	8	889.04	60	3	0.2			0.5	0.1								96	2	0.1	
73	45R-2, 43-47	1C	890.18	60	0.5	0.5					35	0.2	25	0.05			10	0.03	30	0.5	0.1
74	46R-1, 10-13	2B	898.10	60							53	0.5	35	0.2	1	0.2	3	0.02	8		
75	46R-2, 73-79	6B	900.15	60							54	0.5	35	0.15	0		2	0.02	11		
76	48R-1, 46-49	2B	917.16	60	0.3	0.6					60	0.3	30	0.09	0.5	0.1	3	0.03	7		
77	48R-2, 121-131	12	919.21	60	2	0.2	0.5	0.02	0.3	0.4								96	0.5	0.08	
79	49M-1, 4-6	1	928.34	60							50	0.3	17	0.06			2	0.01	31		
80	49M-1, 30-33	3	928.60	60	<1	0.6			<<1	0.5	48	0.2	16	0.05			1	<<0.01	35		
82	50M-1, 43-45	5	931.93	60	<1	0.4			<<1	0.4	32	0.2	5	0.04			<1	<<0.01	62		
83	52M-1, 74-77	4	933.54	60	<1	0.5			<<1	0.3	50	0.2	15	0.05			2	0.02	32		

 Note: This table is also available in [ASCII format](#).

Table T7. Shipboard XRF analyses, Leg 185 Hole 801C. (Continued on next two pages.)

Core, section:	14R-1	14R-3	14R-4	15R-4	15R-7	16R-1	16R-3	16R-4	17R-1	17R-3	18R-1	18R-2	19R-3	20R-2	21R-1	22R-2	23R-1	23R-4
Interval (cm):	75-78	120-122	64-66	69-71	72-74	110-112	50-52	119-121	47-50	85-91	69-73	107-110	37-39	51-55	103-106	57-60	24-27	10-12
Piece number:	2A	10	8A	1	1E	4F	5	6G	7A	6	10	7	1	1	6B	2C	3A	1
Unit:	34	37	38	44	46	47	49	49	49	50	50	50	50	50	50	50	50	50
Depth (mbsf):	604.75	607.98	608.80	618.40	622.10	624.40	626.52	628.62	633.27	636.63	642.89	644.77	654.76	662.63	671.03	675.41	682.14	686.08
SiO ₂	48.54	33.87	48.35	49.26	50.64	46.57	22.75	48.60	49.53	48.51	48.25	48.78	48.53	48.80	49.71	47.94	49.25	49.02
TiO ₂	2.38	0.07	2.27	2.02	2.88	2.30	0.15	2.99	2.99	2.71	2.55	2.88	2.50	2.32	2.13	2.09	2.24	2.31
Al ₂ O ₃	14.56	2.90	14.98	15.47	20.09	15.84	1.73	12.75	13.09	13.91	13.72	15.31	14.89	14.57	13.65	13.66	13.79	14.11
Fe ₂ O ₃	15.12	8.72	13.68	13.50	7.80	16.35	20.52	17.53	15.47	14.46	15.74	14.81	15.80	14.27	14.40	14.01	14.08	14.53
MnO	0.23	0.12	0.22	0.19	0.12	0.21	0.31	0.29	0.26	0.23	0.25	0.20	0.22	0.23	0.22	0.23	0.25	0.24
MgO	6.40	2.87	6.34	5.88	1.24	5.99	13.61	5.97	5.86	5.76	6.58	6.84	7.03	7.01	6.60	6.77	6.78	6.84
CaO	10.99	47.92	11.99	11.56	12.94	11.10	39.89	10.21	10.85	12.00	11.14	8.86	9.35	10.75	11.39	13.83	11.36	11.20
Na ₂ O	2.42	0.12	2.52	2.65	3.22	2.57	—	2.43	2.38	2.36	2.43	2.86	2.75	2.53	2.33	2.21	2.36	2.47
K ₂ O	0.08	1.82	0.15	0.11	0.36	0.07	1.19	0.07	0.18	0.16	0.09	0.21	0.10	0.19	0.07	0.09	0.07	0.07
P ₂ O ₅	0.21	0.03	0.20	0.16	0.26	0.20	0.05	0.28	0.28	0.25	0.23	0.27	0.23	0.24	0.19	0.19	0.20	0.21
Total	100.91	98.41	100.69	100.79	99.53	101.19	100.19	101.11	100.87	100.35	100.96	100.99	101.38	100.88	100.67	101.01	100.36	100.98
LOI	1.92	34.42	3.13	4.42	8.63	4.66	36.21	0.20	0.27	1.80	1.66	2.87	2.60	2.91	0.40	3.59	1.12	1.50
Nb	5	—	4	3	7	6	2	7	8	6	6	6	6	6	5	4	5	5
Zr	140	13	132	111	127	127	44	186	190	166	156	173	155	140	131	129	140	144
Y	46	66	45	36	38	38	25	55	57	55	48	47	43	49	44	43	45	46
Sr	124	63	119	126	191	143	102	114	128	119	122	141	134	125	116	117	119	120
Rb	3	33	4	4	5	3	28	4	5	4	4	5	2	6	3	3	4	3
Zn	121	—	142	129	17	242	43	146	147	143	119	141	136	127	124	99	125	126
Cu	78	41	76	81	44	79	44	74	70	74	82	86	80	76	77	76	77	77
Ni	49	15	68	52	48	67	42	27	49	44	48	53	56	61	52	51	54	50
Cr	113	13	164	134	258	192	14	24	96	92	109	137	102	96	97	97	90	89
V	465	61	450	439	483	435	71	531	513	517	497	544	535	518	464	460	487	500
Ce	8	9	3	4	18	1	—	3	10	11	10	8	10	8	5	4	9	11
Ba	—	290	3	7	26	—	20	—	4	—	—	6	—	3	—	10	6	—

Notes: LOI = loss on ignition. — = not detected; blank = not determined. This table is also available in [ASCII format](#).

Table T7 (continued).

Core, section:	24R-1	24R-2	25R-1	26R-1	27R-2	27R-5	28R-2	29R-1	30R-2	31R-3	32R-1	32R-2	33R-1	34R-2	35R-2	36R-1	36R-4
Interval (cm):	103-107	107-112	141-145	89-92	40-43	8-12	36-38	16-18	98-100	48-50	28-30	17-20	119-123	21-23	116-118	64-66	112-114
Piece number:	11	8	15	8	2A	1	1B	1	3B		1	2	12	1C	5	4	3A
Unit:	50		50	50	50	50	50	51	51	51	51	52	53	53	53	53	53
Depth (mbsf):	692.33	693.70	702.11	711.09	721.38	725.30	730.40	738.06	749.72	759.66	766.58	767.97	776.89	786.75	797.43	804.74	809.31
SiO ₂	48.34	50.92	49.92	48.83	48.80	49.35	48.83	48.5	48.44	48.59	48.59	48.64	48.38	48.92	48.91	48.65	49.16
TiO ₂	2.28	2.14	2.19	2.24	2.12	1.88	1.88	2.51	2.37	2.37	2.63	2.42	2.52	2.61	2.52	2.47	2.57
Al ₂ O ₃	14.28	13.85	14.46	14.90	13.83	14.13	14.31	13.78	13.34	13.3	14.63	13.35	13.79	14.43	13.87	13.85	13.84
Fe ₂ O ₃	14.94	15.07	12.70	13.31	14.76	13.70	13.30	15.11	15.77	15.59	14	16.79	14.75	14.09	14.86	14.46	15.31
MnO	0.22	0.12	0.20	0.22	0.23	0.21	0.23	0.26	0.24	0.24	0.23	0.2	0.24	0.23	0.25	0.24	0.22
MgO	6.70	8.06	6.50	6.58	7.03	7.16	7.04	6.74	6.50	6.37	6.35	6.59	6.93	6.94	6.95	7.15	5.84
CaO	10.59	2.48	11.33	11.52	11.59	11.99	12.47	11.09	11.21	11.27	11.22	8.56	10.84	10.69	11.01	11.08	9.65
Na ₂ O	2.55	1.16	2.46	2.56	2.23	2.10	2.15	2.21	2.26	2.12	2.42	2.19	2.29	2.44	2.16	2.43	2.41
K ₂ O	0.19	0.23	0.08	0.10	0.05	0.09	0.06	0.11	0.07	0.06	0.08	1.15	0.13	0.11	0.09	0.06	0.36
P ₂ O ₅	0.22		0.19	0.20	0.19	0.17	0.17	0.23	0.22	0.22	0.24	0.26	0.24	0.24	0.24	0.22	0.25
Total	100.29	100.61	100.02	100.44	100.81	100.76	100.42	100.54	100.39	100.15	100.39	100.15	100.12	100.72	100.85	100.59	99.61
LOI	2.63	2.60	1.35	1.46	0.20	0.07	0.59	0.00	-0.26	0.86	1.90	2.35	1.05	1.24	1.26	0.98	1.73
Nb	5	4	4	4	4	4	6	5	6	6	6	5	7	8	6	5	5
Zr	146	129	139	139	133	118	117	159	148	147	165	149	158	165	158	159	165
Y	46	56	47	45	44	40	39	52	50	50	52	55	53	46	49	49	57
Sr	126	116	125	128	115	113	122	113	110	108	122	109	119	126	119	118	118
Rb	7	22	3	4	4	3	3	3	3	2	3	27	4	3	3	3	10
Zn	115	154	121	130	109	103	104	137	126	131	138	129	133	134	129	125	121
Cu	76	66	75	77	74	79	77	73	72	72	73	55	76	78	77	73	59
Ni	62	38	72	63	59	64	65	49	47	46	48	33	54	52	52	51	47
Cr	102	110	213	141	117	189	167	89	86	88	102	91	89	96	86	86	82
V	494	436	484	493	464	423	422	519	494	488	531	506	515	537	519	529	551
Ce	7	10	8	9	6	1	6	1	3	1	11	2	2	7	5	6	11
Ba	1	2	12	8	—	13	5	—	—	—	—	—	—	—	—	—	—

Table T7 (continued).

Core, section:	37R-2	37R-5	37R-6	38R-3	39R-2	40R-2	41R-1	42R-2	42R-2	43R-1	44R-2	45R-2	46R-1	46R-2	47R-1	48R-1	48R-3
Interval (cm):	25-27	37-40	33-35	80-82	25-28	53-56	57-59	8-11	19-22	102-104	59-62	44-46	25-27	75-77	51-53	42-44	14-16
Piece number:	1A	1A	1A	9	3	3A	8	1B	1B								
Unit:	54	54	54	55	56	56	56	57	57	58	59	60	60	60	60	60	60
Depth (mbsf):	815.00	818.83	820.13	826.56	833.92	843.51	851.37	861.29	861.40	870.12	880.65	890.19	898.23	900.15	908.19	917.16	919.63
SiO ₂	46.69	49.22	46.76	48.33	48.67	49.08	49.63	49.66	49.83	48.60	48.65	49.42	48.89	50.07	48.76	49.50	48.77
TiO ₂	2.26	2.75	2.29	2.43	2.50	2.27	1.95	1.77	1.77	2.02	2.21	2.05	2.09	2.25	2.1	2.03	2.025
Al ₂ O ₃	12.76	13.11	13.34	14.83	14.29	15.05	14.71	14.78	14.91	14.06	14.42	14.73	14.27	15.32	14.16	13.745	13.55
Fe ₂ O ₃	13.36	16.02	17.77	14.46	14.35	13.30	12.99	12.01	11.84	14.12	14.05	12.36	13.59	11.40	13.94	13.98	14.80
MnO	0.28	0.23	0.21	0.25	0.25	0.21	0.24	0.21	0.22	0.25	0.23	0.23	0.24	0.18	0.26	0.24	0.25
MgO	5.67	6.03	6.40	6.90	7.19	7.36	7.24	7.33	7.28	7.17	7.04	7.13	7.40	7.72	7.13	7.385	7.32
CaO	16.90	10.52	11.37	10.64	10.85	10.65	11.30	12.30	12.49	11.51	11.63	11.21	11.35	10.33	11.225	11.475	11.325
Na ₂ O	2.11	2.21	2.11	2.33	2.25	2.34	2.45	2.27	2.33	2.36	2.38	2.63	2.41	2.64	2.395	2.28	2.275
K ₂ O	0.10	0.13	0.31	0.15	0.10	0.10	0.18	0.05	0.06	0.11	0.06	0.15	0.09	0.17	0.09	0.07	0.075
P ₂ O ₅	0.24	0.25	0.22	0.22	0.22	0.20	0.17	0.15	0.16	0.17	0.20	0.18	0.19	0.2	0.19	0.18	0.18
Total	100.34	100.44	100.76	100.52	100.66	100.54	100.84	100.51	100.87	100.36	100.85	100.08	100.49	100.28	100.245	100.88	100.56
LOI	7.42	0.66	3.66	2.30	1.69	2.05	1.49	0.59	0.92	1.17	1.15	1.17	0.92	1.97	0.73	-0.26	-0.19
Nb	4	6	4	5	6	5	4	3	3	4	5	4	6	6	7	6	
Zr	149	167	137	148	153	143	116	111	111	122	134	126	128	134	130	126	
Y	49	51	46	44	47	41	39	39	38	41	41	44	42	41	43	46	
Sr	118	110	109	119	120	131	124	125	127	116	125	120	121	134	123	119	
Rb	3	4	8	5	3	3	6	3	3	4	2	3	2	2	2	2	
Zn	100	126	92	131	141	122	119	100	98	116	121	117	113	129	115	108	
Cu	64	73	67	74	78	81	79	82	82	77	78	82	82	83	82	81	
Ni	44	39	24	54	58	60	59	67	68	50	49	60	52	68	51	50	
Cr	68	54	92	125	119	116	118	272	283	83	103	142	106	120	105	97	
V	426	563	487	523	528	492	450	408	404	459	480	466	478	470	475	459	
Ce	7	2	4	—	5	9	2	7	6	1	1	7	8	13	1	6	
Ba	6	—	—	—	—	—	3	3	6	—	—	3	—	12	—	8	

Table T8. Summary of vein types.

Vein types	Number	Width (mm)		
		Average	Minimum	Maximum
Carbonate (>90%)	1109	0.8	0.1	16
Saponite (>90%)	1424	0.4	0.1	20
Celadonite (>90%)	42	1.2	0.1	4
Pyrite (>80%)	55	0.13	0.1	0.5
Fe oxyhydroxide (>80%)	21	0.4	0.1	1.5
Silica (>80%)	11	7.8	0.1	25
Carbonate/Saponite	219	0.8	0.1	8
Other	688	0.9	0.1	15
Total	3569			

Note: This table is also available in [ASCII format](#).

Table T9. Volatile and alkali data vs. depth, Leg 185 Hole 801C.

Core, section, interval (cm)	Depth (mbsf)	Sample type	Total C (wt%)	Organic C (wt%)	Inorganic C (wt%)	CO ₂ (wt%)	S (wt%)	H ₂ O (wt%)
185-801C-								
14R-1, 75-78	604.75	Basalt	0.25	0.15	0.10	0.37	0.00	2.70
14R-3, 120-122	607.98	Sediment	9.49	1.71	7.78	28.53	0.00	1.98
15R-7, 72-74	622.10	Hyaloclastite	1.80	0.36	1.44	5.28	0.00	4.86
16R-3, 50-52	626.52	Sediment	11.90	2.15	9.75	35.75	0.00	1.35
17R-1, 47-50	633.27	Basalt	0.12	0.01	0.11	0.40	0.07	1.44
18R-2, 107-110	644.77	Basalt	0.16	0.03	0.13	0.48	0.00	5.22
20R-2, 51-55	662.63	Basalt	0.21	0.00	0.21	0.77	0.16	2.16
21R-1, 103-106	671.03	Basalt	0.09	0.02	0.07	0.26	0.07	0.81
24R-2, 107-112	693.70	Basalt	0.08	0.02	0.06	0.22	0.00	6.12
27R-2, 40-43	721.38	Basalt	0.03	0.00	0.03	0.11	0.02	0.99
29R-1, 16-18	738.06	Basalt	0.04	0.00	0.04	0.15	0.04	2.16
31R-3, 48-50	759.66	Basalt	0.09	0.00	0.09	0.33	0.09	0.72
32R-2, 17-20	767.97	Basalt	0.05	0.01	0.04	0.15	0.00	4.41
34R-2, 21-23	786.75	Basalt	0.04	0.02	0.02	0.07	0.00	1.89
36R-4, 112-114	809.31	Basalt	0.17	0.02	0.15	0.55	0.00	1.98
37R-2, 25-27	815.00	Basalt	1.79	0.03	1.76	6.45	0.04	1.44
37R-6, 33-35	820.13	Basalt	0.53	0.01	0.52	1.91	0.00	2.52
39R-2, 25-28	833.92	Basalt	0.09	0.06	0.03	0.11	0.00	2.16
41R-1, 57-59	851.37	Basalt	0.07	0.03	0.04	0.15	0.00	1.98
42R-2, 19-22	861.40	Basalt	0.10	0.02	0.08	0.29	0.00	1.35
44R-2, 59-62	880.65	Basalt	0.08	0.00	0.08	0.29	0.01	1.71
45R-2, 44-46	890.20	Basalt	0.05	0.00	0.05	0.18	0.02	1.62
47R-1, 51-53	908.21	Basalt	0.03	0.00	0.03	0.11	0.07	1.53
48R-3, 14-16	919.64	Basalt	0.03	0.00	0.03	0.11	0.13	0.90

Note: This table is also available in [ASCII format](#).

Table T10. Alkali budget, Hole 801C.

	Volume (vol%)	K ₂ O (wt%)	Total K (%)
Rock	96.75	0.08	79.40
Alteration halos	1.70	0.24	4.19
Breccia + hyaloclastite	1.50	0.80	12.31
Celadonite veins	0.05	8.00	4.10
Total altered Leg 185 section:		0.09	100.00
Interpillow sediment:	2.30	1.50	27.04
Leg 185 altered basalt + sediment:		0.13	100.00

Notes: Calculations made using logged percentages of different components and shipboard X-ray fluorescence analyses of fresh and altered materials. See ["Alteration Geochemistry,"](#) p. 27, for discussion.

Table T11. Summary of index properties and compressional wave velocities of discrete samples from the igneous section of Site 801 along with lithology, structure, and igneous unit defined during Leg 185. (See table notes. Continued on next three pages.)

Core, section, interval (cm)	Depth (mbsf)	Wet bulk density (g/cm ³)		Grain density (g/cm ³)	Porosity (%)	Void ratio	Water content (bulk (%))	Compressional wave velocity (m/s)			Lithology	Igneous structure	Igneous unit
		(Gravimetric)	(GRAPE)					x direction	y direction	z direction			
129-801B-													
37R-1, 56-58	462.04	2.38	2.34	2.75	19.3		8.3	3622		3461	Aphyric basalt	Flow	
39R-1, 9-11	470.79	2.66	2.52	2.60	3.3		1.3	5138		5035	Chert		
40R-1, 38-40	477.28		2.42		19.1			3565		3805	Aphyric basalt	Flow	
41R-2, 95-97	485.45		2.63		11.6			4454		4843	Aphyric basalt	Flow	
42R-2, 95-97	490.00	2.71	2.65	2.85	9.6		3.6	4694		4838	Aphyric dolerite	Flow	
129-801C-													
1R-1, 90-92	494.60	2.67	2.62	2.84	9.5		3.6	4652		4589	Aphyric microdolerite	Flow	1
1R-3, 82-84	497.13	2.59	2.60	2.77	10.4		4.1	4374		4436	Phyric basalt	Flow	2
1R-5, 29-31	499.84	2.59	2.61	2.71	7.1		2.8	5087		5154	Aphyric basalt	Flow	2
2R-1, 14-16	503.14	2.47	2.48	2.96	13.2		5.4	4266		4267	Phyric basalt	Flow	3
2R-2, 81-83	505.19	2.63	2.65	2.69	9.6		3.7	4866		4866	Aphyric basalt	Flow	3
2R-4, 76-78	507.86	2.66	2.63	2.80	10.1		3.9	4808		4757	Microphyric basalt	Flow	6
3R-1, 32-34	512.52	2.38	2.39	2.84	18.7		8.0	3755		3746	Aphyric basalt	Flow	7
4R-1, 44-46	522.14	2.52	2.49	2.69	8.0		3.2	5112		5141	Hydrothermal deposit (yellow/red)	Hydrothermal	8
5R-1, 103-105	532.23	2.41	2.35	2.65	16.0		6.8	3879		3982	Megaphyric basalt	Pillow/flow	9
5R-2, 87-89	533.33	2.53	2.52	2.67	14.0		5.6	4592		4510	Megaphyric basalt	Pillow/flow	9
5R-3, 43-45	534.20	2.64	2.62	2.77	10.8		4.2	4966		4990	Phyric basalt	Pillow	9
6R-1, 115-117	541.65	2.37	2.36	2.84	23.0		9.8	3479		3690	Aphyric basalt	Flow	15
6R-2, 35-37	542.14	2.80	2.79	2.78	2.4		0.9	5975		5994	Phyric basalt	Flow	16
6R-4, 111-113	545.76	2.36	2.36	2.85	20.3		8.7	3879		3773	Microphyric basalt	Flow	20
6R-5, 68-70	546.71	2.94	2.92	2.70	1.7		0.6	6323		6313	Aphyric basalt	Flow	20
7R-1, 35-37	550.45	2.96	2.92	2.98	1.3		0.5	6414		6333	Aphyric basalt	Flow	21
7R-2, 37-39	551.92	2.67	2.71	2.99	7.9		3.0	5248		5281	Aphyric basalt	Flow	22
8R-1, 65-67	560.15	2.47	2.48	2.81	18.8		7.7	4088		4108	Aphyric basalt	Pillow/flow	24
8R-2, 78-80	561.35	2.97	2.94	2.81	1.0		0.3	6593		6588	Aphyric basalt	Pillow/flow	24
9R-1, 49-51	563.69	2.86	2.85	2.99	3.3		1.2	6442		6367	Aphyric basalt	Flow	25
9R-3, 121-123	567.15	2.88	2.88	2.92	2.5		0.9	6364		6077	Aphyric basalt	Flow	25
9R-4, 137-139	568.58	2.91	2.91	2.93	2.7		0.9	6114		6325	Aphyric basalt	Flow	25
10R-2, 55-57	571.05	2.92	2.90	2.96	2.6		0.9	6224		6218	Aphyric basalt	Flow	25
10R-5, 3-5	574.84	2.92	2.91	2.97	2.1		0.7	6275		6234	Microphyric basalt	Flow	25
10R-6, 65-67	576.81	2.86	2.86	2.96	2.7		1.0	5981		6040	Microphyric basalt	Flow	25
11R-2, 119-121	580.49	2.85	2.84	2.91	2.9		1.0	6050		6102	Microphyric basalt	Flow	27
11R-3, 40-42	581.20	2.87	2.87	2.91	2.3		0.8	6204		6304	Aphyric basalt	Flow	28
12R-1, 70-72	588.00	2.59	2.66	2.75	9.4		3.6	5027		5011	Aphyric basalt	Pillow	31
12R-2, 109-111	589.89	2.92	2.91	2.96	2.1		0.7	6245		6178	Aphyric basalt	Flow	32
185-801C-													
14R-1, 38-40	604.38	2.83	2.42	2.92	4.7	0.05	1.7	5443	5463	5392	Aphyric basalt	Flow	34
14R-2, 81-83	606.12	2.52	2.04	2.85	18.0	0.22	7.3	4195	4239	4286	Aphyric basalt	Flow	34
14R-2, 121-123	606.52	2.82	2.28	2.89	3.6	0.04	1.3	5221	5270	5288	Aphyric basalt	Pillow	35
14R-3, 44-46	607.22	2.56	2.09	2.79	13.4	0.16	5.4	4476	4300	4582	Aphyric basalt	Pillow/flow	37-2
14R-3, 96-98	607.74	2.58	2.03	2.87	15.6	0.19	6.2	3921	4125	4022	Interpillow material (orange)	Pillow	37-5
14R-4, 10-12	608.26	2.63	2.27	2.83	11.0	0.12	4.3	4939	4944	5032	Aphyric basalt	Pillow	37-7
14R-5, 51-53	610.13	2.75	2.34	2.85	5.8	0.06	2.2	5430	5389	5356	Aphyric basalt	Pillow/flow	38-4
15R-1, 12-14	613.82	2.74	2.19	2.79	2.6	0.03	1.0	5882	5815	5882	Interpillow material (white/green)	Breccia	39

Table T11 (continued).

Core, section, interval (cm)	Depth (mbsf)	Wet bulk density (g/cm ³)		Grain density (g/cm ³)	Porosity (%)	Void ratio	Water content (bulk (%))	Compressional wave velocity (m/s)			Lithology	Igneous structure	Igneous unit
		(Gravimetric)	(GRAPE)					x direction	y direction	z direction			
15R-1, 72-74	614.42	2.89	2.32	2.98	4.6	0.05	1.6	5655	5444	4779	Interpillow sediment (red)	Sediment	40
15R-2, 9-11	615.11	2.67	2.16	2.80	7.5	0.08	2.9	5092	4362	4978	Aphyric basalt	Pillow	41-3
15R-3, 50-52	616.91	2.62	2.19	2.77	8.6	0.09	3.4	4910	4863	4630	Aphyric basalt	Pillow	43-5
15R-3, 118-120	617.59	2.82	2.21	2.83	0.6	0.01	0.2	6060	6005	6119	Interpillow material (red/brown)	Sediment	43-8
15R-4, 60-62	618.31	2.81	2.34	2.91	5.3	0.06	1.9	5655	5557	5698	Aphyric basalt	Flow	44
15R-5, 74-76	619.77	2.85	2.31	2.93	4.2	0.04	1.5	5312	5437	5187	Aphyric basalt	Flow	44
15R-6, 14-16	620.12	2.70	2.27	2.90	10.4	0.12	3.9	4733	4394	4585	Aphyric basalt	Flow	45
15R-7, 13-15	621.51	2.38	1.85	2.77	22.4	0.29	9.6	3475	3579	3538	Aphyric basalt (pale green)	Pillow	46-2
15R-7, 51-53	621.89	2.75	2.27	2.77	1.3	0.01	0.5	5240	5453	5312	Interpillow material (brownish red)	Sediment	46-3
16R-1, 89-91	624.19	2.87	2.34	2.96	4.4	0.05	1.6	5695	5605	5728	Aphyric basalt	Pillow	47-3
16R-2, 98-100	625.72	2.47	1.83	2.85	21.1	0.27	8.8	3364	3382	3534	Aphyric basalt (pale green)	Pillow	47-5
16R-3, 8-10	626.10	2.59	2.19	2.70	6.2	0.07	2.5	4962	4896	4736	Hydrothermal deposit (yellow)	Hydrothermal	48
16R-3, 85-87	626.87	2.41	1.92	2.89	25.6	0.34	10.9	3187	3234	3290	Aphyric basalt (green)	Pillow	49-2
16R-4, 1-3	627.44	2.90	2.50	3.11	10.0	0.11	3.5	5824	5749	5933	Aphyric basalt	Flow	49-3
16R-4, 72-74	628.15	2.92	2.45	2.98	3.2	0.03	1.1	5817	5933	5805	Aphyric basalt	Flow	49-3
16R-5, 49-51	629.38	2.84	2.22	2.95	5.9	0.06	2.1	5167	5196	5280	Aphyric basalt	Pillow	49-5
17R-1, 50-52	633.30	2.94	2.43	2.98	2.2	0.02	0.8	5855	5854	5706	Aphyric basalt	Pillow	49-7
17R-3, 37-39	636.15	2.89	2.43	2.98	4.8	0.05	1.7	6131	5713	5753	Aphyric basalt	Pillow	49-11
17R-3, 121-123	636.99	2.60	2.03	2.92	16.8	0.20	6.6	4184	4253	4156	Aphyric basalt	Pillow	49-13
17R-4, 88-90	638.10	2.68	1.51	2.71	1.9	0.02	0.7	4678	5591	5860	Interpillow material (white/green)	Pillow	50-5
18R-1, 79-81	642.99	2.78	2.34	2.89	5.9	0.06	2.2	5330	5329	5451	Aphyric basalt	Pillow	50-8
18R-2, 30-32	644.00	2.74	1.72	2.87	6.6	0.07	2.5	5366	5280	5374	Aphyric basalt	Pillow	50-10
19R-1, 71-73	652.41	2.74	2.34	2.86	6.6	0.07	2.5	4969	5001	5171	Aphyric basalt	Flow	50-14
19R-3, 6-8	654.45	2.85	2.40	2.95	5.0	0.05	1.8	5123	5316	5356	Aphyric basalt	Flow	50-18
20R-1, 45-47	661.15	2.72	2.21	2.93	10.8	0.12	4.1	4758	4744	4737	Aphyric basalt	Flow	50-21
20R-2, 94-96	663.06	2.69	2.19	2.86	9.2	0.10	3.5	4845	4800	4832	Aphyric basalt	Flow	50-24
21R-1, 100-102	671.00	2.91	2.40	2.97	3.2	0.03	1.1	5652	5761	5768	Aphyric basalt	Pillow/flow	50-26
21R-2, 117-119	672.60	2.73	2.32	2.85	6.9	0.07	2.6	5361	5441	5360	Aphyric basalt	Pillow/flow	50-27
21R-3, 70-72	673.35	2.71	2.22	2.85	7.6	0.08	2.9	5100	5184	5226	Aphyric basalt	Pillow/flow	50-27
22R-1, 5-7	673.65	2.65	2.13	2.71	3.5	0.04	1.4	5008			Hydrothermal rubble	Hydrothermal	
22R-1, 114-116	674.74	2.44	2.09	2.88	23.6	0.31	9.9	4057	5155	4711	Aphyric basalt with vein	Pillow/flow	50-36
22R-2, 60-62	675.44	2.84	2.38	2.93	4.9	0.05	1.8	5252	5338	5277	Aphyric basalt	Flow	50-39
23R-1, 39-41	682.29	2.86	2.18	2.95	4.4	0.05	1.6	5563	5641	5670	Aphyric basalt	Flow	50-43
23R-1, 97-99	682.87	2.76	2.19	2.89	7.4	0.08	2.8				Pillow rubble	Flow	50-43
23R-2, 64-66	683.79	2.81	1.34	2.97	8.2	0.09	3.0				Pillow rubble	Flow	50-44
23R-3, 41-43	684.99	2.88	2.34	2.96	3.7	0.04	1.3	5443	5439	5480	Aphyric basalt	Flow	50-45
23R-4, 58-60	686.56	2.78	2.18	2.93	7.9	0.09	2.9	4979	4953	4966	Aphyric basalt	Pillow/flow	50-48
24R-1, 35-37	691.65	2.79	2.28	2.93	7.3	0.08	2.7	5188	5038	5142	Aphyric basalt	Pillow/flow	50-51
24R-2, 44-46	693.07	2.86	2.26	2.98	6.1	0.07	2.2	5371	5489	5543	Aphyric basalt	Flow	50-55
24R-3, 22-24	694.35	2.87	2.37	2.96	4.6	0.05	1.6	5355	5229	5298	Aphyric basalt	Pillow	50-57
25R-1, 95-97	701.65	2.90	2.51	2.97	3.7	0.04	1.3	5312	5399	5482	Aphyric basalt	Pillow	50-61
26R-1, 96-98	711.16	2.80	2.24	2.96	8.4	0.09	3.1	4942	4960	4961	Aphyric basalt	Flow	50-65
26R-2, 100-102	712.53	2.85	2.03	2.96	5.7	0.06	2.0	5433	5467	5435	Aphyric basalt	Flow	50-65
27R-1, 98-100	720.68	2.82	1.93	3.03	10.5	0.12	3.8	4819	4834	4855	Aphyric basalt	Flow	50-68
27R-2, 39-41	721.37	2.94	2.40	3.02	4.3	0.04	1.5	5458	5404	5437	Aphyric basalt	Flow	50-69
27R-3, 84-86	723.32		2.40					5444	5448	5579	Aphyric basalt	Flow	50-71
27R-4, 141-143	725.19	2.91	2.51	2.97	3.1	0.03	1.1	5605	5757	5703	Aphyric basalt	Flow	50-71

Table T11 (continued).

Core, section, interval (cm)	Depth (mbsf)	Wet bulk density (g/cm ³)		Grain density (g/cm ³)	Porosity (%)	Void ratio	Water content (bulk (%))	Compressional wave velocity (m/s)			Lithology	Igneous structure	Igneous unit
		(Gravimetric)	(GRAPE)					x direction	y direction	z direction			
28R-1, 88-90	729.57	2.57	1.62	2.71	8.2	0.09	3.3				Aphyric basalt	Flow	50-71
28R-2, 22-24	730.26	2.92	2.43	2.99	3.4	0.04	1.2	5627	5498	5520	Aphyric basalt	Flow	50-72
28R-3, 144-146	732.98	2.86	2.11	2.95	4.9	0.05	1.7	5222	5212	5279	Sparsely olivine phyric basalt	Flow	51-1
29R-1, 96-98	738.86	2.77	2.35	2.90	6.8	0.07	2.5	4819	4957	4949	Sparsely olivine phyric basalt	Flow	51-2
30R-1, 19-21	747.49	2.81	2.35	2.91	5.1	0.05	1.9	5225	5166	5247	Sparsely olivine phyric basalt	Flow	51-2
30R-2, 101-103	749.75	2.90	2.46	2.96	2.8	0.03	1.0	5548	5726	5629	Sparsely olivine phyric basalt	Flow	51-2
30R-3, 67-69	750.73	2.87	2.44	2.92	2.6	0.03	0.9	5548	5500	5646	Sparsely olivine phyric basalt	Flow	51-2
30R-4, 5-7	751.43	2.89	2.48	2.96	3.2	0.03	1.1				Sparsely olivine phyric basalt	Flow	51-2
30R-5, 12-14	752.28	2.89	2.19	2.99	5.4	0.06	1.9				Sparsely olivine phyric basalt	Flow	51-3
31R-1, 40-42	757.00	2.77	2.06	2.99	11.0	0.12	4.1	4565	4556	4485	Sparsely olivine phyric basalt	Flow	51-5
31R-2, 86-88	758.76	2.99	2.36	3.05	2.9	0.03	1.0	5816	5773	5723	Sparsely olivine phyric basalt	Flow	51-6
31R-3, 50-52	759.68	2.94	2.47	2.99	2.7	0.03	0.9	5463	5683	5747	Sparsely olivine phyric basalt	Flow	51-6
31R-4, 52-54	761.11	2.92	2.40	2.97	2.5	0.03	0.9	5700	5669	5686	Sparsely olivine phyric basalt	Flow	51-6
31R-5, 1-3	762.05	2.93	2.53	2.99	2.7	0.03	0.9	5747	5732	5666	Sparsely olivine phyric basalt	Flow	51-6
31R-7, 93-95	765.67	2.91	2.44	2.97	3.0	0.03	1.0	5614	5555	5585	Sparsely olivine phyric basalt	Flow	51-6
32R-1, 25-27	766.55	2.80	2.13	2.97	8.8	0.10	3.2	4866	4951	5049	Sparsely olivine phyric basalt	Flow	51-6
32R-1, 66-68	766.96	2.74	2.12	2.91	9.4	0.10	3.5				Aphyric basalt	Breccia	52-1
32R-2, 57-59	768.37	2.90	1.88	3.01	5.6	0.06	2.0	5088	5005	5003	Aphyric basalt	Pillow/flow	52-4
33R-1, 11-13	775.81	2.49	2.31	2.58	5.8	0.06	2.4	4970	4975	4999	Aphyric basalt	Pillow/flow	52-4
34R-1, 48-50	785.78		2.34					5149	5071	5165	Sparsely olivine phyric basalt	Pillow/flow	53-2
34R-2, 61-63	787.15	2.58	2.35	2.66	5.3	0.06	2.1	5161	5084	5123	Sparsely olivine phyric basalt	Pillow/flow	53-3
34R-3, 129-131	789.30	2.92	2.43	3.03	5.6	0.06	2.0	5206	5226	5255	Sparsely olivine phyric basalt	Flow	53-7
35R-1, 84-86	795.74	2.76	2.32	2.90	7.0	0.08	2.6	4978	4953	4982	Sparsely olivine phyric basalt	Flow	53-8
35R-2, 4-6	796.31	2.83	2.42	2.96	6.8	0.07	2.5	4967	5005	5042	Sparsely olivine phyric basalt	Flow	53-8
35R-2, 122-124	797.49	2.82	2.30	2.92	5.6	0.06	2.0	5264	5175	5195	Sparsely olivine phyric basalt	Pillow/flow	53-9
35R-4, 9-11	799.21	2.92	2.29	3.02	4.7	0.05	1.6	5308	5269	5263	Sparsely olivine phyric basalt	Flow	53-12
36R-1, 61-63	804.71	2.84	2.35	2.98	7.1	0.08	2.6	5071	5048	5105	Aphyric basalt	Flow	53-14
36R-1, 113-115	805.23	2.85	2.34	2.98	6.6	0.07	2.4	5014	4994	5018	Aphyric basalt	Flow	53-14
36R-2, 11-13	805.55	2.81	2.40	2.93	6.2	0.07	2.3	5151	5112	5144	Aphyric basalt	Pillow	53-15
36R-3, 41-43	807.18	2.78	2.11	2.94	8.3	0.09	3.1	4740	4842	4855	Aphyric basalt	Flow	53-16
36R-4, 106-108	809.25	2.79	2.30	2.91	6.5	0.07	2.4	4902	4921	4970	Aphyric basalt	Flow	53-19
37R-1, 140-142	814.70	2.85	2.36	2.94	4.5	0.05	1.6	5258	5211	5306	Aphyric basalt	Flow	54
37R-2, 42-44	815.17	2.79	2.25	2.90	5.9	0.06	2.2	5209	5230	5234	Aphyric basalt	Flow	54
37R-3, 117-119	817.02	2.91	2.39	2.99	4.2	0.04	1.5	5649	5616	5686	Aphyric basalt	Flow	54
37R-4, 8-10	817.34	2.96	2.47	3.02	2.9	0.03	1.0	5646	5662	5681	Aphyric basalt	Flow	54
37R-5, 79-81	819.25	2.43	2.13	2.94	26.5	0.36	11.2				Aphyric basalt (green-gray)	Flow	54
37R-6, 72-74	820.52	2.87	2.35	2.95	4.0	0.04	1.4	5443	5541	5693	Aphyric basalt	Flow	54
37R-7, 68-70	821.98	2.85	2.31	2.95	5.2	0.05	1.9	5249	5352	5380	Aphyric basalt	Flow	54
38R-1, 35-37	823.15	2.90	2.38	2.99	4.9	0.05	1.7	5405	5442	5462	Aphyric basalt	Flow	54
38R-2, 113-115	825.39		2.35					5158	5093	5170	Aphyric basalt	Flow	54
38R-2, 145-147	825.71	2.65	2.17	2.82	9.8	0.11	3.8				Aphyric basalt	Pillow	55-1
39R-1, 104-106	833.24	2.82	2.36	2.93	5.8	0.06	2.1	5077	5106	5161	Aphyric basalt	Flow	55-6
39R-2, 10-12	833.77	2.84	1.56	3.01	8.7	0.10	3.1				Aphyric basalt	Flow	55-6
39R-2, 80-82	834.47	2.67	1.15	2.70	1.8	0.02	0.7				Aphyric basalt	Flow	55-6
40R-1, 113-115	842.63	2.80	1.60	2.93	6.9	0.08	2.5				Aphyric basalt breccia	Breccia	56
40R-2, 68-70	843.66	2.75	2.19	2.97	11.2	0.13	4.2	4433	4454	4525	Aphyric basalt breccia	Breccia	56
40R-3, 62-64	845.01	2.59	2.15	2.88	9.8	0.11	3.7				Aphyric basalt breccia	Breccia	56

Table T11 (continued).

Core, section, interval (cm)	Depth (mbsf)	Wet bulk density (g/cm ³)		Grain density (g/cm ³)	Porosity (%)	Void ratio	Water content (bulk (%))	Compressional wave velocity (m/s)			Lithology	Igneous structure	Igneous unit
		(Gravimetric)	(GRAPE)					x direction	y direction	z direction			
41R-1, 109-111	851.89	2.84	2.37	2.92	4.1	0.04	1.5	5133	5328	5279	Aphyric basalt	Flow	57
42R-1, 32-33	860.32	2.90	2.38	2.98	4.3	0.04	1.5	5330	5336	5410	Aphyric basalt	Flow	57
42R-2, 4-6	861.25	2.85	2.40	2.96	5.8	0.06	2.1	5075	5028	5086	Aphyric basalt	Flow	57
42R-2, 122-124	862.43	2.41	1.90	2.59	11.9	0.14	5.1				Hyaloclastite breccia	Breccia	58-1
43R-1, 99-101	870.09	2.86	2.34	2.97	6.0	0.06	2.1	5256	5252	5252	Aphyric basalt	Pillow	58-3
43R-2, 112-114	871.68	2.77	2.28	2.96	9.6	0.11	3.5	4753	4642	4723	Aphyric basalt	Flow	58-3
43R-3, 128-130	873.20	2.80	0.05	2.96	8.6	0.09	3.1				Aphyric basalt	Flow	58-3
44R-1, 18-20	878.98	2.80	2.35	2.98	9.0	0.10	3.3	4638	4866	4846	Aphyric basalt	Flow	59
44R-2, 62-64	880.68	2.85	2.32	2.99	7.4	0.08	2.7	4932	5060	5120	Aphyric basalt	Flow	59
44R-3, 32-34	881.88	2.73	2.29	2.91	9.7	0.11	3.6	4730	4558	4727	Aphyric basalt	Flow	59
45R-1, 47-49	888.87	2.74	2.31	2.91	9.0	0.10	3.3				Aphyric basalt	Pillow	60-2
45R-2, 34-36	890.10	2.74	2.23	2.91	9.0	0.10	3.4	4734	4749	4840	Aphyric basalt	Pillow/flow	60-4
45R-2, 72-74	890.48	2.71	0.11	2.91	10.3	0.12	3.9				Aphyric basalt	Flow	60-5
46R-1, 19-21	898.19	2.85	2.33	2.97	5.8	0.06	2.1	5050	4969	5038	Aphyric basalt	Flow	60-7
46R-2, 90-92	900.32	2.73	2.17	2.88	8.1	0.09	3.0	4621	4647	4776	Aphyric basalt	Flow	60-7
46R-3, 36-38	901.07	2.70	2.20	2.84	7.7	0.08	2.9	4704	4800	4880	Aphyric basalt	Pillow/flow	60-8
47R-1, 29-35	907.99	2.75	2.06	2.85	5.7	0.06	2.1	5072	5135	5227	Aphyric basalt	Pillow	60-11
48R-1, 49-51	917.19	2.94	2.29	3.00	3.0	0.03	1.0	5443	5532	5569	Aphyric basalt	Pillow/flow	60-13
48R-2, 98-100	918.98	2.91	2.37	2.97	3.3	0.03	1.2	5582	5581	5571	Aphyric basalt	Pillow/flow	60-15
49M-1, 43-45	928.73	2.78	2.29	2.91	6.8	0.07	2.5	4994	5091	5177	Aphyric basalt	Pillow	60-18
50M-1, 43-45	931.93	2.79	2.08	2.94	7.8	0.09	2.9				Aphyric basalt	Pillow	60-22
51M-1, 37-39	932.37	2.13	2.05	2.68	33.3	0.50	16.0				Hyaloclastite breccia (saponite)	Pillow	60-23
52M-1, 8-10	932.88	2.96	2.36	3.03	3.4	0.04	1.2	5341	5506	5526	Aphyric basalt	Pillow/flow	60-26

Notes: Leg 129 data from tables 6 and 7 in the *Initial Reports*, Leg 129 volume "Site 801" chapter (Lancelot, Larson, et al., 1990). This table is also available in [ASCII format](#).

Table T12. Compressional wave velocity measured on split cores in the x direction. (See table note. Continued on next page).

Core, section, interval (cm)	Depth (mbsf)	Velocity (m/s)	Core, section, interval (cm)	Depth (mbsf)	Velocity (m/s)
185-801C-			22R-3, 74	677.08	5053
14R-1, 44	604.44	5472	23R-1, 19	682.09	5705
14R-1, 90	604.90	5960	23R-1, 37	682.27	5873
14R-2, 34	605.65	6147	23R-2, 34	683.49	5470
14R-2, 108	606.39	3734	23R-2, 76	683.91	5082
14R-2, 122	606.53	5452	23R-2, 131	684.46	5366
14R-3, 23	607.01	4164	23R-3, 43	685.01	5531
14R-3, 80	607.58	4274	23R-4, 36	686.34	4679
14R-3, 116	607.94	4528	24R-1, 14	691.44	5674
14R-4, 39	608.55	4939	24R-1, 109	692.39	4615
14R-4, 123	609.39	5389	24R-2, 45	693.08	5615
14R-5, 38	610.00	5500	24R-3, 25	694.38	5446
14R-5, 80	610.42	5209	25R-1, 58	701.28	4585
15R-1, 17	613.87	5372	25R-1, 97	701.67	5447
15R-1, 74	614.44	5297	25R-1, 141	702.11	4978
15R-1, 124	614.94	4627	26R-1, 20	710.40	3126
15R-2, 9	615.11	5034	26R-1, 44	710.64	4962
15R-2, 115	616.17	4350	26R-1, 90	711.10	5115
15R-3, 16	616.57	4629	26R-1, 121	711.41	5038
15R-3, 94	617.35	5426	26R-2, 31	711.84	4819
15R-4, 45	618.16	5825	26R-2, 104	712.57	5070
15R-4, 98	618.69	5628	27R-1, 18	719.88	5532
15R-5, 15	619.18	6139	27R-1, 64	720.34	4881
15R-5, 72	619.75	5514	27R-2, 41	721.39	5677
15R-6, 32	620.30	5257	27R-2, 101	721.99	5438
15R-6, 108	621.06	3948	27R-3, 53	723.01	5333
15R-7, 32	621.70	3538	27R-3, 125	723.73	5920
15R-7, 105	622.43	4218	27R-4, 27	724.05	5646
16R-1, 58	623.88	6156	27R-4, 116	724.94	6257
16R-1, 120	624.50	4877	27R-5, 81	726.03	5876
16R-2, 23	624.97	4191	28R-1, 10	728.80	5925
16R-2, 87	625.61	4030	28R-1, 38	729.08	5663
16R-3, 27	626.29	5302	28R-1, 77	729.47	5667
16R-3, 59	626.61	4446	28R-1, 131	730.01	5567
16R-3, 89	626.91	3513	28R-2, 24	730.28	5676
16R-3, 127	627.29	5047	28R-2, 57	730.61	5799
16R-4, 77	628.20	5902	28R-2, 101	731.05	4859
16R-4, 125	628.68	4865	28R-2, 129	731.33	5028
16R-5, 46	629.35	4881	28R-3, 15	731.69	5106
16R-5, 96	629.85	4776	28R-3, 79	732.33	4962
17R-1, 48	633.28	5927	28R-3, 146	733.00	5002
17R-1, 120	634.00	6073	29R-1, 17	738.07	5079
17R-2, 52	634.80	5619	29R-1, 47	738.37	5347
17R-3, 38	636.16	5578	29R-1, 77	738.67	4879
17R-3, 81	636.59	5228	29R-1, 98	738.88	4917
17R-4, 44	637.66	5050	29R-2, 20	739.55	5258
17R-4, 89	638.11	5573	30R-1, 27	747.57	5592
18R-1, 56	642.76	5176	30R-1, 93	748.23	5789
18R-2, 61	644.31	5078	30R-2, 12	748.86	5402
18R-2, 111	644.81	4467	30R-2, 100	749.74	5932
19R-1, 72	652.42	5120	30R-3, 69	750.85	5758
19R-3, 7	654.46	5371	30R-3, 121	751.36	5539
20R-1, 41	661.11	4593	30R-4, 14	751.62	5742
20R-1, 114	661.84	4551	31R-1, 65	757.25	4845
20R-2, 49	662.61	5248	31R-1, 119	757.79	5200
20R-2, 97	663.09	4691	31R-2, 16	758.06	5804
20R-3, 43	664.05	5547	31R-2, 78	758.68	5832
21R-1, 19	670.19	5748	31R-3, 32	759.50	5742
21R-1, 92	670.92	5233	31R-3, 89	760.07	5631
21R-2, 8	671.51	5000	31R-3, 129	760.47	5937
21R-2, 81	672.24	5194	31R-4, 21	760.80	5923
21R-3, 11	672.76	5207	31R-5, 22	762.26	5379
21R-3, 71	673.36	4902	31R-5, 115	763.19	5646
22R-1, 45	674.05	5276	31R-6, 27	763.61	5731
22R-1, 116	674.76	4079	31R-6, 73	764.07	5592
22R-2, 48	675.32	4847	31R-6, 115	764.49	5371
22R-2, 82	675.66	5460	31R-7, 36	765.10	5529
22R-3, 42	676.76	5232	31R-7, 80	765.54	5663

Table T12 (continued).

Core, section, interval (cm)	Depth (mbsf)	Velocity (m/s)	Core, section, interval (cm)	Depth (mbsf)	Velocity (m/s)
31R-7, 133	766.07	5261	38R-2, 132	825.58	4633
32R-1, 25	766.55	5208	38R-3, 84	826.60	4504
32R-1, 119	767.49	4741	39R-1, 65	832.85	4633
32R-2, 19	767.99	4197	39R-1, 125	833.45	5453
33R-1, 24	775.94	4936	39R-2, 26	833.93	4662
33R-1, 96	776.66	4967	39R-2, 87	834.54	5123
34R-1, 18	785.48	5187	40R-1, 29	841.79	5164
34R-1, 81	786.11	5077	40R-1, 139	842.89	4711
34R-1, 118	786.48	4435	40R-2, 21	843.19	4795
34R-2, 23	786.77	4880	40R-2, 68	843.66	4625
34R-2, 57	787.11	4701	40R-2, 118	844.16	4650
34R-2, 119	787.73	5230	40R-3, 127	845.66	4378
34R-3, 15	788.16	5075	41R-1, 112	851.92	5516
34R-3, 56	788.57	4847	42R-1, 26	860.26	5502
34R-3, 135	789.36	5312	42R-1, 91	860.91	5222
35R-1, 36	795.26	5559	42R-2, 13	861.34	5289
35R-1, 77	795.67	4844	42R-2, 37	861.58	4906
35R-1, 110	796.00	5407	43R-1, 23	869.33	5266
35R-2, 11	796.38	4980	43R-1, 60	869.70	4964
35R-2, 60	796.87	5162	43R-1, 102	870.12	5361
35R-2, 120	797.47	5354	43R-2, 52	871.08	4636
35R-3, 24	797.86	4980	43R-2, 93	871.49	4509
35R-3, 110	798.72	5167	43R-2, 113	871.69	4700
35R-4, 15	799.27	5037	43R-3, 37	872.29	4645
35R-4, 46	799.58	4172	43R-3, 108	873.00	4952
36R-1, 19	804.29	4877	44R-1, 88	879.68	4754
36R-1, 107	805.17	5201	44R-1, 121	880.01	5158
36R-2, 28	805.72	5154	44R-2, 62	880.68	5012
36R-3, 20	806.97	4818	44R-2, 115	881.21	5058
36R-3, 92	807.69	4686	44R-3, 14	881.70	4746
36R-4, 44	808.63	5225	44R-3, 33	881.89	4738
36R-4, 125	809.44	4779	45R-2, 47	890.23	5027
37R-1, 43	813.73	5493	46R-1, 15	898.15	5083
37R-1, 113	814.43	5297	46R-1, 79	898.79	5334
37R-2, 29	815.04	5167	46R-1, 130	899.30	5315
37R-2, 91	815.66	4974	46R-2, 24	899.66	4921
37R-3, 49	816.34	5462	46R-2, 901	900.33	5019
37R-3, 108	816.93	5604	46R-3, 31	901.02	4772
37R-4, 43	817.69	5315	47R-1, 51	908.21	5544
37R-4, 104	818.30	5694	48R-1, 19	916.89	5570
37R-5, 53	818.99	5316	48R-1, 59	917.29	5544
37R-5, 71	819.17	4142	48R-2, 89	918.89	5489
37R-5, 106	819.52	4159	48R-3, 17	919.67	5836
37R-6, 71	820.51	5520	49M-1, 28	928.58	4973
37R-6, 120	821.00	5461	50M-1, 34	931.84	5460
37R-7, 37	821.67	5213	51M-1, 44	932.44	5506
37R-7, 82	822.12	5194	52M-1, 9	932.89	5703
38R-1, 39	823.19	5450	52M-1, 41	933.21	5388
38R-1, 68	823.48	5547	52M-1, 64	933.44	4681
38R-1, 120	824.00	5222			
38R-2, 47	824.73	5499			

Note: This table is also available in [ASCII format](#).

Table T13. Thermal conductivity values.

Core, section, interval (cm)	Depth (mbsf)	TC (W/[m·K])
129-801B-		
37R-1, 56-58	462.04	1.50
40R-1, 38-40	477.28	1.65
41R-2, 95-97	485.45	1.76
42R-2, 95-97	489.63	1.75
43R-1, 42-44	492.62	1.80
43R-3, 121-123	496.19	1.80
44R-1, 54-56	502.24	1.67
129-801C-		
1R-1, 90-92	494.60	1.82
1R-3, 82-84	497.13	1.62
1R-5, 29-31	489.84	1.91
2R-4, 76-78	507.86	1.82
3R-1, 32-34	512.52	1.60
4R-1, 44-46	522.14	4.98
5R-1, 103-105	532.23	1.65
5R-2, 87-89	533.33	1.65
5R-3, 43-45	534.20	1.73
6R-1, 115-117	541.65	1.69
6R-2, 35-37	542.14	1.74
6R-4, 111-113	545.86	1.49
6R-5, 68-70	546.81	1.94
7R-1, 35-37	550.45	2.02
7R-2, 37-39	551.92	1.80
8R-1, 65-67	560.15	1.60
8R-2, 78-80	561.35	1.95
9R-1, 49-51	563.69	2.10
9R-3, 121-123	567.15	1.95
9R-4, 137-139	568.58	1.97
10R-2, 55-57	571.05	2.16
10R-5, 3-5	574.84	1.99
10R-6, 65-67	576.81	2.11
11R-2, 119-121	580.49	2.24
11R-3, 40-42	581.20	2.43
12R-1, 70-72	588.00	1.75
12R-2, 109-111	589.89	1.79
185-801C-		
14R-2, 36-48	605.67	1.66
15R-5, 70-78	619.73	1.70
15R-6, 0-12	619.98	1.49
16R-4, 114-131	628.57	1.55

Core, section, interval (cm)	Depth (mbsf)	TC (W/[m·K])
17R-1, 40-55	633.20	1.62
18R-1, 76-83	642.96	1.59
19R-1, 0-12	651.70	1.56
20R-2, 44-55	662.56	1.62
21R-2, 0-12	671.43	1.73
22R-2, 74-87	675.58	1.75
23R-1, 33-41	682.23	1.67
24R-3, 23-33	694.34	1.54
25R-1, 92-101	701.62	1.60
26R-2, 7-15	711.60	1.62
27R-2, 97-108	721.95	1.68
28R-1, 54-64	729.24	1.74
29R-1, 51-59	738.41	1.65
30R-2, 113-123	749.87	1.71
31R-2, 72-85	758.62	1.83
31R-6, 36-46	763.70	2.15
32R-1, 20-31	766.50	1.59
33R-1, 84-96	776.54	1.61
34R-2, 112-122	787.68	1.93
35R-2, 114-122	797.41	1.64
36R-2, 8-24	805.52	1.51
37R-3, 50-61	816.35	1.82
38R-2, 86-106	825.12	1.83
39R-1, 103-113	833.23	1.64
40R-2, 16-25	843.14	1.60
41R-1, 97-112	851.77	2.01
42R-2, 10-27	861.31	1.66
43R-2, 110-118	871.66	1.62
44R-2, 58-69	880.64	1.70
45R-2, 45-56	890.21	1.63
46R-1, 101-118	899.01	1.67
47R-1, 48-56	908.18	1.66
48R-2, 85-93	918.85	1.65
49M-1, 25-35	928.55	1.58
50M-1, 32-37	931.82	1.62
51M-1, 5-15	932.05	1.54
52M-1, 35-48	933.15	1.59

Notes: Leg 129 data from tables 6 and 7 in the *Initial Reports*, Leg 129 volume "Site 801" chapter (Lancelot, Larson, et al., 1990). TC = thermal conductivity. This table is also available in [ASCII format](#).

Table T14. Chemical composition of interstitial waters, Hole 801D.

Core, section, interval (cm)	Depth (mbsf)	pH	Alkalinity (mM)	Salinity	SO ₄ (mM)	NH ₄ (μm)	H ₄ SiO ₄ (μm)	PO ₄ (μm)	Ca (mM)	Mg (mM)	Na (mM)	K (mM)	Li (μm)	Fe (μm)	Mn (μm)	Sr (μm)	Cl (mM Titr)	Cl (mM IC)
185-801D-																		
1W-1, 140-150	1.40	7.48	2.437	34.5	27.92	23	218	2	10.27	51.70	480	12.26	44	0	0	91	551	559
1W-2, 140-150	2.90	7.28	3.020	34.5	28.15	24	221	4	10.21	51.22	485	13.10	43			91	553	556
1W-3, 140-150	4.40	7.32	2.472	34.5	28.12	23	200	4	10.47	51.32	481	13.12	43			97	558	561
1W-4, 140-150	5.90	7.57	2.596	35.0	28.26		209	4	10.65	51.73	483	13.09	43			98	586	565
1W-5, 140-150	7.40	7.58	2.572	35.0	27.36	35	172	4	10.73	51.57	482	12.39	43			93	562	563
1W-6, 120-130	8.70	7.63	2.655	35.0	26.55	21	181	4	10.77	51.21	477	12.16	42	0	0	92	563	550

Notes: Titr = measured by titration, IC = measured by ion chromatography, blank spaces = not analyzed. This table is also available in [ASCII format](#).

Table T15. Microbiology and tracer test samples, Hole 801C.

Core	Contamination		Cultivation		Preservation		
	Microsphere	PFT	1 atm	In situ pressure	DNA extraction	Microscopy	In situ hybridization
185-801-							
13R							
14R			X	X	X	X	X
15R	X						
16R			X	X	X	X	X
17R	X						
18R				X			
19R				X			
20R							
21R							
22R							
23R	X	X	X	X	X	X	X
24R				X			
25R							
26R							
27R			X	X	X	X	X
28R				X			
29R							
30R							
31R				X			
32R	X						
33R	X						
34R				X			
35R							
36R							
37R	X	X	X	X	X	X	X
38R							
39R							
40R							
41R							
42R				X			
43R				X			
44R							
45R	X						
46R							
47R							
48R				X			
49M							
50M							
51M				X			
52M	X		X	X	X	X	X

Notes: PFT = perfluorocarbon tracer. This table is also available in [ASCII format](#).

Table T16. Hole 801C cores sampled for in situ microbiological cultures.

Core, section, interval (cm)	Piece	Depth (mbsf)	Temperature (°C)	Pressure (atm)	Analyses	Sample description
185-801C-						
14R-3, 106-110	9	607.8	24	620	Microbiology	Altered interpillow material
16R-5, 84-87	10	629.7	25	622	Microbiology	Altered interpillow material
18R-1, 122-135	16	643.4	25	624	Pressure	Silicified breccia
19R-2, 13-20	3	653.3	26	625	Pressure	Whole-rock sample
23R-1, 119-125	10	683.1	26	628	Microbiology	Massive basalt
24R-1, 112-114	12	692.4	27	629	Pressure	Quartz/celadonite fill
27R-3, 19-34	5	722.7	28	632	Microbiology	Glass/hyaloclastite
28R-3, 86-90	8	732.4	28	633	Pressure	Glassy margin
31R-5, 68-70	2E	762.7	29	636	Pressure	Massive basalt with carbonate vein
34R-2, 95-97	2B	787.5	29	638	Pressure	Carbonate vein
37R-1, 27-33	1	813.6	30	641	Microbiology	Carbonate vein
37R-1, 65-66	1	814.0	30	641	Pressure	Thick, brown calcite vein
42R-2, 70-71	3	861.9	31	645	Pressure	Carbonate-cemented breccia
43R-1, 123-127	6	870.3	31	645	Pressure	Quenched margin
48R-2, 24-28	1	918.2	33	650	Pressure	Massive basalt with pyrite
51M-1, 31-32	1B	932.3	33	652	Pressure	Quenched margin/hyaloclast
52M-1, 50-52	3	933.3	33	652	Microbiology	Clay-filled vein

Notes: Temperature calculated from Larson et al. (1993). Microbiology analyses include: cultivation at 1 atm, epifluorescence microscopy, scanning electron microscopy, DNA extraction, in situ hybridization, and preservation at in situ pressure. Pressure samples were maintained at in situ pressure. This table is also available in [ASCII format](#).

Table T17. Thin sections examined for microbial alteration.

Thin section	Core	Section	Top (cm)	Bottom (cm)	Piece	Depth (mbsf)	Unit	Where sampled	Glass	Microbial alteration
	129-801C-									
7	12R	1	85	89	15	588.15	31	Pillow margin	Yes	Yes
	185-801C-									
13	14R	1	120	122	10	607.96	37	Interpillow sediment	No	No
14	15R	1	27	31	4	613.97	39	Chilled pillow margin	No	No
24	16R	1	107	110	13	629.98	49	Interpillow contact	Yes	No
56	17R	1	35	38	6	633.15	49	Flow margin	Yes	No
26	17R	1	85	91	6	636.63	49	Flow interior	Yes	Yes
51	32R	1	67	69	7	766.97	52	Flow bottom	Yes	No
68	42R	1	126	128	11	881.31	58	Hyaloclastite	Yes	Yes
77	48R	1	121	123	13	919.22	60	Flow margin	Yes	Yes

Table T18. Thin sections used in fluorescent microsphere tests.

Core, section, interval (cm)	Piece	Core wash	Crushed rock	Thin section
185-801C-				
15R-1, 4-7	2	+		
15R-1, 27-31	4			+
15R-3, 123-127	4			-
17R-1, 44-47	7A			-
17R-3, 85-91	6			+
23R-1, 27-28	3B			+
23R-1, 119-125	10		-	-
23R-3, 78-83	6	+		
32R-1, 67-69	7			+
33R-1, 123-124	12			-
37R-1, 27-33	1		-	-
37R-1, 63-64	1D			+
37R-3, 34-35	1A	+		+
45R-1, 17-24	5	+		
45R-1, 63-66	8	+		+
45R-1, 64-67	10	+		
45R-2, 45-48	1C			+
52M-1, 50-52	3	+	-	
52M-1, 74-77	4			+
185-1149B-				
32R-1, 22-42	2	+	-	

Notes: + = presence of microspheres; - = absence of microspheres.
 This table is also available in [ASCII format](#).

Table T19. Hole 801C cores analyzed for PFT microbiological contamination studies.

Core, section	Lithology	Position	Weight (g)	PFT (g)	Drilling fluid (mL)	Drilling fluid/rock (mL/g)
Igneous rocks:						
185-801C-						
37R-1	Basalt, methanol*	Interior	0.93	2.8E-11	2.8E-05	3.0E-05
		Interior	1.60	2.0E-11	2.0E-05	1.2E-05
37R-3	Basalt, water*	Interior	2.09	1.8E-11	1.8E-05	8.7E-06
		Interior	2.69	2.7E-11	2.7E-05	9.9E-06
37R-4	Basalt, flame*	Interior	2.79	3.3E-11	3.3E-05	1.2E-05
		Interior	1.89	2.9E-11	2.9E-05	1.5E-05
		Interior	2.44	1.8E-11	1.8E-05	7.5E-06
37R-6	Basalt, whole rock	Exterior	2.71	9.3E-11	9.3E-05	3.4E-05
		Exterior	1.27	5.8E-11	5.8E-05	4.6E-05
		Exterior	1.94	6.4E-11	6.4E-05	3.3E-05
		Exterior	7.22	1.0E-10	1.0E-04	1.4E-05
185-1149C-						
9R-1	Basalt, flame*	Interior	7.93	1.1E-11	1.1E-05	1.4E-06
		Interior	6.72	4.5E-10	4.5E-04	6.8E-05
	Basalt, whole rock	Exterior	6.83	6.0E-09	6.0E-03	8.8E-04
		Exterior	5.92	2.0E-08	2.0E-02	3.3E-03

Notes: PFT = Perfluorocarbon tracer. * = samples were treated with specified method to remove PFT before isolation of interior rock. Table modified from Smith et al., (in press). This table is also available in [ASCII format](#).

Table T20. WSTP depths, temperatures, and chemistry.

	WSTP 1	WSTP 2
Depth (mbsf)	490	540
Temperature (°C)	15.5	22.3
Volume gas (mL)	—	100
Volume water (mL)	—	310
Chlorinity (mM)	—	527
Salinity	—	33
pH	—	8.38
Alkalinity (mM)	—	2.983
SO ₄ ²⁻ (mM)	—	27.1
Ca (mM)	—	9.9
Mg (mM)	—	51
K (mM)	—	9.8
Sr (μM)	—	86
Li (μM)	—	51
Fe	—	Below detection*
Mn	—	Below detection

Notes: WSTP = water sampling temperature pressure tool. * = see ["Water Sampling,"](#) p. 51. — = no water sample collected. This table is also available in [ASCII format](#).

Table T21. WSTP aliquot distribution.

Aliquot	Volume (mL)	Analysis
Coil reservoir:		
1	3	Culture
2	15	DNA extraction
3	2	Isotope
Overflow reservoir:		
4	40	DNA extraction
5	30	Microbial counts
6	8	Shipboard chemistry (alkalinity, pH, Ca, Mg, SiO ₂ , NH ₄ , PO ₄ , Na, K, Cl)
7	5	Trace metals
8	5	δ ¹⁸ O, δD
9	5	δ ¹³ C
10	25	Tritium
11	125	¹⁴ C
12	17	Archive under pressure
13	50	Headspace gas

Notes: WSTP = water sampling temperature pressure tool. This table is also available in [ASCII format](#).

Table T22. Total cell counts of water collected with WSTP, Hole 801C.

	Total cell abundance (cells/mL)	
	WSTP 1	WSTP 2
Nanopure in:	1100 (± 900)	
1st wash out:	3600 (± 1700)	13500 (± 3600)
2nd wash out:	3400 (± 1100)	Not done
Nanopure in:	2300 (± 6700)	
Final wash out:	2900 (± 1200)	2400 (± 1600)
Sample depth (mbsf):	490	540
Sample:	Unsuccessful	Successful
Coil:	48900 (± 11000)	Not tested
Reservoir:	No sample	9600 (± 6000)

Notes: WSTP = water sampling temperature pressure tool. This table is also available in [ASCII format](#).

Table T23. K₂O analyses of core samples.

Core, section, interval (cm)	Depth (mbsf)	AA K ₂ O (wt%)	XRF K ₂ O (wt%)	Sample descriptions
185-801C-				
14R-1, 75.0	604.75	0.074	0.074	Least-altered basalt flow
14R-2, 93.0	606.24	0.490		Fine-grained, black matte, pillow basalt
14R-2, 120.0	606.51	2.058		Deep green granular interpillow sediment
14R-3, 6.0	606.84	2.883		Emerald green chert, below first interpillow
14R-3, 58.0	607.36	0.340		Aphyric pillow, second unit, fresh
		0.410		
14R-3, 71.0	607.49	2.513		Small interpillow, dark green
14R-3, 96.0	607.74	2.823		Interpillow, deep green, mostly precipitated material
		2.334		
14R-3, 120.0	607.98	1.307	1.200	Interpillow, granular sediment
14R-4, 65.0	608.81	0.167	0.145	Minimally altered basalt
15R-1, 30.0	614.00	2.209		Interpillow, celadonite and carbonate, largely precipitated material
15R-1, 93.0	614.63	0.619		Dark green halo around carbonate vein in green pillow breccia
15R-1, 94.0	614.64	0.000		Lighter core of pale green halo, adjacent to Sample 185-801C-15R-1, 93 cm
16R-3, 11.0	626.13	0.101		Fe-Si hydrothermal deposit
16R-3, 50.0	626.52	0.878	0.760	Interpillow sediment
16R-3, 64.0	626.66	0.333		Base of interpillow, deep green
16R-3, 65.0	626.67	1.638		Top of pale green altered basalt
16R-3, 78.0	626.80	0.355		Altered glass, dark green
		0.290		
16R-3, 86.0	626.88	0.292		Darker green altered basalt
16R-3, 108.0	627.10	0.500		Very dark gray basalt
		0.525		
		0.487		
16R-3, 118.0	627.20	0.300		Dark gray basalt
		0.252		
16R-3, 134.0	627.36	0.123		Gray, least-altered basalt

Notes: Data obtained with shipboard atomic absorption (AA) as in “[Analysis of Potassium in Basalts by Atomic Absorption Spectrometry](#),” p. 24, and with X-ray fluorescence (XRF) as in the “[X-Ray Fluorescence Analysis](#),” p. 22, both in the “Explanatory Notes” chapter. This table is also available in [ASCII format](#).

Table T24. MST and AA data used to calibrate NGR.

Core, section, interval (cm)	MST-NGR data (cps)						AA K ₂ O data				
	20 s-A (half)	20 s-B (half)	20 s-C (half)	60 s-A (half)	60 s-B (half)	20 s (whole)	NGR average	Control sample	K ₂ O (wt%)	K ₂ O (interpolation)	Mixing proportion
185-801C-14R-3:								185-801C-			
10	15.3	13.5	15.6	13.9	14.7	4.1		GrChert:14R-3-6	2.883	0.620	50 basalt-15 Grchert-35 zero
20	13.5	11.7	14.9	14.1	15.3	4.5				0.375	100 basalt
30	13.2	15.4	14.2	14.3	14.0	3.0				0.375	100 basalt
40	14.6	14.8	15.6	14.3	14.5	3.2				0.375	100 basalt
50	13.8	14.8	13.8	14.9	15.3	3.6				0.375	100 basalt
60	15.2	13.7	14.4	15.2	14.0	3.3		Basalt: 14R-3-58	0.375	0.375	100 basalt
70	15.0	15.4	13.6	14.7	15.8	6.1		IP1: 14R-3-71	2.513	0.910	75 basalt-25 IP1
80	17.6	16.9	17.7	16.3	17.5	8.8				0.589	90 basalt-10 IP1
90	18.0	19.3	18.2	18.1	19.0	12.3		IP2: 14R-3-96	2.579	1.477	50 basalt-50 IP2
100	19.0	19.0	18.9	18.9	18.9	11.0				1.917	30 basalt-70 IP2
110	18.2	17.9	17.9	17.6	17.3	8.7				1.392	25 basalt-50 IP3-25 IP2
120	19.9	16.1	17.8	17.4	17.7	12.7		IP3: 14R-3-120	1.307	1.027	30 basalt-70 IP3
130	16.4	16.4	15.2	15.4	15.0	5.8				0.608	75 basalt-25 IP3
Average:	16.1	15.7	16.0	15.8	16.1	6.7					
K ₂ O:	0.93	0.81	0.88	0.82	0.91	0.85	0.87			0.801	
Difference from AA:	16%	1%	10%	2%	14%	7%	8%				
RSD (%):							6%				
20 s readings only, % RSD:							7%				
Other core data for calibration:											
185-801C-14R-1:						Average	1.80	185-801C-14R-1-75	0.074	(AA)	Basalt for whole section
						SD	0.49				
185-801C-14R-4:						Average	1.95	185-801C-14R-4-65	0.167	(AA)	Basalt for whole section
						SD	1.16				
185-801C-25R:						Average	3.88	185-801C-25R-1-141	0.080	(XRF)	Basalt for whole core
						SD	0.80				

Notes: MST = multisensor track, AA = atomic absorption, NGR = natural gamma radiation, GrChert = green chert, IP = interpillow, RSD = relative standard deviation, SD = standard deviation, XRF = X-ray fluorescence. NGR data for half- and whole-round cores, readings taken every 10 cm for 20 or 60 s. NGR K₂O calculated from calibration shown in Figure F93B, p. 168. K₂O interpolated from control samples using mixing proportions given.

Table T25. Section, core, and hole averages for MST-NGR and K₂O data.

Interval	MST-NGR (cps)	K ₂ O-MST (wt%)	K ₂ O-Core (wt%)	K ₂ O-NGT (wt%)
185-801C-14R-3	6.70	0.86	0.80	0.96
185-801C-14R	3.89	0.45	0.45	0.53
185-801C-5R through 52M (all tholeiites)	2.89	0.31	Nd	Nd
185-801C-5R through 39R (logged tholeiites)	2.81	0.30	Nd	0.36
185-801C (all tholeiites) 3 cps filter	Nd	0.33	Nd	Nd

Notes: MST = multisensor track, NGR = natural gamma radiation, NGT = natural gamma tool logging data, cps = counts per second, Nd = not determined. MST-NGR data >3 cps is significant; for data >3 cps, the calibration is used; and for data <3 cps, an average value for minimum altered basalt is used (0.08 wt% K₂O).